PhD Thesis

Design and Development of Novel Structured ZnO Based Semiconductor/Dye Sensitized Solar Cells

DIPANKAR BARPUZARY

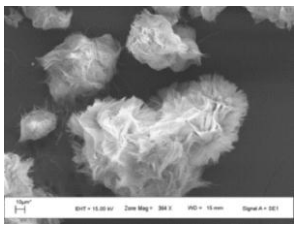
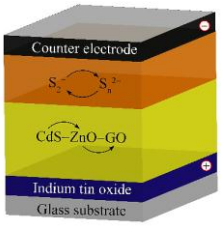

SSSC (PCE ≈ 2.8%)

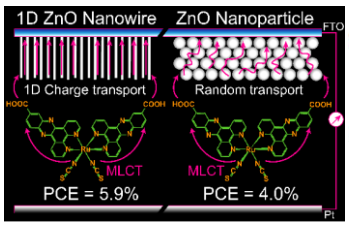

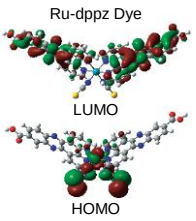

DSSC (PCE ≈ 6.9%)

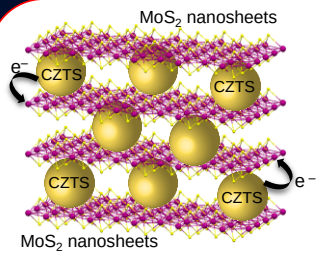

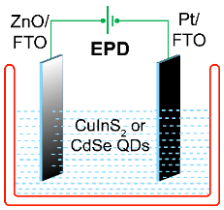

QDSC (PCE ≈ 4.8%)

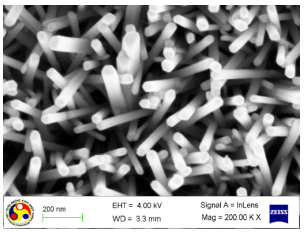

DSSC (PCE ≈ 5.7%)

DEPARTMENT OF CHEMISTRY
INDIAN INSTITUTE OF TECHNOLOGY
GUWAHATI, INDIA
April 2015

Design and Development of Novel Structured ZnO Based Semiconductor / Dye Sensitized Solar Cells

A Dissertation Submitted to the
Indian Institute of Technology Guwahati
as Partial Fulfillment of the Degree of

DOCTOR of PHILOSOPHY

by

Dipankar Barpuzary

Roll No: 10612229

Department of Chemistry

Indian Institute of Technology Guwahati

Guwahati – 781039, Assam, India

April 2015

STATEMENT

I hereby declare that the scientific matter embodied in this thesis entitled, "**Design and Development of Novel Structured ZnO Based Semiconductor/Dye Sensitized Solar Cells**" is the outcome of the research work carried out by me under the supervision of Dr. Mohammad Qureshi, at the Department of Chemistry, Indian Institute of Technology Guwahati, Guwahati, Assam, India, for the award of the degree of Doctor of Philosophy. To the best of my knowledge, the work delineated on this thesis is original and has not been submitted elsewhere for any degree of any other Institute or University.

In keeping with the scientific tradition, whatever work done by others has been utilized, due acknowledgement has been made.

IIT Guwahati
April 2015

Dipankar Barpuzary
Candidate

Dr. Mohammad Qureshi
Associate Professor
Department of Chemistry
Indian Institute of Technology Guwahati
Guwahati – 781036, Assam, India
Tel: +91- 361 2582320; Fax: +91 - 361 2582349
Email: mq@iitg.ernet.in

CERTIFICATE

Certified that the work described in this thesis entitled "**Design and Development of Novel Structured ZnO Based Semiconductor/ Dye Sensitized Solar Cells**" by Mr. Dipankar Barpuzary, Department of Chemistry, Indian Institute of Technology Guwahati has been carried out under my supervision and has not been submitted elsewhere for a degree.

Guwahati
April 2015

Mohammad Qureshi
Thesis supervisor
Department of Chemistry
Indian Institute of Technology Guwahati
Guwahati – 781039, Assam, India

ACKNOWLEDGEMENTS

My endeavour of complete five years of PhD would not have been so easy without the kindness, grace, attention, encouragement, and support of those who have helped me along the way. Today, while bringing it to the end, I would like to scratch the surface in terms of the amount of people I can name to accolade for making this thesis a reality with a lot of enduring memories.

My thesis supervisor, Dr. Mohammad Qureshi, have contributed a great deal to my development as a researcher and person. Being a PhD student of Dr. Qureshi placed me in an advantageous position from day one. His insatiable curiosity, desire to produce excellent science, work ethic, and willingness to help put me in the perfect environment to succeed. I thank him for taking me into his group at the Materials Science Laboratory (MSL), IITG and helping to improve my ability to design and carry out research projects independently, along with the ability to present my ideas in a better way. The freedom he gave me in project design during the stay at MSL allowed me to own the successes and failures that always provided me self-confidence and persistence necessary to produce a good work, in whatever field. I am grateful to Dr. Qureshi for his sincere effort to create an atmosphere in the lab that promotes cordiality, team-works, presentations, and scientific discussions. Apart from the academics, he was always been nice to me in his own way and guided me in right directions. Whenever I was being ecstatic or upset, his good sense of humour always could read my mind. It's been 5 years I worked with him, still I find it hard to open up during our conversations, not because of my anxiousness but because of all the respect. Thank you Sir for continually being a path shower in my life.

I thank my doctoral committee members for the perceptive advices and invaluable suggestions through timely assessments during the PhD course. I am grateful to the faculty and staff at the Department of Chemistry, IIT Guwahati for providing a delightful working environment during this period. I thank Dr. Saurabh S. Soni (Sardar Patel University, Gujrat, India) for teaching me to fabricate dye-sensitized solar cells at the struggling phase of research carrier. I thank Dr. Aditya N. Panda for DFT study and Dr. Chivukula V. Sastri for his suggestions during the dye synthesis.

No words can ever be adequate to express my heartiest thank to all the lab mates to support, encourage, and help me in work, and to maintain a pleasant working environment throughput my PhD tenure. I thank my senior Dr. Ziyauddin Khan for graciously taking so much of time to make me acclimatize to the lab environment, procedures, instrumentation, along with providing encouragement through the early stages of my research career. Special thank is due to my junior Tridip for timely help, scientific conversations, and wonderful time we shared in the last four years. I thank my juniors Momina, Anindya, Gaurangi and Shaad, whose presence made my stay at MSL joyful and memorable, especially Avishek for his indelible help, motivation and encouragement.

I thank Dr. Himanshu S. Jena as a friend cum mentor for helping me in instrumentation and sample analysis at the beginning stages, and for fostering intellectual and scientific discussions. I thank our joint-lab mates Dr. Rajen, Subhashis, Suranjan, Suman, Manoj, Dr. Sangita, and Afsana for companionship and enjoyable moments. I thank other group members Dr. Natarajan, Dr. Jayanta, Ashim M., Saugata, Dr. Muruli, Dr. Subbarao, Radhakrishna, Ashish, Dipjyoti, and all my friends at IITG for making the time spent in the laboratory and outside pleasant and memorable.

I am lucky to have Achyut, Himanshu, Navajyoti, Gautam and Debanga as my friends. I would like to express my sincere gratitude to these wonderful people whose care and love allowed me to express all the ups and downs of my life.

I would like to thank Dr. Babulal Das, Madhurjya Borah, Dr. Kula K. Senapati and Kesho Singh for their time to teach me to operate the instruments (XRD, SEM, FESEM, EDX etc.) and to analyze samples in need. I am thankful to all the operators at the Department of Chemistry and Central Instruments Facility (CIF), IITG for their time and help in characterizing all the materials.

Scholarship support from CSIR–UGC, India and IIT Guwahati are acknowledged.

Finally, my PhD would not have been completed without the eternal love, care, bless, support and encouragement of my parents, Nripendra Barpuzary and Bijoya Barpuzary, and my brother, Mriganka Barpuzary. When I was unsure of an issue or struggling to overcome an obstacle, their useful advices and optimism always helped to provide me a solution to the problem. My parents are the main soul and inspiration for each and every step that I have achieved in my life. Specially, I thank my love, Bhawna, who has put her own career on hold and joined me in this attempt of completing PhD. Her drive to accept nothing but to wait and support me for five years has been the best inspiration for me. I also thank all my family members to provide me encouragement and fun times during family get-togethers.

Dipankar

Dedicated to my parents

Mr. Nripendra Puzary
&
Mrs. Bijoya Puzary

TABLE OF CONTENTS

PhD Thesis Synopsis Report

Thesis Title:	Design and Development of Novel Structured ZnO Based Semiconductor / Dye Sensitized Solar Cells
Name of the Candidate:	Mr. Dipankar Barpuzary
Registration Number:	10612229
Thesis Supervisor:	Dr. Mohammad Qureshi
Department:	Chemistry
Institute:	Indian Institute of Technology Guwahati, Assam-781039

Chapter 1 addresses basic concepts, mechanisms and working principles of semiconductor/ dye-sensitized solar cells including a brief detail of performance parameters allied with their photovoltaic property, feasibility and practicability. The chapter is concluded with the current state-of-the-art scenario and challenges related to ZnO based photovoltaic cells along with recent advancements of the sensitizers, electrolytes and counter electrode materials.

Chapter 2 describes general procedures followed to fabricate semiconductor/dye-sensitized solar cells. Basic instrumentation techniques/methods used for materials characterization, device fabrication and characterization, along with detailed procedures followed to evaluate photovoltaic parameters of any device are demonstrated. Rudimentary concepts and understanding of specific instrumentations such as, solar simulator (Newport Sol3A), incident photon-to-current conversion efficiency analyzer (IQE 200), and electrochemical impedance spectroscopy (EIS) measurements are being demonstrated.

Chapter 3 presents an idea to utilize a ternary composite of ZnO, CdS, and graphene oxide (GO), wherein hierarchical ZnO–CdS heteroarrays are well-embedded onto 1.0 wt % of GO sheets, as a one-coat paintable solution for semiconductor-sensitized solar cells (SSCs). Accomplishment of an efficient physical separation of photogenerated charge carriers within the hybrid ZnO–CdS–GO photoanode results in an excellent PCE of ~2.82 % for the SSCs against Pt as a counter electrode and a S^{2-}/S_n^{2-} redox couple as the electrolyte. In contrast, identical SSCs constructed with Ag as a counter electrode shows a deprived PCE ~1.96 %. It can be ascribed to the possible corrosion of Ag electrode when comes in direct contact with S^{2-}/S_n^{2-} electrolyte. Notably, a favorable band energy alignment among CdS, ZnO, and GO entities of hybrid photoanode facilitates the electronic interactions between ZnO–CdS and GO. This in turn minimizes the charge recombination and alleviates the device efficiency. It is further confirmed by the poor performances of GO-free SSCs fabricated with

ZnO–CdS photoanode counterparts, which afforded a PCE of ~1.92 % (for Pt) and ~1.08 % (for Ag). Electronic interactions between ZnO–CdS and GO are confirmed from drastic quenching of fluorescence, reduced exciton lifetime and Raman scattering measurements.

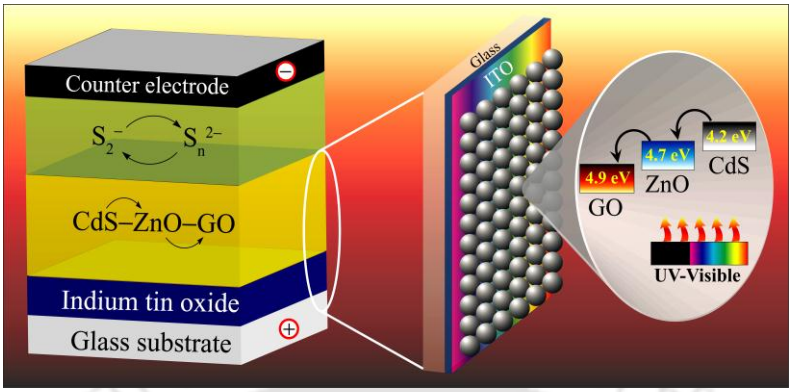

ACS Applied Mater. Interfaces 2013, 5, 11673−11682
J. Phys. Chem. C 2012, 116, 150–156

Chapter 4 presents a maverick approach to mimic the common properties of a heteroleptic type Ru dyes for dye-sensitized solar cells (DSCs) fabricated using a newly synthesized dye $Ru^{II}(dppz\text{-}COOH)_2(NCS)_2$ as an efficient photosensitizer for one-dimensional ZnO nanowires (1D ZnO NWs), Pt as a counter electrode, and CoII/III-complexes of 2,2´-bipyridine (bpy) and 1,10-phenanthroline (phen) as the redox electrolytes. The key features of the new Ru dye is two-fold: (1) a broad visible range absorption due to an intense metal-to-ligand charge transfer (MLCT) absorption band, and (2) an efficient dye loading capacity due to its optimal size. The electronic structure of Ru dye, as computed from DFT at a B3LYP/LANL2DZ/6-31G level, probes its typical MLCT transition and a favorable charge transfer feasibility from the LUMO of dye to the conduction band (CB) of ZnO via the anchoring carboxylic groups. A combination of 1D ZnO NWs and an efficient dye afforded excellent PCEs of ~5.9 % and ~5.6 % for the DSCs using Co-bpy and Co-phen based electrolytes, respectively.

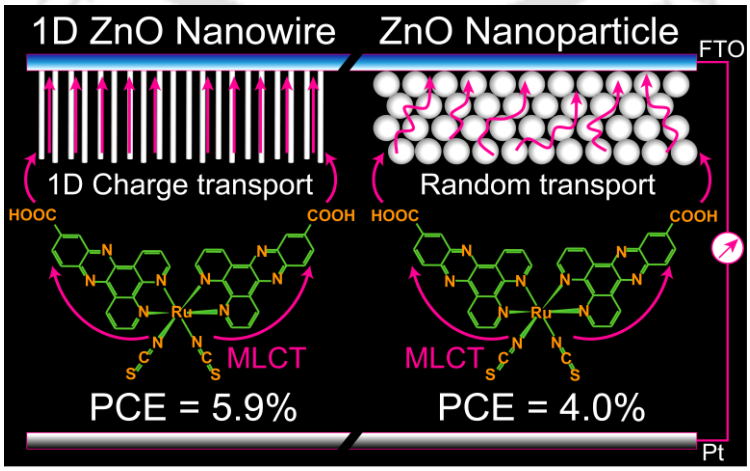

J. Phys. Chem. C 2015, 119, 3892−3902

The pivotal role of inherently faster charge transport property of the ZnO NWs to enhance the device efficiency is evidenced from the lower performances of identical DSCs fabricated with ZnO nanoparticle (NP) counterparts, yielding PCEs of ~3.5 % (Co-bpy) and ~3.6 % (Co-phen). The overall photovoltaic performances of the DSCs establish a promising light harvesting feature of the dye and a prominent charge transport through single crystalline ZnO NWs in contrast to the ZnO NPs. Electrochemical impedance spectroscopy (EIS) analysis provides an insight into the interfacial charge transfer dynamics, recombination kinetics, and a prolonged photoinduced electron lifetime of the DSCs composed of ZnO NWs in contrast to ZnO NPs.

Chapter 5 presents the combined effects of ZnO NWs and a newly synthesized metal-free, donor–π linker–acceptor (D–π–A) type, carbazole dye (SK1) through the fabricated DSCs. An excellent PCE of ~5.7 % has been achieved by employing Co-bpy as the one-electron redox mediator and ~4.7 % for the traditional I_3^-/I^- electrolyte. To claim the persuasive role of superior electron transport property of the 1D ZnO NWs to enhance the device efficiency, a comparative study by means of the DSCs fabricated with ZnO NPs has been demonstrated, which resulted in PCEs of ~3.6 % and ~3.2 % for Co-bpy and I_3^-/I^- couples, respectively.

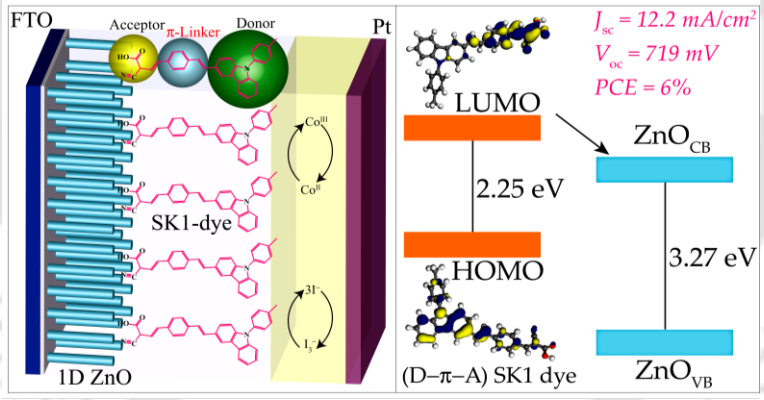

ACS Applied Mater. Interfaces 2014, 6, 12629–12639

In addition, presence of electronic interactions between the SK1 dye and ZnO favoring a photogenerated charge migration from the LUMO of SK1 to the CB of ZnO are evidenced from the significant quenching of photoluminescence and exciton lifetime decay of SK1 dye, when anchored to ZnO architectures. The spectroscopic and electrochemical techniques are used to estimate the band energetics of the dye. DFT calculations at a B3LYP/6-31+G(d) level probes the electronic distributions of SK1 dye in its HOMO and LUMO levels. A typical D–π–A configuration of SK1 provides an intramolecular charge transfer feasibility prompting an electron migration from the carbazole unit (donor) to the cyanoacrylic moiety (acceptor)

via an oligo-phenylenevinylene (π-linker) group, witnessing an electron transfer from the LUMO of SK1 dye to the CB of ZnO through anchoring carboxylic groups.

Chapter 6 presents the utilization of a noble-metal-free counter electrode material based on Cu_2ZnSnS_4 (CZTS) microspheres loaded with MoS_2 for efficient solar cells based on ZnO NWs co-sensitized with $CuInS_2$ and CdSe quantum dots (QDs). An ex-situ electrophoretic deposition route is employed to deposit the QDs onto ZnO NWs that are epitaxially grown on ZnO seed layered FTO substrates. ZnO NWs have also established an excellent stability against the external bias conditions applied to fabricate the photoanodes of the devices.

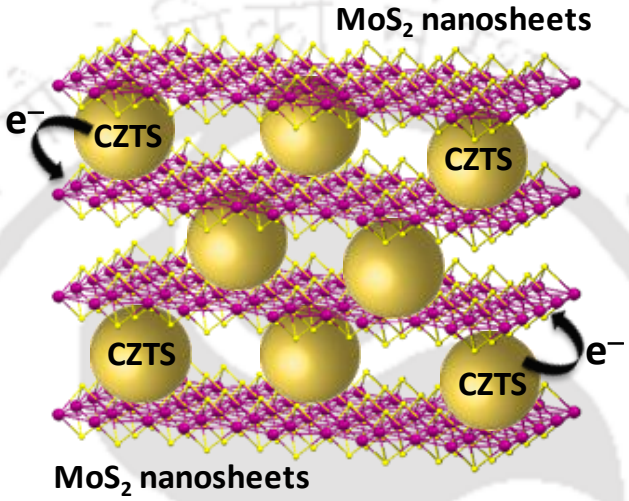

J. Mater. Chem. A 2015, 3, 14378–14388

Superior photovoltaic performance of $CuInS_2$–CdSe QD co-sensitized cells (PCE ~4.5 %) are compared with that of bare $CuInS_2$ (PCE ~1.3 %) and CdSe (PCE ~2.8 %) counterparts. The present study also demonstrates an enhanced photovoltaic performance of the devices fabricated with 1.0 wt % of MoS_2 loaded CZTS based counter electrodes in contrast to bare CZTS. Hydrothermal loading of MoS_2 to CZTS generates an electrically interconnected network of CZTS microspheres, leading to a facile charge transport in the counter electrode of the devices. MoS_2 in its nanosheet form acts as electrical bridges that interlink the CZTS microspheres. Additionally, a favorable band alignment of CZTS and MoS_2 stimulates the charge transfer dynamics in CZTS–MoS_2 composite. Electron transport and recombination kinetics of the devices are measured using electrochemical impedance spectroscopy.

Chapter 1

Introduction and Literature Review

This chapter address the basic concepts, mechanisms and working principles of semiconductor/ dye-sensitized solar cells including a short detail of the specific performance parameters related to the photovoltaic property its feasibility, and practicability of the devices. The chapter is concluded with a brief literature survey of current state-of-the art scenario and challenges related to ZnO architecture based photovoltaic cells for the energy conversion.

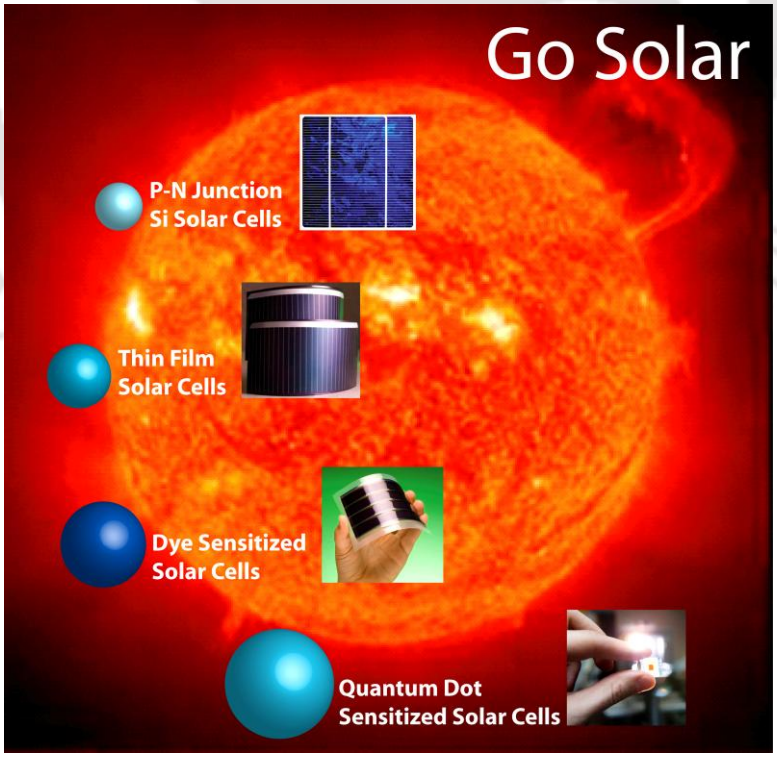

1.1. IMPORTANCE OF SOLAR CELLS: AN OVERVIEW

Rising global energy demand has estimated a hike in the present annual consumption of energy by more than 50 % till the end of next two decades. Statistical analysis showed an annual global energy consumption rate of ~13 TW in the year 2000, while a constant growth of population and energy demand has projected a need of ~28 TW of energy by 2050.[1–3] The statistics of annual global energy consumption and production capacity from different renewable and non-renewable energy sources are shown in Figure **1.1**.[4–6] Assuming that the current strategies and existing practices remain persistent, most of the energy production is expected to be fulfilled from fossil fuels (coal, oil, natural gas). However, a commensurate increase of CO_2 emission by combustion of fuels is also anticipated. Despite there exist several renewable natural resources (hydroelectric, solar, wind, hydrothermal, and biomass), solar power has been deemed as the most economic and viable source for the development of a globally sustainable society.[7] Notably, a large flux (~1.7 × 10^5 TW) of solar energy strikes on the earth's surface, which predicts a practical terrestrial global solar power of ~600 TW. Therefore, a pragmatic approach to use even a ~10 % of this colossal amount of energy can generate a global power supply up to ~60 TW. To meet the same, more scientific efforts are needed in the development of economic strategies that can access to a direct solar harvesting feasibility. In view of this, recent technological advancements of direct solar-to-electricity conversion devices have been materialized as one of the most promising alternatives.

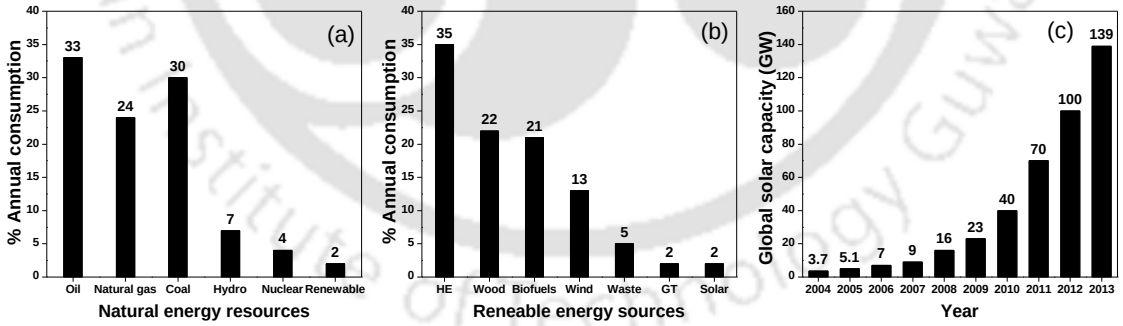

Figure 1.1 (a) World annual energy consumption by source, 2012.[5] (b) Renewable energy as share of total primary energy consumption rate, 2011.[6] (c) Improvement in the solar photovoltaic total global capacity from the year 2004 to 2013.[7] (HE = hydroelectric, GT = geothermal, PV = photovoltaic)

Brian O'Regan and Michael Grätzel of the University of California, Barkeley, USA co-invented the modern version of a solar cell based on a thin layer of TiO_2 nanoparticles impregnated with a Ru dye in 1988, which was developed further and published in 1991 as the first high efficiency dye-sensitized solar cell (DSC).[8] As a result of their accomplishment, the current state-of-the-art

scenario of photovoltaic technology has been modified and improved dramatically. The maverick approch by Grätzel *et al* have paved a way to achieve high power conversion efficiency (PCE) and opened exciting opportunities to discover novel materials. The challenge to review the DSC research field has also spurred the researchers to develop, synthesize, and modify the innovative or prevailing materials to be incorporated in solar cells for high throughput.[9] In this regard, targeting superior PCE clutched with cost-effective fabrication routes, a large variety of semiconductor materials, organic molecules, metal complexes, and polymers are explored as the molecular components for the construction of solar cells of diverse configurations.[9–13] An open-ended research testing a number of structures, prototypes, and modules of DSCs have developed further a new class—semiconductor-sensitized solar cells (SSCs)—as a prototype, relying on the same working principles as that of DSCs.[14–16] The SSCs involve semiconductor nanomaterials or quantum dots (QDs) as the light harvesting units (in contrast to the dyes in the case of DSCs) have also shown promising efficiency to convert the solar photons into electricity.[11]

If we look back at the practical acquirement of direct conversion of the solar energy into electricity, the conventional Si-based solar cells have primarily gained a promising commercial enactment.[17] Even if high efficiency, eco-friendliness, and earth-abundant material source have built a stable platform for this class of solar cells, their energy-intensive fabrication and high-cost processing still demand the production of alternate high-efficiency devices at a larger scale for an extensive indoor–outdoor applications.[18] Indeed, recent growth of DSCs and SSCs exhibiting PCEs up to ~13 % and ~8.5 %, respectively, have challenged the traditional Si-based solid-state photovoltaic at a nano and molecular level.[19,20] Thus, concerning the key issues like scalability, compatibility, and practical execution, DSCs and SSCs have been deemed to be the most popular alternatives of Si-based photovoltaic assemblies affording PCEs of ~14–17 %.[9,21–26] DSCs and SSCs are advantageous due to their structural diversity and a facile functionalization tunability of different components by chemical modification to fulfil the basic prerequisites for better device performance such as, light absorption, charge separation, and electron transport. In addition, wet-chemical processed low-cost fabrication compatibility of a few constituents of DSCs by means of specialized techniques like screen printing,[27] doctor blading,[28] inkjet printing,[29] and spray deposition[30] stimulate their potential role to achieve high throughput. Paradigms include the fabrication of a reliable DSC with an active area of ~225 cm^2, the largest single-cell DSC in the world, affording a PCE up to ~7.2 %.[31] The advancements of economic tools to meet a reliable

production of such modules enriched with good performance, stability, and durability need further development of manufacturing technologies. Prime target to promote a cheaper industrial processing of photovoltaic cells at a larger scale demands a mass production in flexible, light weight, thin, and bendable forms, to facilitate portable and wearable applications.[32] Specially, DSCs avail a compelling feature of a roll-to-roll production compatibility due to their adaptable fabrication onto flexible transparent conductive oxide (TCO) substrates under low temperature and pressure based conditions.[33] It also provides an upper hand to the DSCs over conventional thin film solar cells based on Si or copper indium gallium selenide, requiring expensive vacuum equipments.[34] Despite the possibilities to fabricate SSCs onto polyethylene terephthalate (PET) based flexible TCOs has been already explored,[31,35,36] they still demand enormous advancements to meet a pronounced mass production level similar to that of the DSCs.

Figure 1.2 Examples of a few flexible DSC modules launched by different companies for the practical applications. Source: Google, G24i Innovations Ltd., UK.

A few companies such as, G24i, BASF, Bosch, Sony, Toyota, Panasonic, Dyesol, *etc*. have already entrenched pilot production lines to generate light-weight, flexible, and thin DSC modules to harness visible light into electrical energy.[9,33] For instance, flexible camouflaged solar panel for military,[37] solar lantern,[38] and backpacks loaded with flexible DSC modules[39] (Figure **1.2**) have already gained primary consumer applications. Essentially these type of bigger DSC modules are comprised of a number of tiny DSCs that are connected in series. In these modules, the highest possible ratio of active area per device is often sought to achieve superior performance efficiency. However, to meet a practically executable level, bigger DSC modules have some limitations. The most common issues that are often encountered and need sincere attention are (1) limited weight against smaller tolerance and (2) possibility of defect formation by the materials used for insulation between adjacent cells or protection of current collectors. All these points are directly relevant to the advancements of solar cell based commercial products. In future, the applications of DSCs and SSCs might include roofing and other building materials.

1.2. COMPONENTS OF DYE/ SEMICONDUCTOR-SENSITIZED SOLAR CELLS

In the brief overview of solar cell technology, the promising role of newly developed strategies (DSCs and SSCs) to convert the solar energy directly into electricity is already been discussed.[40] Following an identical framework, basic model of both DSCs and SSCs is composed of an anode and a cathode separated by an electrolyte, as shown in Figure **1.3**. The anode consists of a TCO coated with a thin and transparent film of a wide band gap oxide material that is sensitized with a dye/semiconductor; whereas the cathode is a metal or non-metal coated on TCO substrate. The primary configuration of DSCs or SSCs comprises of four key components, as discussed below.

(a) At the heart of the device is a thin film (~8–10 μm) of a wide-band gap semiconductor oxide (ZnO, TiO_2, SnO_2 *etc*.) deposited on a TCO substrate, which is often an indium tin oxide (ITO) or F-doped tin oxide (FTO) coated glass or FTO coated PET substrate.

(b) The component attached to the surface of oxide film is a monolayer of charge-transfer dye or a mono/multi-layer of semiconductor, acting as the photosensitizer.

(c) A redox electrolyte to regenerate the sensitizer. The common electrolytes used in DSCs are iodide/triiodide (I_3^-/I^-) and cobalt$^{II/III}$ complex based redox couple in acetonitrile, while an aqueous solution of sulfide/polysulfide (S^{2-}/S_n^{2-}) redox couple is used in SSCs.

(d) A metal/non-metal based counter electrode. The most common counter electrode is a thin layer of Pt, deposited on a TCO by spray deposition or spin coating method.

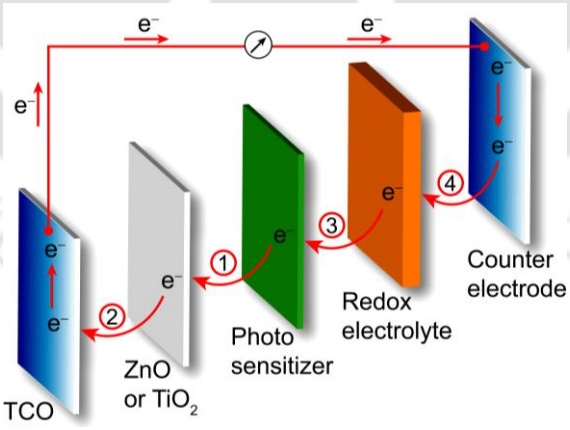

Figure 1.3 Schematic showing the electron transfer and the components of a typical sensitizer-based solar cell.

When light is illuminated, photons having an energy of ~0.5–3.5 eV, strikes the top of the DSCs or SSCs and penetrate to the sensitizer through the TCO and transparent oxide film. The photons of energy equal to, or more than the band gap of dye/semiconductor sensitizer produce an

effective excitation of electron from the highest-occupied molecular orbital (HOMO)/valence band (VB) to the lowest-unoccupied molecular orbital (LUMO)/conduction band (CB), generating an electron–hole pair. This pair, called as exciton, then relaxes with a binding energy of ~1.0–0.14 eV.[41–43] The excitonic binding energy of a typical semiconductor remains within a few millielectron volts, while the same in the case of organic dyes are relatively higher due to their localized electron and hole wave functions and lower dielectric constant values (ε ≈ 3–4).

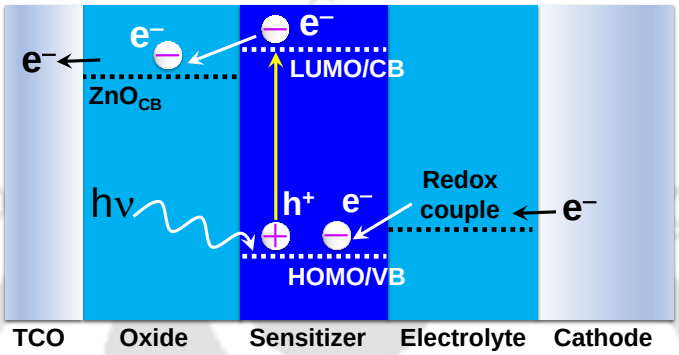

Figure 1.4 Schematic band diagram of a sensitizer-based solar cells under normal operating conditions. HOMO/VB and LUMO/CB represents ground and excited state of the dye/semiconductor sensitizer, respectively.

To generate photocurrent in a device, this Coulombic bound electron–hole pair needs to get separated into its individual components (Figure **1.4**), if not then it eventually recombines and loses *via* competitive processes like radiative photon emission (fluorescence) and non-radiative thermal decay. For the DSCs and SSCs, exciton dissociation relies on the gradients of potential difference created across the interface of sensitizer material and mesoscopic oxide film. The photoinduced electron transfers from the sensitizer to the CB of oxide through the interfacial bonds between the sensitizer and oxide. In order to get an effective injection, the oxide material should possess a more positive CB potential in contrast to that of the LUMO/CB of dye/semiconductor sensitizer. Meanwhile, the sensitizer loses an electron and gets oxidized. The oxidized sensitizers bonded to the oxide film do not have energy channels to diffuse into photoanode. As a result, they get reduced immediately by the redox couple present in the electrolyte. Notably, to accept electrons from the redox couple efficiently, the HOMO/VB level of the sensitizer must be more positive than that of the redox potential of the electrolyte.[44] The redox couple is finally reduced by mechanically diffusing to the bottom of the cell, where the counter electrode re-introduces an electron after flowing through an external load. The electron migration from the anode to counter electrode basically closes the device circuit.[45]

1.3. WORKING PRINCIPLE

To have a better understanding, the mechanism and basic charge transfer processes taking place in DSCs and SSCs can be further explained in a step-wise manner as explained below.

(a) Sensitizers adsorbed onto semiconductor oxide (SCO) excite the electrons upon photon absorption from the ground state (S) to excited state (S^*) and quickly inject them to the CB of SCO. At the same time, the photosensitizer generates its oxidized state (S^+).

$$S + h\nu \rightarrow S^* \quad (1)$$

$$S^* \rightarrow S^+ + e^-(\text{SCO}) \quad (2)$$

(b) The accumulated electrons, injected from the LUMO/CB of sensitizer to the CB of SCO, are transported through a TCO back contact to the counter electrode by external circuit.

(c) The oxidized sensitizer (S^+) accepts electron from the redox electrolyte (E) leading to the regeneration of the ground state (S), and in turn, the electrolyte gets oxidized to E^+.

$$S^+ + e^- \rightarrow S \quad (3)$$

$$E - e^- \rightarrow E^+ \quad (4)$$

$$E^+ + e^- \rightarrow E \quad (5)$$

(d) The oxidized electrolyte (E^+) then diffuses toward the counter electrode, accepts the electron and again gets reduced to E.

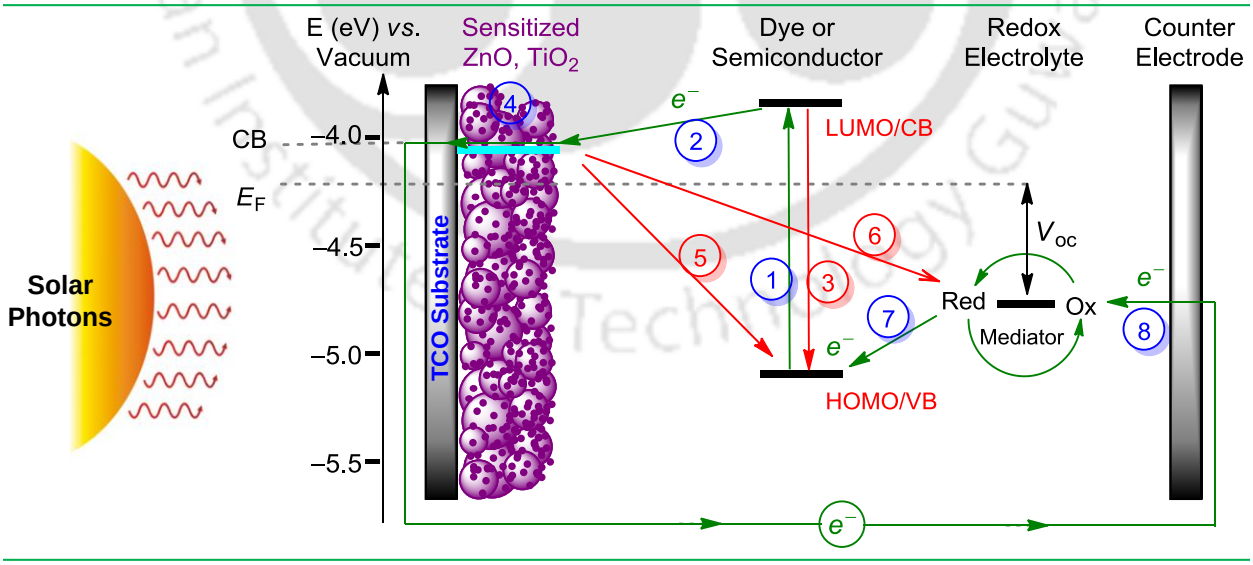

Figure 1.5 Schematic showing the prime components of a dye- or semiconductor sensitized solar cell along with the step-wise charge transfer processes taking place in the device circuit. Green and red colored arrows represent the basic forward and back electron transfer processes taking place within the device.

The current understanding of charge transfer processes concludes that the performance of a DSC or SSC primly depends on four energy levels of their constituting components—(1) excited state (LUMO/CB) of sensitizer, (2) ground state (HOMO/VB) of sensitizer, (3) Fermi level of oxide layer, and (4) redox potential of electrolyte.[46] Hegfeldt *et al*. have discussed the mechanism of charge transfer dynamics and kinetics picture for DSCs.[47] A similar picture can again explain the working principles of a sensitizer-based solar cell of the present work (Figure **1.5**). The reactions **1** and **2** explain the photogeneration of electron–hole pair from the sensitizer and the injection of electrons into oxide semiconductor film on TCO, respectively. Even if there exist a number of different perspectives of charge injection process,[9] DSCs usually undergo an ultrafast dynamics with an injection rate within a fs scale, while for SSCs this rate remains within a ps range.[48] It is observed that the charge separation is taken care of by a kinetic competition between two processes—(1) excited-state charge transfer to the CB of oxide film (reaction **2**) and (2) decay of excited-state to the corresponding HOMO/VB of sensitizer (reaction **3**). Notably, to achieve a higher photocurrent, the time scale of electron injection reaction should be much faster than the radiative decay of sensitizer. Ideally, photogenerated electron accumulated in CB of oxide layer should transport all along the semiconductor film efficiently, without recombination to sensitizer (reaction **5**) or to electrolyte (reaction **6**). However, in real time devices, the presence of such back electron transfer reactions attenuates their overall output electric power. To minimize such electron loss, a process called as necking ($TiCl_4$ treatment) is often carried out to the oxide film. The back electron transfer probability can be evaluated by the recombination reactions taking place at the oxide/sensitizer/electrolyte interface during the transport of electrons from one oxide particle to the adjacent particle within the oxide layer.[49,50] The recombination to sensitizer species usually occurs in a micro to millisecond range, while the recombination to electrolyte takes place in an order of millisecond to seconds. On the other hand, the photogenerated hole remains on the sensitizer due to a well-separated nature of the HOMO/VB level of sensitizer in contrast to that of the other energy levels of the device. The oxidized sensitizer is therefore regenerated back by gaining an electron from the redox couple in the electrolyte in a micro to nanosecond time scale.[9,51] The electrolyte in turn gets oxidized, and then diffuses to the counter electrode to accept electron from the external load to regenerate within a nanosecond scale. Thus, the photoexcited electrons that are injected from the sensitizer to oxide semiconductor film flows through an external load and finally get collected back at the counter electrode.

1.4. SOLAR CELL PERFORMANCE PARAMETERS

Photovoltaic performance of a solar cell can be defined by means of a few physical parameters: (1) short-circuit current density (J_{sc}), (2) open-circuit voltage (V_{oc}), (3) fill factor (*FF*), (4) power conversion efficiency (PCE, η), and (5) incident photon-to-current conversion efficiency (IPCE). In general, the solar radiation striking the earth's surface is maximum when the sky is clear and the sun is directly overhead, creating the shortest path length through the atmosphere. This path length is known as the air mass (AM) and can be expressed as AM = 1/cos φ, where φ is called as the Zenith angle (angle of elevation of the sun) as shown in Figure **1.6a**. To compare solar cells characterized in different laboratories all over the world, a simulated solar spectrum of AM 1.5 G (global) corresponding to a φ = 42° and a normalized integrated irradiance of 1000 W.m^{-2} is used as the standard to test their efficiency.

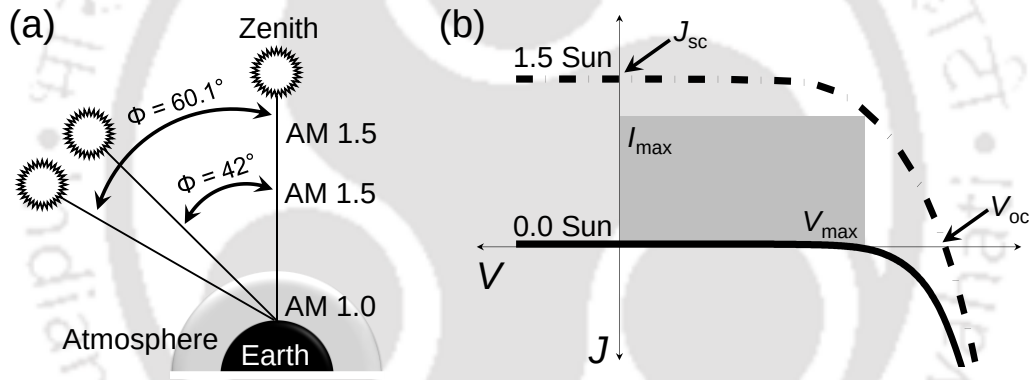

Figure 1.6 (a) Solar radiation path length in air mass (AM) unit and the zenith angle. (b) Typical photocurrent–voltage (*J*–*V*) curve of a solar cell under the dark conditions and AM 1.5 G simulated solar illumination.

Performance parameters of a solar cell like J_{sc}, V_{oc}, maximum power (P_{max}), *FF*, and *PCE* can be evaluated from its corresponding photocurrent–potential (*J*–*V*) curve. A schematic *J*–*V* curve showing the effect of light on current characteristics is shown in Figure **1.6b**. In principle, J_{sc} is the current flowing through a solar cell when voltage across the cell is zero, and is obtained by the collection of electrons that are generated under photoexcitation. The number of photoinduced electrons increase with an increase in intensity of incident light due to a release of more number of photons to strike the device. To eliminate the area dependence of solar cells, the value of J_{sc} is expressed in mA.cm^{-2} unit. On the other hand, V_{oc} of a solar cell is the maximum obtainable voltage at zero current. It can also be defined as the difference between the Fermi level of oxide semiconductor coated on TCO and redox potential of electrolyte. The *FF*, which can take values

between 0 and less than 1, is defined as the ratio of the maximum power (P_{max}) of a solar cell per unit area divided by the V_{oc} and J_{sc} values, according to eq. (6).

$$FF = \frac{P_{max}}{J_{sc} \times V_{oc}} = \frac{J_{max} \times V_{max}}{J_{sc} \times V_{oc}} \quad (6)$$

where P_{max} of a solar cell can be obtained from the product of photocurrent and photovoltage at the maximum power output (square box shown in Figure **1.6b**). The overall PCE for a solar cell is given by the relation among J_{sc}, V_{oc}, FF, and the intensity of the incident light (P_{in}), eq. (7)

$$\eta = \frac{J_{sc} \times V_{oc} \times FF}{P_{in}} \quad (7)$$

Another fundamental parameter related to the performance of a solar cell is IPCE, which accounts for the number of photons generated in the cell at specific wavelength (λ). IPCE corresponds to the photocurrent density produced in the external circuit under monochromatic illumination divided by the photon flux that strikes the cell. It can be expressed using eq. (8).

$$IPCE = 1240 \times \frac{J_{sc}(\lambda)}{\lambda \times P_{in}(\lambda)} \quad (8)$$

1.5. MATERIALS DEVELOPMENT

1.5.1. Nanostructured Semiconductor Metal Oxide Electrode

A key to the breakthrough for DSCs in 1991 was the involvement of a randomly packed TiO_2 nanoparticulate film, with an enormously high internal surface area, to support the monolayer of a Ru dye sensitizer.[8] As a common feature of this maverick approach, nanocrystalline TiO_2 in particle form and diverse specific morphologies are continuously being explored as the electron transport building block of sensitizer-based solar cells. Even if TiO_2 exhibits highest PCEs for both DSCs (~13.6 %)[19] and SSCs (~8.5 %),[20] a number of alternate n-type semiconductors like binary (ZnO, SnO_2, Nb_2O_5) and ternary ($SrTiO_3$, Zn_2SnS_4) metal oxides or their core–shell structures have also been used as scaffolding for hosting the sensitizers and to provide efficient electron transport.[52–67] Amongst them, ZnO-based nanoarchitectures have been studied most comprehensively due to their intrinsic peculiarities such as, (1) wide band gap similar to that of TiO_2, (2) superiority in electron mobility,[68–71] (3) highly crystalline hexagonal wurtzite structure, (4) lesser grain boundaries, and (5) readily tunable morphologies. A comparative study of basic electronic and optical properties of ZnO with TiO_2 and SnO_2 is shown in Table **1.1**.[72–83] In principle, unique combination of esteemed properties of ZnO opens wide possibilities to generate

richest family of nanostructures—spanning from randomly assembled nanoparticles to highly ordered nanotube arrays or single-crystalline nanorods—for the design and development of DSCs and SSCs.[84,85] Moreover, excellent electron mobility, high CB edge enabling larger V_{oc} values among various candidates to electron transporters, with considerable superiority in device efficiency (~7.5 % for DSCs and ~6.2 % for SSCs)[86,87] make ZnO a competitive alternate to the TiO_2 benchmarks. Indeed, for DSCs, ZnO is the first candidate to reveal the possibility of an irreversible electron injection from a dye molecule into the CB of a semiconductor material.

Table 1.1 Structural and electronic properties of electron transporting oxide materials generally used in solar cells.

Parameter	**ZnO**	**TiO_2**	**SnO_2**	**Ref.**
Crystal structure	wurtzite	rutile, anatase	rutile	72–75
Band gap (eV)	3.2–3.4	3.0–3.2	3.6–3.8	72–76
Conduction band minimum (eV)	–4.36	–4.41	–4.88	77
Electron effective mass	0.26	9.0	0.275	78–80
Static dielectric constant ($\varepsilon_{\perp,//}$)	9.26, 8.2	86, 170	14, 9	81
Electron mobility ($cm^2\ v^{-1}\ s^{-1}$)	130–200	0.1–4	200–250	72, 80, 82
Effective electron diffusion coefficient ($cm^2\ s^{-1}$)	1.1×10^{-4}	4.3×10^{-4}	7.3×10^{-5}	83

Recent advancements on ZnO based nanoarchitectures have presented attractive features, not only through the applications in DSCs and SSCs, but also in polymer solar cells,[88,89] QD solar cells (QDSCs),[90,91] and light emitting diodes.[92] A large variety of morphologies of ZnO, obtained by different techniques (hydrothermal, chemical bath deposition, electrophoretic deposition, spray pyrolysis, polyol hydrolysis, chemical vapor deposition *etc*.), are being utilized to improve the efficiency of DSCs, as shown in Table **1.2**[93–114] Notably, even if the use of ZnO in DSCs has been significantly increased in recent years, it is still the runner up to TiO_2 counterparts in terms of efficiency. It can be ascribed to two possible issues: (1) the formation of interfacial charge transfer state between the dye and ZnO surface, which practically limits an efficient generation of photoinduced free-charge carriers[115,116] and (2) a lower chemical stability of ZnO against both acidic and basic conditions, in contrast to that of TiO_2.[9,117] In addition to DSCs, benefits of electron transport property and tunable morphologies of ZnO have also received promising interest in the advancements of SSCs in the past few years, especially in QDSCs. QDSCs are a special class of SSCs wherein inorganic semiconductor QDs are employed to harvest the solar photons. QDs also enable a size-controlled band gap tunability, enhanced light absorption, higher extinction coefficients, a multiple exciton generation by carrier multiplication or impact ionization, a feasible extraction of hot charge carriers, *etc*.[14,118–120]

Table 1.2 Photovoltaic performance of different morphologies of ZnO, their combinations, and composites with other semiconductor materials reported for dye-sensitized solar cells (NWs: nanowires, NPs: nanoparticles).

ZnO structures	Sensitizer	J_{sc} (mA.cm^{-2})	V_{oc} (V)	FF (%)	η (%)	Ref.
Hierarchical aggregates	N719	19.8	0.64	59	7.5	86
ZnO NWs/TiO_2 shell	N719	15.5	0.77	-	7.0	93
Commercial nanopowders	N719	18.1	0.62	58	6.6	94
ZnO tetrapod/SnO_2/ZnO core–shell NPs	N719	16.3	0.65	59	6.3	95
ZnO aggregates/TiO_2 shell	N3	15.8	0.70	56	6.3	96
Hierarchical aggregates	N3	21.0	0.66	44	6.1	97
Nanosheet	D149	18.0	0.53	63	6.1	98
Oriented porous film	D149	12.2	0.69	65	5.6	99
NPs + scattering hollow cavities	N719	15.7	0.56	62	5.5	100
NPs	D102	17.4	0.63	48	5.4	101
Hierarchical aggregates	N3	18.7	0.65	45	5.4	102
Hierarchical aggregates	D205	12.2	0.65	67	5.3	103
ZnO/Nb_2O_5 shell	N719	12.4	0.71	59	5.2	104
Tetrapod-like ZnO nanopowders	D149	12.4	0.60	65	4.9	105
Nanosheets/NWs	N719	10.9	0.68	65	4.8	106
Self-assembled nanostructures	N719	10.7	0.71	62	4.7	107
NWs/NPs	N3	15.2	0.61	46	4.2	108
Hierarchical NWs/nanoporous layer	D149	12.3	0.57	58	4.1	109
Mesoporous film	N719	11.8	0.65	52	4.0	110
Hierarchical NWs	N719	8.8	0.68	53	2.6	111
NWs	D102	14.1	0.55	34	2.6	112
Nanorods	Z907	6.4	0.72	49	2.3	113
NWs	N719	9.3	0.67	34	2.1	114

Since the dawn of QDSC design and fabrication, nanocrystalline TiO_2 matrices are being used as the electron transporters. However, enormously high surface area of TiO_2 films tends to clog the mesopores upon QD loading, eventually hindering the free-charge injection, smooth diffusion of electrolyte, and adequate loading of QDs to the interior of oxide films.[121] To avoid such glitches, open-type structured (nanorods, nanowires, tetrapods, nanotubes, nanosheets) sensitizer scaffolds have been developed to achieve a facilitated photogenerated carrier transport, a retarded electron–hole recombination rate, and facilitated diffusion of redox electrolytes in the devices.[122] Most of these open-type structures are built on a one-dimensional (1D) geometric platform and hence, hold single or quasi-single crystallinity. The 1D structures also favor charge transport and minimizes recombination, thereby improving electron collection due to the existence of a grain boundary-free unidirectional pathway toward the external circuit. In this regard, rational design and development of a plethora of 1D ZnO nanowire morphologies has got a real knack due to their aptness of crystallization and anisotropic growth, in contrast to the TiO_2 counterparts.[123–138] Superior performance of 1D ZnO nanostructures over randomly packed nanoparticulate films are

evident from the results presented in Table **1.3**.[123–138] However, 1D ZnO nanostructures have some limitations. One of the possible issues is their low surface area stunting sufficient sensitizer uptake. To improve the present scenario of ZnO based DSCs and QDSCs, in this thesis, we have intended to cast some light on—(1) surface engineering, (2) careful control of the concentration and sensitization time, and (3) the exploration of best techniques to use for sensitizer uptake.

Table 1.3 Photovoltaic performance of different open-type morphologies of ZnO and their combinations reported for semiconductor quantum dot sensitized solar cells. (NWs: nanowires, NPs: nanoparticles).[87,123–138]

ZnO structures	Sensitizer	J_{sc} (mA.cm^{-2})	V_{oc} (V)	FF (%)	η (%)	Ref.
ZnO tetrapods	ZnSe/CdSe/ZnSe	17.3	0.76	47	6.2	87
Branched nanorods–nano-tetrapod	CdS/CdSe	16.5	0.70	45	5.2	123
NP film/microsphere	CdS/CdSe	17.1	0.56	53	5.0	124
NW array	$Zn_xCd_{1-x}Se$	18.0	0.65	40	4.7	125
NPs passivated with TiO_2	CdS/CdSe	15.4	0.62	49	4.6	126
NW array	ZnSe/CdSe	11.9	0.83	45	4.5	127
NPs	CdS/CdSe	10.4	0.68	62	4.4	128
Nano-tetrapods	CdS/CdSe	13.8	0.72	42	4.2	129
NW array	CdS/CdSe	17.3	0.62	38	4.1	130
NW array	ZnSe/CdSe	11.4	0.81	43	4.0	131
NW array	CdS/CdSe	12.6	0.68	42	3.6	132
ZnO nanorods passivated with TiO_2	CdS/CdSe	9.9	0.61	52	3.1	133
Branched n-Si NW/ZnO nanorods	CdS/CdSe	11.0	0.71	38	3.0	134
Nanosheets	CdS/CdSe	19.3	0.49	28	2.6	135
NPs/nanorods	CdS/CdSe	7.8	0.55	57	2.4	136
NWs/mesoporous hollow spheres	CdS/CdSe	9.0	0.51	51	2.3	137
NWs	CdS/CdSe	8.3	0.55	51	2.3	138

1.5.2. Sensitizer Materials

As a common feature of electron transporting materials for solar cells, the wide-band gap of ZnO inhibits solar photon harvesting and hence, necessitates its surface sensitization using a favorable molecular dye or semiconductor. Being a crucial part in DSCs and SSCs, the photosensitizer should fulfill a few prerequisites such as, (1) light absorption ability covering a wide visible region and a part of near-infrared (NIR) region, (2) a good anchoring ability to bind with ZnO, (3) a more positive LUMO/CB potential of dye/semiconductor sensitizer than that of the CB of ZnO, (4) capability of a non-aggregated uptake on ZnO surface, and (5) photo, electrochemical, and thermal stability. Based on these criteria, researchers are fortified to diversify into a number of sensitizers such as, metal–organic dyes, organic dyes, and semiconductor nanostructures. The advent of DSCs introduced a concept to utilize a ruthenium (Ru(II)) complex of carboxylated

bipyridine ligand as a sensitizer.[8] Similar type of Ru dyes containing bipyridyl and polypyridyl ligands are further explored due to their advantages such as, broad range visible light absorption, favorable band alignment, moderately longer lifetime in excited state, and high electrochemical stability.[9,99,139] In addition, Ru→ligand and ligand→Ru mediated charge separations and facile possibilities of intense metal to ligand charge transfer (MLCT) transitions in visible region made these Ru dyes a popular choice.[140] To extend the molar absorptivity of such homoleptic-type Ru dyes, along with new promises to optimize the redox potential and suppress dye aggregation onto oxide films, heteroleptic-type Ru dyes have been developed (Figure **1.7**). Unlike homoleptic type Ru dyes, a heteroleptic design bears two ancillary ligands (excluding –NCS) of different types: (1) one with extended π-conjugation ensuring an efficient light harvesting antenna function and (2) a second ligand offering dye adsorption onto semiconductor (ZnO, TiO_2) surface.

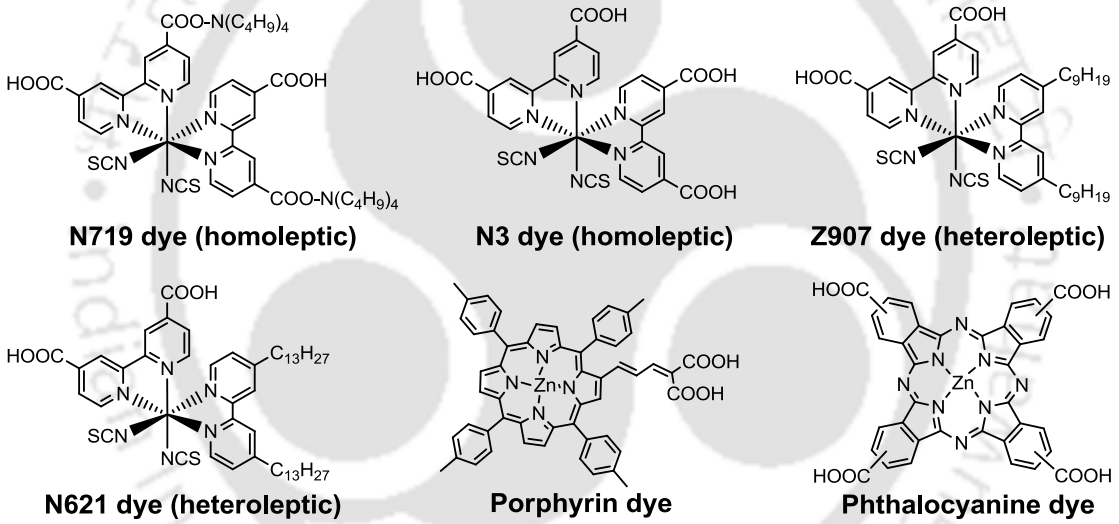

Figure 1.7 Commonly used metal–organic dyes (Ru dye, porphyrin, phthalocyanines) for dye-sensitized solar cells.

However, a common feature of both prototype homoleptic and heteroleptic-type Ru dyes is that they contain a similar type of –COOH group to anchor onto semiconductor surface.[141] Even if the current scenario to enrich the DSC efficiency is focused on the advancements of Ru dyes, it is fair enough to note that they still lack in absorbing light up to the NIR region. In this regard, many porphyrin and phthalocyanine dyes (Figure **1.7**) manifesting an intense spectral response from the visible to NIR regime, along with good chemical, photo-, and thermal stability, have been explored, achieving a PCE up to ~13 %.[19,142] However, a bulky dimension of such dyes necessitates a coadsorber during the dye sensitization process, to suppress dye aggregation.

In the past 15 years, a lot of effort has been devoted to design a wide range of Ru dyes for DSCs. Despite being efficient, their reliance on expensive Ru metal source, laborious synthesis, and tricky purification steps persuaded the researchers to develop metal-free organic dyes as the compelling alternatives. Consequently, numerous metal-free derivatives of indoline, carbazole, thiafulvene, coumarin *etc*. are adapted as sensitizers in DSCs, achieving promising PCEs up to ~10 % (Figure **1.8**).[143–148] Paramountcy is therefore given to such dyes due to their ascendancy in, (1) lower band gap, (2) higher molar extinction coefficient, (3) facile molecular design possibility, and (4) tunable optical and electrical properties. Moreover, a facile coalition of favorable groups into the main organic framework can benefit from the generation of a series of donor–acceptor (D–A) and donor–π-linker–acceptor (D–π–A) type configurations to improve the solar light harvesting, along with a promoted intramolecular charge transfer dynamics.[149]

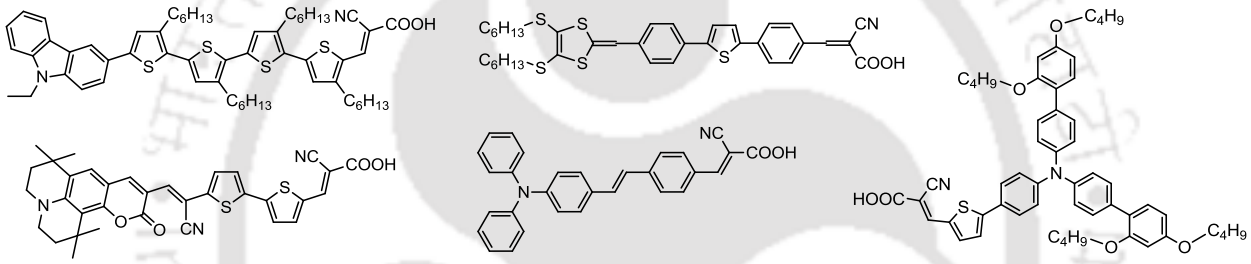

Figure 1.8 Examples of metal-free neutral organic dyes employed in highly efficient dye-sensitized solar cells.

As discussed earlier, a rapid growth of DSC technology bears testimony to the success of nanostructured solar cells. However, an immediate hurdle in DSCs is to use dyes that encounter with durability and stability issues, often caused by degradation of dyes under prolonged solar irradiance.[150] A virtuous attempt to reconcile the need for stability improvement is to replace dye sensitizers by semiconductor nanostructures, thus captivating the realm of SSCs. A recent surge of semiconductor sensitizers, particularly QDs, has gained the most alluring interest due to their considerable superiority over dyes in numerous aspects such as, (1) higher stability, (2) enhanced optical absorption coefficients, (3) low cost, and (4) more tunable properties by means of easier synthetic routes with the control over size, shape, and composition.[151] Moreover, adoption of QD sensitizers allows to get rid of a stability bottleneck encountered by ZnO, when is encompassed with dyes containing acidic anchoring groups. For ZnO based QDSCs, the challenge to improve the efficiency basically includes the tactics to overcome the limiting factors such as, (1) specific band gap of single QD stunting the absorptivity, (2) relatively low hole transport rate leading to

recombination of charge carriers to the electrolyte, (3) charge hopping within QD multilayer, and (4) a weak electronic anchoring of QD onto ZnO.[152,153] In this regard, relying on specific routes with their own merits and demerits, different techniques have been applied to improve QDSC performance. One promising strategy is to design 1D ZnO based photoanodes to generate continuous pathways for a faster charge transport prior to recombination. Another key factor is to load single QDs (CdS, CdSe, $CuInS_2$, PbS, Bi_2S_3) or a sequential assembly of different QDs onto ZnO nanostructures by means of either *in-situ* or *ex-situ* approaches enabling good anchoring between the QDs and ZnO.[14] Multiple QD loading provide additional benefits such as, an enhanced light harvesting and a facilitated electron injection dynamics. Generally, chemical bath deposition (CBD) and successive ionic-layer adsorption and reaction (SILAR) techniques are applied to achieve an *in-situ* growth of QDs, while *ex-situ* approaches involve direct adsorption, bifunctional linker-assisted binding, and electrophoretic deposition methods.[154–156]

1.5.3. Redox Couples for Electrolyte

On top of the metal oxides and sensitizers, another crucial part in DSCs and QDSCs is electrolyte, which accounts for inner charge carrier transport between electrodes and a continuous regeneration of the sensitizer and itself.[157] The electrolyte solely contributes to the light-to-electric conversion efficiency and durability of the cells. All the key parameters (J_{sc}, FF, and V_{oc}) that leverage the PCE of a device are directly affected by the electrolyte. For instance, J_{sc} is altered by the transport of redox couple present in the electrolyte, whereas FF is affected by the diffusion of charge carriers in electrolyte and the charge transfer resistance at the electrolyte/electrode interface. Similarly, V_{oc} is affected by the redox potential of electrolyte. Therefore, the development objectives of DSC and QDSCs should also focus on the assortment of a pertinent electrolyte that promises the charge transfer kinetics and hence, device performance.[51] Based on chemical and physical stability, composition, redox potential, corrosiveness, light absorptivity, and device specific applications, an intense research explored different possibilities for redox couples to develop the ubiquitous and indispensable electrolyte systems for DSCs and SSCs.[158] In addition, the selection of electrolyte depends on the favorable band alignment between the sensitizer and electrolyte to accomplish an efficient regeneration of oxidized sensitizers.[151] Paradigms include I_3^-/I^- and cobalt$^{II/III}$ complex containing redox couples (in acetonitrile) in DSCs, and a S^{2-}/S_n^{2-} couple (in water) in QDSCs.

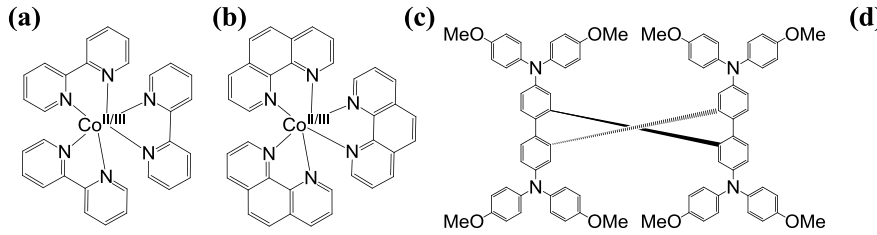

(d)

Electrolyte system	Redox potential (in Volt)	(in eV)
I^-/I^{3-}	0.35	-4.75
Co-bpy	0.56	-5.06
Co-phen	0.62	-5.12
Spiro-OMeTAD	0.61	-5.11

Figure 1.9 Structure of liquid state electrolytes (a) $Co^{II/III}$-tris-(2,2′-bipyridine), (b) $Co^{II/III}$-tris-(1,10-phenanthroline), and solid-state hole conductor (c) spiro-OMeTAD. (d) Redox potentials of different electrolyte systems.

Besides, electrical additives (*t*-butyl pyridine, guanidium thiocyanate, 1-methyl-benzimidazole, *etc*.) can also be mixed to the electrolyte to enhance the device efficiency by means of, (1) uplifting of redox couple potential, (2) shifting of CB edge of ZnO, (3) minimized ZnO surface blocking, and (4) retarded recombination kinetics.[159,160] Even if the use of liquid electrolytes with interfacial affinity and high ionic conductivity has grounded superb PCEs,[19,20] durability of DSCs or QDSCs is still limited by virtue of volatilization and leakage of solvent, instability, corrosive nature of the electrolyte, and encapsulation difficulty.[157] To reduce the deteriorated effects of liquid electrolytes, recently developed solid-state electrolytes and hole conducting materials have delineated an ample of stability and durability.[161] However, PCE of solid-state DSCs and QDSCs still lag behind their liquid electrolyte counterparts due to the low conductivity and poor interfacial electrolyte/electrode contacts. The design and synthesis of novel electrolytes with more efficient charge carrier transport property and long-term stability is still on the way. Redox potentials and structures of commonly used liquid- and solid-state electrolytes in solar cells are depicted in Figure **1.9**.[99,100,162]

1.5.4. Counter Electrode Materials

Counter electrode, an integral part of solar cells, is vital to collect electrons from the external load and to catalyze the reduction of redox couple in electrolyte. These electrons are conducted from the electrolyte to excited sensitizers to bring them back to ground state.[51] Since the inception of DSCs, Pt is recognized as the most promising candidate for counter electrodes.[163] Intrinsic features like good conductivity, larger effective surface area, and high catalytic activity offer excellent prospects for Pt to act as an effective counter electrode against I_3^-/I^- redox couple. However, for cobalt and sulfide redox couple containing electrolytes, Pt is not a favorable counter electrode.[164] In case of cobalt complex based electrolytes, a large dispute in the electrochemical behavior of ligands tends to decrease the catalytic activity of Pt.[165] On the other

hand, an indelible chemisorption of S-compounds onto Pt surface, often caused by S^{2-}/S_n^{2-} redox couple, deteriorates its conductivity and electrocatalytic activity and also increases the charge transfer resistance at the Pt/electrolyte interface.[166] To overcome such practical and economic barriers, the scientific thrust has explored several noble metal-free and cost-effective alternatives (carbon materials, transition metal compounds, conducting polymers or hybrids, and inorganic chalcogenide materials) as the efficient counter electrodes.[164] It should be noted that the ideal functioning of any counter electrode requires to fulfil a few benchmark parameters such as, an optical transparency of ~80% at 550 nm, a sheet resistance of ~20 Ω sq^{-1}, and a charge transfer resistance of ~2–3 $\Omega.cm^2$.[167] However, in most cases, it is difficult to incorporate all these intriguing properties into one material to achieve an efficient operation. It is therefore imperative to continue our interest in the advancements of counter electrode materials with multifunctional, versatile and modulated properties.

1.6. CONCLUSIONS AND OUTLOOK

Since the discovery of DSCs in 1991, a substantial growth of solar cell technology exploring a wide variety of materials has been continuously demonstrating superior performances in terms of high-efficiency. Recent advances in this area have also witnessed the new pathways to develop high-performance photovoltaic assemblies. In the brief discussion on DSCs and SSCs/QDSCs, we have focussed on the variety of interesting roles of semiconductor oxide materials, molecular dyes, QD sensitizers, electrolytes, and counter electrode materials to enhance the device performance. Excellent electronic as well as the surface properties of ZnO could be employed in the devices by means of nanoparticulate, branched, and one-dimensional morphological forms that can open exciting and new directions to improve the overall charge-transfer dynamics of the devices. Coupling of ZnO with excellent light harvesting semiconductor nanostructures or molecular dyes presents a contemporary approach to design and develop wide variety of novel materials for the photovoltaic applications. Even if a diverse combination of sensitizers exhibited best prospects in both DSCs and QDSCs, experimental techniques applied to incorporate them into nanostructured ZnO frameworks as the hosts need more scientific attention. For instance, monolayered dye or QD absorbers exhibit inferior device performance owing to their poor absorptivity in the visible region. In this regard, favorable band alignment mediated combinations of different sensitizers seemed to be a popular choice to fulfil the light harvesting rudiments involving solution processed synthetic routes. Besides, a facile chemical and surface

modification of both ZnO and sensitizer can be performed to enrich surface and electrochemical properties of ZnO–sensitizer couples for best results. In tandem with the advancements of ZnO and sensitizer materials for DSCs and QDSCs, modification of the surface properties of counter electrode materials can also promote the device performance. Superior electrical conductivity, chemical robustness, non-corrosive nature, and high stability of newly developed noble metal-free materials for counter electrodes have outperformed the traditional Pt based electrodes in terms of comparable sheet resistance, optical transparency, and mechanical strength. Thus, recent development of multifunctional and advanced materials for solar cell technology in countless aspects has been deemed to be the most demanding strategy at the current stage. Nevertheless, it is still challenging to stabilize the large area production of highly efficient DSCs and SSCs onto flexible substrates at a roll-to-roll processing scale.

1.7. MOTIVATION OF THE PRESENT WORK

- Superior electron mobility, a direct band gap, and flexibility in economic preparation of a great variety of exciting morphologies make ZnO a promising backbone material for the advancements of dye/ semiconductor-sensitized solar cells.
- Excellency in electron transportation and sensitizer scaffolding make ZnO nanostructures a propitious component of DSCs and QDSCs, which in some aspects exhibit strikingly superior performances in contrast to those of the traditional TiO_2 counterparts.
- Spanning from randomly oriented nanoparticulate films to well-aligned 1D geometries, improved electron collection efficiencies found for ZnO based DSCs and QDSCs seem to suggest that TiO_2 nanostructures are not the only way to break the efficiency bottleneck.
- Involvement of 1D ZnO nanowires in the photoanodes can provide a better way ensuring a robust coverage of sensitizers, efficient charge separation and transport, at the same time that smooth diffusion of electrolyte and a rapid regeneration of oxidized sensitizer.
- A progressive drift from DSCs to QDSCs possibly intends to overcome the indelible loss of photoinduced free-charge carriers that often occurs due to the formation of interfacial charge transfer states between the dye molecule and ZnO surface.
- Further improvements in performance of ZnO-based photovoltaic cells can be achieved by controlling the surface chemistry of ZnO to develop or modify its interaction with different dyes, quantum dots, and electrolytes.

1.8. REFERENCES

1. Service, R. F. *Science* **2005**, *309*, 548–551.
2. Potocnik, J. *Science* **2007**, *315*, 810–811.
3. http://www.eia.doe.gov/oiaf/ieo/index.html; US Department of Energy, **2007**; Vol. 2008.
4. BP Statistical Review of World Energy **2013** (http://instituteforenergyresearch.org/wp-content/uploads/2013/06/bp-review-blog-post-graphs.png).
5. U.S. Energy Information Administration (http://www.eia.gov/totalenergy/data/annual/perspectives.cfm).
6. Renewable Energy Policy Network for the 21st Century (REN21) *Renewables* **2014** Global Status Report (Paris: REN 21 Secretariat).
7. Schiermeier, Q., Tollefson, J., Scully, T., Witze, A., Morton, O. *Nat.* **2008**, *454*, 816–823.
8. O'Regan, B.; Grätzel, M. *Nat.* **1991**, *353*, 737–740.
9. Hagfeldt, A.; Boschloo, G.; Sun, L.; Kloo, L.; Pettersson, H. *Chem. Rev.* **2010,** *110*, 6595–6663.
10. Ye, L.; Zhang, S.; Huo, L.; Zhang, M.; Hou, J. *Acc. Chem. Res.* 2014, *47*, 1595−1603.
11. Mora-Seró, I.; Bisquert, J. *J. Phys. Chem. Lett.* **2010**, *1*, 3046–3052.
12. Mishra, A.; Fischer, M. K. R.; Buerle, P. *Angew. Chem., Int. Ed.* **2009**, *48*, 2474−2499.
13. Mayer, A. C.; Scully, S. R.; Hardin, B. E.; Rowell, M. W.; McGehee, M. D. *Mater. Today* **2007**, *10*, 28–33.
14. Kamat, P. V. *J. Phys. Chem. C* **2008**, *112*, 18737–18753.
15. Tada, H.; Fujishimaa, M.; Kobayashi, H. *Chem. Soc. Rev.* **2011**, *40*, 4232–4243.
16. Santra, P. K.; Kamat, P. V. *J. Am. Chem. Soc.* **2012**, *134*, 2508–2511.
17. Solar Photovotaics. A Technologist's View (http://www.carboninsights.org/?p=818).
18. Imahori, H.; Umeyama, T.; Ito, S. *Acc. Chem. Res.* **2009**, *42*, 1809–1818.
19. Mathew, S.; Yella, A.; Gao, P.; Humphry-Baker, R.; Curchod, B. F.; Ashari-Astani, N.; Tavernelli, I.; Rothlisberger, U.; Nazeeruddin, M. K.; Grätzel, M. *Nat. Chem.* **2014**, *6*, 242−247.
20. Chuang, C.-H. M.; Brown, P. R.; Bulović, V.; Bawendi, M. G. *Nat. Mater*. **2014**, 13, 796–801.
21. Ye, L.; Zhang, S.; Huo, L.; Zhang, M.; Hou, J. *Acc. Chem. Res.* **2014**, *47*, 1595−1603.
22. Park, S. H.; Roy, A.; Beaupre, S.; Cho, S.; Coates, N.; Moon, J. S.; Moses, D.; Leclerc, M.; Lee, K.; Heeger, A. J. *Nat. Photonics* **2009**, *3*, 297–302.
23. Li, G.; Shrotriya, V.; Huang, J.; Yao, Y.; Moriarty, T.; Emery, K.; Yang, Y. *Nat. Mater*. **2005**, *4*, 864–868.
24. Ma, W.; Yang, C.; Gong, X.; Lee, K.; Heeger, A. J. *Adv. Funct. Mater*. **2005**, *15*, 1617–1622.
25. Peet, J.; Kim, J. Y.; Coates, N. E.; Ma, W. L.; Moses, D.; Heeger, A. J.; Bazan, G. C. *Nat. Mater*. **2007**, *6*, 497–500.
26. Chen, H-Y.; Hou, J.; Zhang, S. *Nat. Photonics* **2009**, *3*, 649–653.
27. Gemeiner, P.; Mikula, M. *Acta Chimica Slovaca* **2013**, *6*, 29–34.
28. Kontosa, A. I.; Kontosa, A. G.; Tsouklerisa, D. S.; Bernardc, M.-C.; Spyrellisd, N.; Falaras, P. *J. Mater. Process. Technol*. **2008**, *196*, 243–248.
29. Kuscer, D.; Stavber, G., Trefalt, G.; Kosec, M. *J. Am. Chem. Soc.* **2012**, *95*, 487–493.
30. Okuya, M.; Nakade, K.; Osa, D.; Nakano, T.; Kumara, G. R. A.; Kaneko, S. *J. Photochem. Photobiol., A* 2004, *164*, 167–172.
31. 3GSolar Energy Modules (http://www.3gsolar.com/?p=382).
32. Chen, J.; Lei W.; Li, C.; Zhang, Y. Cui, Y. Wanga, B.; Deng, W. *Phys. Chem. Chem. Phys.* **2011**, *13*, 13182–13184.

33. Hashmi, G.; Miettunen, K.; Peltola, T.; Halme, J.; Asghar, I.; Aitola, K.; Toivola, M.; Lund, P. *Renewable Sustainable Energy Rev.* **2011**, *15*, 3717–3732.
34. McConnell, R. D. *Renewable Sustainable Energy Rev.* **2002**, *6*, 271–293.
35. Huang, X.; Huang, S.; Zhang, Q.; Guo, X.; Li, D.; Luo, Y.; Shen, Q.; Toyoda, T.; Meng, Q. *Chem. Commun.* **2011**, *47*, 2664–2666.
36. Li, Y.; Wei, L.; Wu, C.; Liu, C.; Chen, Y.; Liu, H.; Jiao, J.; Mei, L. *J. Mater. Chem. A* **2014**, *2*, 15546–15552.
37. http://www.asx.com.au/asxpdf/20080527/pdf/319b6m8lzhpv3g.pdf.
38. http://www.sony.net/Products/SC-HP/cx_news/vol56/pdf/sideview56.pdf.
39. http://www.g24i.com/pages,indoor-applications,65.html.
40. Chung, In.; Lee, B.; He, J.; Chang, R. P. H.; Kanatzidis, M. G. *Nature* **2012**, *485*, 486–489.
41. Hill, I. G.; Kahn, A.; Soos, Z. G.; Pascal , R. A. J. *Chem. Phys. Lett.* **2000**, *327*, 181–188.
42. Alvarado, S. F.; Seidler, P. F.; Lidzey, D. G.; Bradley, D. D. C. *Phys. Rev. Lett.* **1998**, *81*, 1082–1085.
43. Kersting, R.; Lemmer, U.; Deussen, M.; Bakker, H. J.; Mahrt, R. F.; Kurz, H.; Arkhipov, V. I.; Bässler, H.; Göbel, E. O. *Phys. Rev. Lett.* **1994**, *73*, 1440–1443.
44. Kwon, Y. S.; Song, I.; Lim, J. C., Song, I. Y.; Siva, A.; Park, T. *ACS Appl. Mater. Interfaces* **2012**, *4*, 3141–3147.
45. Hamann, W. T.; Jensen, A. R.; Martinson, A.; Ryswykac, H.; Hupp, J. *Energy. Environ. Sci.* **2008**, *1*, 66–78.
46. Hara, K. and Arakawa, H. In A. Luque and S. Hegedus. Handbook of Photovoltaic Science and Engineering. John Wiley & Sons. doi:10.1002/0470014008.ch15. ISBN 0-471-49196-9.
47. Hagfeldt, A. and Grätzel, M. *Chem. Rev.* **1995**, *95*, 49–68.
48. Hodes, G. *J. Phys. Chem. C* **2008,** *112*, 17778–17787.
49. Bisquert, J.; Fabregat-Santiago, F.; Mora-Sero, I.; Garcia-Belmonte, G.; Gimenez, S. *J. Phys. Chem. C* **2009**, *113*, 17278–17290.
50. Huang, S. Y.; Schlichthorl, G.; Nozik, A. J.; Grätzel, M.; Frank, A. J. *J. Phys. Chem. B* **1997**, *101*, 2576–2582.
51. Reddy, K. G.; Deepak, T. G.; Anjusree, G. S.; Thomas, S.; Vadukumpully, S.; Subramanian, K. R. V.; Nair, S. V.; Nair, A. S. *Phys. Chem. Chem. Phys.* **2014**, *16*, 6838–6858.
52. Anta, J. A.; Guillén, E.; Tena-Zaera, R. *J. Phys. Chem. C* **2012**, *116*, 11413−11425.
53. Li, L.; Zhai, T.; Bando, Y.; Golberg, D. *Nano Energy* **2012**, *1*, 91−106.
54. Zhang, Q.; Cao, G. *Nano Today* **2011**, *6*, 91−109.
55. Hossain, M. A.; Jennings, J. R.; Koh, Z. Y.; Wang, Q. *ACS Nano* **2011**, *5*, 3172–3181.
56. Birkel, A.; Lee, Y.-G.; Koll, D.; Meerbeek, X. V.; Frank, S.; Choi, M. J.; Kang, Y. S.; Char, K.; Tremel, W. *Energy Environ. Sci.* **2012**, *5*, 5392–5400.
57. Snaith, H. J.; Ducati, C. *Nano Lett.* **2010**, *10*, 1259–1265.
58. Huang, Q.; Li, F.; Gong, Y.; Luo, J.; Yang, S.; Luo, Y.; Li, D.; Bai, X.; Meng, Q. *J. Phys. Chem. C*, **2013**, *117*, 10965–10973.
59. Sayama, K.; Sugihara, H.; Arakawa, H. *Chem. Mater.* **1998**, *10*, 3825–3832.
60. Xia, J.; Masaki, N.; Jiang, K.; Yanagida, S. *J. Photochem. Photobiol. A* **2007**, *188*, 120–127.
61. Jose, R.; Thavasi, V.; Ramakrishna, S. *J. Am. Ceram. Soc.* **2009**, *92*, 289–301.
62. Burnside, S.; Moser, J.-E.; Brooks, K.; Grätzel, M.; Cahen, D. *J. Phys. Chem. B* **1999**, *103*, 9328–9332.

63. Hwang, D.; Jin, J.-S.; Lee, H.; Kim, H.-J.; Chung, H.; Kim, D. Y.; Jang, S.-Y.; Kim, D. *Sci. Rep.* **2014**, *4*, 7353.
64. Tan, B.; Toman, E.; Li, Y.; Wu, Y. *J. Am. Chem. Soc.* **2007**, *129*, 4162–4163.
65. Jayabala, P.; Sasirekhab, V.; Mayandic, J.; Jeganathand, K.; Ramakrishnan, V. *J. Alloys Compd*. **2014**, *586*, 456–461.
66. Hod, I.; Shalom, M.; Tachan, Z.; Rühle, S.; Zaban, A. *J. Phys. Chem. C* **2010**, *114*, 10015–10018.
67. Kim, C. W.; Suh, S. P.; Choi, M. J.; Kang, Y. S.; Kang, Y. S. *J. Mater. Chem. A* **2013**, *1*, 11820–11827.
68. Zhang, Q.; Dandeneau, C. S.; Zhou, X.; Cao, G. *Adv. Mater*. **2009**, *21*, 4087–4108.
69. Arnold, M. S.; Avouris, P.; Pan, Z. W.; Wang, Z. L. *J. Phys. Chem. B* **2003**, *107*, 659–663.
70. Look, D. C.; Reynolds, D. C.; Sizelove, J. R.; Jones, R. L.; Litton, C. W.; Cantwell, G.; Harsch, W. C. *Solid State Commun*. **1998**, *105*, 399−401.
71. Forro, L.; Chauvet, O.; Emin, D.; Zuppiroli, L.; Berger, H.; Levy, F. *J. Appl. Phys.* **1994**, *75*, 633−635.
72. Özgür, Ü.; Alivov, Ya. I.; Liu, C.; Teke, A.; Reshchikov, M. A.; Doˇgan, S.; Avrutin, V.; Cho, S.-J.; Morkoç, H. *J. Appl. Phys*. **2005**, *98*, 041301.
73. Diebold, U. *Surf. Sci. Rep*. **2003**, *48*, 53–229.
74. Scanlon, D. O.; Dunnill, C. W.; Buckeridge, J.; Shevlin, S. A.; Logsdail, A. J.; Woodley, S. M.; Catlow, C. R. A.; Powell, M. J.; Palgrave, R. G.; Parkin, I. P.; Watson, G. W.; Keal, T. W.; Sherwood, P.; Walsh, A.; Sokol, A. A. *Nat. Mater*. **2013**, *12*, 798–801.
75. Batzill, M.; Diebold, U. *Prog. Surf. Sci*. **2005**, *79*, 47–154.
76. Matar, S. F.; Campet, G.; Subramanian, M. A. *Prog. Solid State Chem*. **2011**, *39*, 70–95.
77. Tvrdy, K.; Frantsuzov, P. A.; Kamat, P. V. *Proc. Natl. Acad. Sci. USA*. **2011**, *108*, 29–34.
78. Oskam, G.; Hu, Z.; Penn, R. L.; Pesika, N.; Searson, P. C. *Phys. Rev. E* **2002**, *66*, 011403.
79. K. J. Button, C. G. Fonstad, W. Dreybrodt, Phys. Rev. B 1971, 4, 4539.
80. Jarzebski, Z. M.; Marton, J. P. *J. Electrochem. Soc*. **1976**, *123*, 299C–310C.
81. Young, K. F.; Frederikse, H. P. R. *J. Phys. Chem. Ref. Data* **1973**, *2*, 313.
82. Tang, H.; Prasad, K.; Sanjinès, R.; Schmid, P. E.; Lévy, F. *J. Appl. Phys*. **1994**, *75*, 2042–2047.
83. Tiwana, P.; Docampo, P.; Johnston, M. B.; Snaith, H. J.; Herz, L. M. *ACS Nano* **2011**, *5*, 5158–5166.
84. Wang, Z. L. *Mater. Today* **2004**, *7*, 26−33.
85. Klingshirn, C. *ChemPhysChem* **2007**, *8*, 782−803.
86. Memarian, N.; Concina, I.; Braga, A.; Rozati, S. M.; Vomiero, A.; Sberveglieri, G. *Angew. Chem., Int. Ed*. **2011**, *50*, 12321−12325.
87. Yan, K. Y.; Zhang, L. X.; Qiu, J. H.; Qiu, Y. C.; Zhu, Z. L.; Wang, J. N.; Yang, S. H. *J. Am. Chem. Soc*. **2013**, *135*, 9531–9539.
88. Krebs, F. C.; Nielsen, T. D.; Fyenbo, J.; Wadstrøm, M.; Pedersen, M. S. *Energy Environ. Sci*. **2010**, *3*, 512–525.
89. Ajuria, J.; Etxebarria, I.; Cambarau, W.; Muñecas, U.; Tena-Zaera, R.; Jimeno, J. C.; Pacios, R. *Energy Environ. Sci*. **2010**, *4*, 453–458.
90. Kramer, I. J.; Sargent, E. H. *ACS Nano* **2011**, *5*, 8506–8514.
91. Semonin, O. E.; Luther, J. M.; Choi, S.; Chen, H.-Y.; Gao, J.; Nozik, A. J.; Beard, M. C. *Science* **2011**, *334*, 1530–1533.
92. Sessolo, M.; Bolink, H. J. *Adv. Mater*. **2011**, *23*, 1829–1845.

93. Xu, C.; Wu, J.; Desai, U. V.; Gao, D. *J. Am. Chem. Soc*. **2011**, *133*, 8122–8125.
94. Saito, M.; Fujihara, S. *Energy Environ. Sci*. **2008**, *1*, 280–283.
95. Chen, W.; Qiu, Y.; Zhong, Y.; Wong, K. S.; Yang, S. *J. Phys. Chem. A* **2010**, *114*, 3127–3138.
96. Park, K.; Zhang, Q.; Garcia, B. B.; Zhou, X.; Jeong, Y.-H.; Cao, G. *Adv. Mater*. **2010**, *22*, 2329–2332.
97. Zhang, Q.; Dandeneau, C. S.; Candelaria, S.; Liu, D.; Garcia, B. B.; Zhou, X.; Jeong, Y.-H.; Cao, G. *Chem. Mater*. **2010**, *22*, 2427–2433.
98. Lin, C.-Y.; Lai, Y.-H.; Chen, H.-W.; Chen, J.-G.; Kung, C.-W.; Vittal, R.; Ho, K.-C. Energy Environ. Sci. 2011, 4, 3448–3455.
99. Yoshida, T.; Zhang, J. B.; Komatsu, D.; Sawatani, S.; Minoura, H.; Pauporte, T.; Lincot, D.; Oekermann, T.; Schlettwein, D.; Tada, H.; Wohrle, D.; Funabiki, K.; Matsui, M.; Miura, H.; Yanagi, H. *Adv. Funct. Mater*. **2009**, *19*, 17–43.
100. Sheng, X.; Zhao, Y.; Zhai, J.; Jiang, L.; Zhu, D. *Appl. Phys. A: Mater. Sci. Process*. **2007**, *87*, 715–719.
101. Ambade, S. B.; Mane, R. S.; Han, S.-H.; Lee, S.-H.; Sung, M.-M.; Joo, O.-S. *J. Photochem. Photobiol., A* **2011**, *222*, 366–369.
102. Zhang, Q. F.; Chou, T. R.; Russo, B.; Jenekhe, S. A.; Cao, G. Z. *Angew. Chem., Int. Ed*. **2008**, *47*, 2402–2406.
103. Cheng, H.-M.; Hsieh, W.-F. *Energy Environ. Sci*. **2010**, *3*, 442–447.
104. Ueno, S.; Fujihara, S. *Electrochim. Acta* **2011**, *56*, 2906–2913.
105. Chiu, W. H.; Lee, C. H.; Cheng, H. M.; Lin, H. F.; Liao, S. C.; Wu, J. M.; Hsieh, W. F. *Energy Environ. Sci*. **2009**, *2*, 694–698.
106. Xu, F.; Dai, M.; Lu, Y. N.; Sun, L. T. *J. Phys. Chem. C* **2010**, *114*, 2776–2782.
107. Ranga Rao, A.; Dutta, V. *Nanotechnology* **2008**, *19*, 445712.
108. Yodyingyong, S.; Zhang, Q. F.; Park, K.; Dandeneau, C. S.; Zhou, X. Y.; Triampo, D.; Cao, G. Z. *Appl. Phys. Lett*. **2010**, *96*, 073115.
109. Guérin, V.-M.; Pauporté, T. *Energy Environ. Sci*. **2011**, *4*, 2971–2979.
110. Pérez-Hernández, G.; Vega-Poot, A.; Pérez-Juárez, I.; Camacho, J. M.; Arés, O.; Rejón, V.; Peña, J. L.; Oskam, G. Sol. *Energy Mater. Sol. Cells*. **2012**, *100*, 21–26.
111. Ko, S. H.; Lee, D.; Kang, H. W.; Nam, K. H.; Yeo, J. Y.; Hong, S. J.; Grigoropoulos, C. P.; Sung, H. J. *Nano Lett*. **2011**, *11*, 666–671.
112. Chen, G.; Zheng, K.; Mo, X.; Sun, D.; Meng, Q.; Chen, G. *Mater. Lett*. **2010**, *64*, 1336–1339.
113. Xie, Y.; Joshi, P.; Darling, S. B.; Chen, Q.; Zhang, T.; Galipeau, D.; Qiao, Q. *J. Phys. Chem. C* **2010**, *114*, 17880–17888.
114. Xu, C. K.; Shin, P.; Cao, L. L.; Gao, D. *J. Phys. Chem. C* **2010**, *114*, 125–129.
115. Siefermann, K. R.; Pemmaraju, C. D.; Neppl, S.; Shavorskiy, A.; Cordones, A. A.; Vura-Weis, J.; Slaughter, D. S.; Sturm, F. P.; Weise, F.; Bluhm, H. *et al*. *J. Phys. Chem. Lett.* **2014**, *5*, 2753–2759.
116. Strothkämper, C.; Bartelt, A.; Sippel, P.; Hannappel, T.; Schütz, R.; Eichberger, R. *J. Phys. Chem. C* **2013**, *117*, 17901–17908.
117. Chou, T. P.; Zhang, Q.; Cao, C. *J. Phys. Chem. C* **2007**, *111*, 18804−18811.
118. Kamat, P. V. *J. Phys. Chem. Lett*. **2013**, *4*, 908–918.
119. Kamat, P. V. *Acc. Chem. Res*. **2012**, *45*, 1906–1915.

120. Tisdale, W. A.; Williams, K. J.; Timp, B. A.; Norris, D. J.; Aydil, E. S.; Zhu, X. Y. *Science*, **2010**, *328*, 1543−1547.
121. Seol, M.; Ramasamy, E.; Lee, J.; Yong, K. *J. Phys. Chem. C* **2011**, *115*, 22018–22024.
122. Tian, J.; Uchaker, E.; Zhang, Q.; Cao, G. *ACS Appl. Mater. Interfaces* **2014**, *6*, 4466−4472.
123. Zhu, Z.; Qiu, J.; Yan, K.; Yang, S. *ACS Appl. Mater. Interfaces* **2013**, *5*, 4000–4005.
124. Tian, J. J.; Lv, L. L.; Wang, X. Y.; Fei, C. B.; Liu, X. G.; Zhao, Z. X.; Wang, Y. J.; Cao, G. Z. *J. Phys. Chem. C* **2014**, *118*, 16611–16617.
125. Xu, J.; Yang, X.; Wang, H.; Chen, X.; Luan, C.; Xu, Z.; Lu, Z.; Roy, V. A. L.; Zhang, W.; Lee, C.-S. *Nano Lett*. **2011**, *11*, 4138–4143.
126. Tian, J.; Zhang, Q.; Uchaker, E.; Gao, R.; Qu, X.; Zhang, S.; Cao, G. *Energy Environ. Sci*. **2013**, *6*, 3542–3547.
127. Xu, J.; Yang, X.; Yang, Q.-D.; Wong, T.-L.; Lee, S.-T.; Zhang, W.-J.; Lee, C.-S. *J. Mater. Chem.* **2012**, *22*, 13374–13379.
128. Li, C.; Yang, L.; Xiao, J.; Wu, Y.-C.; Sødergaard, M.; Luo, Y.; Li, D.; Meng, Q.; Iversen, B. B. *Phys. Chem. Chem. Phys*. **2013**, *15*, 8710–8715.
129. Cheng, H.-M.; Huang, K.-Y.; Lee, K.-M.; Yu, P.; Lin, S.-C.; Huang, J.-H.; Wu, C.-G.; Tang, J. *Phys. Chem. Chem. Phys*. **2012**, *14*, 13539–13548.
130. Seol, M.; Kim, H.; Tak, Y.; Yong, K. *Chem. Commun*. **2010**, *46*, 5521–5523.
131. Xu, J.; Yang, X.; Wong, T.-L.; Lee, C.-S. *Nanoscale* **2012**, *4*, 6537–6542.
132. Seol, M.; Ramasamy, E.; Lee,J.; Yong, K. *J. Phys. Chem. C*, **2011**, *115*, 22018–22024.
133. Tian, J.; Zhang, Q.; Uchaker, E.; Liang, Z.; Gao, R.; Qu, X.; Zhang, S.; Cao, G. *J. Mater. Chem. A* **2013**, *1*, 6770–6775.
134. Sudhagar, P.; Song, T.; Lee, D. H.; Mora-Seró, I.; Bisquert, J.; Laudenslager, M.; Sigmund, W. M.; Park, W. I.; Paik, U.; Kang, Y. S. *J. Phys. Chem. Lett*. **2011**, *2*, 1984–1990.
135. Wu, G.; Shen, Y.; Wu, Q.; Gu, F.; Cao, M.; Wang, L. *J. Alloys Compd.* **2013**, *551*, 176–179.
136. Kim, S.-K.; Raj, C. J.; Kim, H.-J. *Electron. Mater. Lett*. **2014**, *10*, 1137–1142.
137. Chetia, T. R.; Barpuzary, D.; Qureshi, M. *Phys. Chem. Chem. Phys*. **2014**, *16*, 9625–9633.
138. Zhang, J.; Sun, C.; Bai, S.; Luo, R.; Chen, A.; Sun, L.; Lin, Y. *Electrochim. Acta* **2013**, *106*, 121–126.
139. Ardo, S. and Meyer, G. J. *Chem. Soc. Rev*. **2009**, *38*, 115–164.
140. Jiang, K. J.; Masaki, N.; Xia, J. B.; Noda, S.; Yanagida, S. *Chem. Commun.* **2006**, 2460–2462.
141. Wang, Q.; Ito, S.; Grätzel, M.; Fabregat-Santiago, F.; Mora-Seró, I.; Bisquert, J.; Bessho, T.; Imai, H. *J. Phys. Chem. B* **2006**, *110*, 25210−25221.
142. Wang, Z.; Liang, M.; Wang, L.; Hao, Y.; Wang, C.; Sun, Z.; Xue, S. *Chem. Commun.* **2013**, *49*, 5748–5750.
143. Yella, A.; Humphrey-Baker, R.; Curchod, B. F. E.; Ashari-Astani, N.; Teuscher, J.; Polander, L. E.; Mathew, S.; Moser, J. -E.; Tavernelli, I.; Rothlisberger, U.; Grätzel, M.; Nazeeruddin, M. K.; Frey, J. *Chem. Mater.* **2013**, *25*, 2733–2739.
144. Mishra, A.; Fischer, M. K. R.; Buerle, P. *Angew. Chem. Int. Ed.* **2009**, *48*, 2474–2499.
145. Ito, S.; Miura, H.; Uchida, S.; Takata, M.; Sumioka, K.; Liska, P.; Comte, P.; Péchyb, P.; Grätzel, M. *Chem. Commun.* **2008**, 5194–5196.
146. Xianga, W.; Huangb, W.; Bachbcd, U.; Spiccia, L. *Chem. Commun*. **2013**, *49*, 8997–8999.
147. Guo, K.; Yan, K.; Lu, X.; Qiu, Y.; Liu, Z.; Sun, J.; Yan, F.; Guo, W.; Yang, S. *Org. Lett.* **2012**, *14*, 2214–2217.

148. Wang, Z.- S.; Cui, Y.; Dan-oh, Y.; Kasada, C.; Shinpo, A.; Hara, K. *J. Phys. Chem. C* **2008**, *112*, 17011–17017.
149. Hwang, S.; Lee, J. H.; Park, C.; Lee, H.; Kim, C.; Park, C.; Lee, M.-H.; Lee, W.; Park, J.; Kim, K.; Park, N.-G.; Kim, C. *Chem. Commun.* **2007**, 4887−4889.
150. Grätzel, M. *Acc. Chem. Res*. **2009**, *42*, 1788–1798.
151. Xu, J.; Chen, Z.; Zapien, J. A.; Lee, C.-S.; Zhang, W. *Adv. Mater*. **2014**, *26*, 5337–5367.
152. Lightcap, I. V.; Kamat, P. V. *J. Am. Chem. Soc*. **2012**, *134*, 7109−7116.
153. Kouhnavard, M.; Ikeda, S.; Ludin, N. A.; Khairudin, N. B. A.; Ghaffari, B. V.; Mat-Teridi, M. A.; Ibrahim, M. A.; Sepeai, S.; Sopian, K. *Renewable Sustainable Energy Rev*. 2014, *37*, 397–407.
154. Choi, Y.; Seol, M.; Kim, W.; Yong, K. *J. Phys. Chem. C* **2014**, *118*, 5664−5670.
155. Becker, M. A.; Radich, J. G.; Bunker, B. A.; Kamat, P. V. *J. Phys. Chem. Lett*. **2014**, *5*, 1575−1582.
156. Liu, I.-P.; Chang, C.-W.; Teng, H.; Lee, Y.-L. *ACS Appl. Mater. Interfaces* **2014**, *6*, 19378–19384.
157. Wu, J.; Lan, Z.; Lin, J.; Huang, M.; Huang, Y.; Fan, L.; Luo, G. *Chem. Rev*. **2015**, *115*, 2136–2173.
158. Yu, Z.; Vlachopoulos, N.; Gorlov, M.; Kloo, L. *Dalton Trans*. **2011**, *40*, 10289–10303.
159. Kambe, S.; Nakade, S.; Kitamura, T.; Wada, Y.; Yanagida, S. *J. Phys. Chem. B* **2002**, *106*, 2967–2972.
160. Nakade, S.; Saito, Y.; Kubo, W.; Kanzaki, T.; Kitamura, T.; Wada, Y.; Yanagida, S. *Electrochem. Commun*. **2003**, *5*, 804–808.
161. Chung, I.; Lee, B.; He, J.; Chang, R. P. H.; Kanatzidis, M. G. *Nature* **2012**, *485*, 486–489.
162. Noha, J. H.; Jeona, N. J.; Choia, Y. C.; Nazeeruddin, M. K.; Grätzel, M. Seok, S. I. *J. Mater. Chem. A* **2013**, *1*, 11842–11847.
163. Hsieh, T.-L.; Chen, H.-W.; Kung, C.-W.; Wang, C.-C.; Vittal, R.; Ho, K.-C. *J. Mater. Chem.* **2012**, *22*, 5550–5559.
164. Yun, S.; Hagfeldt, A.; Ma, T. *Adv. Mater*. **2014**, *26*, 6210–6237.
165. Sapp, S. A.; Elliott, C. M.; Contado, C.; Caramori, S.; Bignozzi, C. A. *J. Am. Chem. Soc*. **2002**, *124*, 11215–11222.
166. Savariraj, A. D.; Viswanathan, K. K.; Prabakar, K. *ACS Appl. Mater. Interfaces* **2014**, *6*, 19702−19709.
167. Trancik, J. E.; Barton, S. C.; Hone, J. *Nano Lett*. **2008**, *8*, 982–987.

Chapter 2

Experimental Section

This chapter describes the general fabrication procedures for semiconductor/dye sensitized solar cells. Basic instrumental techniques and methods used to characterize different materials and devices, along with a detailed evaluation of photovoltaic performance of solar cells are included. Rudimentary concepts and understanding of specific instrumentations such as, solar simulator (Newport Sol3A), incident photon-to-current conversion efficiency analyzer (Oriel IQE 200), and electrochemical impedance spectroscopy (EIS) measurements are being demonstrated.

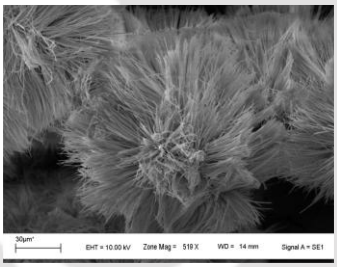

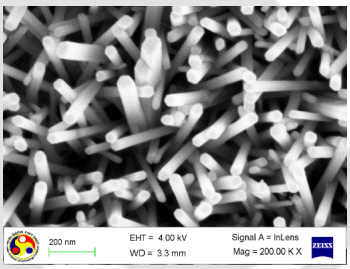

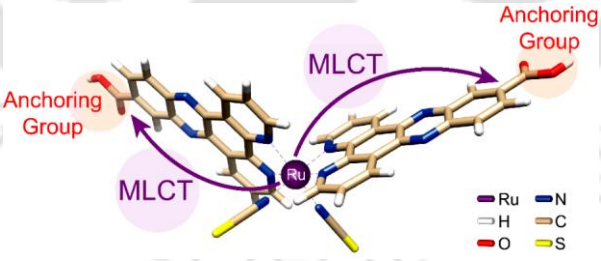

2.1. INTRODUCTION

ZnO presents excellent electron mobility among all wide band gap semiconductor materials explored, as the electron collector and sensitizer scaffold in semiconductor/ dye-sensitized solar cells. The suitability of ZnO to prepare the richest family of nanostructures has led to a plethora of applications in solar cells wherein ZnO nanoparticles, branched structures, and vertically aligned one-dimensional (1D) nanostructures are utilized as photoanodes. In contrast to a random arrangement of ZnO nanoparticles, well-aligned 1D ZnO nanowire networks exhibit promising features such as, a grain boundary-free direct pathway for rapid electron transport and collection, and a minimized charge carrier recombination kinetics. Synthesis of novel structured ZnO based photoanodes for solar cells, as described in this chapter using wet-chemical hydrothermal route, seems to support the real progress in the field up to date.

2.2. SYNTHESIS

2.2.1. Chemicals and Materials Used

Zinc chloride (Merck), sodium hydroxide (Merck), zinc acetate dihydrate (Merck), ethanolamine (Himedia), 2-methoxyethanol (Himedia), zinc nitrate hexahydrate (Merck), plastic syringe fitted with 0.2 μm polytetrafluoroethylene (PTFE) membrane filter (Axiva Sichem Biotech, India), indium tin oxide (ITO) coated glass substrate (surface resistivity ~8–10 Ω/□, Delta Technologies, Ltd., USA) and F-doped tin oxide (FTO) coated glass substrate (surface resistivity ~7–10 Ω/□, Aldrich, USA), hexamethylenetetramine (Himedia), thioglycolic acid (Merck) were purchased.

2.2.2. Synthesis of ZnO Nanoparticles

ZnO nanoparticles were synthesized by following a reported protocol.[1] $ZnCl_2$ (5.5 g, 40 mmol) was dissolved in distilled water (200 mL) and a 5 M NaOH (16 mL) aqueous solution was added drop wise with gentle stirring at 90 °C. The reaction mixture stirred further for 1 h at 90 °C and cooled to room temperature. As-obtained ZnO nanoparticles were separated by sedimentation method. The supernatant dispersion was washed with water till the traces of NaCl were removed completely (confirmed by $AgNO_3$ test). Purified ZnO nanoparticles were dispersed in 2-propanol under an ultrasonic treatment (10 min) to resist agglomeration, collected by centrifugation, and calcined at 350 °C in a muffle furnace (3 h) to obtain in powder form (Yield = 52 %).

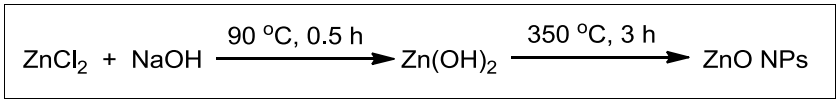

2.2.3. Growth of One-Dimensional ZnO Nanowires on FTO Substrates

Growth of ZnO nanowires over ZnO seed layer coated FTO substrates was carried out using a hydrothermal route.[2] First, a seed solution of ZnO was prepared by mixing $Zn(CH_3COO)_2.2H_2O$ (0.2 g) and ethanolamine (55 μL) in 2-methoxyethanol (3.0 mL) for 8 h and then filtered through a 0.2 μm PTFE filter. FTO coated glass substrates were cleaned with soap solution, washed with distilled water, and treated under an ultrasonic bath for 15 min in each of acetone and 2-propanol, dried by blowing argon and finally subjected to ozone treatment for 30 min. The ZnO seed solution was spin coated on FTO substrates and heated at ~175 °C for 10 min. This procedure was repeated for one more time to obtain a uniform ZnO seed layer film on FTO substrates. The ZnO seed layered FTO substrates were then separately dipped (FTO side down) into a 30.0 mL aqueous solution of $Zn(NO_3).6H_2O$ (50 mM) and hexamine (50 mM) in Teflon vessels, sealed inside a stainless steel autoclave, and maintained at 90 °C (2 h) in an electronic oven to complete the uniform growth of 1D ZnO nanowires. ZnO nanowire grown FTO substrates were taken out, rinsed with ethanol, and heated at 175 °C for 10 min to remove any traces of water and ethanol.

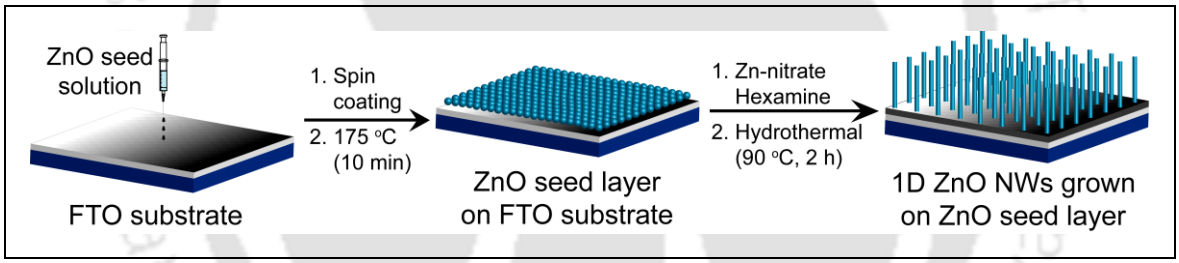

2.2.4. Synthesis of Hierarchical ZnO–CdS and ZnO–CdS–GO Composites

To synthesize ZnO–CdS, CdS nanorods were hydrothermally grown over *ex-situ* generated ZnO nanoparticles following the strategy developed by our group.[3,4] ZnO was synthesized *ex-situ* to resist the formation of ZnS from Zn^{2+} and S^{2-} ions due to a lower solubility product of ZnS over CdS. Typically, ZnO nanoparticles (3 mmol) were dispersed in distilled water (10 mL) under an ultrasonic bath for 30 min. Thioglycolic acid (1 mL, 9 mmol) was added and stirred for 30 min, followed by the addition of an aqueous solution of $Cd(CH_3COO)_2 \cdot 2H_2O$ (2.39 g, 9 mmol). The reaction mixture was stirred further for 30 min at room temperature, poured into a Teflon vessel, sealed inside a stainless steel autoclave, and kept in an electronic oven. A temperature of 140 °C was maintained for 48 h to complete the hydrothermal growth of CdS over ZnO. The autoclave was cooled to room temperature and the solid product was collected by centrifugation (5000

rpm), and washed with each of water and ethanol for three times. ZnO–CdS solid powder was finally obtained by drying in an electronic oven at 60 °C for 4 h (Yield = 57 %).

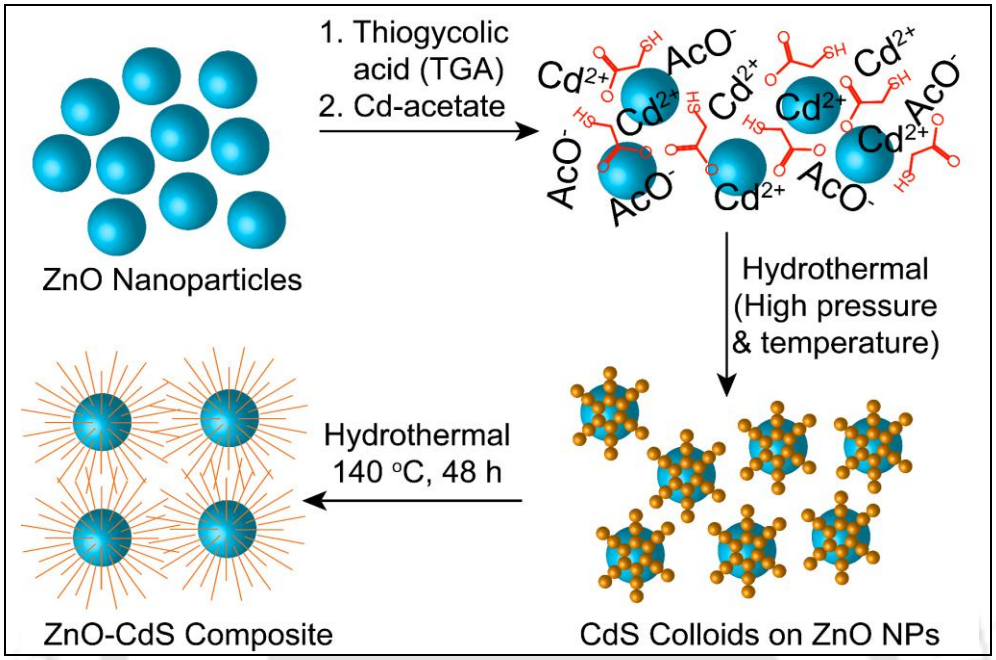

Similarly, to synthesize ZnO–CdS–GO, 1.0 wt % of GO (with respect to ZnO–CdS yield) was dispersed in water (10 mL) under ultrasonic bath for 1 h. ZnO nanoparticles (3 mmol), $Cd(CH_3COO)_2 \cdot 2H_2O$ (2.39 g, 9 mmol), and thioglycolic acid (1 mL, 9 mmol) were added to the GO solution, and an exact procedure used for ZnO–CdS synthesis was followed. ZnO–CdS–GO product was then collected by centrifugation (25,000 rpm). The solid powder of ZnO–CdS–GO was finally obtained by drying in an electronic oven at 60 °C for 4 h (Yield = 53 %).

2.3. CHARACTERIZATION OF MATERIALS AND DEVICES

2.3.1. General Methods

The synthesized compounds (photoanode materials, dye molecules, redox electrolytes, and counter electrode materials) and fabricated solar cells were characterized using a number of techniques. The instrumental methods/tools used in the present investigations include:

1. Powder X-ray diffraction (XRD) using Bruker D8 Advance X-ray diffractometer having a Cu–Kα (λ = 1.54 Å) radiation source, and operating at ~40 kV and ~40 kA.
2. UV–vis diffused reflectance absorption spectra by JASCO V-650 spectrophotometer.
3. Fourier transform infrared spectroscopy (FTIR) using Perkin Elmer FTIR instrument.
4. NMR spectroscopy using 400 MHz and 600 MHz Bruker Advance NMR instruments.

5. Mass spectroscopy using Agilent 6545 Q-TOF LC/MS instrument.
6. Scanning electron microscope (SEM), LEO1430vp, operating at 10–15 kV.
7. Field-emission scanning electron microscope (FESEM), Model Zeiss Gemini, operating at 3–10 kV.
8. Energy-dispersive X-ray spectroscopy (EDS) analysis using INCA, Oxford instruments.
9. Transmission electron microscopy (TEM), JEOL JEM 2100, operating at 200 kV.
10. Photoluminescence using Horiba Jobin Vyon Fluoromax-4 spectrophotometer.
11. Time resolved photoluminescence using LifeSpec II Edinburgh instrument having a lamp with frequency of 5 MHz and Nd:YAG lasers of different excitation wavelengths.
12. Laser micro Raman spectroscopy using Horiba LabRAM HR spectrometer equipped with He–Ne lasers having different excitation wavelengths.
13. BET surface area using Quantachrome Autosorb-IQ MP.
14. Spin coating using SPIN-150 spin coater.
15. Film/layer thickness measurement using a Veeco Dektak 150 surface profilometer.
16. Cyclic voltammetry (CV) using CH instruments, Model CHI600E.
17. Photocurrent–voltage (*J*–*V*) curves of solar cells using Keithley Sourcemeter series 2420.
18. Standard solar spectrum using a Newport ORIEL Sol3A solar simulator fitted with a Xenon arc lamp, power 450 W.
19. Incident photon-to-current conversion efficiency (IPCE) analysis using Newport ORIEL IQE-200 fitted with a 250 W quartz tungsten halogen lamp.
20. Electrochemical impedance spectroscopy (EIS) using CH instruments, Model CHI600E.

2.3.2. Theoretical Study

Electronic density distribution of frontier molecular orbitals of metal-free SK1 dye molecule is estimated from density functional theory (DFT) calculations using Accelrys Materials Studio 4.0. Molecular geometries are optimized in DMol3 program package using generalized gradient approximation (GGA) with BLYP as the basis set. These simulations are carried out in a vacuum for the single molecule. On the other hand, the electronic structure of $Ru(dppz\text{-}COOH)_2(NCS)_2$ dye is investigated by DFT calculations using the Gaussian 09 software[5] at B3LYP level, with the LANL2DZ ECP basis set for the Ru atom and 6-31G basis set for all the other atoms. No symmetry constraint was imposed during the optimization. Absorption and infrared spectra of the Ru dye was computed at time-dependent DFT (TDDFT) level.

2.4. GENERAL FABRICATION OF ZnO–CdS–GO BASED SOLAR CELL

2.4.1. Materials Used

(1) ITO or FTO coated glass substrate (2 × 2 cm, 2 slides for 1 cell).

(2) ZnO–CdS–GO paste: Suspend 5.0 g of ZnO–CdS–GO nano-powder in an agate mortar, add 15 mL of *tert*-butanol, and mix until the suspension/paste is uniform (**Step 1**).

(3) Spacer: Cut a thermosetting sealant film with a dimension of 2.0 cm × 1.5 cm and make a hole (1.5 cm × 0.8 cm) on the film.

(4) Liquid electrolyte: Prepare a 2.0 M S and 2.0 M Na_2S solution in distilled water.

(5) Counter electrode: Prepare a 5 mM H_2PtCl_6 solution in 2-propanol.

(6) Binder clips (small, 2 pieces for 1 cell), hot plate, tweezers, pipets, Scotch tape, *etc*.

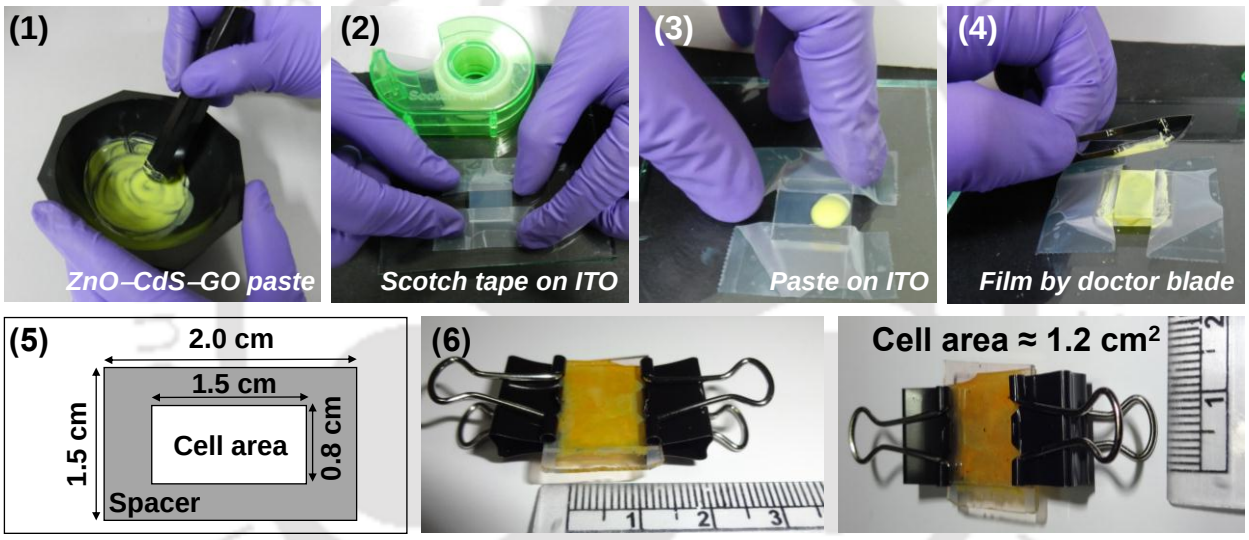

2.4.2. Device Construction

(1) Put Scotch tape on the conducting side of ITO or FTO coated glass substrate (**Step 2**).

(2) Put ZnO–CdS–GO paste (**Step 3**) and flatten it with a blade on the same side of ITO/FTO substrate by doctor blade technique (**Step 4**). Remove the Scotch tape and make the film area of ~1.2 cm^2 (1.5 cm × 0.8 cm) and then dry at 45 °C overnight on a hot plate.

(3) Spin coat H_2PtCl_6 on the conductive side of ITO/FTO glass and heat at 450 °C (15 min).

(4) Place the spacer on top of the ZnO–CdS–GO film (**Step 5**) and put 50 µL of electrolyte solution into the hole.

(5) Immediately place the Pt deposited ITO/FTO glass (facing Pt layer to the spacer) and fix the slides with binder clips (**Step 6**).

2.5. GENERAL FABRICATION OF DYE-SENSITIZED SOLAR CELL

2.5.1. Materials Used

(1) FTO coated glass substrate (2 × 2 cm, 2 slides for 1 cell).

(2) ZnO paste: Grind 5.0 g ZnO nanoparticles, 25 mL terpineol, and 15 mL PEG−PPG−PEG copolymer in an agate mortar for 1 h to get a uniform paste/suspension (**Step 1**).

(3) Dye solution: Prepare a 0.3 mM dye solution in ethanol (or 1:1 ethanol/dichloromethane).

(4) Spacer: A thermosetting sealant film (2.0 cm × 1.5 cm) with a cut hole (1.5 cm × 0.8 cm).

(5) Liquid electrolyte: (a) 0.5 M LiI, 0.05 M I_2, 0.1 M guanidium thiocyanate, and 0.5 M 4-*tert*-butylpyridine or (b) 0.2 M $[Co(bpy)_3](PF_6)_2$, 0.02 M $[Co(bpy)_3](PF_6)_3$, and 0.5 M 4-*tert*-butylpyridine solution in acetonitrile/valeronitrile (9:1, v/v) solvent mixture.

(6) Counter electrode: Pt based electrode as shown in Section **2.4.1**.

(7) Binder clips (small, 2 pieces for 1 cell), hot plate, tweezers, pipets, Scotch tape, *etc*.

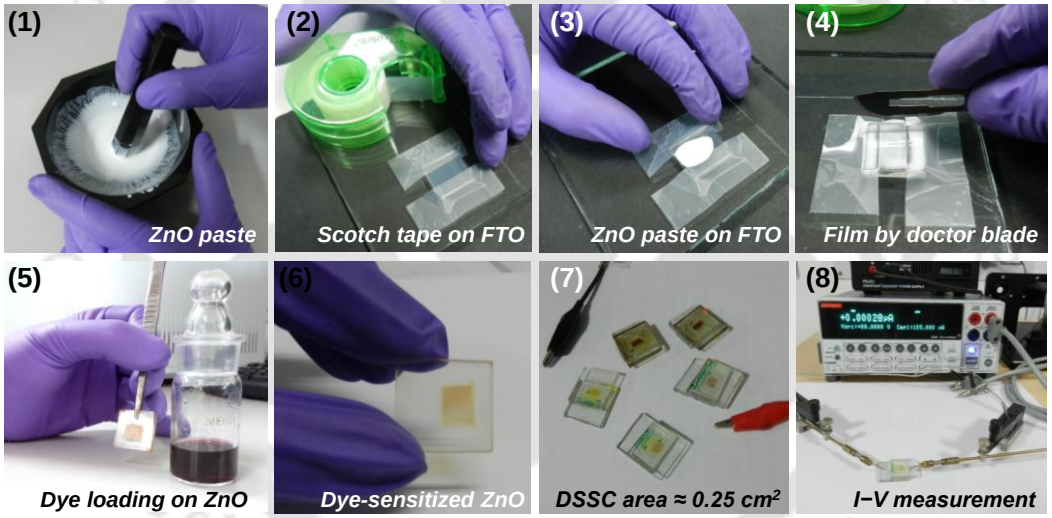

2.5.2. Device Construction

(1) Put Scotch tape on the conducting side of FTO coated glass substrate (**Step 2**).

(2) Put ZnO paste (**Step 3**) and make a film by doctor blade technique (**Step 4**), remove the Scotch tape, make the film area of ~0.25 cm^2, and heat at 450 °C for 30 min.

(3) Dip the ZnO electrode into dye solution, remove, and dry by blowing Ar gas (**Steps 5, 6**).

(4) Place the thermosetting sealant on top of the dye-sensitized ZnO film, place the Pt counter electrode, and heat to glue the FTO substrates (**Step 7**).

(5) Insert 20 µL of electrolyte solution into the hole pre-drilled on Pt coated electrode. Cover the back side of counter electrode by fixing a glass slide using Araldite adhesive.

2.6. EVALUATION OF SOLAR CELLS

2.6.1. Equipments Used

(1) Light source: AM 1.5 G simulated solar illumination (AAA) (intensity of 1000 $W.m^{-2}$).

(2) Electrical connection cables.

(3) Keithley 2400 SourceMeter integrated with variable resistance.

2.6.2. Device Characterization

(1) Connect the solar cell, Keithley 2400 SourceMeter using connecting cables.

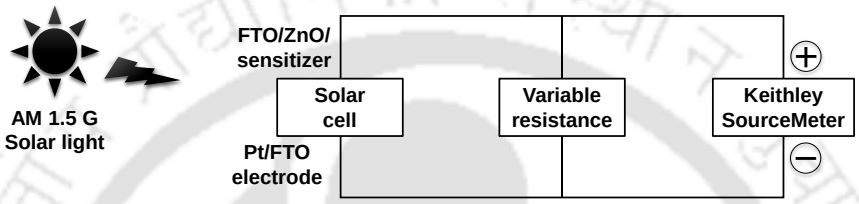

(2) Create a dark condition and measure the dark current value by sweeping the voltage in a range of −0.5 V to +1.5 V. Repeat this step for 5 times to check the consistency.

(3) Turn on the light and measure its intensity using a power meter or photodiode calibrator. It is required to calculate power conversion efficiency (PCE) of the solar cell.

(4) Shine the standard solar light from ZnO/sensitizer electrode side of the solar cell, repeat step 2 to measure the current.

(5) Plot the voltage (*x*-axis) versus current (*y*-axis) curve as shown below.

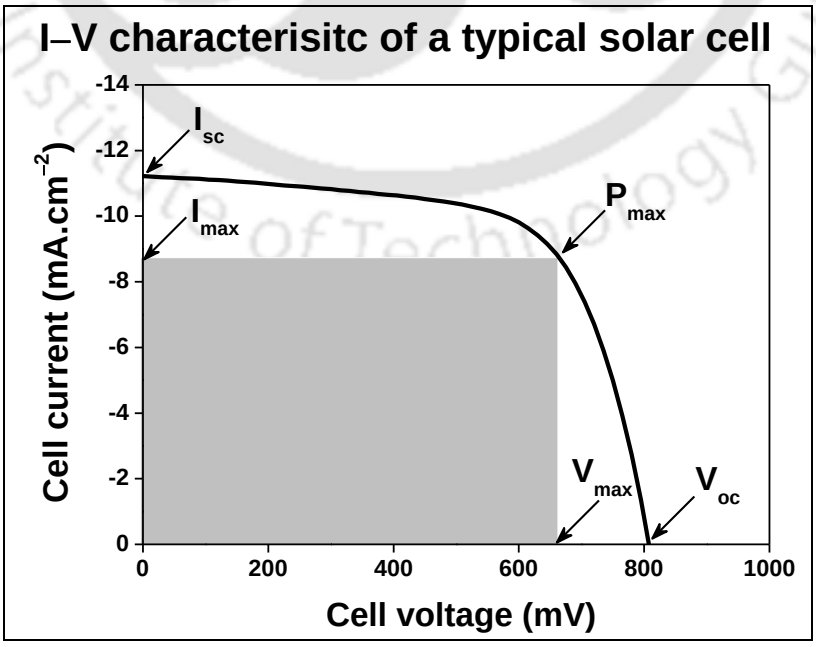

(6) Calculate maximum power (P_{max}) and fill factor (FF) from the current–voltage plot.

$$FF = \frac{I_{max} \times V_{max}}{I_{sc} \times V_{oc}} = \frac{P_{max}}{I_{sc} \times V_{oc}}$$

(7) Calculate power conversion efficiency (PCE, η) as follows.

$$PCE = \frac{\text{Output power}}{\text{Input power}} \times 100\ (\%)$$

$$= \frac{P_{max}\,(mW.cm^2)}{\text{Light intensity}\,(mW.cm^2)} \times 100\ (\%)$$

$$= \frac{I_{sc}\,(mA.cm^2) \times V_{oc}\,(V) \times FF}{\text{Light intensity}\,(mW.cm^2)} \times 100\ (\%)$$

The current and power have to be normalized by the active cell area.

V_{oc} is open circuit voltage, and I_{sc} is short circuit current.

I_{max} and V_{max} are the maximum cell current and maximum voltage, respectively.

P_{max} is the maximum power point of the cell, expressed as, $P_{max} = I_{max} \times V_{max}$.

2.6.3. Working Principle of Solar Simulator

Solar simulator basically involves a standard air mass (AM) 1.5 G (global) solar illumination that is equivalent to natural sunlight. An illumination intensity ~1000 $W.m^2$ is considered worldwide to test and compare efficiency of solar cell in different laboratories. Working of a solar simulator starts with a Xenon arc lamp that acts as the light source. The light is first reflected by an ellipsoidal reflector and then allowed to pass through mirrors, integrated optical lens, an AM 1.5 G filter, and collimated lens prior to fall onto the sample solar cell. The current generated in the solar cell under the light illumination is then recorded using a Keithley SourceMeter.

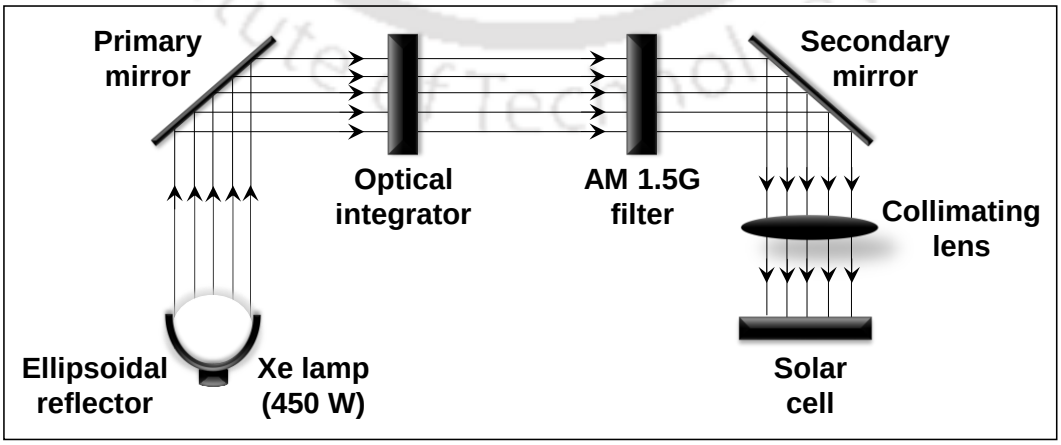

Scheme 2.1 Block diagram of Oriel Sol3A solar simulator generating AM 1.5 G standard solar illumination.

2.6.4. Quantum Efficiency Measurement of Solar Cells

Incident photon-to-current conversion efficiency (IPCE) or the external quantum efficiency (EQE) of a solar cell is given by the ratio of the number of electrons generated under photoexcitation to the number of photons incident on the device.

$$\text{IPCE (or EQE)} = \frac{\text{No. of electrons photogenerated in the solar cell}}{\text{No. of photons incident on the solar cell under illumination}}$$

To measure EQE, internal quantum efficiency (IQE) of a solar cell should also be evaluated. IQE accounts for the internal efficiency of the solar cell and is accountable to the losses associated with the incident photons reflected back from the surface of the cell. Spectral response of the cell as a function of wavelength is measured in terms of EQE. Oriel IQE 200 instrument has a 250 W quartz tungsten halogen (QTH) lamp as the light source. The light is allowed to pass through a Cornerstone monochromator equipped with gratings to create the scanning monochromatic light. The light is then passed through the optical chopper, falls onto solar cell, and the signal is amplified by a Merlin lock-in amplifier unit, and finally detected by the detector.

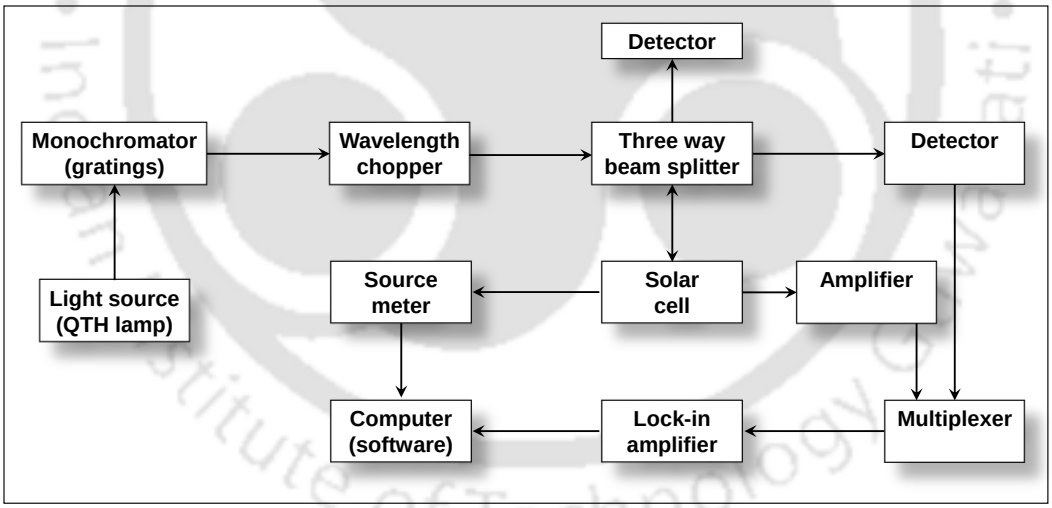

Scheme 2.2 Block diagram of incident photon-to-current conversion efficiency (IPCE) analyzer, Oriel IQE 200.

2.6.4. Electrochemical Impedance Spectroscopy (EIS) Measurement

Electrochemical impedance data of a dye/semiconductor-sensitized solar cell is represented in the form of either a Nyquist plot or a Bode plot.[6] A typical Nyquist plot of a dye-sensitized solar cell depicts three semicircles that are responsible for three key photoelectrochemical processes taking place during the cell operation, as follows: (1) charge transfer at the counter electrode, (2) charge transfer at the ZnO/sensitizer/electrolyte interface, and (3) Nernst diffusion of the redox couple

through the electrolyte and ZnO film. The semicircle associated with the Nernst diffusion process often appears at low-frequency (10^{-2} to 10^{-1} Hz) and requires a longer time for analysis. However, to eliminate the detrimental effects of slow evaporation of volatile electrolytes, EIS data requisition time for the cells tested in this thesis was limited to a couple of minutes per cell. Related to the theme of presented work, paramountcy was given to the charge transfer processes occurring at the ZnO/sensitizer/electrolyte interface and counter electrode/electrolyte interface. In view of this, a frequency range of 10^5 to 10^{-1} Hz was selected for EIS data acquisition, where the Nernst diffusion of electrolyte was not observed. For better understanding of the concept and the interfaces, a schematic is shown in Scheme **2.3** along with the performance parameters.

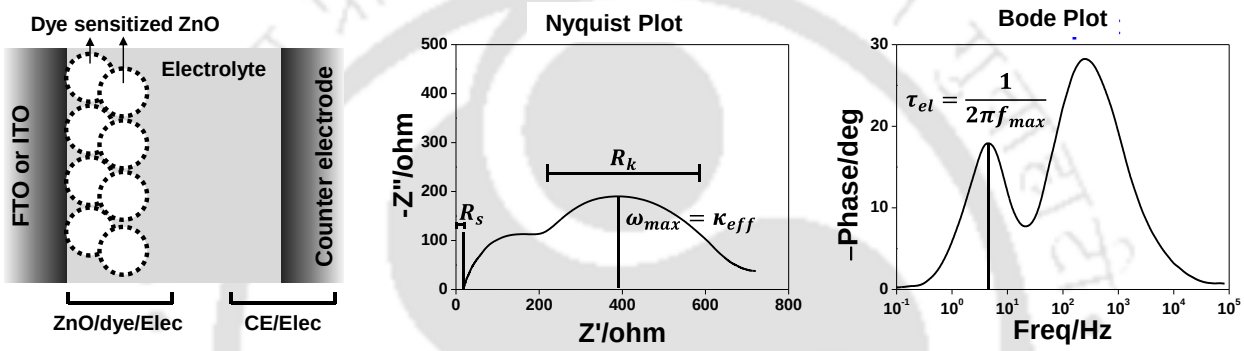

Scheme 2.3 Block diagram illustrating the ZnO/dye/electrolyte (ZnO/dye/Elec) and counter electrode/electrolyte (CE/Elec) interfaces of a typical dye/semiconductor-sensitized solar cell, along with their corresponding Nyquist and Bode phase plots and the derivable parameters.

REFERENCES

1. Becheri, A.; Dürr, M.; Nostro, P. L.; Baglioni, P. *J. Nanopart. Res.* **2008**, 10, 679–689.
2. Park, H.; Chang, S.; Jean, J.; Cheng, J. J.; Araujo, P. T.; Wang, M.; Bawendi, M. G.; Dresselhaus, M. S.; Bulović, V.; Kong, J.; Gradečak, S. *Nano Lett.* **2013**, *13*, 233–239.
3. Barpuzary, D.; Khan, Z.; Vinothkumar, N.; De, M.; Qureshi, M. *J. Phys. Chem. C* **2012**, *116*, 150–156.
4. Khan, D.; Barpuzary, D.; Baswant, O.; Sutradhar, S.; Qureshi, M. *Mater. Lett.* **2011**, *65*, 1168–1171.
5. Frisch, M. J.; Trucks, G. W.; Schlegel, H. B.; Scuseria, G. E.; Robb, M. A.; Cheeseman, J. R.; Scalmani, G.; Barone, V.; Mennucci, B.; Petersson, G. A.; *et al.* Gaussian 09, Revision D.01; Gaussian, Inc.: Wallingford, CT, **2013**.
6. Phadke, S.; Du Pasquier, A.; Birnie, D. P. *J. Phys. Chem. C* **2011**, *115*, 18342–18347.

Chapter 3

Novel Ternary Hybrid Composite of ZnO, CdS, and Graphene Oxide as a One-coat Paintable Solution for Solar Cell

This chapter describes the hydrothermal synthesis and utilization of a ternary hybrid composite of ZnO, CdS and graphene oxide (GO), wherein ZnO–CdS nanourchins are well-embedded onto the GO sheets, as a novel photoactive material for the semiconductor-sensitized solar cells. The key features of novel ZnO–CdS–GO composite based photoanode, the intriguing effects of 1.0 wt % of GO loading to ZnO–CdS, and the electronic interactions of GO with binary ZnO–CdS, to afford an impressive power conversion efficiency of the fabricated device are demonstrated.

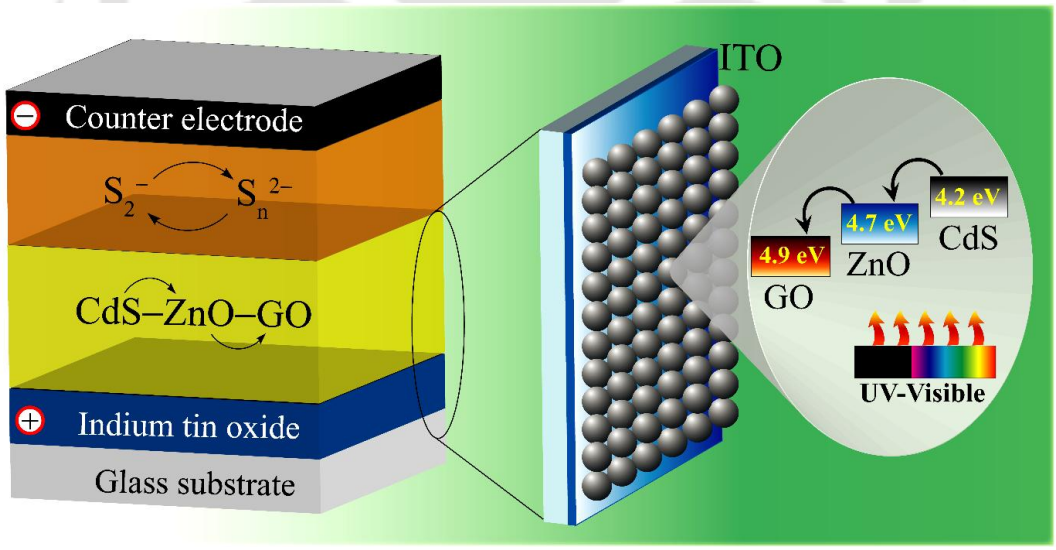

ACS APPLIED MATERIALS & INTERFACES

D. Barpuzary, M. Qureshi **2013**, 5, 11673–11682

THE JOURNAL OF PHYSICAL CHEMISTRY C

D. Barpuzary *et al.* **2012**, 116, 150–156

3.1. INTRODUCTION

Semiconductor-sensitized solar cells (SSCs) have gained significant academic and technological prominence among the researchers for the improvement of photovoltaic power generation from the solar energy. Inorganic semiconductor nanomaterials are one of the promising candidates to generate photovoltaic assemblies due to their intrinsic peculiarities such as, size-quantized tunable band gap, multiple exciton generation, high electron mobility, faster charge transport, long-term stability, *etc*.[1,2] In view of this, a proximal band alignment mediated charge transfer and an efficient visible light harvesting ability can be readily achieved by coupling wide- and narrow-band gap semiconductor nanomaterials, as shown in Scheme **3.1a**.[3–8] Recently, mesoscopic ZnO based nanostructures, in contrast to commonly used TiO_2 scaffolds, have been considered as a popular choice among the wide-band gap materials in photovoltaics due to its excellent electron mobility (~200–2000 $cm^2.V.s^{-1}$), faster charge transport, extended electron diffusion length and an ease of synthesize to achieve desired morphologies.[9–11] However, in SSCs, the limited visible light absorptivity of ZnO due to a direct band gap of ~3.3 eV necessitates its surface modification by coupling with a narrow-band gap semiconductor (CdS, CdSe) to achieve an enhanced light absorption and hence the device performance.[12–15] ZnO based electrodes are often sensitized by depositing CdS or CdSe quantum dots (QDs) by successive ion layer adsorption and reaction (SILAR) and chemical bath deposition methods.[16,17] However, a thicker QD layer affording a high surface coverage blocks the mesopores of the oxide scaffold, which eventually limits the electron transport in the device due to the charge hopping and also inhibits the smooth diffusion of redox couple through the mesopores. In this context, targeting the advancement of semiconductor-coupled devices, rational design and development of one-dimensional (1D) core–shell hierarchical hetero-assemblies is an excellent approach that allows to accomplish higher surface area, more exposed surfaces for sufficient solar absorption, smooth diffusion of electrolyte, efficient physical separation of photogenerated charge carriers, and most importantly, generates the 1D pathways prompting the charge transfer/migration in the devices. Another approach to improve the semiconductor-coupled device performance is to enhance the absorption profile of semiconductor coupled/sensitized structures by coupling with a dye (mostly squaranine) that can selectively capture the photons up to the near-infrared region (Scheme **3.1b**).[18] Even if semiconductor–dye super-sensitization concept enables an effective migration of photoinduced holes from the semiconductor to dye, it has some limitations. One of the possible

issues is a restricted scavenging of photogenerated holes by the redox electrolyte directly from the semiconductor surface.

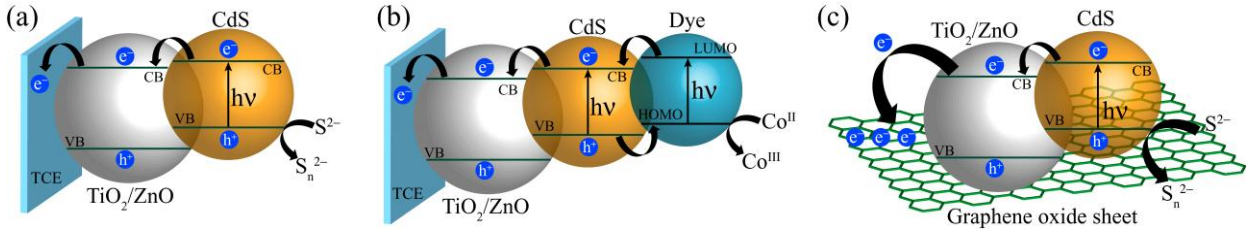

Scheme 3.1 Basic charge transfer processes involved in commonly reported CdS-sensitized solar cells: (a) Binary semiconductor coupled, (b) Semiconductor–dye supersensitization, and (c) Ternary semiconductor–graphene oxide coupled concepts.[3–8,18–20]

One more facile route to maximize the device output is to improve the electron–hole separation (charge separation) and transfer processes of semiconductor-coupled heteroarrays by intervening graphene oxide (GO) sheets to the semiconductor framework, as shown in Scheme **3.1c**.[19,20] The intrinsic excellent electron transport property allows GO to be incorporated as an electron acceptor (sink) to the photoactive materials in the devices, thereby improving the charge-transfer dynamics of the host material even at a smaller loading of GO.[21] Although the structural and chemical inhomogeneity makes it complicated to define an electronic band gap of GO,[22] theoretical and experimental evidences suggest the presence of a band gap defined by the sp^2/sp^3 domains.[23] In essence, excellent intriguing properties of GO and semiconductor nanomaterials have paved a way to utilize their coupled structures in a myriad of technological applications including solar cell, hydrogen production, photocatalysis, fuel cell, Li-ion battery, capacitor, *etc*.[24–28] Furthermore, the robust electronic interacting ability of GO with semiconductors adds a further knob to enviably tune the optical and electrical properties of the semiconductor–GO coupled structures, affording impressive power conversion efficiency (PCE) of photovoltaic assemblies. Paradigms include the use of ternary inorganic–organic–GO hybrids achieving incident photon-to-current conversion efficiencies (IPCEs) beyond ~80%.[29]

This chapter describes the design and synthesis of a novel ternary hybrid composite of ZnO, CdS, and GO as a one-coat paintable solution in performing the role of a photoanode for the SSCs, wherein binary ZnO–CdS heteroarrays are well-embedded onto the GO sheets. The photoconversion properties of the hybrid ternary-system-based photoanodes are evaluated in the photovoltaic devices against Pt and Ag as the counter electrodes with S^{2-}/S_n^{2-} redox couple as the electrolyte. The key features of ZnO–CdS–GO are 3-fold: (1) CdS nanorods hierarchically grown over the ZnO nanoparticle act as a sensitizer, enhancing the visible light absorption,[30] (2) a direct,

fast, and efficient charge transport and separation due to the 1D core–shell type architecture,[31] and (3) band position proximity of CdS, ZnO, and GO entities facilitating an efficient electron transfer from the CdS to ZnO to GO. Current investigations resulted in an enhanced photovoltaic performance of ZnO–CdS–GO based SSCs over ZnO–CdS counterparts, confirming a favorable photogenerated electron–hole separation within the photoactive layer upon 1.0 wt % of GO loading as an electron sink to ZnO−CdS.[19] The electronic interactions of GO to ZnO–CdS, achieved under a hydrothermal route, is evidenced from the drastic quenching of steady-state photoluminescence (PL), reduced exciton lifetime, and Raman scattering measurements. A magnified view of the ZnO−CdS−GO based SSC is illustrated in Scheme **3.2**.

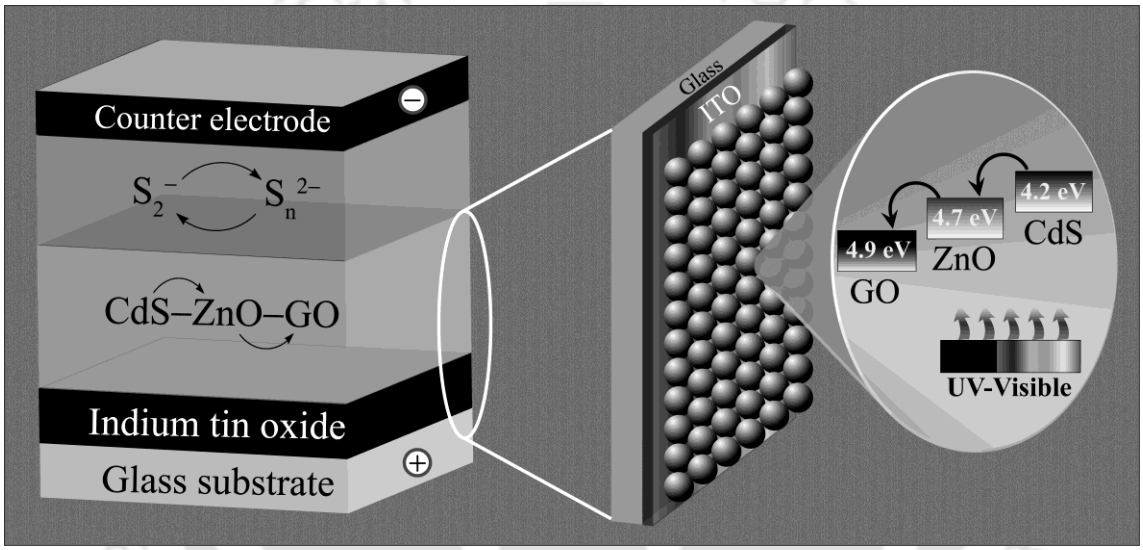

Scheme 3.2 Schematic of the solar cell ITO/ZnO–CdS–GO (~12μm)/Pt. Magnified view shows the proximal band alignment mediated electron transfer within the ternary ZnO–CdS–GO photoactive layer.

3.2. EXPERIMENTAL SECTION

3.2.1. Synthesis of ZnO Nanoparticles

ZnO nanoparticles were synthesized by following the protocol reported by Becheri *et al*.[32] $ZnCl_2$ (5.5 g, 40 mmol) was dissolved in 200 mL of distilled water. An aqueous solution of 5 M NaOH (16 mL) was added drop wise over a period of 15 min with gentle stirring at 90 °C. The reaction mixture was allowed to stir for 1 h at 90 °C, cooled down to room temperature and as-obtained ZnO nanoparticles were then separated by sedimentation method. The supernatant dispersion was washed several times with water till the complete removal of NaCl (confirmed by $AgNO_3$ test). The purified ZnO NPs were dispersed in 2-propanol under ultrasonic treatment for a period of 10 min to resist the agglomeration, collected by centrifugation and finally calcined at 350 °C in a muffle furnace for 3 h to obtain in the powder form (Yield = 52 %).

3.2.2. Synthesis of CdS Nanorods

CdS nanorods were synthesized as reported by our group.[29] Typically, $Cd(CH_3COO)_2.2H_2O$ (2.39 g, 9 mmol) and thioglycolic acid (1.0 mL, 9 mmol) were mixed in ethylenediamine (10 mL) and stirred for 30 min. The growth of freestanding CdS nanorods was then performed under a hydrothermal treatment at 140 °C (7 h). As-obtained solid was separated by centrifugation, and washed three times with distilled water and ethanol each. The sample was dried at 60 °C for 2 h in an electronic oven and obtained in the powder form (Yield = 48 %).

3.2.3. Synthesis of Graphene Oxide

Graphene oxide was synthesized from graphite by a modified Hummer's method.[33] Typically, 187 mL of conc. H_2SO_4 was added to a mixture of 2.5 g of graphite and 1.87 g of $NaNO_3$ under stirring in an ice bath, followed by the addition of 11.25 g of $KMnO_4$ over 1 h. The mixture was continuously stirred for another 2 h in an ice bath, and subjected to vigorous stirring at 35 °C for 7 d. In the next step, 350 mL of 5 wt % H_2SO_4 aqueous solution was slowly added to the reaction mixture under continuous stirring. The temperature was increased rapidly to 98 °C and stirred further for 2 h. The temperature was again reduced to 60 °C and 4.7 mL of H_2O_2 (48 wt % aqueous solution) was added to remove the unreacted $KMnO_4$. The reaction mixture was cooled to room temperature and stirred for 2 h. The undesired ions and other inorganic impurities were removed from the reaction mixture by centrifugation. The as-obtained solid was then purified in two steps. In the first step, 1.0 L aqueous solution of 3 wt % H_2SO_4 and 0.5 wt % H_2O_2 was added to the precipitate, sonicated for 1 h, and the impurities were removed by centrifugation (10,000 rpm) for 20 min. The sonication and centrifugation processes were then repeated for three more times. In the second step, a sonication for 1 h, followed by the centrifugation for 20 min, was repeated using a 1000 mL of a 3 wt % HCl aqueous solution. Once all the impurities were removed, GO was extracted in distilled water by ultrasonic treatment, and finally dried in a vacuum oven at 50 °C to obtain the GO sheets (1.7 g).

3.2.4. Synthesis of Binary ZnO–CdS and Ternary ZnO–CdS–GO Composites

To synthesize ZnO–CdS, the growth of CdS nanorods was performed on *ex-situ* generated ZnO using hydrothermal strategy. An *ex-situ* synthesis of ZnO was carried out to resist the formation of ZnS from the Zn^{2+} and S^{2-} ions due to a lower solubility product of ZnS over CdS. Typically, ZnO nanoparticles (3 mmol) were dispersed in distilled water (10 mL) under an ultrasonic bath for 30 min. Thioglycolic acid (1 mL, 9 mmol) was added and stirred for 30 min, followed by the

addition of an aqueous solution of $Cd(CH_3COO)_2 \cdot 2H_2O$ (2.39 g, 9 mmol). The reaction mixture was stirred further for 30 min at room temperature, poured into a Teflon vessel, sealed inside a stainless steel autoclave and kept in an electronic oven. A temperature of 140 °C was maintained (48 h) to complete the hydrothermal growth of CdS over ZnO. The autoclave was cooled to room temperature and the solid product was collected by centrifugation (5000 rpm), and washed with each of water and ethanol for three times. The ZnO–CdS solid powder was finally obtained by drying in an electronic oven at 60 °C for 4 h (Yield = 57 %). In a similar way, to synthesize ZnO–CdS–GO, first, GO (1.0 wt %, with respect to ZnO–CdS) was dispersed in 10 mL of distilled water under ultrasonic bath for 1 h. In the next step, ZnO nanoparticles (3 mmol), $Cd(CH_3COO)_2 \cdot 2H_2O$ (2.39 g, 9 mmol), and thioglycolic acid (1 mL, 9 mmol) were added and the same procedure for ZnO–CdS synthesis was followed. As-synthesized ZnO–CdS–GO composite was collected by centrifugation (25,000 rpm). The solid powder of ZnO–CdS–GO was finally obtained by drying in an electronic oven at 60 °C for 4 h (Yield = 53 %).

3.2.5. Device Fabrication and Characterization

Indium tin oxide (ITO) coated glass substrates (sheet resistance ~8–10 Ω/sq, Delta Technologies Ltd., USA) were cleaned by soap solution and distilled water, followed by ultrasonic treatment for 15 min in each of acetone and *iso*-propanol. ITO substrates were taken out from the solvent, dried by blowing Ar and subjected to ozone treatment for 30 min prior to use. Scotch tape was fixed to the edges of ITO substrates to get an active area of ~1.2 cm^2 for the cells. ZnO–CdS–GO (2.0 g) was taken in an agate mortar and ground for 1 h with *tert*-butanol (added drop wise time to time) to get a paste and coated over ITO substrates by doctor blade technique. The solvent was evaporated by drying in an electronic oven overnight at 40 °C and a thickness of ~10–15 μm was measured for the ZnO–CdS–GO layer using a surface profilometer. A detailed procedure for the fabrication of photoanode is shown in Figure **3.1**. A Pt coated ITO substrate or Ag deposited glass substrate was used as the counter electrode for the device characterization. To prepare Pt counter electrode, an H_2PtCl_6 solution in ethanol (~2 mg/mL) was spin coated on a pre-cleaned ITO substrate, followed by calcination at 450 °C (ramp ~5 °C/min) for 15 min in a muffle furnace and cooled to room temperature. To prepare Ag counter electrode, the glass substrates were cleaned in soap solution, distilled water, acetone and *iso*-propanol under the ultrasonic treatment for 15 min (for each), dried by blowing Ar and subjected to ozone treatment for 10 min. Silver was thermally evaporated onto the glass substrates at a deposition rate of 2.0 Å/s at ~10^{-7} mbar vacuum. The photovoltaic cells were constructed by sandwiching the photoanodes and

respective counter electrodes. A drop of sulfide/polysulfide (S^{2-}/S_n^{2-}) electrolyte, prepared by dissolving 2.0 M S and 2.0 M Na_2S in distilled water, was then injected to each of the cells. To probe the effects of GO loading in the device performance, GO-free devices were constructed with ITO/ZnO–CdS photoanode against Pt/Ag counter electrode and S^{2-}/S_n^{2-} electrolyte. To fabricate the photoanodes, a ZnO–CdS paste was obtained by grinding ZnO–CdS in *tert*-butanol for 1 h. The paste was coated on pre-cleaned ITO substrates to get a ZnO–CdS film (~10–15 μm thick) and was dried overnight at 40 °C. Hereafter, all the fabricated devices are abbreviated as ZCGO-Pt (ITO/ZnO–CdS–GO/Pt), ZC-Pt (ITO/ZnO–CdS/Pt), ZCGO-Ag (ITO/ZnO–CdS–GO/Ag) and ZC-Ag (ITO/ZnO–CdS/Ag).

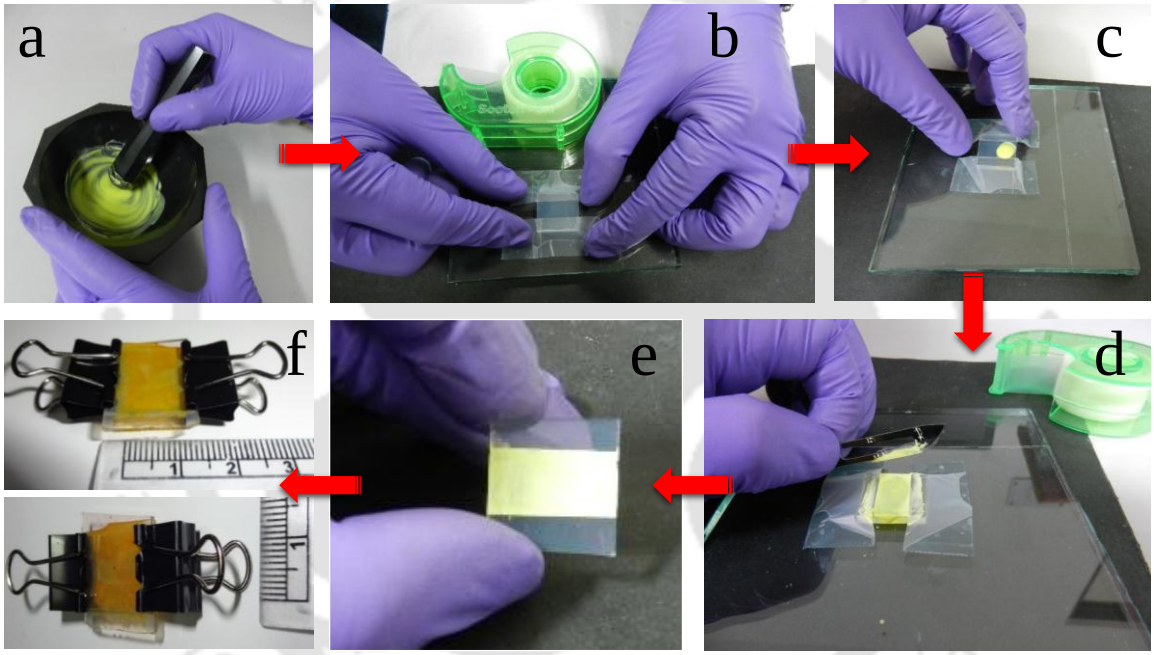

Figure **3.1** General procedure followed to fabricate the ITO/ZnO–CdS–GO photoanode. (a) Grinding ZnO–CdS–GO powder in *tert*-butanol to get a paste, (b) fixing of scotch tape on ITO substrates, (c) ZnO–CdS–GO paste onto the ITO substrate, (d) ZnO–CdS–GO film coated on ITO by doctor blade technique, (e) ITO/ZnO–CdS–GO photoanode after drying overnight at 40 °C, (f) fabricated device ITO/ZnO–CdS–GO/Pt with an active area ~1.2 cm^2.

To have a better understanding of the thickness and layer interface of the ZnO–CdS–GO layer, a cross-sectional filed-emission scanning electron microscopy (FESEM) image and energy-dispersive X-ray spectroscopy (EDX) pattern were recorded for a dummy photoanode fabricated on a glass substrate, as shown in Figure **3.2**. To prepare the sample, a ZnO–CdS–GO paste was coated on a pre-cleaned, ozonized glass substrate by doctor blade technique and then dried overnight at 40 °C. The glass substrate was mounted at an angle of 60° on the sample holder of the SEM instrument. Figure **3.2** shows a thickness of ~10–12 μm for the ZnO–CdS–GO layer, which was further confirmed using the surface profilometer.

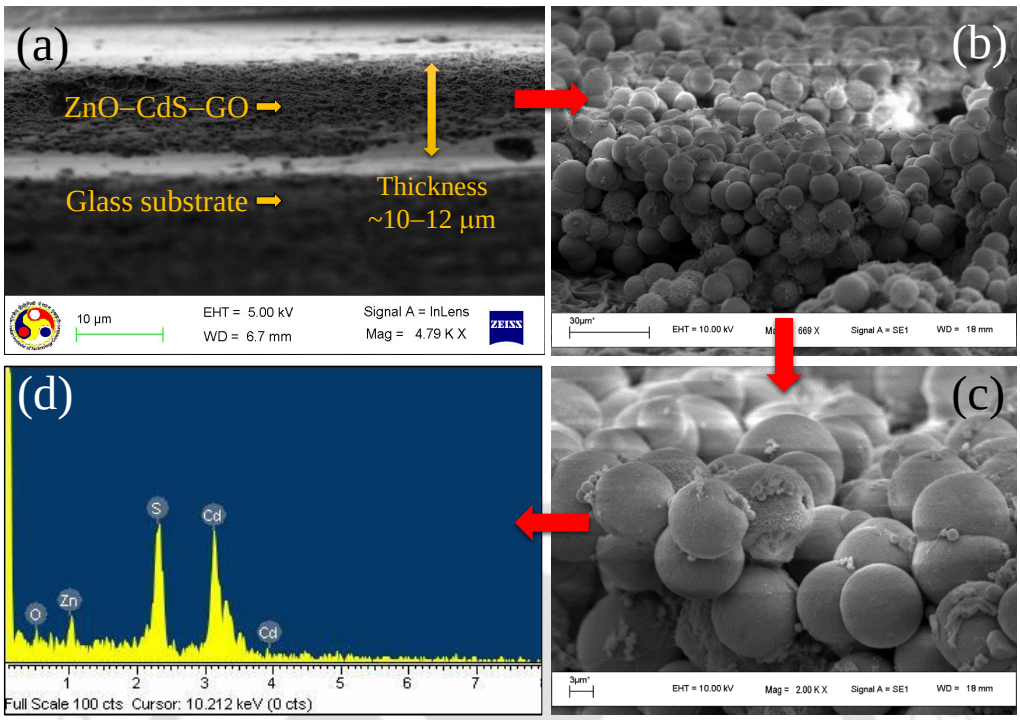

Figure 3.2 (a–c) Cross-sectional FESEM images at different magnifications of a dummy ZnO–CdS–GO photoanode fabricated on glass substrate showing the thickness of ~10–12 µm for the ZnO–CdS–GO layer. (d) EDX pattern of the ZnO–CdS–GO film confirming the presence of elements: Zn, O, Cd, and S.

3.3. RESULTS AND DISCUSSIONS

3.3.1. Mechanism for the Formation of Hierarchical ZnO–CdS Nanourchins

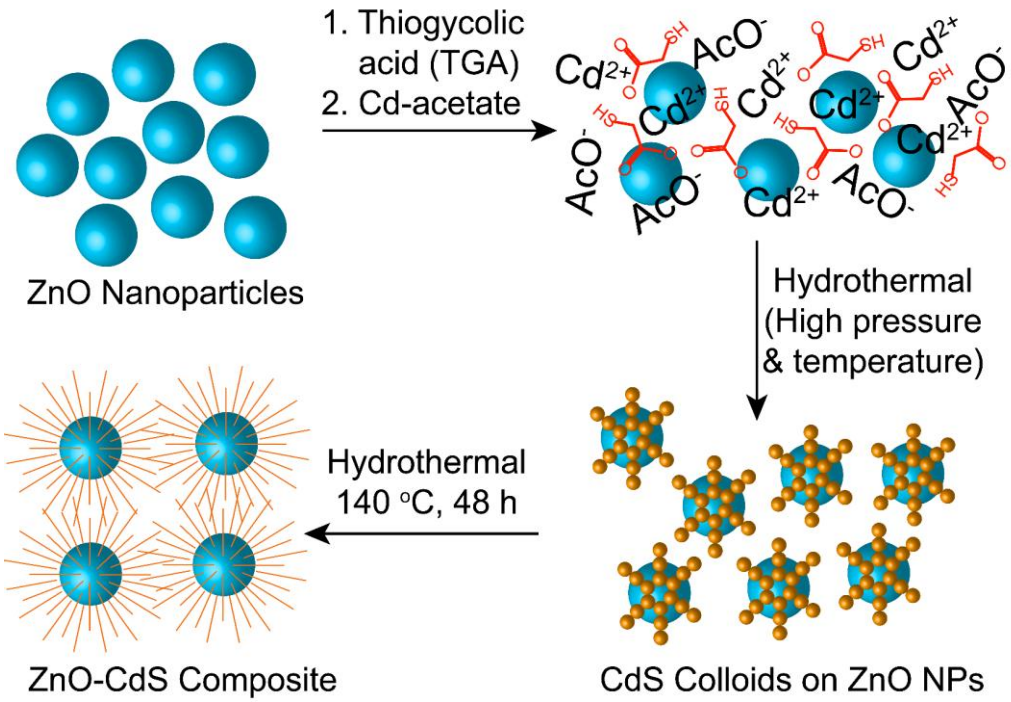

Scheme 3.3 Schematic showing the hydrothermal synthesis of ZnO–CdS nanourchins following the impregnated growth of 1D CdS nanorods onto the *ex-situ* generated ZnO nanoparticles.[29]

The mechanism for hydrothermal synthesis of ZnO–CdS, carried out by an impregnated growth of CdS nanorods onto the *ex-situ* synthesized ZnO nanoparticles, can be explained as shown in Scheme **3.3**.[29] First, the addition of thioglycolic acid to ZnO nanoparticles (pre-dispersed in water) and a continuous stirring of ~30 min results in a preferable attachment of S^{2-} ions (Lewis base) to the ZnO surface due to the Lewis acidity centre on Zn. Further addition of an aqueous solution of $Cd(CH_3COO)_2 \cdot 2H_2O$, followed by a continuous stirring of ~30 min, persuades the formation of CdS colloidal particles over ZnO. In the next step, these saturated colloidal particles act as the seeds for crystal growth of CdS nanorods over ZnO from the supersaturated vapours of Cd^{2+} and S^{2-} under the hydrothermal treatment for 48 h at 140 °C.

3.3.2. Powder X-ray Diffraction Analysis

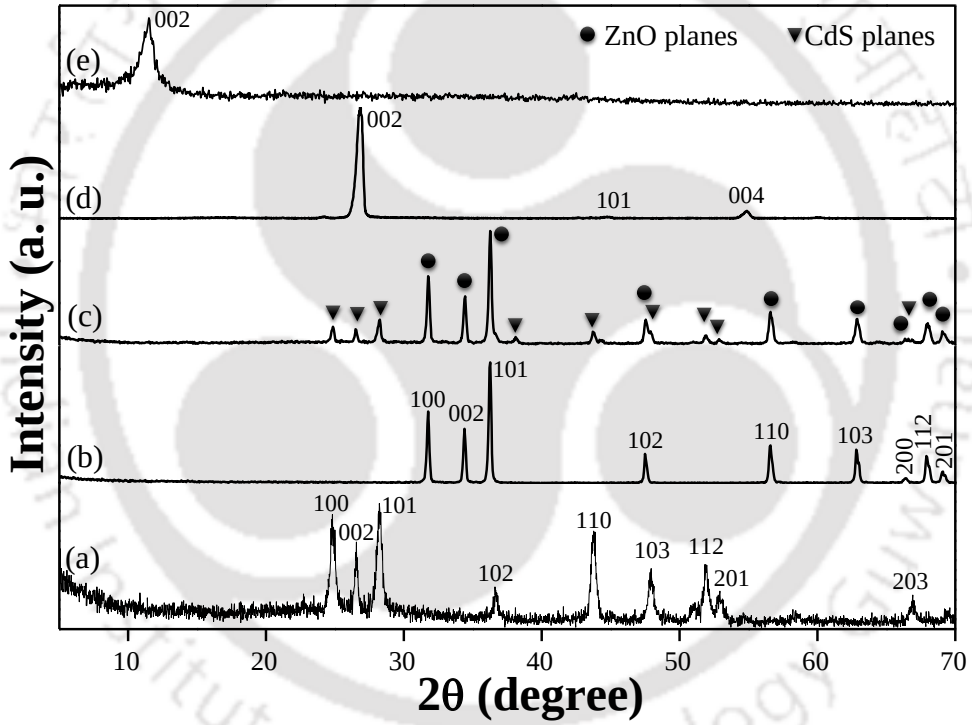

Figure 3.3 Powder X-ray diffraction (XRD) patterns for (a) CdS nanorods, (b) ZnO nanoparticles, (c) ZnO–CdS composite, (d) graphite, and (e) graphene oxide.

Powder X-ray diffraction (XRD) patterns for CdS nanorods, ZnO nanoparticles, bare ZnO–CdS, graphite and GO are shown in Figure **3.3**. The lattice planes (100), (002), (101), (102), (110), (103), (112), (201) and (203) from Figure **3.3a** can be indexed to the formation of hexagonal phase of CdS nanorods with lattice constants of a = 0.4136 nm and c = 0.6713 nm (JCPDC Ref. No. 06-0314). Figure **3.3b** shows the diffractogram for ZnO nanoparticles with the lattice planes (100), (002), (101), (102), (110), (103), (200), (112) and (201), indexed to the hexagonal phase of ZnO and lattice constants of a = 0.3249 nm and c = 0.5205 nm (JCPDC Ref. No. 05-0664).

Figure **3.2c** shows the diffraction peaks for CdS in the diffractogram for ZnO–CdS composite, confirming the retention of structure and crystallinity of freestanding CdS NRs even after their radial growth over ZnO nanoparticles. The XRD pattern for graphite, Figure **3.3d**, exhibits a sharp diffraction peak at 2θ = 26.5° for the (002) graphite plane composed of graphene sheets. Interestingly, the graphite peak disappears for GO and a low-intensity peak at 2θ = 10.5° appears corresponding to the characteristic diffraction peak for (002) GO plane, as shown in Figure **3.3e**.

3.3.3. Normalized UV–vis Absorption Spectra

The UV–vis DRS spectra of the ZnO–CdS and ZnO–CdS–GO based photoanodes are recorded to examine their light-harvesting abilities, as shown in Figure **3.4**. The absorbance data recorded within a wavelength range of 200–800 nm against a blank ITO as the reference have shown almost identical absorption profiles for both the photoanodes that can be correlated to the band energy components of individual systems. As can be seen, there are two distinct absorption edges, at ~330 (for ZnO) and ~500 nm (for CdS) in each of the curves. A slight red shift in the absorption steep of ZnO–CdS occurs upon GO loading, which ensures the charge delocalization in ZnO–CdS–GO due to the electronic interaction of GO to ZnO–CdS. In addition, GO enhances the molar absorptivity of ZnO–CdS in the visible region.[34,35] Notably, Figure **3.4** represents the completely diminished absorption spectra after 570 nm for both ZnO–CdS and ZnO–CdS–GO, which indicates the absence of any impurity energy level transitions.

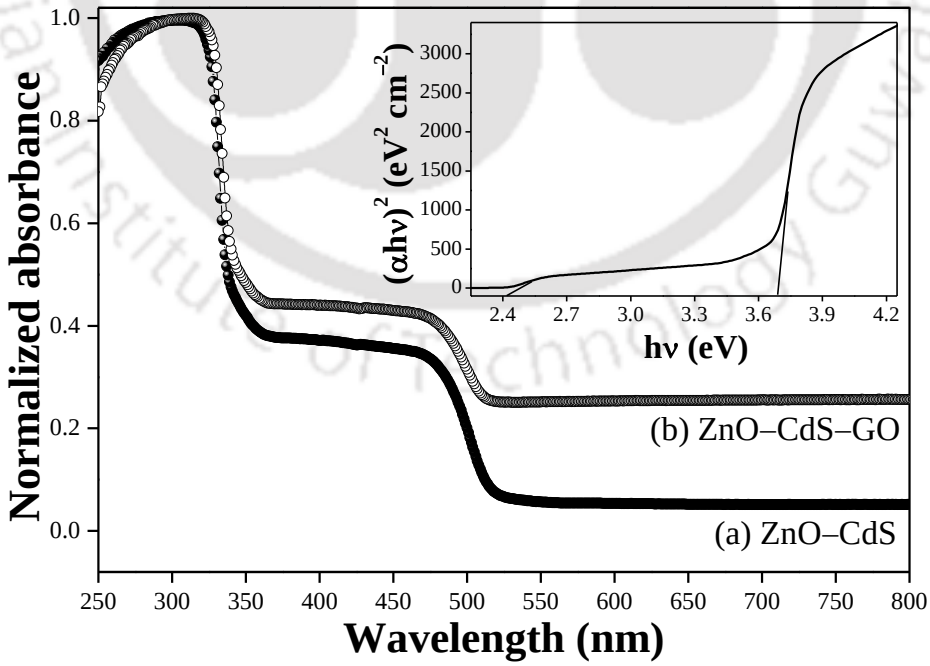

Figure 3.4 UV–vis DRS absorption spectra of (a) ZnO–CdS (filled circles) and (b) ZnO–CdS–GO (empty circles) photoanodes. Inset shows the Tauc plot for ZnO–CdS estimating the band gaps of ZnO and CdS.

The optical band gaps of individual components of ZnO–CdS are also estimated from the Tauc's plot as shown in the inset to Figure **3.4**, where $(\alpha h\nu)^2$ is plotted as a function of photon energy ($h\nu$).[30] The estimated band gap energies for ZnO–CdS are found to be ~3.7 and ~2.5 eV, which corresponds to the individual band gaps of ZnO and CdS components, respectively. The optical band gaps are calculated using Tauc's relationship following eq.s (1) and (2)

$$(\alpha h\nu)^2 = C(h\nu - E_g) \quad (1)$$

$$\alpha = \frac{1}{t} \times A \times \log e \quad (2)$$

where α is the absorption coefficient of ZnO–CdS at specific wavelength value, h is the Planck's constant, C is the proportionality constant, ν is the frequency of incident light, E_g is the band gap of the components of ZnO–CdS, and t is the thickness (in cm) of ZnO–CdS film.

3.3.4. Materials Morphology

The representative SEM images of hydrothermally synthesized ZnO–CdS–GO composite coated on ITO substrates are shown in Figures **3.5a** and **3.5b**. A higher-magnification image of bare ZnO–CdS nanourchins (Figure **3.5c**) clearly demonstrates a radial growth of CdS nanorods onto ZnO nanoparticles. Figure **3.5d** shows the energy-dispersive X-ray spectroscopy (EDX) pattern of ZnO–CdS, confirming the presence of elements Cd, S, Zn, and O. Thus, the ZnO-templated 1D growth of CdS nanorods is confirmed by the SEM images.

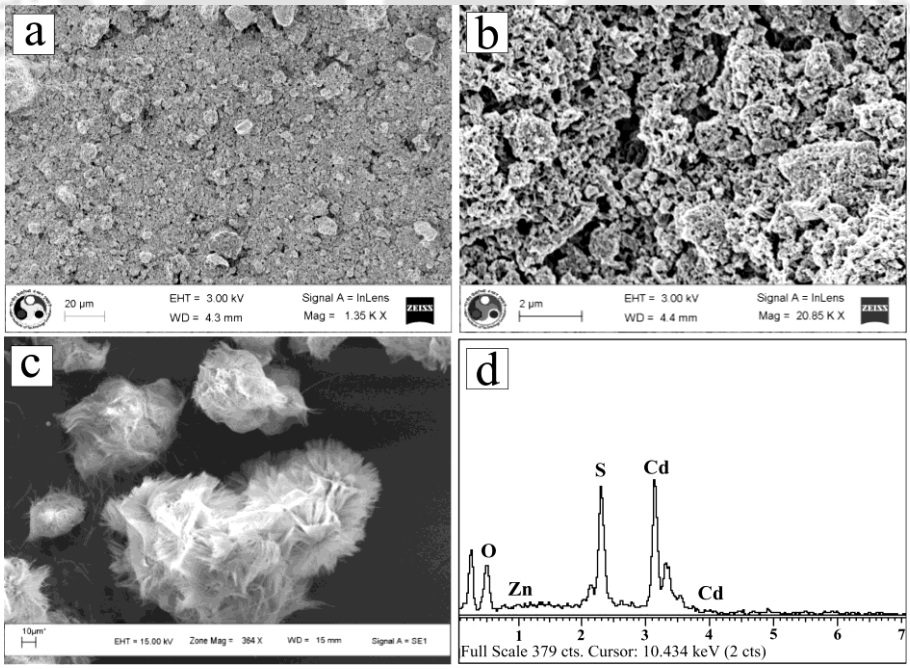

Figure 3.5 Scanning electron microscopy (SEM) images of (a, b) ZnO–CdS–GO composite layer painted on the ITO substrate and (c) bare ZnO–CdS at higher magnification. (d) Energy dispersive X-ray spectroscopy (EDX) pattern of bare ZnO–CdS powder sample.

The nanocomposites were further studied by transmission electron microscopy (TEM) and high-resolution TEM (HRTEM). Figure **3.6a** shows a TEM image of CdS nanorods, while Figure **3.6b** represents the star-shaped image of ZnO–CdS composites exhibiting a diameter of ~500 nm for ZnO–CdS core–shell structures. The star shape arises due to the hierarchical alignment of CdS nanorods over ZnO nanoparticles.[30] The sample preparation for TEM analysis was carried out by dispersing the solid sample in acetone for ~30 min under ultrasonic treatment. The rod-shaped structures that are seen near the star in Figure **3.6b** are of bare CdS nanorods that are coming out of the hierarchical arrangement under ultrasonic treatment during the TEM sample preparation. Figures **3.6c** and **3.6d** represent the TEM and HRTEM images of the ZnO–CdS–GO composite. The HRTEM image of ZnO–CdS–GO composite shows the well-defined lattice fringes of ZnO and CdS entities with the respective interplanar *d*-spacings of ~0.17 nm and ~0.29 nm, that are assignable to the interplanar spacing of (102) and (101) planes of ZnO and CdS, respectively.

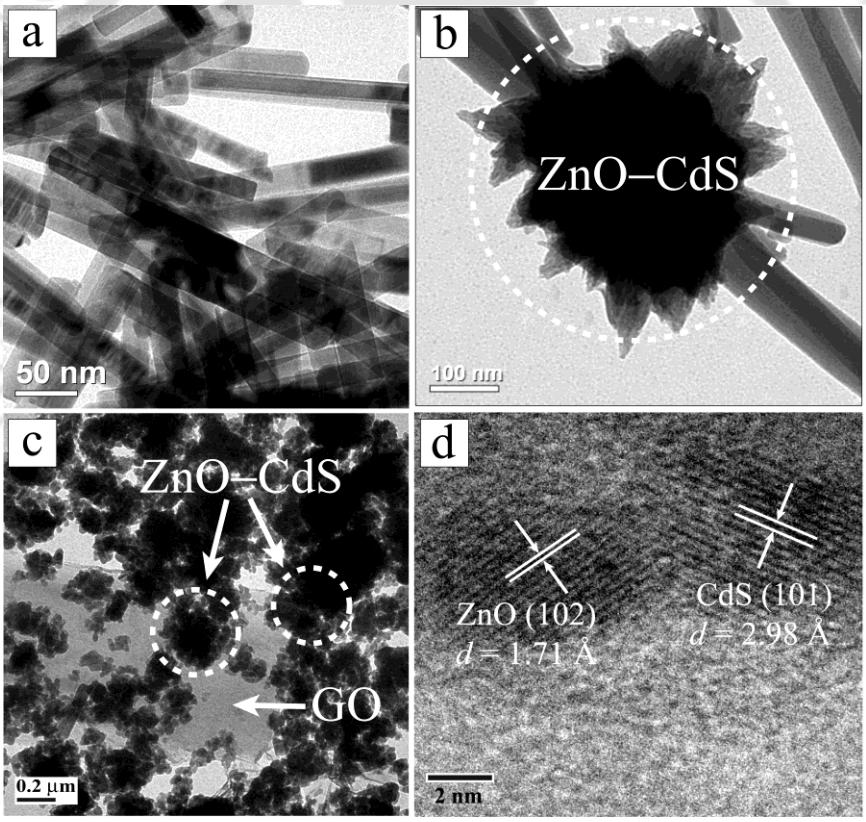

Figure 3.6 Transmission electron microscopy (TEM) images of (a) CdS nanorods, (b) ZnO–CdS nanourchins, and (c) ZnO–CdS–GO composite. (d) High-resolution TEM (HRTEM) image of ZnO–CdS–GO.

3.3.5. Steady-state Photoluminescence (PL) and Time-resolved PL Studies

To probe the electronic interactions between ZnO–CdS and GO, steady-state photoluminescence (PL) spectra of ZnO–CdS and ZnO–CdS–GO based photoanodes fabricated on ITO substrates are

recorded at a 320 nm excitation. As can be seen, Figure **3.7a** shows a drastic quenching of the fluorescence emission band at ~398 nm for the ZnO–CdS–GO based photoanode in contrast to ZnO–CdS. The significant quenching of PL emission of ZnO–CdS upon 1.0 wt % of GO loading confirms the presence of excited-state electronic interactions between ZnO–CdS and GO that corresponds to the inhibited photoinduced electron–hole recombination. Consequently, the non-radiative decay processes occurring in ZnO–CdS becomes more prominent upon GO loading due to the possible interfacial charge transfer from ZnO–CdS to GO.

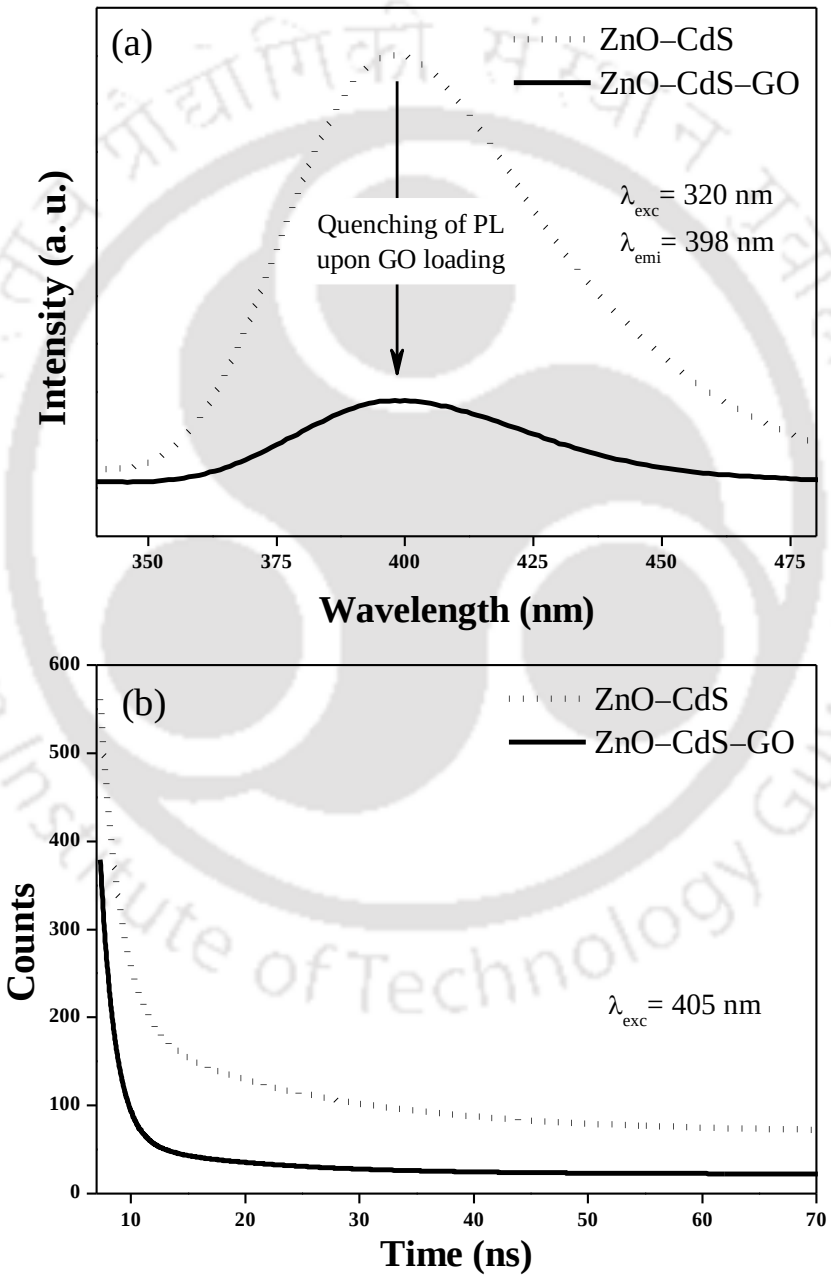

Figure 3.7 (a) Steady-state PL spectra at an excitation wavelength of 320 nm with an emission at 398 nm and (b) TRPL spectra at a 405 nm excitation for ZnO–CdS (dotted lines) and ZnO–CdS–GO (solid lines) photoanodes.

To further gain insight into the excited-state emission decay behaviour of GO-loaded ZnO–CdS, time-resolved PL (TRPL) spectra and exciton lifetime measurements of ZnO–CdS and ZnO–CdS–GO photoanodes are performed using a 405 nm Nd:YAG laser excitation. The TRPL spectra are depicted in Figure **3.7b** and the detailed spectroscopic and fitting parameters (χ^2) for emission decays of the photoanodes are listed in Table **3.1**. Interaction of GO drastically quenches the exciton lifetime of ZnO–CdS through the interfacial charge-transfer processes occurring in ZnO–CdS–GO, which follows a similar mechanism as reported by Son *et al* for quenching of PL lifetime of ZnO in presence of graphene.[36] Functional groups like carboxyl (−COOH), hydroxyl (−OH), and epoxy of GO can easily bind to ZnO–CdS under hydrothermal conditions. Further, it makes the efficient transfer of photoexcited electrons possible from the ZnO–CdS to GO and hence, the static quenching in exciton lifetime is observed. To calculate the exciton lifetimes of the photoanodes, the TRPL curves were fitted with a bi-exponential function by following eq. (3) using FAST software provided by Edinburgh Instruments. The average values (τ_1, τ_2) corresponding to the fast and slow emission decay lifetimes are thus obtained.

$$I(t) = \sum \alpha_i \exp(-\frac{t}{\tau_i}) \tag{3}$$

where α_i is the initial intensity of the decay component i having a lifetime of t. The average lifetimes τ_1 and τ_2 of ZnO–CdS are calculated using eq. (4).

$$\langle \tau \rangle = \left(\sum_i \alpha_i \tau_i^2 \right) \Big/ \left(\sum_i \alpha_i \tau_i \right) \tag{4}$$

$$k_{et} = \frac{1}{\tau_{\text{ZnO–CdS–GO}}} - \frac{1}{\tau_{\text{ZnO–CdS}}} \tag{5}$$

Significantly, coupling of GO decreases the exciton lifetime of ZnO–CdS from ~0.93 ns (τ_1) and ~4.05 ns (τ_2) to ~0.78 ns (τ_1) and ~2.52 ns (τ_2). The average emission decay lifetime ($\langle\tau\rangle$) was also decreased from 3.63 ns to 2.06 ns upon GO loading. Considering non-radiative processes as the only pathway for excited-state decay, charge transfer rate constants (k_{et}) can be calculated by eq. (5) and were found to be ~2.74 × 10^8 s^{-1} (ZnO–CdS) and ~4.85 × 10^8 s^{-1} (ZnO–CdS–GO).

Table 3.1. Fitting parameter (χ^2), initial intensity (α_1, α_2), excited-state lifetime (τ_1, τ_2), and average exciton lifetime ($\langle\tau\rangle$) for ZnO–CdS and ZnO–CdS–GO films on ITO coated glass substrates.

Photoanode	χ^2	α_1	α_2	τ_1 (ns)	τ_2 (ns)	$\langle\tau\rangle$ (ns)	k_{et} (s^{-1})
ZnO–CdS	1.01	14.98	22.57	0.932	4.052	3.63	2.74×10^8
ZnO–CdS–GO	1.02	35.34	30.40	0.778	2.521	2.06	4.85×10^8

3.3.6. Raman Spectroscopic Analysis

Figure **3.8** depicts the room-temperature Raman spectra of the ZnO–CdS and ZnO–CdS–GO based photoanodes and of GO, excited by a He–Ne laser operating at 514.5 nm, over the spectral range of 100–2000 cm^{-1}. Figure **3.8a** shows almost no intense Raman peaks for ZnO–CdS photoanode, while ZnO–CdS–GO counterpart (Figure **3.8b**) shows the two characteristic longitudinal optical (LO) peaks for CdS at 298 cm^{-1} and 592 cm^{-1}. It could be ascribed to the serious limitation of visible–Raman spectroscopy technique in characterizing luminescent samples due to the presence of fluorescence background interference.[37] Basically, highly intense and broad fluorescence peaks, compared to the Raman scattering, hinders the Raman signal of fluorescent samples. One of the best ways to obtain the Raman signal is to remove the luminescent species. In the present work, the 1.0 wt % loading of GO into ZnO–CdS sufficiently quenches the fluorescence emission arising from the ZnO–CdS composite and thereby exhibits the Raman peaks, which is in good agreement with the effective electronic interactions between ZnO–CdS and GO as obtained from the PL quenching and TRPL studies. On the other hand, Figure **3.8c** shows two distinct Raman peaks at 1358 cm^{-1} and 1599 cm^{-1}, which are, respectively, the characteristic D (sp^3 C atoms) and G (sp^2 C atoms) bands for GO nanosheets with a observed defect density ratio (I_D/I_G) of ~0.86.

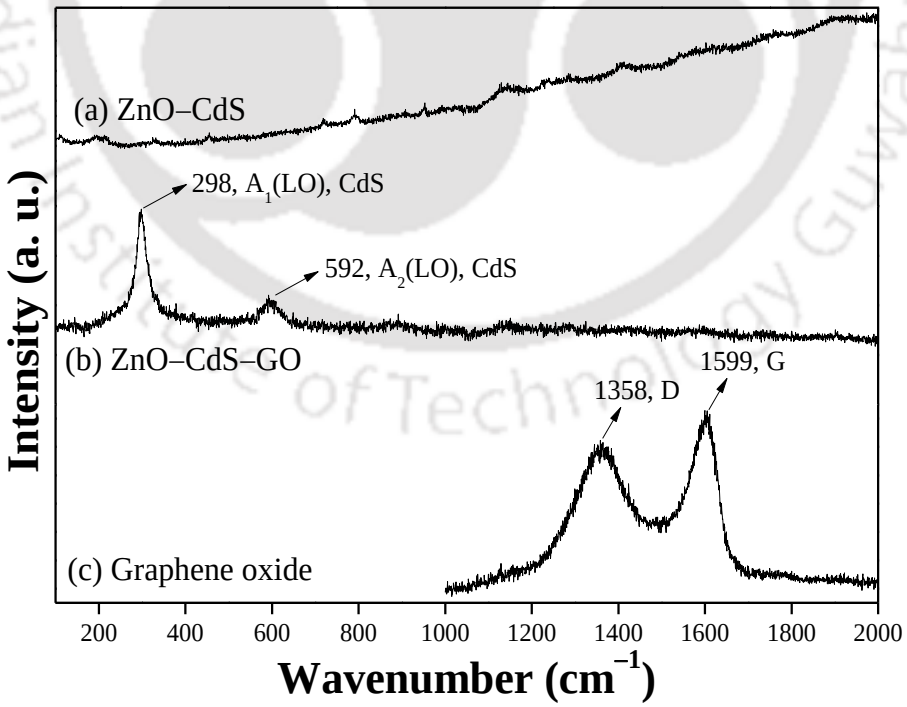

Figure 3.8 Raman spectra for (a) ZnO–CdS (blue line) and (b) ZnO–CdS–GO (red line) photoanode coated on ITO substrate and for (c) GO sheets (black line) at a 514.5 nm laser excitation.

3.3.7. Photovoltaic Performance

Photovoltaic properties of the SSCs are evaluated from the photocurrent–voltage (*J*–*V*) plots measured under AM 1.5 G simulated solar light at intensity of 100 mW/cm^2 (Figures **3.9A**). The performance parameters such as, short-circuit current density (J_{sc}), open-circuit voltage (V_{oc}), fill factor (FF), PCE (η), and maximum IPCE (IPCE$_{max}$; Figure **3.9B** are summarized in Table **3.2**. The intriguing role of GO in device performance, utilizing the hybrid ternary ZnO–CdS–GO photoanode, is evaluated by comparing the *J*–*V* curves for GO-free devices. As can be seen, the cell ZCGO-Pt (ITO/ZnO–CdS–GO/Pt) exhibited the highest $J_{sc} \approx 7.3$ mA/cm^2, a $V_{oc} \approx 703$ mV and FF ≈ 54.6%, affording a maximum PCE ≈ 2.8% against Pt as the counter electrode. In contrast, the GO-free device ZC-Pt (ITO/ZnO–CdS/Pt) afforded a decreased PCE ≈ 1.92% with a $J_{sc} \approx 5.3$ mA/cm^2, a $V_{oc} \approx 672$ mV and FF ≈ 54.2%. It is worth to note that the GO-loaded photoanode significantly enhanced the PCE of the devices by ~47% and J_{sc} value by ~38%, which is indicative of an improved electron transfer in ZnO–CdS based device upon 1.0 wt % of GO loading. Similarly, in the case of Ag counter electrode based cells (ZCGP-Ag and ZC-Ag), GO loading to ZnO–CdS increases the PCE from ~1.08% to ~1.96%, J_{sc} from ~3.3 mA/cm^2 to ~5.7 mA/cm^2, V_{oc} from ~523 mV to ~565 mV, and FF from ~61.7% to ~63.2%. In the device architecture, ZnO–CdS–GO photoanodes consist of binary ZnO–CdS well-embedded into GO sheets; such a configuration facilitates the charge transfer within the system. In addition, the nanodimension of crystalline ZnO and CdS in the composite favor a rapid surface migration of the photogenerated electrons and holes.[38] Interestingly, the band alignment among CdS, ZnO, and GO allows the electrons and holes to be separated within the ZnO–CdS–GO photoanode itself, thereby reducing the charge recombination process resulting in an improved photovoltaic performance of GO-based devices.[19,20,39] It has also been observed that the Pt counter electrode based devices are more efficient than the Ag counterpart.

Evidently, ZCGO-Pt and ZC-Pt cells have shown an enhancement in J_{sc} by ~2 mA/cm^2 and V_{oc} by ~130 mV, as compared to ZCGO-Ag and ZC-Ag cells. The improved J_{sc} value, in the case of Pt, is due to the higher work function o Pt (~6.3 eV) than that of Ag (~4.7 eV). Further, it can be explained on the basis of a favorable electron transport to the Fermi level of the metal electrode, because of a higher work function of Pt counter electrode. Instead, V_{oc} values of SSC depend on the potential difference between the quasi-Fermi level of the semiconductor and the work function of the electrolyte. Moreover, Ag counter electrode encounters with stability issues when comes in direct contact with S^{2-}/S_n^{2-} electrolyte due to the possible formation of Ag_2S,

which is confirmed from the powder XRD pattern recorded for a S^{2-}/S_n^{2-} electrolyte treated Ag counter electrode, as shown in Figure **3.10**. Even if the formation of Ag_2S is significantly less in quantity, it shows a severe effects in altering the charge migration and, hence, the electron–hole recombination to lower the V_{oc} in Ag-based devices, compared to the Pt. It is also observed that the reduced recombination of electrons and holes in the presence of GO induces an increase in V_{oc}, compared to that observed in the GO-free devices.

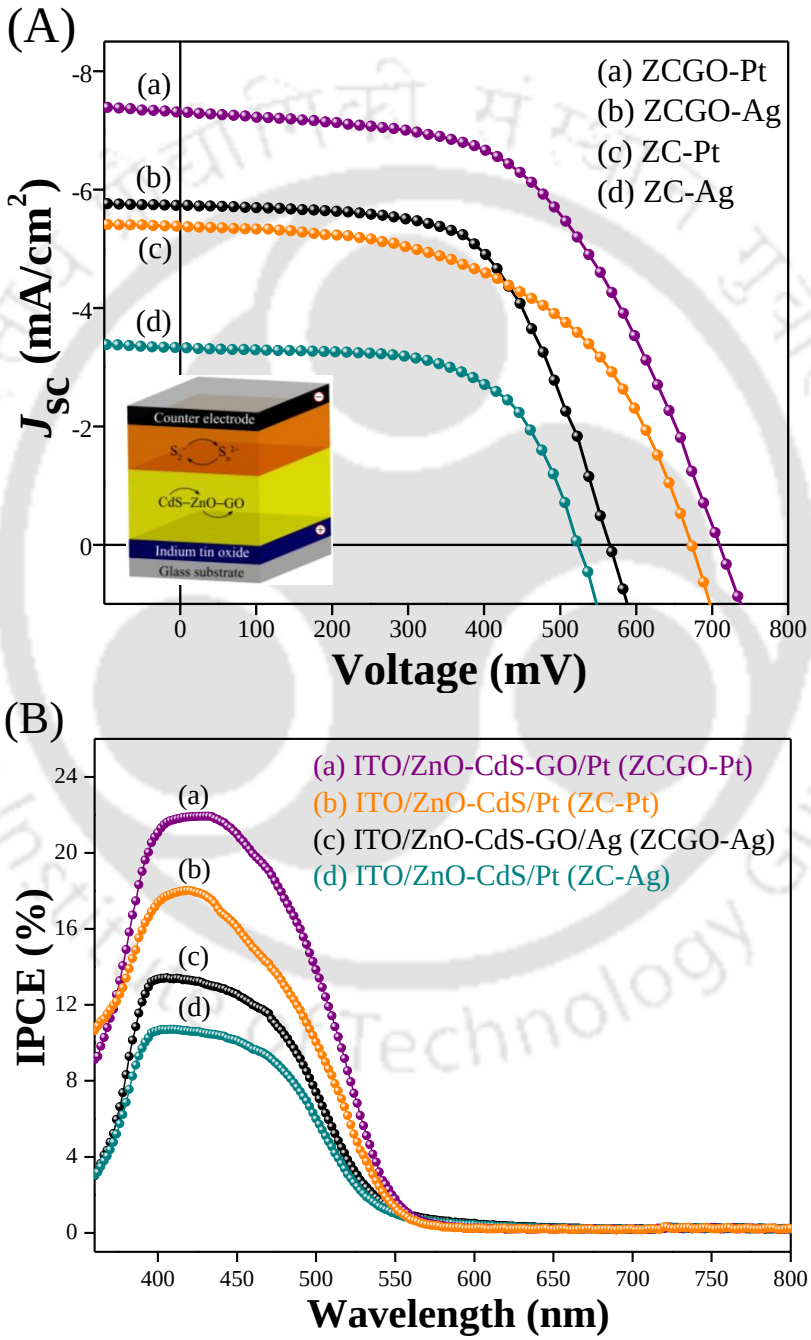

Figure 3.9 (A) Current density–voltage (*J*–*V*) curve for the photovoltaic devices: (a) ZCGO-Pt, (b) ZCGO-Ag, (c) ZC-Pt and (d) ZC-Ag under AM 1.5G simulated solar illumination with an intensity of 100 mW/cm^2. (B) Corresponding incident photon-to-current conversion efficiency (IPCE) plots for the fabricated devices.

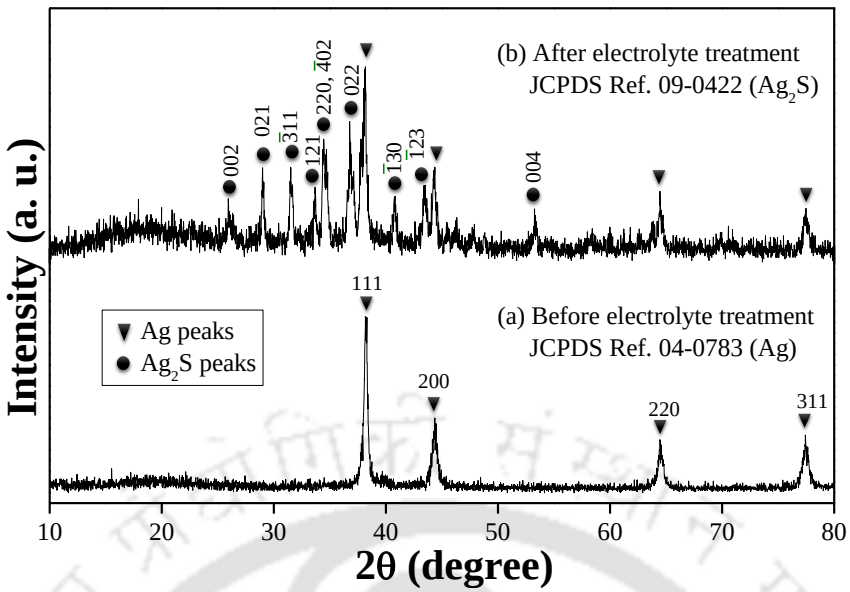

Figure 3.10 Powder X-ray diffraction (XRD) pattern for the fabricated Ag counter electrodes deposited onto the glass substrates (a) before and (b) after the treatment with sulfide/polysulfide electrolyte.

Table 3.2 Short-circuit photocurrent density (J_{sc}), open-circuit voltage (V_{oc}), fill factor (FF), power conversion efficiency (η) and maximum incident photon-to-current conversion efficiency ($IPCE_{max}$) values for the fabricated solar cells with respect to different photoanodes and counter electrodes.

Solar cell	Photoanode	Counter electrode	J_{sc} (mA/cm^2)	V_{oc} (mV)	FF (%)	η (%)	$IPCE_{max}$ (%)
ZC-Pt	ZnO–CdS	Pt	5.3	672	54.2	1.92	18
ZCGO-Pt	ZnO–CdS–GO	Pt	7.3	703	54.6	2.82	22
ZC-Ag	ZnO–CdS	Ag	3.3	523	61.7	1.08	11
ZCGO-Ag	ZnO–CdS–GO	Ag	5.7	565	63.2	1.96	13

The IPCE spectra of the fabricated devices account for the efficiencies of (1) light harvesting by CdS photosensitizer, (2) electron injection within the components of hybrid ZnO–CdS–GO, and (3) photoinduced electron collection by the ITO substrate. Therefore, it is expected to acquire maximum IPCE values for the SSCs at the specific wavelength regions where UV–vis absorption of the photoanodes are maximum. The UV–vis spectra of both the photoanodes show maximum absorption in a wavelength range of ~330–550 nm (Figure **3.4**). From Figure **3.9B**, the IPCE curves for all the devices showed the ability to convert the photons to electrons within the same wavelength range. Enhanced IPCE upon GO loading is ascribed to the proximal band alignments of ZnO and CdS resulting in a favorable charge transfer from CdS to ZnO. The loading of GO as an electron sink enhances the physical separation of photogenerated electrons and holes within ZnO–CdS–GO due to the presence of electronic interactions between ZnO–CdS and GO.[20,35]

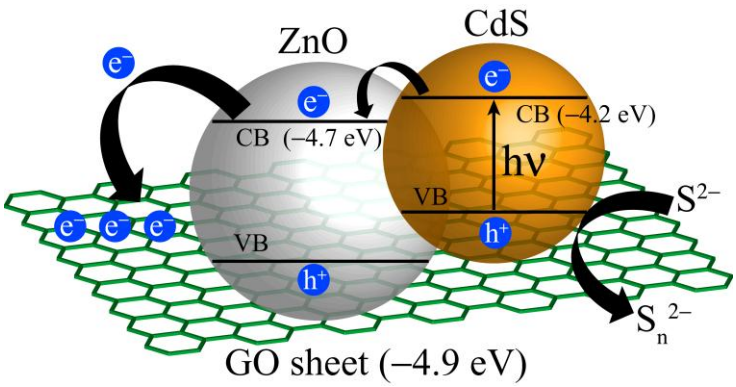

Scheme 3.4 Band energy alignment mediated photogenerated charge transfer processes involved in ternary hybrid photoanode ZnO–CdS–GO and the compensation of holes by sulfide/polysulfide redox electrolyte.

A favorable band alignment mediated feasible charge transfer in ZnO–CdS–GO induces the efficient electron–hole separation, as shown in Figure **3.4**. In contrast, lower IPCE values of the GO-free devices indicate a poor physical separation of electron–hole pairs in the absence of GO. Thus, the higher IPCE values for the devices fabricated with ZnO–CdS–GO photoanodes can be correlated to an enhanced J_{sc} and PCE values of the SSCs. Similar proficiency in the maximum IPCE values, notably from ~11% to ~13%, has also been observed for ZnO–CdS–GO hybrid in contrast to the ZnO–CdS counterpart, in the case of Ag counter electrodes.

3.4. SUMMARY

- Present work manifests the fabrication of SSCs involving a novel photoanode material based on the most commonly used components ZnO, CdS, and graphene oxide (GO).
- A simple hydrothermal strategy is utilized to synthesize the ternary hybrid ZnO–CdS–GO composite, which practically offers an inexpensive way to achieve an effective electronic coupling between the functional groups of GO and ZnO–CdS.
- Hybrid ZnO–CdS–GO has demonstrated an efficient electron transfer based on the band alignments of ZnO, CdS, and GO entities within the composite.
- Graphene oxide acts as an electron acceptor (sink) for an effective separation of the photogenerated charge carriers.

3.5. REFERENCES

1. Huang, Y.; Duan, X.; Wei, Q.; Lieber, C. M. *Science* **2001**, *291*, 630–633.
2. Hagfeldt, A.; Boschloo, G.; Sun, L.; Kioo, L.; Pettersson, H. *Chem. Rev*. **2010**, *110*, 6595–6663.
3. Han, S. E.; Chen, G. *Nano Lett*. **2010**, *10*, 1012–1015.
4. McAlpine, M. C.; Friedman, R. S.; Jin, S.; Lin, K. H.; Wang, W. U.; Lieber, C. M. *Nano Lett*. **2003**, *3*, 1531–1535.
5. Wang, W.; Zhao, Q.; Laurent, K.; Leprince-Wang, L.; Liao, Z.- M.; Yu, D. *Nanoscale* **2012**, *4*, 261–268.
6. Tak, Y.; Hong, S. J.; Lee, J. S.; Yong, K. *J. Mater. Chem.* **2009**, *19*, 5945–5951.
7. Tak, Y.; Hong, S. J.; Lee, J. S.; Yong, K. *Crystal Growth & Design*, **2009**, *9*, 2627–2632.)
8. Guerguerian, G.; Elhordoy, F.; Pereyra, C. J.; Marotti, R. E.; Martín, F.; Leinen, D.; Ramos-Barrado. J. R.; Dalchiele, E. A. *Nanotechnol*. **2011**, *22*, 505401.
9. Hayashi, H.; Lightcap, I. V.; Tsujimoto, M.; Takano, M.; Umeyama, T.; Kamat, P. V.; Imahori, H. *J. Am. Chem. Soc*. **2011**, *133*, 7684–7687.
10. She, J.; Xiao, Z.; Yang, Y.; Deng, S.; Chen, J.; Yang, G.; Xu, N. *ACS Nano* **2008**, *2*, 2015–2022.
11. Lu, X.-H.; Wang, D.; Li, G.-R.; Su, C.-Y.; Kuang, D.-B.; Tong, Y.-X. *J. Phys. Chem. C* **2009**, *113*, 13574–13582.
12. Kim, H.; Jeong, H.; An, T. K.; Park, C. E.; Yong, K. *ACS Appl. Mater. Interfaces* **2013**, *5*, 268–275.
13. Rakshit, T.; Mondal, S. P.; Manna, I.; Ray, S. K. *ACS Appl. Mater. Interfaces* **2012**, *4*, 6085–6095.
14. Wang, X.; Liu, G.; Chen, Z.-G.; Li, F.; Wang, L.; Lu, G. Q.; Cheng, H.-M. *Chem. Commun*. **2009**, 3452–3454.
15. Leschkies, K. S.; Divakar, R.; Basu, J.; Enache-Pommer, E.; Boercker, J. E.; Carter, C. B.; Kortshagen, U. R.; Norris, D. J.; Aydil, S. A. *Nano Lett*. **2007**, *7*, 1793–1798.
16. Emin, S.; Fanetti, M.; Abdi, F. F.; Lisjak, D.; Valant, M.; van de Krol, R.; Dam, B. *ACS Appl. Mater. Interfaces* **2013**, *5*, 1113–1121.
17. Lightcap, V.; Kamat, P. V. *J. Am. Chem. Soc*. **2012**, *134*, 7109–7116.
18. Choi, H.; Nicolaescu, R.; Paek, S.; Ko, J.; Kamat, P. V. *ACS Nano*, **2011**, *5*, 9238–9245.
19. Khan, Z.; Chetia, T. R.; Vardhaman, A. K.; Barpuzary, D; Sastri, C. V.; Qureshi, M. *RSC Advances* **2012**, *2*, 12122–12128.
20. Luo, Q.- P.; Yu, X.- Y.; Lei, B.- X.; Chen, H.- Y.; Kuang, D.- B.; Su C.- Y. *J. Phys. Chem. C* **2012**, *116*, 8111–8117.
21. Barpuzary, D.; Qureshi, M. Graphene filled polymer in photovoltaics. In *Graphene-Based Polymer Nanocomposites in Electronics*, Sadasivuni, K. K., Ponnamma, D., Kim, J., Thomas, S., Eds.; Springer Series on Polymer and Composite Materials; Springer: 2015; 157–191.
22. Mathkar, A.; Tozier, D.; Cox, P.; Ong, P.; Galande, C.; Balakrishnan, K.; Reddy, A. L. M.; Ajayan, P. M. *J. Phys. Chem. Lett*. **2012**, *3*, 986–991.
23. Eda, G.; Mattevi, C.; Yamaguchi, H.; Kim, H.; Chhowalla, M. *J. Phys. Chem. C* **2009**, *113*, 15768–15771.
24. Lee, Y.-Y.; Tu, K.- H.; Yu, C.- C.; Li, S.- S.; Hwang, J.- Y.; Lin, C.- C.; Chen, K.- H.; Chen, L.- C.; Chen, H.- L.; Chen, C.- W. *ACS Nano* **2011**, *5*, 6564–6570.
25. Yang, H.; Guai, G. H.; Guo, C.; Song, Q.; Jiang, S. P., Wang, Y.; Zhang, W.; Li, C. M. *J. Phys. Chem C* **2011**, *115*, 12209–12215.
26. Kamat, P. V. *J. Phys. Chem. Lett*. **2010**, *1*, 520–527.

27. Kamat, P. V. *J. Phys. Chem. Lett.* **2011**, *2*, 242–251.
28. Bao, J.; Zimmler, M. A.; Capasso, F.; Wang, X.; Ren, Z. F. *Nano Lett*. **2006**, *6*, 1719–1722.
29. Khan, D.; Barpuzary, D.; Baswant, O.; Sutradhar, S.; Qureshi, M. *Mater. Lett*. **2011**, *65*, 1168–1171.
30. Barpuzary, D.; Khan, Z.; Vinothkumar, N.; De, M.; Qureshi, M. *J. Phys. Chem. C* **2012**, *116*, 150–156.
31. Sun, B.; Hao, Y.; Guo, F.; Cao, Y.; Zhang, Y.; Li, Y.; Xu, D. *J. Phys. Chem. C* **2012**, *116*, 1395–1400.
32. Becheri, A.; Dürr, M.; Nostro, P. L.; Baglioni, P. *J. Nanopart. Res.* **2008**, 10, 679–689.
33. Becerril, H. A.; Mao, J.; Liu, Z.; Stoltenberg, R. M.; Bao, Z.; Chen, Y. ACS Nano **2008**, *2*, 463–470.
34. Zhang, H.; Lv, X.; Li, Y.; Wang, Y.; Li, J. *ACS Nano*, **2010**, *4*, 380–386.
35. Hou, J.; Wang, Z.; Kan, W.; Jiao, S.; Zhu, H.; Kumar, R. V. *J. Mater. Chem.* **2012**, *22*, 7291–7299.
36. Son, D. I.; Kwon, B. W.; Park, D. H.; Seo, W.- S.; Yi, Y.; Angadi, B.; Lee, C.- L.; Choi, W. K. *Nature Nanotechnology* **2012**, *7*, 465–471.
37. Chen, J.; Feng, Z.; Ying, P.; Li, C. *J. Phys. Chem. B* **2004**, *108*, 12669–12676.
38. Ashokkumar, M. *Int. J. Hydrogen Energy* **1998**, *23*, 427–438.
39. Li, S.- S.; Tu, K.- H.; Lin, C.- C.; Chen, C.- W.; Chhowalla, M. *ACS Nano* **2010**, *4*, 3169–3174.

Chapter 4

Ruthenium(II) Dipyridophenazine Complex as An Efficient Sensitizer for Dimensional ZnO Nanowire Based Dye-Sensitized Solar Cell

This chapter demonstrates a one-dimensional ZnO nanowire based dye-sensitized solar cell involving a newly synthesized Ru(II)dipyridophenazine complex as an efficient photosensitizer. An excellent light harvesting property of due to an intense MLCT band and a favorable band energetics of the dye molecule facilitating the photogenerated charge transfer from the dye to ZnO are probed experimentally and re-confirmed using DFT. The intrinsic faster charge transport property of ZnO nanowires in contrast to that of ZnO nanoparticles to improve the device performance is being described.

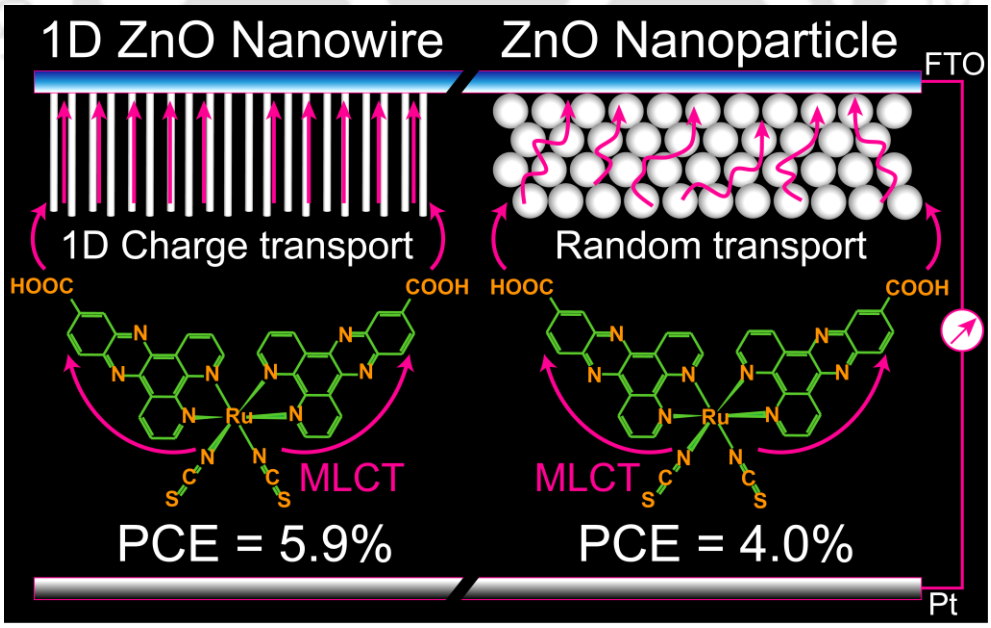

THE JOURNAL OF PHYSICAL CHEMISTRY C D. Barpuzary *et al.* **2015**, 119, 3892−3902

4.1. INTRODUCTION

Emerging technological research towards the design and fabrication of ZnO based dye-sensitized solar cells (DSCs) have shown a great deal of interest in generating robust and highly efficient solar-to-electricity conversion devices engulfing an ever-increasing global energy demand.[1,2] The basic design of a typical DSC includes a mesoscopic oxide film as the photoanode, a molecular dye absorber, a redox electrolyte, and a counter electrode (mostly, Pt). The current scenario to enrich the efficiency of DSCs is mainly focused on Ru based dyes, exhibiting an excellent power conversion efficiency (PCE) up to ~11%, due to the fascinating advantages such as, (1) broad range visible light absorption (2) intense metal to ligand charge transfer (MLCT) transitions (3) metal to ligand (Ru–L) and ligand to metal (SCN–Ru) based charge separation (4) favorable band alignments with the sensitizer scaffolds (for example: TiO_2/ZnO) (5) moderately longer exciton lifetime and (6) a high (electro)chemical stability.[3–8] In view of this, several homoleptic and heteroleptic type Ru dyes (Figure **4.1**) having bipyridyl or polypyridyl ligands are utilized in DSCs notably to enhance the molar absorptivity, leading to an efficient solar harvesting.[9,10]

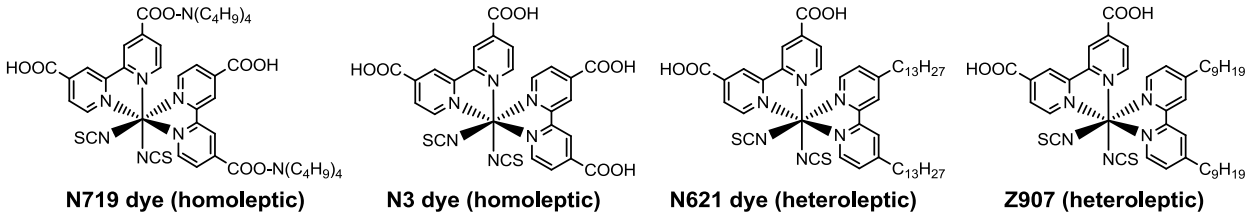

Figure 4.1 Examples of the best-performed commercial homoleptic and heteroleptic type Ru dyes commonly used in dye-sensitized solar cells.[9,10]

Homoleptic type Ru dyes involved in DSCs are composed of two identical ancillary ligands (excluding −NCS) directly attached to the metal center, fulfilling the basic prerequisites like light absorption and dye adsorption.[11] A breakthrough in further improving the efficiency of DSCs is the use of heteroleptic type Ru dyes having two ancillary ligands of different types—one with an extended π-conjugation ensuring a light harvesting antenna function and a second ligand offering dye anchoring onto the semiconductor surface. The advent of heteroleptic dyes offers enhanced molar extinction coefficients, broad visible range absorptivity, and prominent thermal stability of the DSCs. One common feature of prototype homoleptic and heteroleptic sensitizers is that they adsorb onto the semiconductor surface using a similar kind of carboxylic anchoring group attached to the ancillary ligands.[12,13] Heteroleptic design also offers facile molecular engineering possibilities to enhance and broaden their MLCT absorption band by means of modified ligands *via* an extended or bifurcated conjugation of the light-absorbing chromophoric units.[14] However,

an extended π-conjugated ring makes the dye molecule bulkier that tends to decrease the quantity of dye loading thereby effectively reducing the overall efficiency. Paramountcy is therefore been given to size optimization of chromophoric units in heteroleptic type Ru dyes, balancing the synergistic effect of the two crucial and inversely proportional factors: (1) intensity of MLCT band, and (2) quantity of dye loading. To mimic bulky heteroleptic dyes, by a dipyridophenazine based homoleptic type Ru dye that enables an intense MLCT absorption and an efficient dye loading would therefore be a promising approach. In this regard, structurally modified 1,10-phenanthroline ligand based Ru dyes have paved a way to achieve supreme PCEs ~7%.[15–21]

Another crucial factor that governs the efficiency of DSCs is a suitable redox electrolyte. Although the traditional iodide/triiodide (I_3^-/I^-) couple is the most popular choice of electrolyte used in DSCs, it encounters with a few limitations such as, high absorptivity in the visible region and a corrosive nature. To avoid such glitches, cobalt based electrolytes have been explored exhibiting superior performances over the I_3^-/I^- system, due to their noncorrosive nature, lower visible light absorptivity, and a higher redox potential for a more efficient dye regeneration in contrast to the I_3^-/I^- counterparts.[22–25] In tandem with the development of Ru dyes and electrolytes, excellent electron transport properties and dye adsorptivity of the semiconductor photoanode materials depending on their crystallinity and surface morphology are also technically explored to enhance the device efficiency. Since the discovery of DSCs, mesoscopic TiO_2 based films are extensively being utilized as the electron transport material in the photoanodes. Recently, ZnO architectures built at a nanoscale in diverse morphologies have rivaled the TiO_2 photoanodes due to their superior electron transport property, wide-band gap, and benchtop synthetic routes, achieving promising PCEs ~7.5%.[1] Paradoxically, ZnO based DSCs encounter with the possible formation of an interfacial charge transfer state between the dye and ZnO surface that limits the efficient photogeneration of free-charge carriers, and hence exhibit lower PCEs in contrast to the TiO_2 counterparts.[26,27] In this regard, 1D nanowire (NW) structures of ZnO have exhibited remarkably improved performances due to their ability to generate 1D charge transfer pathways, minimized charge recombination rate, increased electron diffusion length, and sufficient surface area for dye loading.[28–30] In addition, a favorable packing of the vertically aligned ZnO NW network allows to get rid of the limited ionic diffusion of cobalt electrolytes through the narrow pores of the photoanodes.[31]

This chapter demonstrates the combined effects of 1D ZnO NWs and newly synthesized dye, *cis*-Ru(dppz-COOH)$_2$(NCS)$_2$ (dppz-COOH: dipyrido[3,2-*a*:2′,3′-*c*]phenazine-11-carboxylic acid), through an efficient photovoltaic cell affording PCE up to ~5.9% against Pt as the counter electrode with cobalt complexes of 2,2′-bipyridyl (bpy) and 1,10-phenanthroline monohydrate (phen) as the electrolytes. The key features of Ru(dppz-COOH)$_2$(NCS)$_2$ dye is two-fold: (1) a broad visible range absorptivity due to an intense MLCT transition band, and (2) an efficient dye loading capacity due to an optimal size. The computational study using density functional theory (DFT) is carried out at a B3LYP/LANL2DZ/6-31G level to probe the electronic structure of the dye (Figure **4.2**). The absorption and infrared (IR) spectra of the dye are computed at a time-dependent DFT (TDDFT) level.

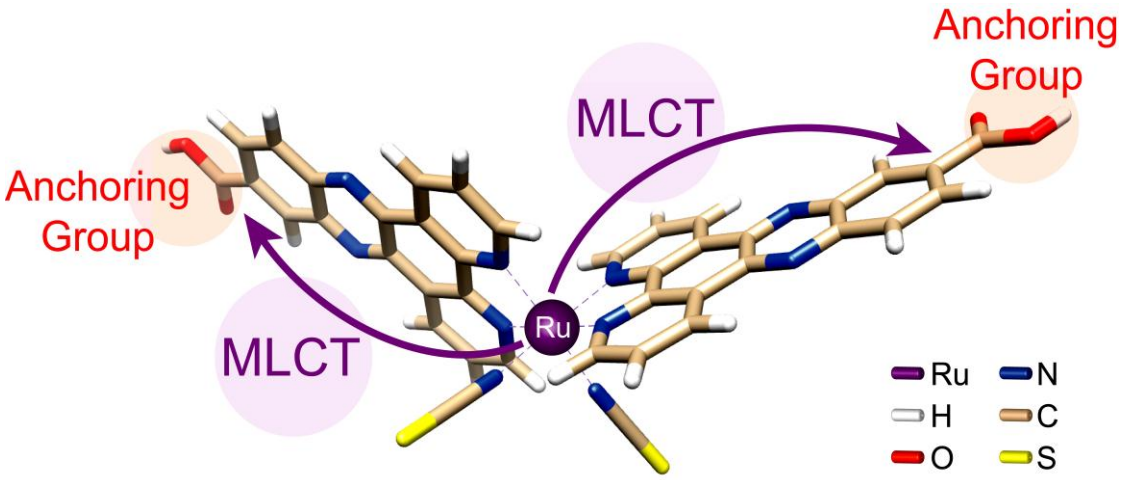

Figure 4.2 Optimized molecular structure of Ru^{II}(dppz-COOH)$_2$(NCS)$_2$ photosensitizer as computed from the density functional theory (DFT) calculations carried out at a B3LYP/LANL2DZ/6-31G level.

4.2. EXPERIMENTAL SECTION

4.2.1. Synthesis of 1,10-Phenanthroline-5,6-dione (phen-dione)

To synthesize 1,10-phenanthroline-5,6-dione (phen-dione; Scheme **4.1**), conc. H_2SO_4 (100 mL), followed by conc. HNO_3 (50 mL), were added dropwise to a mixture of phen (5.0 g, 25 mmol) and KBr (29.75 g, 250 mmol) in an ice bath, and heated at 80 °C (2 h) under magnetic stirring.[32] The reaction mixture was poured onto ice-cold water (1.5 L) after cooling to room temperature, neutralized with $NaHCO_3$, extracted with CH_2Cl_2, and dried over anhydrous Na_2SO_4. The evaporation of CH_2Cl_2 solvent yielded the crude sample of phen-dione, which was then purified by filtering through a column using neutral alumina as the stationary phase and CH_2Cl_2 as the eluent. $R_f \approx 0.46$ in CH_2Cl_2/MeOH (20:1, v/v); yield = 4.34 g, 75%. MS, *m*/*z*: $[M]^+$ for $C_6H_6N_2O_2$ = 210.12. ^{1}H NMR (400 MHz, $CDCl_3$, δ in ppm): 9.17 (2H), 8.53 (2H), 7.62 (2H).

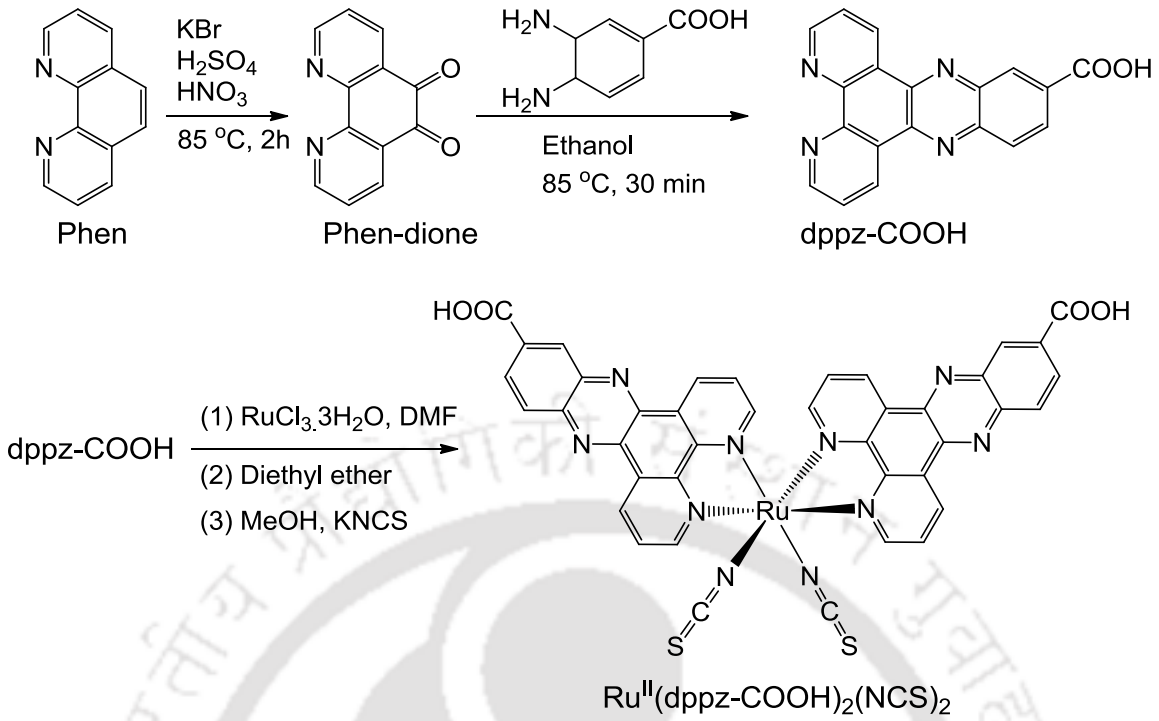

Scheme 4.1 Synthesis protocol for 1,10-phenanthroline-5,6-dione, dipyrido[3,2-a:2′,3′-c]phenazine-11-carboxylic acid (dppz-COOH) ligand and $Ru^{II}(dppz\text{-}COOH)_2(NCS)_2$ complex.

4.2.2. Synthesis of Dipyrido[3,2-a:2′,3′-c]phenazine-11-carboxylic Acid (dppz-COOH)

Synthesis of dppz-COOH was carried out by utilizing a Schiff base condensation reaction (Scheme **4.1**).[33] Typically, phen-dione (1.0 g, 4.76 mmol) and 3,4-diaminobenzenoic acid (0.8 g, 5.23 mmol) were refluxed in absolute ethanol (50 mL) in a round-bottom flask for 30 min under N_2 atmosphere. A light brown colored precipitate of dppz-COOH was obtained, which was filtered under vacuum, dried and recrystallized from ethanol (yield = 1.28 g, 83%). MS, *m/z*: for $[M + H]^+$ for $C_{19}H_{10}N_4O_2$ = 327.25. ^{1}H NMR (400 MHz, CF_3COOD, δ in ppm): 10.23 (2H), 9.312 (3H), 8.69 (1H), 8.59 (s, 1H), 8.36 (2H).

4.2.3. Synthesis of $Ru^{II}(dppz\text{-}COOH)_2(NCS)_2$ Complex

In the typical synthesis of the dye,[34] $RuCl_3 \cdot 3H_2O$ (1.0 g, 3.82 mmol) and dppz-COOH (2.5 g, 7.66 mmol) were dissolved in *N*,*N*′-dimethylformamide (75 mL), refluxed under Ar atmosphere for 8 h and cooled to room temperature. The solution was then concentrated to one-half of its original volume in the rotary evaporator. Diethyl ether was added to the reaction mass and the mixture was allowed to settle for 24 h in the refrigerator to get a dark-red, highly insoluble solid precipitate, which was filtered out, washed with diethyl ether, and dried to get the solid mass of $Ru(dppz\text{-}COOH)_2Cl_2$ (yield = 2.13 g, 68%). In the next step, $Ru(dppz\text{-}COOH)_2Cl_2$ (0.4 g, 4.8 mmol) was suspended in minimum amount of distilled water and dilute aqueous NaOH solution

was added dropwise to neutralize to pH ≈ 7, until a red-violet solution appeared. The solvent was evaporated to one-half in the rotary evaporator and methanol (60 mL) and KNCS (3.2 g, 32.96 mmol) were added. The solution was refluxed for 5 h in the dark under Ar atmosphere and finally evaporated to dryness. The solid was redissolved in distilled water, and the complex, $Ru(dppz\text{-}COOH)_2(NCS)_2$, was then precipitated by the addition of 1.0 M HCl at pH ≈ 2. The dark product was filtered and dried under vacuum (yield = 0.348 g, 83%). MS, *m*/*z*: for $[M + H]^+$ $C_{40}H_{22}N_{10}O_5RuS_2$ = 871.65. ^{1}H NMR (400 MHz, CF_3COOD, δ in ppm): 10.17 (4H), 9.60 (2H), 9.41 (2H), 8.83 (4H), 8.55 (2H), 8.34 (2H), 7.90 (2H). Anal. Calcd for $RuC_{40}H_{22}N_{10}O_5S_2$: C, 54.11%; H, 2.50%; N, 15.78%. Found: C, 54.32%; H, 2.69%; N, 15.76%.

4.2.4. Synthesis of $[Co(bpy)_3](PF_6)_2$ and $[Co(bpy)_3](PF_6)_3$ Complexes

Synthesis of $[Co(bpy)_3](PF_6)_2$ and $[Co(bpy)_3](PF_6)_3$ were carried out by following the procedure reported by Liu *et al*.[35] To synthesize the cobalt(II) salt, a solution of $CoCl_2{\cdot}6H_2O$ (0.5 g, 2.0 mmol) in a minimum amount of methanol was added drop wise to a solution of bpy (1.10 g, 6.8 mmol) in methanol under continuous stirring and then refluxed for 30 min. The completion of the reaction was monitored using TLC. The solution was allowed to cool to room temperature, and KPF_6 (2.40 g, 13 mmol) in water was slowly added under gentle stirring to precipitate the complex. The solid product was filtered out, washed with distilled water, and dried in vacuum to isolate $[Co(bpy)_3](PF_6)_2$ complex (yield = 1.34 g, 68%). ^{1}H NMR (400 MHz, DMSO-d_6, δ in ppm): 8.67 (6H), 8.38 (6H), 7.94 (6H), 7.44 (6H). MS, *m*/*z*: for $[M]^+$ $C_{30}H_{24}CoF_{12}N_6P_2$ = 817.27.

To synthesize the cobalt(III) complex, a solution of $CoCl_2{\cdot}6H_2O$ (0.5 g, 2.0 mmol) in a minimum amount of methanol was added drop wise to a solution of bpy (1.10 g, 6.8 mmol) in methanol under continuous stirring and then refluxed for 30 min. Once the reaction mixture was cooled to room temperature, an equivalent of Br_2 solution in methanol was added drop wise to it and then allowed to stir for another 10 min resulting in the formation of an orange precipitate. The solution was filtered to discard the yellow precipitate, and the clear solution was evaporated to dryness in the rotary evaporator. The residue was dissolved in methanol (15.0 mL) and an aqueous solution of KPF_6 (2.4 g, 13 mmol) was added to precipitate out $[Co(bpy)_3](PF_6)_3$, which was filtered out, washed with water, and dried in vacuum to yield the solid product (yield = 1.78 g, 77%). ^{1}H NMR (400 MHz, DMSO-d_6, δ in ppm): 9.034 (6H), 8.604 (6H), 7.808 (6H), 7.438 (6H). MS, *m*/*z*: $[M]^+$ for $C_{30}H_{24}CoF_{12}N_6P_3$ = 962.23.

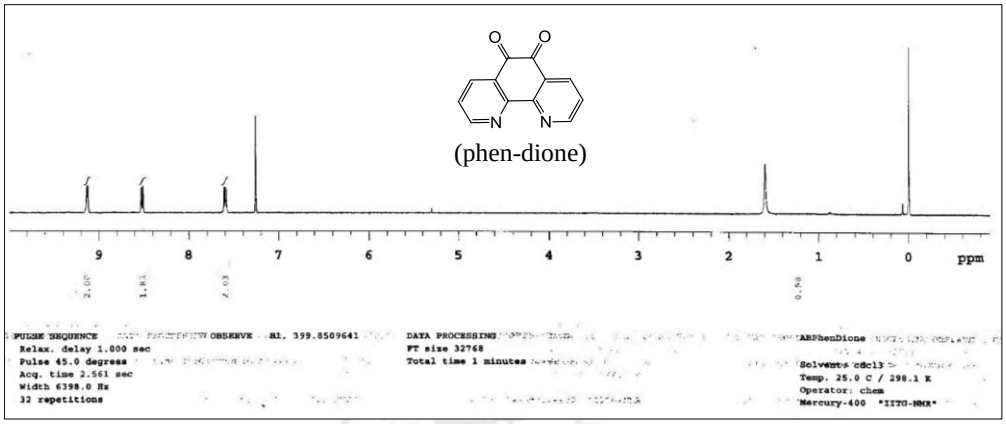

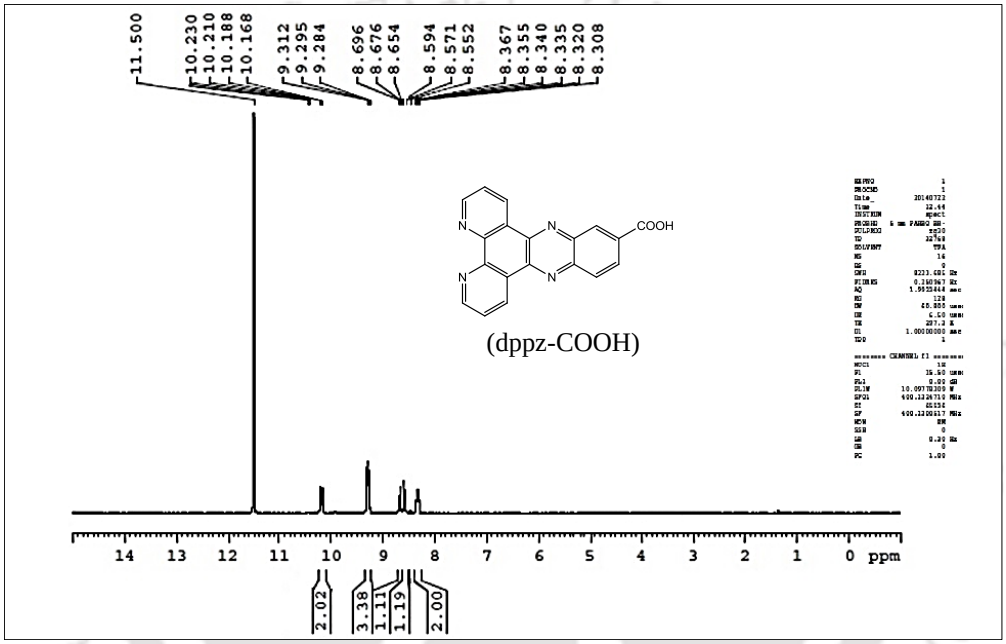

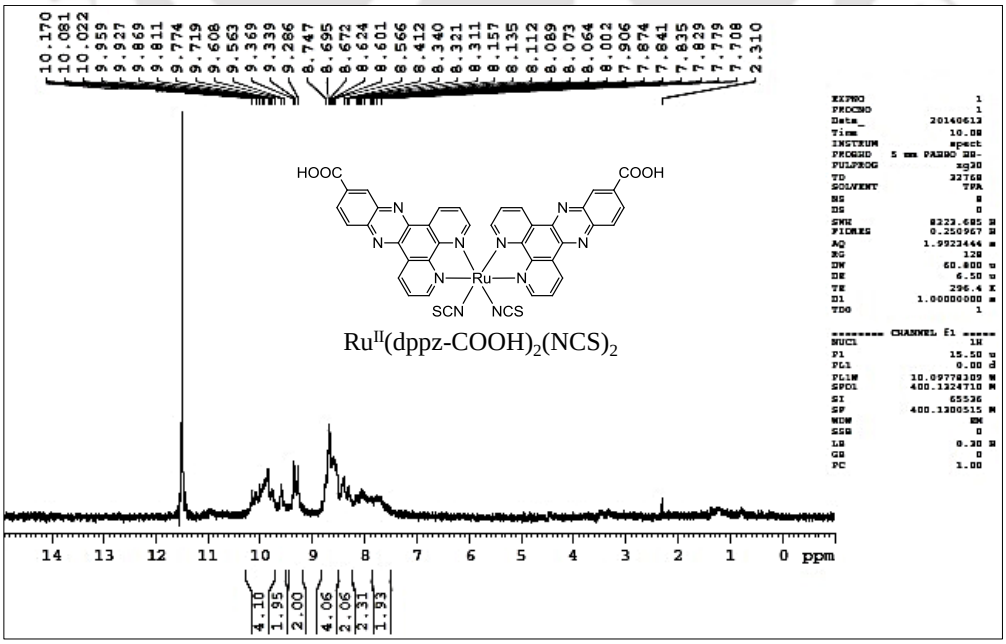

4.2.5. Synthesis of $[Co(phen)_3](PF_6)_2$ and $[Co(phen)_3](PF_6)_3$ Complexes

Cobalt complexes with phen were synthesized by following the identical procedure as reported for $[Co(bpy)_3](PF_6)_2$ and $[Co(bpy)_3](PF_6)_3$ complexes, only by using phen instead of bpy.[35]

$[Co(phen)_3](PF_6)_2$. Yield = 1.59 g, 72%. ^{1}H NMR (400 MHz, DMSO-d_6, δ in ppm): 9.07 (6H), 8.55 (6H), 8.53 (6H), 8.04 (6H). MS, *m*/*z*: for $[M]^+$ $C_{30}H_{24}CoF_{12}N_6P_2$ = 921.17.

$[Co(phen)_3](PF_6)_3$. Yield = 2.02 g, 79%. ^{1}H NMR (400 MHz, DMSO-d_6, δ in ppm): 9.15 (6H), 8.56 (6H), 7.96 (6H), 7.66 (6H). MS, *m*/*z*: for $[M]^+$ $C_{30}H_{24}CoF_{12}N_6P_2$ = 1066.11.

4.2.6. Growth of One-Dimensional ZnO Nanowires on FTO Substrates

The growth of ZnO NWs over ZnO seed layer coated FTO substrates was performed by employing a hydrothermal route.[29,36] A ZnO seed solution was prepared by stirring a mixture of $Zn(CH_3COO)_2.2H_2O$ (0.2 g) and ethanolamine (55 µL) in 2-methoxyethanol (3.0 mL) for 8 h and then filtered through a 0.2 µm PTFE membrane filter. Fluorine doped tin oxide (FTO) coated glass substrates were then cleaned with soap solution, washed with distilled water, and treated under an ultrasonic bath for 15 min in each of acetone and 2-propanol, dried by blowing argon and finally subjected to ozone treatment for 30 min. ZnO seed solution was spin coated on the FTO substrates and heated at ~175 °C for 10 min. This procedure was repeated for one more time to obtain a uniform ZnO seed layer on FTO substrates. ZnO seed layered FTO substrates were then separately dipped (FTO side down) into a 30.0 mL aqueous solution of $Zn(NO_3).6H_2O$ (50 mM) and hexamethylenetetramine (50 mM) in Teflon vessels, sealed inside a stainless steel autoclave and then maintained at 90 °C for 2 h in an electronic oven to complete the uniform growth of ZnO NWs. The ZnO NW grown FTO substrates were taken out, rinsed with ethanol and then heated at 175 °C for 10 min to remove any traces of water and ethanol.

4.2.7. Synthesis of ZnO Nanoparticles

ZnO nanoparticles (NPs) were synthesized by a method as discussed earlier in Chapter 3 Section 3.2.1. Typically, $ZnCl_2$ was first converted to $Zn(OH)_2$ by adding NaOH solution and then heated at 90 °C, collected by centrifugation, washed with water and finally calcined to get the ZnO NPs.

4.2.8. Device Fabrication and Characterization

To prepare ZnO NW based photoanode, ZnO-grown FTO substrate was dipped into a 0.3 mM dye solution in ethanol/dichloromethane (1:1, v/v), taken out after 3 h, rinsed with ethanol, and dried under hot air blow. The fabrication of ZnO NW based photoanode is shown in Scheme **4.2**.

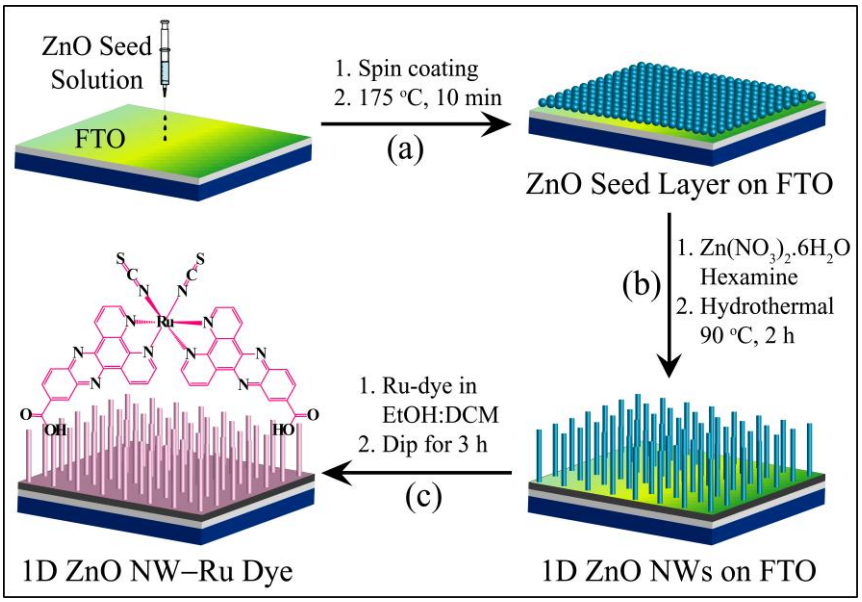

Scheme 4.2 General procedure for fabrication of ZnO nanowire based photoanode: (a) spin coating of ZnO seed solution on FTO substrate and heating at ~175 °C for 10 min, (b) hydrothermal growth of ZnO nanowires over ZnO seed layered FTO substrate at 90 °C for 2 h using a 0.5 M zinc nitrate and 0.5 M hexamine aqueous solution, (c) dye sensitization by dipping the ZnO film into a 0.3 mM dye solution in ethanol/dichloromethane (1:1, v/v) for 3 h.

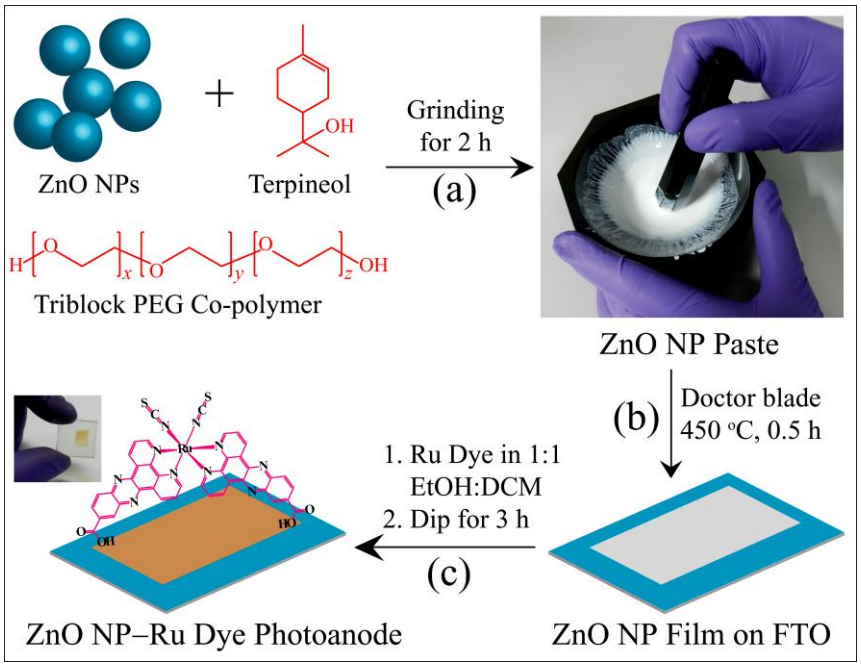

Scheme 4.3 General procedure for fabrication of ZnO nanoparticle based photoanode: (a) ZnO nanoparticle paste formation by grinding ZnO nanoparticles in terpineol and PEG-PPG-PEG triblock co-polymer for 2 h, (b) ZnO film deposition onto FTO substrate by doctor blade technique and calcination at 450 °C for 30 min, (c) dye sensitization by dipping the ZnO film into a 0.3 mM dye solution in ethanol/dichloromethane (1:1, v/v) for 3 h.

To fabricate the ZnO NP based photoanode, a ZnO NP paste was prepared by mixing ZnO NPs (0.50 g), terpineol (2.5 mL), and triblock PEG-PPG-PEG copolymer (1.5 mL) in an agate mortar for 2 h. Pre-cleaned, ozonized FTO substrates were fixed on a glass plate by using Scotch tape to

obtain an active area ~0.25 cm^2 and the ZnO paste was then coated by doctor blade technique. Scotch tape was removed and the ZnO NP coated FTO substrates were calcined at 450 °C for 30 min. A thickness of ~6–8 μm for the ZnO NP films was confirmed by surface profilometer. The ZnO NP films were sensitized with the dye solution for 3 h, rinsed with ethanol, and dried under hot air blow. The fabrication of NP-based photoanode is shown in Scheme **4.3**. To prepare Pt counter electrodes, a 50 mM H_2PtCl_6 solution in 2-propanol was spin coated onto a number of pre-cleaned, ozonized FTO substrates, followed by calcination at 450 °C for 15 min. The devices were constructed by sandwiching the photoanodes and counter electrodes using low-temperature thermoplastic sealant (~50 μm thick). A drop of electrolyte solution was inserted to complete the devices and then sealed with glass cover slits using Araldite adhesive. The electrolyte solutions were prepared by dissolving 0.20 M $[Co^{II}(L)_3](PF_6)_2$, 0.02 M $[Co^{III}(L)_3](PF_6)_3$, and 0.5 M 4-*tert*-butylpyridine in an acetonitrile/valeronitrile (9:1, v/v) solvent mixture (L = bpy and phen).

To perform the dye desorption measurements, dye-sensitized ZnO photoanodes were first immersed into a 0.1 mM NaOH solution in ethanol/water (1:1, v/v) mixture. The photoanodes were removed from the solution after the complete desorption of dye in a certain period of time, and then UV–vis absorbance of each of the remaining sample of NaOH solutions were recorded. The concentration of the desorbed dye per cm^2 film area was calculated from the absorbance data and molar extinction coefficient of the dye following the Beer's law.

4.3. RESULTS AND DISCUSSIONS

4.3.1. Powder X-ray Diffraction Analysis

Powder XRD patterns of hydrothermally-grown 1D ZnO NWs on glass substrates and ZnO NPs are recorded to endorse their phase purity, as shown in Figure **4.3**. Notably, the XRD pattern of ZnO NWs (Figure **4.3a**) shows a strong appearance of a (002) diffraction peak at $2\theta \approx 34.6°$, indicating a preferential growth of ZnO NWs along (002) lattice plane,[29] which further reflects a typical 1D growth of ZnO NWs along the *c*-axis normal to the substrate. The observed lattice planes (100), (002), (101), (102), and (103) for ZnO NWs are indexed to a hexagonal phase of ZnO with the lattice constants of a = 0.3249 nm and c = 0.5208 nm (JCPDS Ref. No. 36-1451). Similarly, the lattice planes (100), (002), (101), (102), (110), (103), (200), (112), and (201) for bare ZnO NPs (Figure **4.3b**) are indexed to the hexagonal phase of ZnO with the lattice constants of a = 0.3248 nm and c = 0.5205 nm. Notably, no characteristic high intensity (002) diffraction peak was observed in the powder XRD pattern for the ZnO NPs.

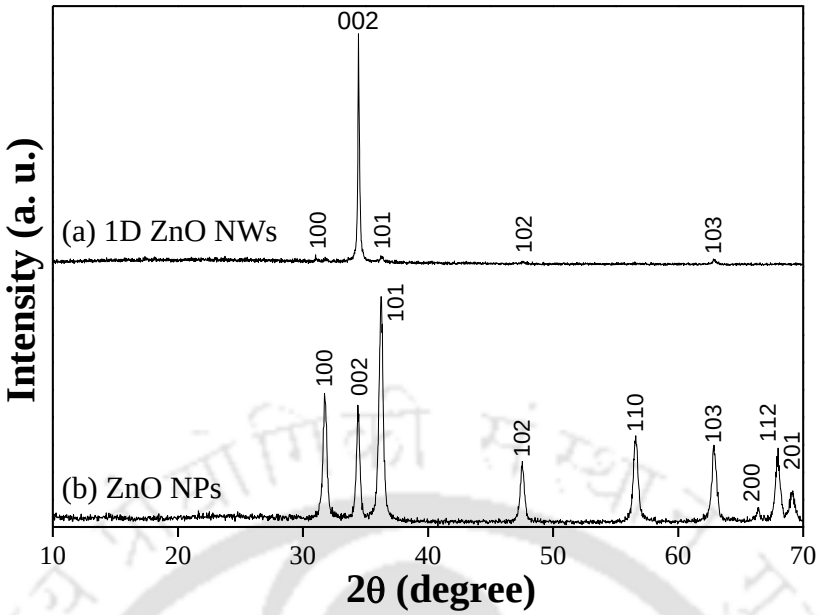

Figure 4.3 Powder XRD patterns for (a) one-dimensional ZnO nanowires and (b) ZnO nanoparticles films on ZnO seed layered glass substrates. Please note the preferential growth of ZnO nanowires along the (002) lattice plane.

4.3.2. Atomic Force Microscopy Imaging of the Photoanodes

The surface topographic imaging of the ZnO based photoanodes fabricated on ZnO seed layered FTO substrates are constructed using atomic force microscopy (AFM). The AFM images shown in Figure **4.4** clearly reveal nearly similar porous type packing of both ZnO NW and ZnO NP based photoanodes. As can be seen, 1D ZnO NWs exhibit a better distribution of voids/spacing within the NW network in contrast to that of the ZnO NPs. This indicates a smooth diffusion of electrolyte possible through the ZnO NW network in contrast to the NP films. *Please note*: To get the representative AFM images, the raster scan was performed in a scan area of 2.0 μm × 2.0 μm for the 1D ZnO NW films, while a scan area of 1.0 μm × 1.0 μm was fixed for the ZnO NP film. However, the scale bars for the AFM images are inserted accordingly in Figure **4.4**.

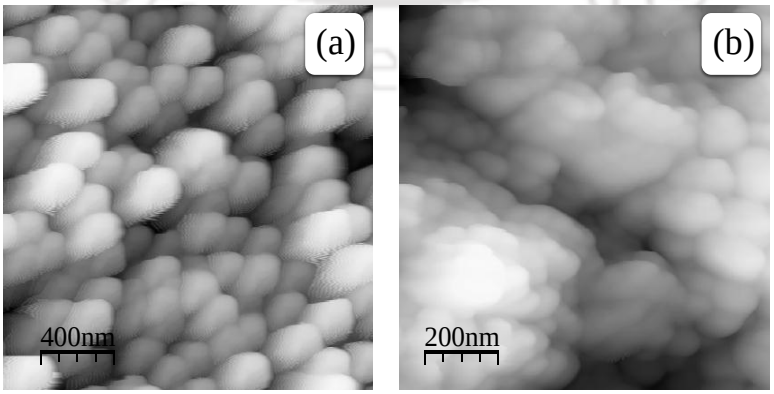

Figure 4.4 Atomic force microscopy (AFM) images of (a) one-dimensional ZnO nanowire (area = 2.0 μm × 2.0 μm) and (b) ZnO nanoparticle (area = 1.0 μm × 1.0 μm) films fabricated on ZnO seed layered FTO substrates.

4.3.3. Normalized UV–Vis DRS Absorption Spectra

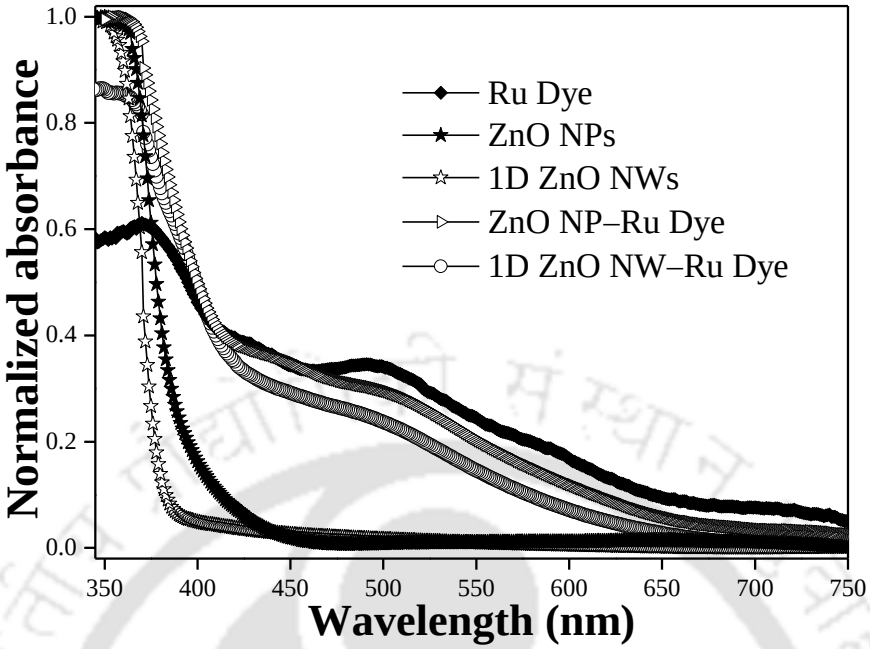

Figure 4.5 Normalized UV–vis diffused reflectance spectra of the dye film (filled box), ZnO NP film (filled star), 1D ZnO NW film (empty star), dye-sensitized ZnO NP film (empty triangle), and dye-sensitized 1D ZnO NW film (empty circle), all on FTO coated glass substrates.

Normalized UV–vis diffused reflectance absorption spectra of the Ru dye film, dye-sensitized ZnO NP film and dye-sensitized 1D ZnO NW film, all on FTO coated glass substrates, recorded against wavelength range of 300–750 nm against a blank FTO substrate as the reference are shown in Figure **4.5**. The dye film was prepared by drop-casting a dye solution (in anhydrous ethanol/dichloromethane, 1:1, v/v) on FTO coated glass substrate, followed by drying at 40 °C in a vacuum electronic oven. The UV–vis spectrum of a Ru dye film (filled box) has shown two intense absorption bands, one at ~371 nm due to the dppz-COOH intraligand $\pi \rightarrow \pi^*$ transitions and a second low-energy band at ~430–491 nm due to the Ru($d\pi$) → dppz-COOH(π^*) MLCT transition. Notably, the absorption spectrum of dye shows the characteristic absorption properties of heteroleptic polypyridyl complexes[37–39] with an estimated high molar extinction coefficient of $\sim 14.3 \times 10^3\ M^{-1}\ cm^{-1}$ at 491 nm. Alternately, the absorption spectra of ZnO NPs (filled star) and ZnO NWs (empty star) show their typical absorption steeps at ~383 and ~378 nm, respectively, where a slight red shift of ~5 nm is observed due to the reduced dimension of ZnO NPs in contrast to that of ZnO NWs. This is in good agreement with an apparent shift of ~0.04 eV in the estimated optical band gap energies of ZnO NPs (~3.23 eV) and ZnO NWs (~3.27 eV) from the Tauc's plot (Figure **4.6**), where $(\alpha h\nu)^2$ is plotted as a function of photon energy ($h\nu$).[29,40] The optical band gaps are calculated using Tauc's relationship following eq.s (1) and (2)

$$(\alpha h\nu)^2 = C\,(h\nu - E_g) \quad (1)$$

$$\alpha = (A \times log\ e) / t \quad (2)$$

where α is the absorption coefficient of ZnO at a certain wavelength value, *h* is the Planck's constant, *C* is the proportionality constant, ν is the frequency of incident light, E_g is the band gap of ZnO, and *t* is the thickness (in cm) of ZnO film. It should also be noted that the UV–vis spectra of dye-sensitized ZnO NP (empty triangle) and dye-sensitized ZnO NW (empty circle) films represent the significant absorption profiles for both the parts (ZnO and the dye), indicating an improved molar absorptivity of ZnO films (NWs and NPs) upon dye loading.

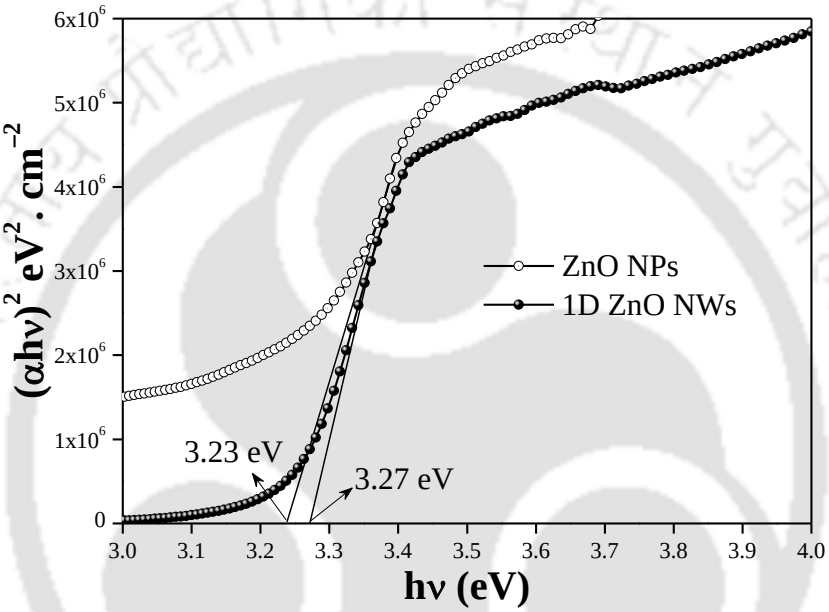

Figure 4.6 Tauc plot to estimate the band gaps for (a) one-dimensional ZnO nanowire and (b) ZnO nanoparticle films fabricated onto the ZnO seed layered glass substrates.

4.3.4. Materials Morphology

In tandem with high crystallinity, hydrothermal growth dependent vertical length (accountable for 1D charge transfer pathways) and surface morphology (responsible for dye loading) of the ZnO NWs also play a vital role in boosting the device efficiency. A well-oriented 1D distribution favoring an efficient dye loading, and a thickness of ~6–8 μm of the ZnO NWs grown on FTO are confirmed from field-emission scanning electron microscopy (FESEM) images (Figures **4.7a** and **4.7b**). Transmission electron microscopy (TEM) image (Figure **4.7c**) of the NWs further confirms their 1D shape with an average diameter of ~40–50 nm. The high-resolution TEM (HRTEM) image (Figure **4.7d**) of ZnO NWs shows well-distinct lattice fringes only for the (002) lattice plane, indicating a single crystalline nature of the NWs without any crystal dislocations. An interplanar *d*-spacing of ~0.52 ± 0.005 nm along the [0002] direction of ZnO NW crystal

structure, assignable to (002) lattice plane, is identified from the inverse fast Fourier transform (IFFT) of the HRTEM image (Figure **4.7e**). The spherical shaped bare ZnO NPs with an average diameter of ~40–50 nm are also observed from their TEM image, as shown in Figure **4.7f**.

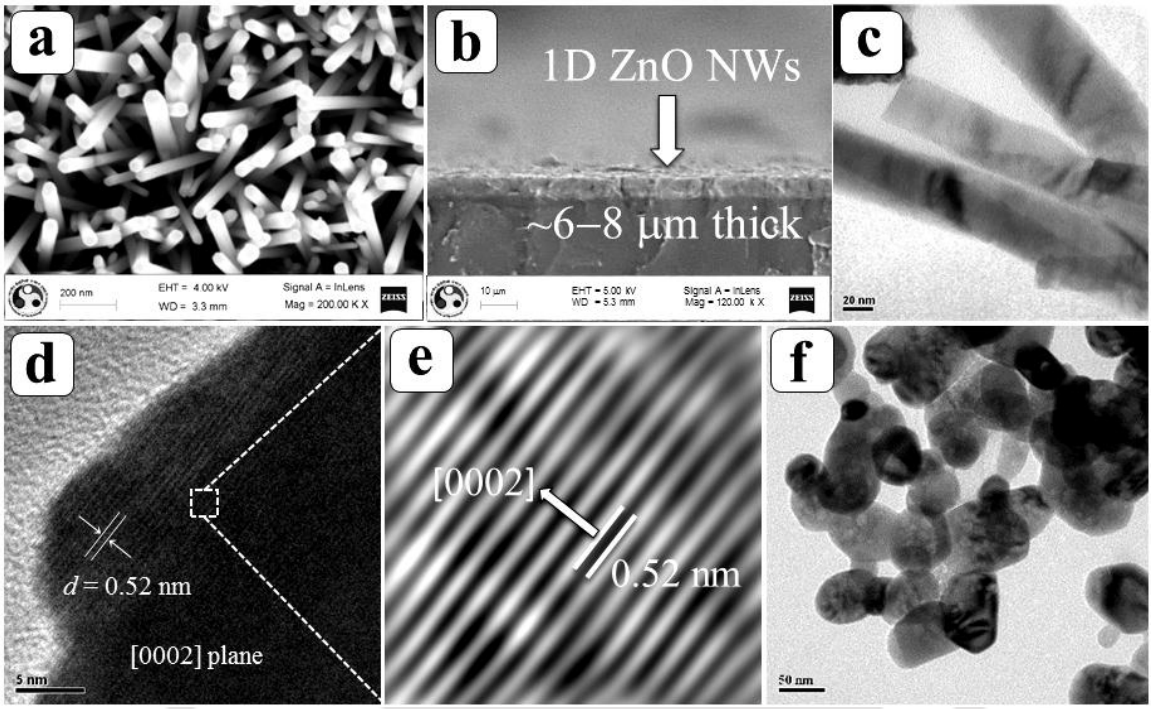

Figure 4.7 (a) Field-emission scanning electron microscopy (FESEM) image of one-dimensional ZnO nanowires grown over ZnO seeded FTO substrates. (b) Cross-sectional FESEM image showing a thickness of ~6–8 μm for the ZnO nanowires. (c, d) Transmission electron microscopy (TEM) and high-resolution TEM (HRTEM) images ZnO nanowires. (e) Inverse fast Fourier transform (IFFT) of the HRTEM image of ZnO nanowires showing the (0002) lattice plane and an interplanar *d*-spacing of ~0.52 ± 0.005 nm. (f) TEM image of bare ZnO nanoparticles.

4.3.5. Density Functional Theory (DFT) Calculations and Electronic Structure

Electronic structure calculations were performed by means of the density functional theory (DFT) method using the Gaussian 09 software.[41] DFT studies were carried out at B3LYP level, with the LANL2DZ ECP basis set for the Ru atom and 6-31G basis set for all the other atoms. No symmetry constraint was imposed during the optimization. Vibrational frequency analyses were performed to confirm that the optimized structure is a true minimum. The ground state optimized structure with the frontier molecular orbitals, namely, HOMO–1, HOMO, LUMO, and LUMO+1, are shown in Figure **4.8**. As can be seen, the electron density distributions at the HOMO and HOMO–1 levels are primarily localized on the Ru atom and on the NCS ligands, whereas the electrons at the LUMO and LUMO+1 levels are delocalized on the dppz-COOH ligand. This is indicative of a good spatial separation of the electrons and holes in the dye upon photoexcitation, witnessing a reduced electron–hole recombination rate, thus probing an efficient output current in the devices. A well-separated electron density distribution from the HOMO to

LUMO levels also endorses the characteristic MLCT transition, Ru(dπ) → dppz-COOH(π*). Moreover, the electronic localization on the dppz-COOH at the LUMO level favors an efficient photoinduced electron injection from the dye to ZnO through the anchoring −COOH groups. The proximal band energy alignment of the LUMO of the dye (at ~3.47 eV as estimated from DFT) and the CB of ZnO (at ~4.3 eV) induces an efficient photoexcited electron transfer pathway.

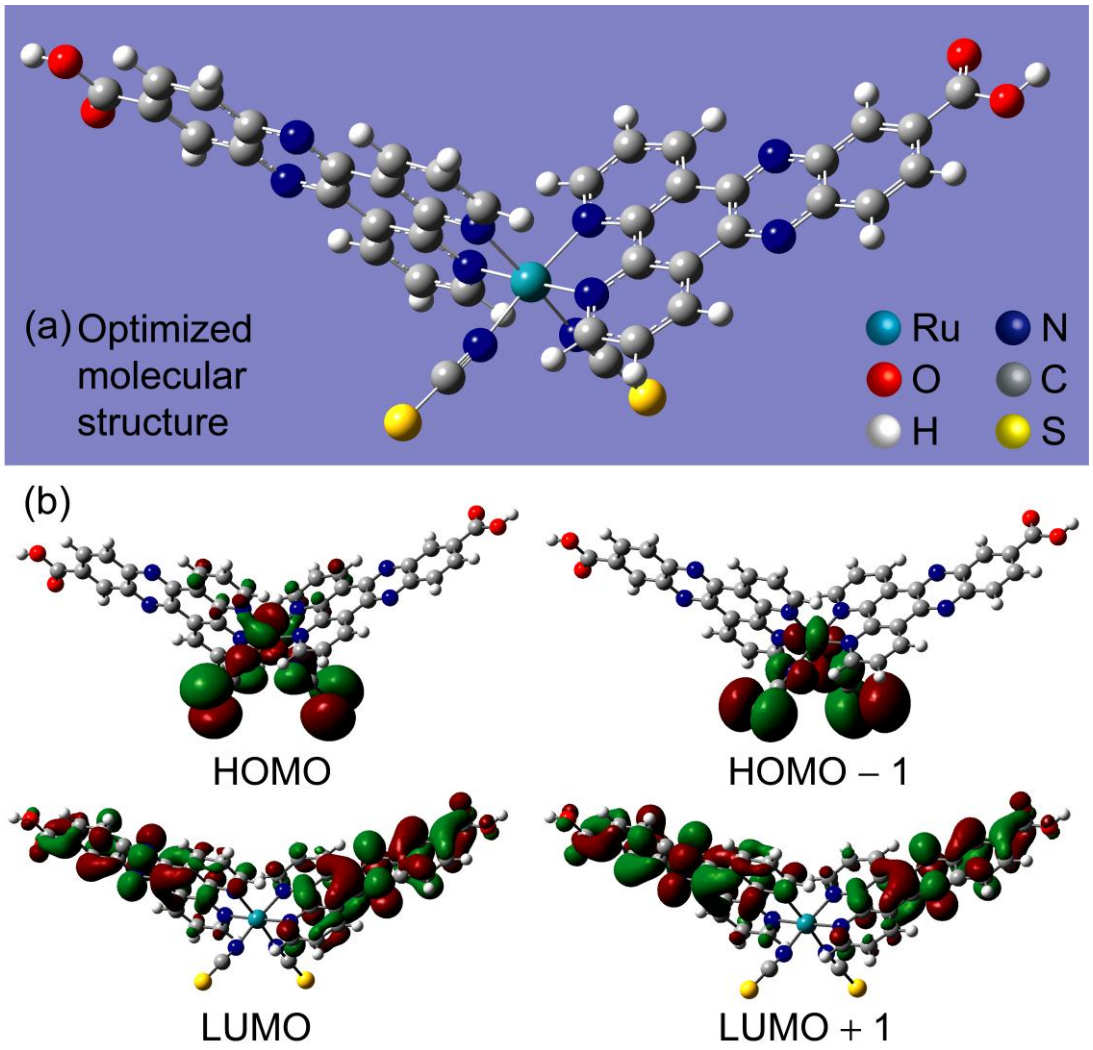

Figure 4.8 Optimized geometry and frontier molecular orbitals (HOMO–1, HOMO, LUMO, and LUMO+1) of $Ru^{II}(dppz\text{-}COOH)_2(NCS)_2$, obtained from density functional theory at B3LYP/LANL2DZ/6-31G level.

Time-dependent DFT (TDDFT) calculations were carried out to establish the MLCT transition of the dye molecule. The theoretical absorption profile of the dye showing an intense absorption in a wide visible range (Figure **4.9a**) ascribes its MLCT transition. The theoretically calculated UV–vis absorption maxima is also relatively comparable to the experimental spectra; however, they differ by an energy gap of ~0.2 eV. TDDFT computed IR data for the dye also matches well with the experimentally recorded Fourier transform IR (FTIR) data (Figure **4.9b**).

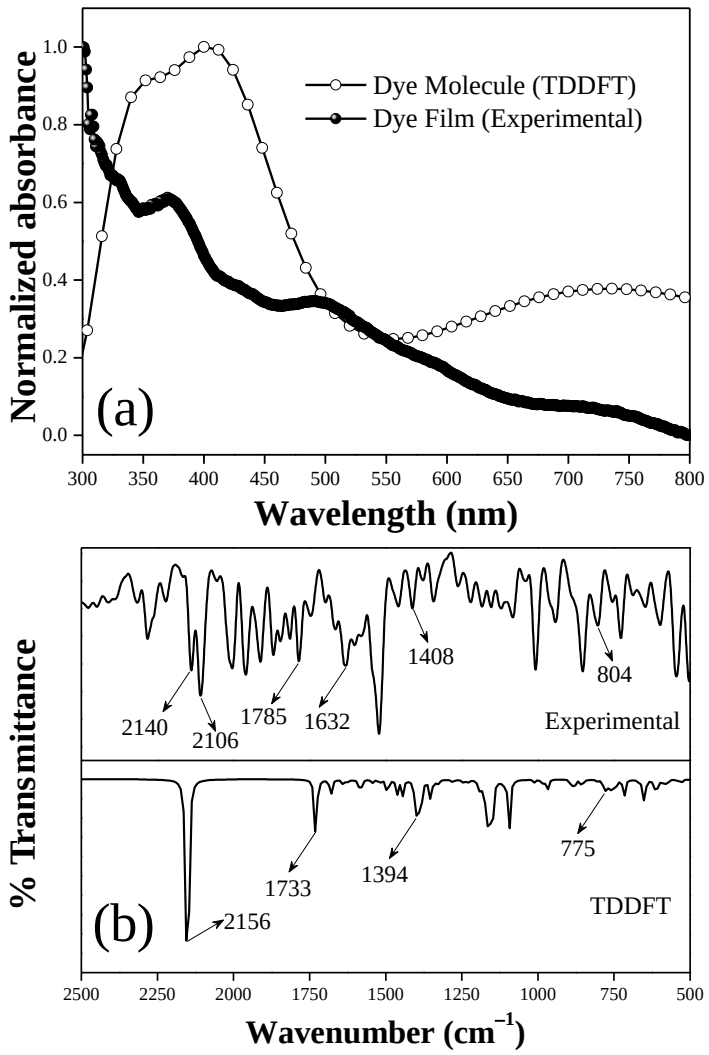

Figure 4.9 (a) Normalized UV–vis absorption and (b) infrared spectra of $Ru^{II}(dppz–COOH)_2(NCS)_2$ dye as obtained from the experimental data and time-dependent density functional theory (TDDFT) study.

4.3.6. Chemisorption, BET Surface Area, and FTIR Analysis

The quantity of dye chemisorbed onto the fabricated photoanodes is evaluated by employing a dye adsorption–desorption process using 0.1 mM NaOH solution in ethanol/water (1:1, v/v).[42] Notably, an optimum quantity of dye loading is observed with values ~1.29 × 10^{-7} mol cm^{-2} for 1D ZnO NW and ~1.42 × 10^{-7} mol cm^{-2} for ZnO NP films. Marginally higher dye loading, as observed for the ZnO NP in contrast to ZnO NW, can be ascribed to a slightly higher BET surface area of the ZnO NP film (~28.2 m^2 g^{-1}) compared to that for ZnO NWs (~21.7 m^2 g^{-1}), which is evident from the typical type IV isotherms with H3 hysteresis loops for ZnO, as shown in Figure **4.10**. The pore area *vs*. pore diameter plots (inset to Figure **4.10**) show pore diameters within the range of ~2–10 nm for both the photoanodes, which is indicative of the characteristic mesoporous nature affording efficient dye loading competency of the photoanodes.

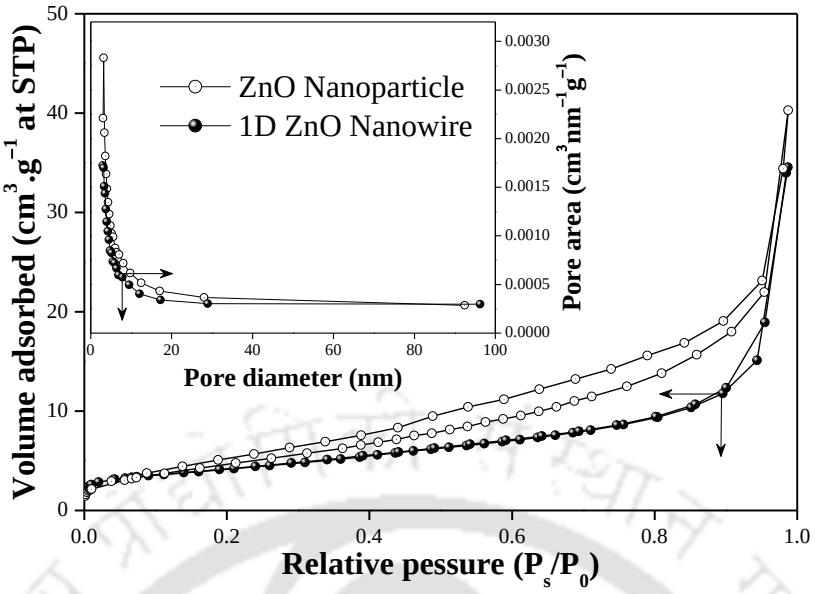

Figure 4.10 Nitrogen adsorption–desorption isotherms for ZnO nanoparticles and one-dimensional ZnO nanowires. *Inset*: Barrett−Joyner−Halenda pore-size distribution plots showing the pore area versus pore diameter.

FTIR spectrum recorded for the dye molecule shows the typical $\nu_{C=O}$ stretching, $\nu_{C—O}$ asymmetric stretching and $\nu_{C—O}$ symmetric stretching modes at ~1785, ~1632, and ~1408 cm^{-1}, respectively, responsible for the carboxylate groups, as shown in Figure **4.9b**.[43,44] In addition, a doublet with peaks at ~2106 and ~2140 cm^{-1}, confirms the *cis*-configuration of two NCS ligands in the dye molecule. Further the appearance of a $\nu_{C=S}$ resonance at ~804 cm^{-1} (instead of a weak band at ~700 cm^{-1} for the S-linkage) indicates the coordination of NCS ligand to Ru center only through the N atom. Notably, a *cis* geometric arrangement of the ancillary ligands confirms the anchoring of the dye molecule to ZnO through both −COOH groups residing on dppz-COOH ligand, which allows an effective anchoring of the dye molecule to ZnO surface and an efficient photoinduced charge injection from the dye molecule to the conduction band (CB) of ZnO.[45]

4.3.7. Electrochemical Study of Ru(dppz-COOH)$_2$(NCS)$_2$ Dye

Cyclic voltammogram of the Ru-dye (Figure **4.11**), recorded against Ag/AgCl as a reference electrode using dry acetonitrile solvent with 0.1 M tetrabutylammonium hexafluorophosphate as a supporting electrolyte and a scan rate of 50 mV s^{-1}, has shown an onset oxidation potential of ~0.944 V, calibrated using ferrocene/ferrocenium (Fc/Fc$^+$) redox couple. The oxidation potential is then converted to the corresponding HOMO level, using eq. (3), assuming the absolute HOMO level of ferrocene to be −4.8 eV ($E_{1/2}$ observed at ~0.404 V).[46] The estimated HOMO level of the dye at −5.34 eV favors a faster regeneration of the dye using cobalt based redox electrolytes: Co-bpy ($E_{redox} \approx -5.06$ eV) and Co-phen ($E_{redox} \approx -5.12$ eV).[35,47] The LUMO level of the dye is

estimated at −3.65 eV, using eq. (4), where an optical band gap (E_g) of ≈1.89 eV has been obtained from the absorption onset of the dye (Figure **4.5**). Close proximity and a slightly higher LUMO level (−3.65 eV) of the dye with respect to the CB potential (−4.3 eV) of ZnO result in a facilitated electron transfer from the LUMO of dye to the CB of ZnO.

$$E_{HOMO} = -(E_{onset,\,ox} - E_{1/2,\,ferrocene} + 4.8)\ eV \quad (3)$$

$$E_{LUMO} = E_g - E_{HOMO} \quad (4)$$

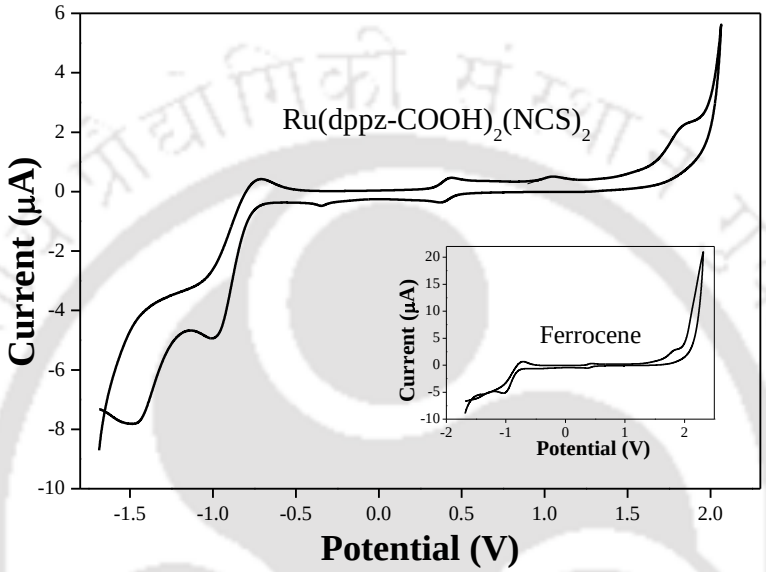

Figure 4.11 Cyclic voltammogram of $Ru^{II}(dppz–COOH)_2(NCS)_2$ dye recorded in dry acetonitrile solvent at a scan rate of 50 $mV.s^{-1}$ using 0.1 M tetrabutylammonium hexafluorophosphate as the supporting electrolyte. *Inset*: Cyclic voltammogram of ferrocene under the same conditions.

4.3.8. Photovoltaic Performance

Photovoltaic performance of the fabricated DSCs are evaluated against Pt as a counter electrode with $Co^{III/II}(bpy)_3$ and $Co^{III/II}(phen)_3$ redox shuttles at 100 mW cm^{-2} under AM 1.5 G simulated solar illumination. Figure **4.12a** shows the photocurrent–voltage (*J*–*V*) curves for ZnO NW and ZnO NP photoanode based DSCs. A short-circuit current density (J_{sc}) ≈ 11.22 mA/cm^2, an open circuit voltage (V_{oc}) ≈ 807 mV, and a fill factor (FF) ≈ 63.5% affording a PCE ≈ 5.9% have been exhibited by the DSC fabricated with ZnO NWs in the presence of Co-bpy redox couple, while using the Co-phen couple resulted in the following values: J_{sc} ≈ 11.10 mA/cm^2, V_{oc} ≈ 826 mV, and FF ≈ 60.5%, yielding a PCE ≈ 5.6%. The pivotal role of faster charge transport property offered by ZnO NWs to enhance the device efficiency is confirmed from the relatively lower performance of the identical DSCs fabricated using ZnO NPs, which yielded J_{sc} ≈ 8.76 mA/cm^2, V_{oc} ≈ 672 mV, FF ≈ 66.7%, and PCE ≈ 3.9% for Co-bpy, and J_{sc} ≈ 8.89 mA/cm^2, V_{oc} ≈ 702 mV, FF ≈ 64.5%, and PCE ≈ 4.0% for Co-phen redox couple. The overall performance of all the ZnO

based DSCs can be accredited to three key features: (1) optimum loading of the photosensitizer onto ZnO surface by the anchoring carboxylic groups, (2) favorable band alignment mediated efficient photoexcited electron injection from the LUMO of the dye to the CB of ZnO, and (3) inherently fast charge transport by the ZnO based photoanodes, especially through 1D NWs. The overall photovoltaic performances of all the fabricated DSCs are summarized in Table **4.1**.

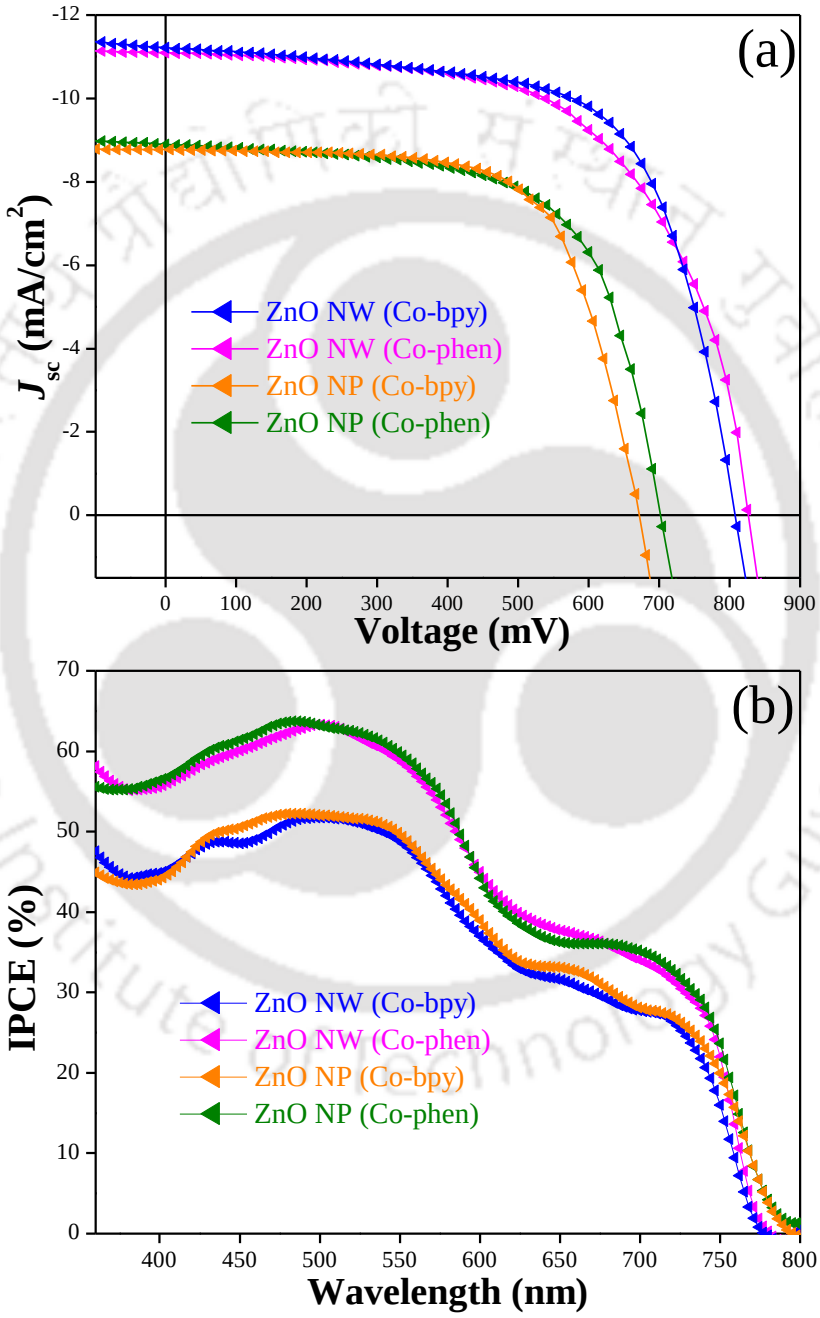

Figure 4.12 (a) Short-circuit current density–voltage (J_{sc}–V) plots for the dye-sensitized solar cells fabricated with ZnO (nanowires and nanoparticle) based photoanodes employing [$Co^{III/II}(bpy)_3$] and [$Co^{III/II}(phen)_3$] redox couples as the electrolyte, under AM 1.5 G simulated solar illumination with an intensity of 100 mW.cm^{-2}. (b) Incident photon-to-current conversion efficiency (IPCE) plots for the fabricated cells.

Table 4.1 Short-circuit photocurrent density (J_{sc}), open-circuit voltage (V_{oc}), fill factor (FF), power conversion efficiency (η) and maximum incident photon-to-current conversion efficiency ($IPCE_{max}$), and photoinduced electron lifetime (τ_{el}) values for the fabricated dye-sensitized solar cells having photoanodes based on ZnO nanowires and ZnO nanoparticles employing $Co^{III/II}(bpy)_3$ and $Co^{III/II}(phen)_3$ redox couples.[a]

DSC photoanode	Redox couple	J_{sc} (mA/cm^2)	V_{oc} (mV)	*FF* (%)	*PCE* (η, %)	$IPCE_{max}$ (%)	τ_{el} (ms)
ZnO NW	Co-bpy	~11.22	~807	~63.5	~5.9	~63	29.4
		(11.01±0.3)	(798±25)	(62.8±1.2)	(5.8±0.2)	(61.2±1.8)	
ZnO NW	Co-phen	~11.10	~826	~60.5	~5.6	~64	25.9
		(10.97±0.6)	(811±13)	(58.9±1.8)	(5.5±0.4)	(63.1±1.1)	
ZnO NP	Co-bpy	~8.76	~672	~66.7	~3.9	~51	17.6
		(8.14±0.7)	(657±19)	(66.1±0.9)	(3.7±0.2)	(49.8±2.1)	
ZnO NP	Co-phen	~8.89	~702	~64.5	~4.0	~52	15.1
		(8.23±0.5)	(672±27)	(63.1±1.7)	(3.7±0.2)	(51.4±0.8)	

[a]Data reported are the results of the best performed devices out of 5 devices for each configuration. The average values and standard deviations for the parameters evaluated for 5 device configurations are given in parentheses.

To have a better understanding of the photocurrent characteristics, the incident photon-to-current conversion efficiency (IPCE) of the fabricated DSCs are recorded against a wavelength range of 360–800 nm. Figure **4.12b** depicts a prominent photosensitization of the dye throughout the visible region reaching the maximum IPCE values of ~64% and ~52% (at ~491 nm) for the ZnO NW and ZnO NP based DSCs, respectively. The IPCE plot shows a broad plateau within the visible region (~360–775 nm) for all the devices accounting for an efficient solar harvesting by the Ru dye, which is well-agreed from its UV–vis absorption profile (Figure **4.5**). In addition, a close proximity of the LUMO level of dye to the CB of ZnO induces a favorable photoexcited charge transfer from the dye (LUMO/S*) to ZnO (CB), as shown in Figure **4.13**.

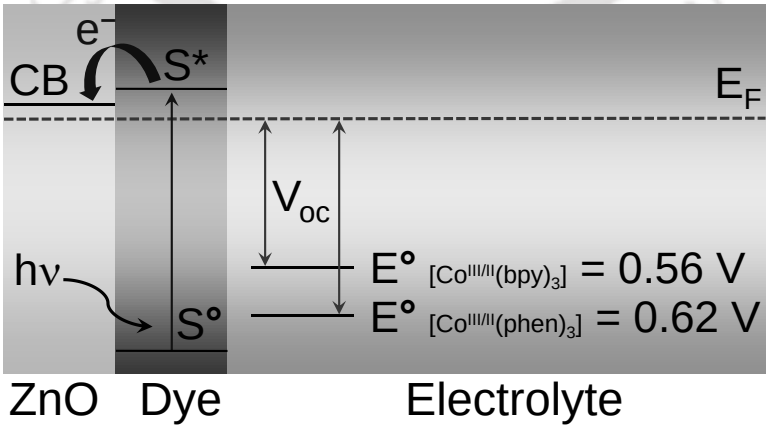

Figure 4.13 Schematic showing the basic energy diagram and the charge transfer processes taking place within ZnO, dye, and the cobalt based redox electrolyte.

Moreover, for both Co-bpy and Co-phen redox couples, remarkably enhanced IPCE values for the ZnO NW based DSCs in contrast to the ZnO NP counterparts reveal the superior 1D charge transport property of the ZnO NWs. Notably, moderately high IPCE values of the DSCs are observed by using Co-phen redox couple as compared to the case with the Co-bpy counterpart. This could be due to a lower recombination at the ZnO/electrolyte interface intercepted by the increased driving force for recombination of the Co-phen system, which is further supported by a relatively positive redox potential of Co-phen ≈0.62 V in contrast to Co-bpy ≈0.56 V.[35,47]

4.3.9. Electrochemical Impedance Spectroscopy Analysis

Faster charge transport prompting a longer electron lifetime in the photoanodes composed of ZnO NWs (as compared to the ZnO NPs) to enhance the overall efficiency of the fabricated DSCs is examined by the electrochemical impedance spectroscopy (EIS) measurements. EIS analysis for the DSCs typically elucidates the characteristics of interfacial charge transfer and recombination processes taking place in the cell, namely, at the interface between the counter electrode and electrolyte (10^3–10^5 Hz, high-frequency region), the ZnO/dye/electrolyte interface (10^{-1}–10^3 Hz, mid-frequency region), and the diffusion of electrolyte (10^{-1}–10^{-2} Hz, low-frequency region).[48] To focus primarily on the superior electron transport property of ZnO NWs over ZnO NPs in the devices, in the present work, EIS data acquisition time to test the fabricated cells was limited to only a couple of min per cell, at which the Nernst diffusion process responsible for the electrolyte does not normally appear. Nyquist and Bode phase plots of the impedance data for the DSCs composed of ZnO (NWs and NPs) are recorded over a frequency range of 10^{-1}–10^5 Hz at room temperature under the dark conditions at a sinusoidal alternating current (AC) perturbation and an applied bias of V_{oc}. Nyquist plots for both ZnO NW and ZnO NP based DSCs have shown two semicircles (Figure **4.14a**): the first one at the mid-frequency region ascribing the charge transfer process occurring at the ZnO/dye/electrolyte interface and the second one at the high-frequency region signifying the redox reactions occurring at the Pt/electrolyte interface. In contrast, the maximum peak frequency (ω_{max}) of the semicircle in the mid-frequency region is correlated to electron recombination rate (k_{eff}) at the ZnO/dye/electrolyte interface. Further, the recombination rate is inversely related to the lifetime of an electron (τ_{el}) in the working electrode. The diameter of the semicircle (R_k) ascribes the charge transfer resistance at ZnO/dye/electrolyte interface. Notably larger diameters of the semicircles in the mid-frequency region, as observed for ZnO NW based devices, indicate an enhanced charge recombination resistance compared to the case of the ZnO NP counterpart. This in turn reflects a prolonged electron lifetime for the

DSCs composed of ZnO NWs. In addition, ZnO NW based photoanodes anticipate an ease of electrolyte diffusion through the void type packing arrangement of vertically oriented nanowire network, alleviating the overall photoinduced charge transport property of the fabricated devices.

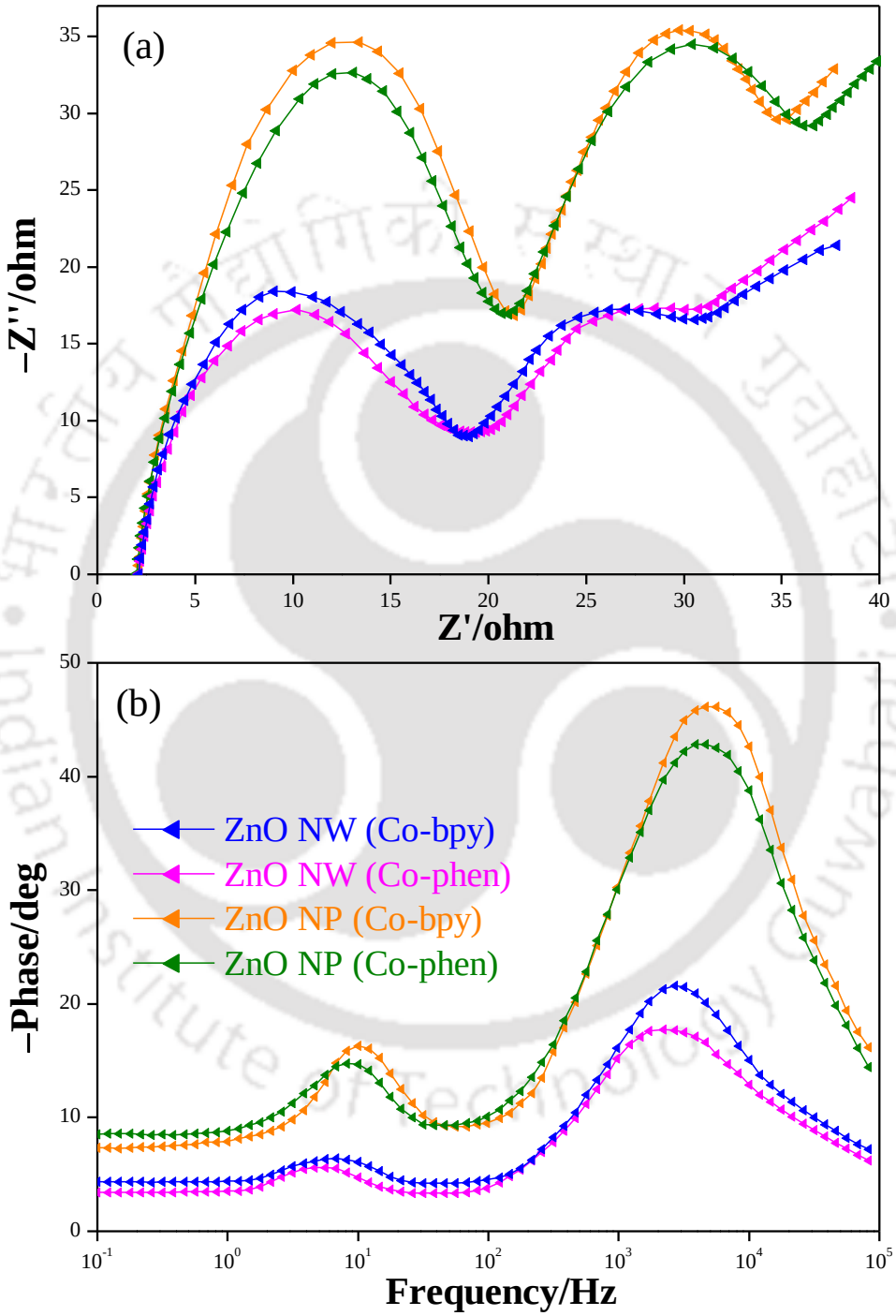

Figure 4.14 (a) Nyquist and (b) Bode phase plots for the fabricated DSCs composed of ZnO NW and ZnO NP based photoanodes employing $[Co^{III/II}(bpy)_3]$ and $[Co^{III/II}(phen)_3]$ redox electrolytes, both under the dark conditions at open-circuit voltage and in a frequency range of 10^{-1}–10^5 Hz.

Figure **4.14b** shows the corresponding Bode phase plots for the DSCs, each showing two

distinct peaks at the mid- and high-frequency regions confirming the two diode interfaces present in the devices. Evidently the phase angle peak, responsible for the electron diffusion time constant in the photoanodes, located at the mid-frequency region shifts to a lower frequency value from ~9.04 Hz (Co-bpy) and ~10.56 Hz (Co-phen) for ZnO NPs to ~5.41 Hz (Co-bpy) and ~6.13 Hz (Co-phen) for ZnO NWs, respectively. This is indicative of a longer photoinduced electron lifetime for the ZnO NWs based photoanodes, in contrast to ZnO NP, in the devices. The values of τ_{el} can be estimated from the Bode phase plot, using eq. (5).

$$\tau_{el} = \frac{1}{2\pi f_p} \tag{5}$$

where f_p is the observed maximum peak frequency in the mid-frequency region. In essence, EIS analysis reveals higher τ_{el} values of ~29.4 ms (Co-bpy) and ~25.7 ms (Co-phen) for ZnO NW based DSCs as compared to ~17.6 ms (Co-bpy) and ~15.1 ms (Co-phen) for the NP counterpart, ascribing a retarded electron–hole recombination in the ZnO NWs in the fabricated devices.

4.4. SUMMARY

- A maverick approach to mimic the heteroleptic dyes by means of a newly synthesized $Ru(dppz\text{-}COOH)_2(NCS)_2$ dye for 1D ZnO nanowire based DSCs has been demonstrated.
- $Ru(dppz\text{-}COOH)_2(NCS)_2$ dye exhibited an intense MLCT absorption band throughout the visible region owing to the π-conjugated dipyridophenazine ring, and at the same time, retained an efficient dye loading capacity due to its optimal size.
- DFT calculations probed the characteristic MLCT transitions of the dye molecule owing to the dipyridophenazine ligand and photoinduced charge transfer feasibility from the LUMO of the dye to the conduction band of ZnO via the carboxylic anchoring groups.
- The persuasive role of excellent electron transport through ZnO nanowires to improve the device efficiency is demonstrated from the relatively lower performance of identical DSCs fabricated with ZnO nanoparticles.
- Electrochemical impedance spectroscopy revealed a prolonged photoinduced electron lifetime for the DSCs composed of ZnO nanowires as compared to ZnO nanoparticles.

4.5. REFERENCES

1. Anta, J. A.; Guillén, E.; Tena-Zaera, R. *J. Phys. Chem. C* **2012**, *116*, 11413–11425.
2. Hagfeldt, A.; Boschloo, G.; Sun, L.; Kloo, L.; Pettersson, H. *Chem. Rev.* **2010**, *110*, 6595–6663.
3. Zhang, S. F.; Yang, X. D.; Numata, Y. H.; Han, L. Y. *Energy & Environ. Sci.* **2013**, *6*, 1443–1464.
4. Grätzel, M.; Janssen, R. A.; Mitzi, D. B.; Sargent, E. H. *Nature* **2012**, *488*, 304–312.
5. Chiba, Y.; Islam, A.; Watanabe, Y.; Komiya, R.; Koide, N.; Han, L. Y. *Jpn. J. Appl. Phys.* **2006**, *45*, L638–L640.
6. Nazeeruddin, M. K.; Pechy, P.; Renouard, T.; Zakeeruddin, S. M.; Humphry-Baker, R.; Comte, P.; Liska, P.; Cevey, L.; Costa, E.; Shklover, V.; Spiccia, L.; Deacon, G. B.; Bignozzi, C. A.; Grätzel, M. *J. Am. Chem. Soc.* **2001**, *123*, 1613–1624.
7. Nazeeruddin, M. K.; Kay, A.; Rodicio, I.; Humphry-Baker, R.; Mueller, E.; Liska, P.; Vlachopoulos, N.; Grätzel, M. *J. Am. Chem. Soc.* **1993**, *115*, 6382–6390.
8. Jiang, K. J.; Masaki, N.; Xia, J. B.; Noda, S.; Yanagida, S. *Chem. Commun.* **2006**, 2460–2462.
9. Abbotto, A.; Manfredi, N. *Dalton Trans.* **2011**, *40*, 12421–12438.
10. Chen, C. Y.; Wang, M.; Li, J. Y.; Pootrakulchote, N.; Alibabaei, L.; Ngoc-le, C. H.; Decoppet, J. D.; Tsai, J. H.; Grätzel, C.; Wu, C. G.; Zakeeruddin, S. M.; Grätzel, M. *ACS Nano* **2009**, *3*, 3103–3109.
11. Angelis, F. D.; Fantacci, S.; Selloni, A.; Grätzel, M.; Nazeeruddin, M. K. *Nano Lett.* **2007**, *7*, 3189–3195.
12. Nazeeruddin, M. K.; De Angelis, F.; Fantacci, S.; Selloni, A.; Viscardi, G.; Liska, P.; Ito, S.; Takeru, B.; Grätzel, M. *J. Am. Chem. Soc.* **2005**, *127*, 16835−16847.
13. Wang, Q.; Ito, S.; Grätzel, M.; Fabregat-Santiago, F.; Mora-Seró, I.; Bisquert, J.; Bessho, T.; Imai, H. *J. Phys. Chem. B* **2006**, *110*, 25210−25221.
14. Huang, W.-K.; Wu, H.-P.; Lin, P.-L.; E. W.-G., Diau. *J. Phys. Chem. C* **2013**, *117*, 2059−2065.
15. Yu, Q. Y.; Huang, J. F.; Shen, Y.; Xiao, L. M.; Liu, J. M.; Kuang, D. B.; Su, C. Y. *RSC Adv.* **2013**, *3*, 19311–19318.
16. Yin, J. F.; Bhattacharya, D.; Hsu, Y. C.; Tsai, C. C.; Lu, K. L.; Lin, H. C.; Chen, J. G.; Ho, K. C. *J. Mater. Chem.* **2009**, *19*, 7036–7042.
17. Lia, X.; Guic, J.; Yanga, H.; Wud, W.; Lia, F.; Tiand, H.; Huanga, C. *Inorg. Chim. Acta* **2008**, *361*, 2835–2840.
18. A. Reynal, A. Forneli, E. Martinez-Ferrero, A. Sanchez-Diaz, A. Vidal-Ferran, E. Palomares, E. *Eu. J. Inorg. Chem.* **2008**, *2008*, 1955–1958.
19. Chen, C. Y.; Lu, H. C.; Wu, C. G.; Chen, J. G.; Ho, K. C. *Adv. Funct. Mater.* **2007**, *17*, 29–36.
20. Onozawa-Komatsuzaki, N.; Kitao, O.; Yanagida, M.; Himeda, Y.; Sugihara, H.; Kasuga, K. *New J. Chem.* **2006**, *30*, 689–697.
21. Stephenson, M.; Reichardt, C.; Pinto, M.; Wachtler, M.; Sainuddin, T.; Shi, G.; Yin, H.; Monro, S.; Sampson, E.; Dietzek, B.; McFarland, S. A. *J. Phys. Chem. A* **2014**, *118*, 10507–10521.
22. Bai, Y.; Zhang, J.; Zhou, D.; Wang, Y.; Zhang, M.; Wang, P. *J. Am. Chem. Soc.* **2011**, *133*, 11442–11445.
23. Tsao, H. N.; Yi, C.; Moehl, T.; Yum, J.-H.; Zakeeruddin, S. M.; Nazeeruddin, M. K.; Grätzel, M. *ChemSusChem* **2011**, *4*, 591–594.
24. Zhou, D.; Yu, Q.; Cai, N.; Bai, Y.; Wang, Y.; Wang, P. *Energy Environ. Sci.* **2011**, *4*, 2030–2034.
25. Kashif, M. K.; Nippe, M.; Duffy, N. W.; Forsyth, C. M.; Chang, C. J.; Long, J. R.; Spiccia, L.; Bach, U. *Angew. Chem., Int. Ed.* **2013**, *52*, 5527–5531.

26. Siefermann, K. R.; Pemmaraju, C. D.; Neppl, S.; Shavorskiy, A.; Cordones, A. A.; Vura-Weis, J.; Slaughter, D. S.; Sturm, F. P.; Weise, F.; Bluhm, H. *et al*. *J. Phys. Chem. Lett.* **2014**, *5*, 2753–2759.
27. Strothkämper, C.; Bartelt, A.; Sippel, P.; Hannappel, T.; Schütz, R.; Eichberger, R. *J. Phys. Chem. C* **2013**, *117*, 17901–17908.
28. Gonzalez-Valls, I.; Lira-Cantu, M. *Energy & Environ. Sci.* **2009**, *2*, 19–34.
29. Barpuzary, D.; Patra, A. S.; Vaghasiya, J. V.; Solanki, B. G.; Soni, S. S.; Qureshi, M. *ACS Appl. Mater. Interfaces* **2014**, *6*, 12629–12639.
30. Chetia, T. R.; Barpuzary, D.; Qureshi, M. *Phys. Chem. Chem. Phys.* **2014**, *16*, 9625–9633.
31. Fan, J. D.; Hao, Y.; Cabot, A.; Johansson, E. M. J.; Boschloo, G.; Hagfeldt, A. *ACS Appl. Mater. Interfaces* **2013**, *5*, 1902–1906.
32. Dyer, J.; Grills, D. C.; Matousek, P.; Parker, A. W.; Towrie, M.; Weinstein, J. A.; George, M. W. *Chem. Commun.* **2002**, 872–873.
33. Bing, Y. J.; Leungb, L. M.; Menglian, G. *Tetrahedron Lett.* **2004**, *45*, 6361–6363.
34. Sullivan, B. P.; Salmon, D. J.; Meyer, T. *J. Inorg. Chem.* **1978**, *17*, 3334–3341.
35. Liu, Y.; Jennings, J. R.; Huang, Y.; Wang, Q.; Zakeeruddin, S. M.; Grätzel, M. *J. Phys. Chem. C* **2011**, *115*, 18847–18855.
36. Park, H.; Chang, S.; Jean, J.; Cheng, J. J.; Araujo, P. T.; Wang, M.; Bawendi, M. G.; Dresselhaus, M. S.; Bulović, V.; Kong, J.; Gradečak, S. *Nano Lett.* **2013**, *13*, 233–239.
37. McConnell, A. J.; Lim, M. H.; Olmon, E. D.; Song, H.; Dervan, E. E.; Barton, J. K. *Inorg. Chem.* **2012**, *51*, 12511–12520.
38. Ettedgui, J.; Diskin-Posner, Y.; Weiner, L.; Neumann, R. *J. Am. Chem. Soc.* **2011**, *133*, 188–190.
39. Giribabu, L.; Bessho, T.; Srinivasu, M.; Vijaykumar, C.; Soujanya, Y.; Reddy, V. G.; Reddy, P. Y.; Yum, J. H.; Grätzel, M.; Nazeeruddin, M. K. *Dalton Trans.* **2011**, *40*, 4497–4504.
40. Barpuzary, D.; Khan, Z.; Vinothkumar, N.; De, M.; Qureshi, M. *J. Phys. Chem. C* **2012**, *116*, 150–156.
41. Frisch, M. J.; Trucks, G. W.; Schlegel, H. B.; Scuseria, G. E.; Robb, M. A.; Cheeseman, J. R.; Scalmani, G.; Barone, V.; Mennucci, B.; Petersson, G. A. *et al.* Gaussian 09, Revision D.01, Gaussian, Inc., Wallingford, CT, **2013**.
42. Fan, K.; Liu, M.; Peng, T. Y.; Ma, L.; Dai, K. *Renewable Energy* **2010**, *35*, 555–561.
43. Keis, K.; Lindgren, J.; Lindquist, S.-E.; Hagfeldt, A. *Langmuir* **2000**, *16*, 4688–4694.
44. Nazeeruddin, M. K.; Kay, A.; Rodicio, I.; Humphry-Baker, R.; Mueller, E.; Liska, P.; Vlachopoulos, N.; Grätzel, M. *J. Am. Chem. Soc.* **1993**, *115*, 6382–6390.
45. Hara, K.; Sugihara, H.; Tachibana, Y.; Islam, A.; Yanagida, M.; Sayama, K.; Arakawa, H. *Langmuir* **2001**, *17*, 5992– 5999.
46. Popere, B. C.; Pelle, A. M. D.; Thayumanavan, S. *Macromolecules* **2011**, *44*, 4767–4776.
47. Feldt, S. M.; Gibson, E. A.; Gabrielsson, E.; Sun, L.; Boschloo, G.; Hagfeldt, A. *J. Am. Chem. Soc.* **2010**, *132*, 16714–16724.
48. Phadke, S.; Du Pasquier, A.; Birnie, D. P. *J. Phys. Chem. C* **2011**, *115*, 18342–18347.

Chapter 5

Metal-Free, D–π–A-Type, Carbazole Dye For A Highly Efficient 1D ZnO Nanowire Based Dye-Sensitized Solar Cell

This chapter describes demonstrates a newly synthesized donor–π linker–acceptor (D–π–A) type, carbazole derivative (SK1) as a sensitizer for one-dimensional ZnO nanowire based dye-sensitized solar cell. The persuasive role of inherently faster electron transport property of ZnO nanowires in contrast to ZnO nanoparticles, enhancing the device efficiency is demonstrated. The electronic distributions of SK1 dye, as computed from DFT, probes its D–π–A mediated intramolecular charge transfer possibility favoring an efficient photoexcited charge migration from the LUMO of SK1 to the conduction band of ZnO.

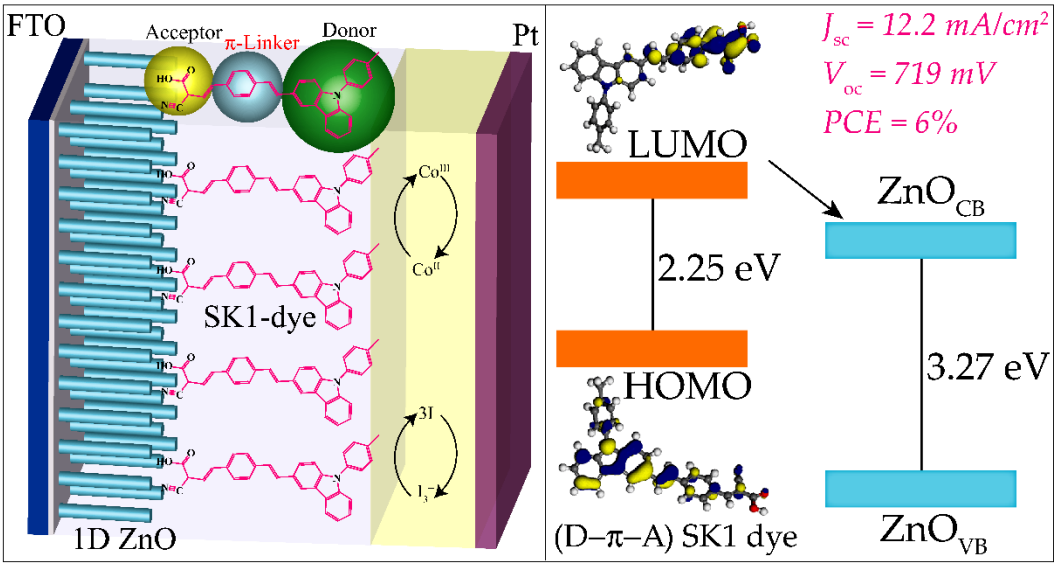

ACS APPLIED MATERIALS & INTERFACES

D. Barpuzary *et al.* **2014**, 6, 12629–12639

5.1. INTRODUCTION

Dye-sensitized solar cells (DSCs) have emerged as an efficient and promising candidate for the solar to electrical energy conversion devices. The performance of these cells primarily depends on the development of three key components: (1) semiconductor nanomaterials having inherently efficient electron transport property, (2) broad solar light absorbing dyes to harvest the sunlight to excite electrons and inject them into the semiconductor scaffold, and (3) noncorrosive redox mediators with enhanced dye regeneration.[1,2] Even if the excellent power conversion efficiency (PCE) up to ~13 % have been attained for DSCs by using the metal-based dyes such as, porphyrins, N3, N719, Z907, phthalocyanines, *etc*.; however, most of them are expensive and laborious to synthesize with tricky purification routes.[3] An alternate way to improve the DSC performance is to use the metal-free organic dyes or their donor–acceptor (D–A) combinations as the sensitizers in conjugation with cobalt-based electrolytes.[3,4] Several metal-free derivatives of carbazole, indoline, thiafulvene, coumarin, *etc*., have shown PCEs reaching ~10 % in DSCs due to their low-band gap, high molar extinction coefficients, and facile molecular design.[5–8] Major advantage of D–A type dyes is the tunability of absorption and electrical properties *via* suitable incorporation of chromophoric groups of different types. A facile molecular engineering of the organic dyes by intervening π-conjugated linker groups into the D–A framework can further improve the molar absorptivity and intramolecular charge transfer feasibility, thereby generating a donor–π linker–acceptor (D–π–A) class of dyes for a better device output.[9,10]

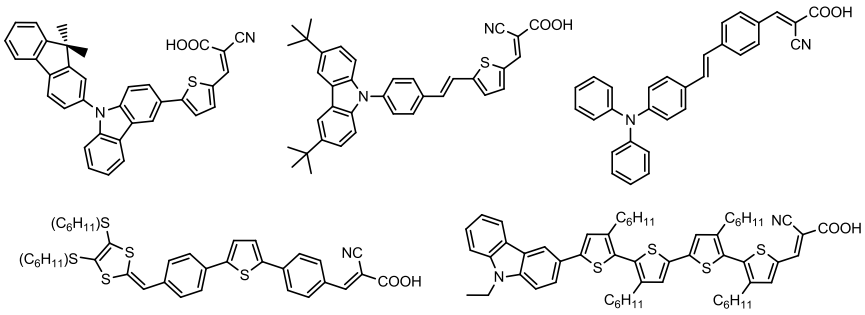

Figure 5.1 Examples of a few highly efficient metal-free dyes, based on the donor–acceptor (D–A) and donor–π linker–acceptor (D–π–A) type concepts, for dye-sensitized solar cells.[9–13]

A few of the D–A and D–π–A type dyes from the available literature are represented in Figure **5.1**. Chao *et al*. have reported TiO_2 based DSCs using a series of D–π–A-type carbazole dyes to achieve PCEs up to ~5.2 % with a high open-circuit voltage (V_{oc}) beyond ~1.0 V by employing different types of halide-based redox electrolytes.[11–13] However, in the recent past, the advent of cobalt based redox electrolytes has shown tremendous improvements in device performance due

to their low visible-light absorptivity, noncorrosive nature, and a higher redox potential, in contrast to the traditional iodide/triiodide (I_3^-/I^-) counterpart.[14–18]

In addition to the development of organic dyes and electrolytes for DSCs, ZnO based sensitizer scaffolds have also gained extensive interest as the electron collector material over the much studied TiO_2 due to their superior electron mobility, faster charge transport, and ease of synthesis to get desired dimensions and morphologies.[19–21] In particular, one-dimensional (1D) nanowire (NW) networks have shown additional benefits such as, direct and effective pathways for charge transport, lower electron hopping, higher interfacial area, and smooth diffusion of the electrolyte.[22–25] However, ZnO based photoanodes sometimes might encounter with the stability issues while sensitizing with dye molecules containing acidic (–COOH) anchoring groups.[19] To overcome the probable limitation, in the case of ZnO-based DSCs, dye-sensitization process should be optimized with great precision in terms of dye concentration and dipping time.

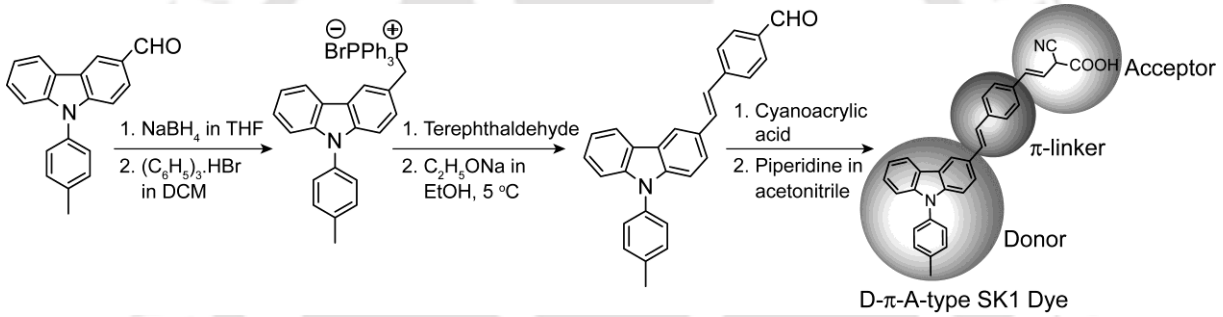

Scheme 5.1 Synthesis procedure of 2-cyano-3-(4-(2-(9-p-tolyl-9H-fluoren-6-yl)vinyl)phenyl) acrylic acid (SK1) dye and the predicted donor–π linker–acceptor (D–π–A) groups.

Based on the current understanding, in this chapter, we have demonstrated an efficient DSC affording a PCE ~5.7%, fabricated using hydrothermally grown 1D ZnO NWs and a newly synthesized metal-free, D–π–A-type, carbazole derivative (SK1), 2-cyano-3-(4-(2-(9-*p*-tolyl-9*H*-fluoren-6-yl)vinyl)phenyl)acrylic acid (Scheme **5.1**). To confirm the promising role of 1D NWs to improve device efficiency, photovoltaic performance of identical DSCs fabricated with ZnO nanoparticles (NPs) are evaluated against Pt as a counter electrode and I_3^-/I^- and cobalt-tris(2,2′-bipyridine) (Co-bpy) as the electrolytes. Electronic distributions of SK1 dye are computed from density functional theory (DFT) that probes a D–π–A mediated intramolecular charge transfer from the carbazole (donor) unit to the cyanoacrylic (acceptor) group *via* oligo-phenylenevinylene (π-linker) unit, resulting in a photoinduced charge transfer from the LUMO of SK1 dye to the conduction band (CB) of ZnO. Electronic interactions between SK1 and ZnO are further studied by steady-state photoluminescence (PL) and time-resolved PL decay measurements.

5.2. EXPERIMENTAL SECTION

5.2.1. Synthesis of SK1 Dye

To synthesize SK1 dye (Scheme **5.1**), the aldehyde was first reduced to corresponding alcohol by treating with $NaBH_4$ in tetrahydrofuran (THF) at 5 °C, followed by stirring for 6 h. The reaction mass was then poured into ice-cold water, extracted in dichloromethane (DCM), dried over anhydrous Na_2SO_4, and finally the solvent was removed under vacuum to get the alcohol (oil). Addition of $(C_6H_5)_3P{\cdot}HBr$ in DCM to this alcohol yielded a white colored Wittig salt, which was separated out by adding diethyl ether, and then condensed with terpthaldehyde in ethanol in the presence of C_2H_5ONa (base) at a temperature of ~5–10 °C. This reaction mixture was stirred further for 2 h, poured into water, and neutralized with dil. HCl to get the yellow colored solid crude. The solid was dissolved in THF and refluxed (4 h) after the addition of a catalytic amount of I_2. The reaction mixture was then poured into dil. alkali solution to isolate the solid aldehyde, which was purified using column chromatography (EtOAc:*n*-hexane, 3:7, v/v). It was dissolved in acetonitrile and refluxed (3 h) after the addition of cyanoacetic acid and a catalytic amount of piperidine. The solvent was removed under reduced pressure and the crude was finally purified using column chromatography (EtOAc:*n*-hexane, 1:1, v/v) to yield the orange colored SK1 dye. ^{1}H NMR ($CDCl_3$, 400 MHz) δ (ppm): 11.00 (s, 1H), 8.30 (s, 2H), 8.20 (s, 2H), 7.86 (s, 1H), 7.72 (s, 3H), 7.42 (d, 4H), 7.41 (d, 2H), 7.40 (d, 2H), 7.20 (d, 2H), 1.90 (s, 3H). ^{13}C NMR (DMSO-d_6, 400 MHz) δ (ppm): 21.09, 64.05, 116.90, 125.24, 126.52, 127.55, 127.66, 128.41, 128.69, 129.47, 130.28, 130.38, 130.87, 131.09, 132.10, 132.19, 134.04, 145.79, 153.23. MS (ESI) *m*/*z*: $[M]^+$ for $C_{31}H_{22}N_2O_2$, Calcd, 454.16; Found, 453.80. Anal. Calcd. for $C_{31}H_{22}N_2O_2$: C, 81.83; H, 5.10; N, 6.16; O, 7.03. Found: C, 81.70; H, 5.13; N, 6.10; O, 7.07.

5.2.2. Synthesis of $[Co(bpy)_3](PF_6)_2$ and $[Co(bpy)_3](PF_6)_3$ Complexes

Synthesis of $[Co(bpy)_3](PF_6)_2$ and $[Co(bpy)_3](PF_6)_3$ complexes from cobalt chloride salt and 2,2´-bipyridine (bpy) ligand were carried as discussed earlier in Chapter 4 Section **4.2.4**.[26]

5.2.3. Growth of One-Dimensional ZnO Nanowires on FTO Substrates

One-dimensional ZnO NWs were hydrothermally grown onto FTO coated glass substrates using the method as discussed earlier in Chapter **4** Section **4.2.6**. Typically, ZnO seed layer was spin coated onto the cleaned FTO substrates and the hydrothermal growth of 1D ZnO NWs was completed at 90 °C (2 h) in a 50 mM $Zn(NO_3)_2.6H_2O$ and 50 mM hexamine aqueous solution.[27]

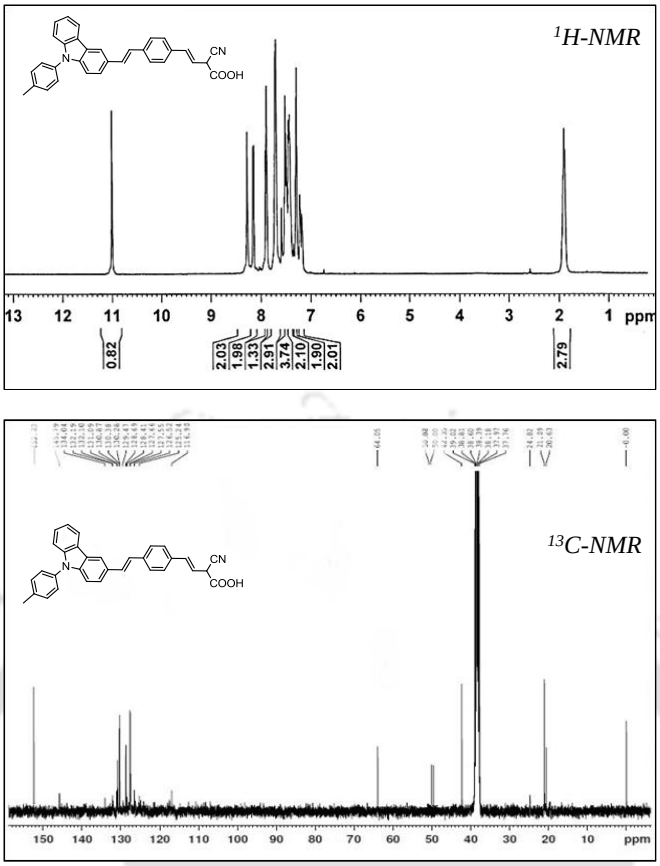

5.2.4. Synthesis of Bare ZnO Nanowires

Bare ZnO NWs in the absence of any ZnO seed layer were synthesized by following a reported hydrothermal route.[28] Typically, 3 mL aqueous solution of 1.5 mM $Zn(NO_3)_2 \cdot 6H_2O$ and 30 mM NaOH was taken in a teflon vessel containing distilled water (0.5 mL), absolute ethanol (30 mL), and ethylenediamine (5.5 mL) and sonicated for 30 min. The Teflon vessel was sealed inside a stainless steel autoclave and then maintained at 180 °C for 20 h in an electronic oven. The solid product was collected by centrifugation after cooling to room temperature, washed with distilled water and ethanol several times, and finally dried in an electronic oven at 60 °C for 4 h.

5.2.5. Synthesis of ZnO Nanoparticles

ZnO nanoparticles (NPs) were synthesized by a method as discussed earlier in Chapter 3 Section 3.2.1. Typically, $ZnCl_2$ was converted to $Zn(OH)_2$ by adding NaOH solution and heated at 90 °C, collected by centrifugation, washed with water and calcined at 250 °C to get ZnO NPs.[29]

5.2.6. Device Fabrication and Characterization

To fabricate ZnO NW-based DSCs, 1D ZnO NW grown FTO substrates were first immersed into a 0.3 mM SK1 dye solution in ethanol:dichloromethane (1:1, v/v) for ~8 h for sensitization. The

substrates were removed from the solution, rinsed with ethanol, dried under hot air blow, and further used as the photoanode. The fabrication of 1D ZnO NW based photoanode is shown in Scheme **5.2**. To fabricate the ZnO NP-based photoanodes, a ZnO NP paste was obtained by mixing and grinding ZnO NPs (0.5 g), terpineol (2.5 mL), and a triblock PEG–PPG–PEG copolymer (1.5 mL) in an agate mortar for 3 h. The ZnO paste was coated by doctor blade technique over the ZnO seed layered FTO substrates and then calcined at 450 °C for 1 h to get a ~8–10 μm thicker ZnO NP films, as confirmed using surface profilometer. These substrates were dipped in the SK1 dye solution for ~8 h, removed from the solution, rinsed with ethanol, and finally dried under hot air blow. The fabrication of ZnO NP based photoanode is illustrated in Scheme **5.3**. The dye-sensitization time for ZnO NW and NP films was set at ~8 h for a dye concentration of 0.3 mM, which was based on the study on the effect of dye loading on ZnO films as reported by Chou *et al*.[30] In the present work, an optimum adsorptivity of the SK1 dye was confirmed from the FTIR and chemisorption measurements; however, the possibility of slight decomposition of the ZnO films by the dye cannot be ruled out completely due to the presence of –COOH anchoring group. To estimate the amount of dye adsorbed onto the ZnO films, each of the dye-sensitized ZnO films was dipped into 0.1 mM NaOH solutions in ethanol/water (1:1, v/v) for a certain period of time.[31] The UV–vis absorbance of each solution was recorded and the concentration of the desorbed dye per cm^2 film area is calculated from the molar extinction coefficient of SK1 dye using Beer's law. To fabricate the counter electrodes, a 50 mM H_2PtCl_6 solution in ethanol was spin coated on pre-cleaned, ozonized FTO substrate, followed by calcination at 450 °C for 10 min. The photovoltaic cells were constructed by sandwiching the photoanodes and counter electrodes with low-temperature thermoplastic sealant (thickness ~50 μm). A drop of electrolyte solution was inserted after sealing the two electrodes to complete the devices. The fabricated devices were stored under the dark conditions for 24 h prior to carry out the photovoltaic measurements. Notably, to obtain a cell area of ~0.16 cm^2 for the DSCs, a mask with an area of ~0.16 cm^2 was used to fabricate the ZnO NW (hydrothermal) and ZnO NP (doctor blade) films on FTO substrates prior to follow the dye sensitization step. The Co-bpy redox electrolyte was prepared by dissolving 0.2 M $[Co(bpy)_3](PF_6)_2$, 0.02 M $[Co(bpy)_3](PF_6)_3$, and 0.5 M 4-*tert*-butylpyridine in acetonitrile/valeronitrile (9:1, v/v) mixture, while I_3^-/I^- electrolyte was prepared by dissolving 0.5 M LiI, 0.05 M I_2, 0.1 M guanidium thiocyanate, and 0.5 M 4-*tert*-butylpyridine in acetonitrile/valeronitrile (9:1, v/v) mixture.

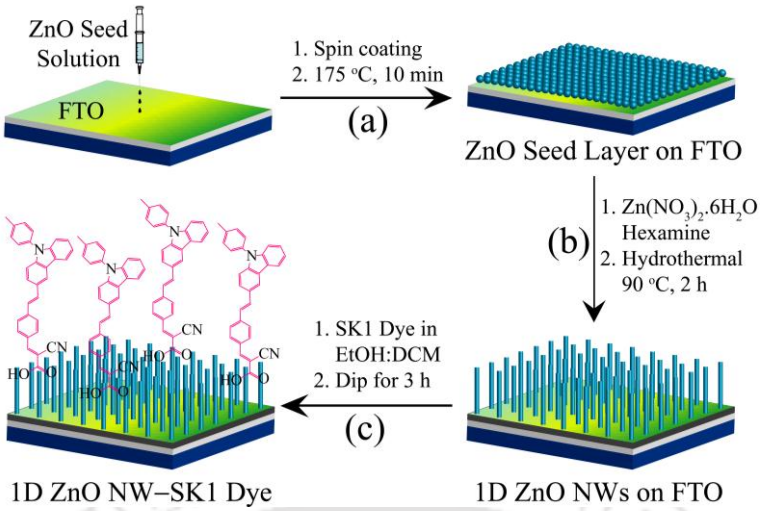

Scheme 5.2 General procedure for fabrication of ZnO nanowire based photoanode: (a) spin coating of ZnO seed solution on FTO substrate and heating at ~175 °C for 10 min, (b) hydrothermal growth of ZnO nanowires over ZnO seed layer at 90 °C for 2 h using a 0.5 M zinc nitrate and 0.5 M hexamine aqueous solution, (c) dye sensitization by dipping the ZnO film into a 0.3 mM SK1 dye solution in ethanol/dichloromethane (1:1, v/v) for 8 h.

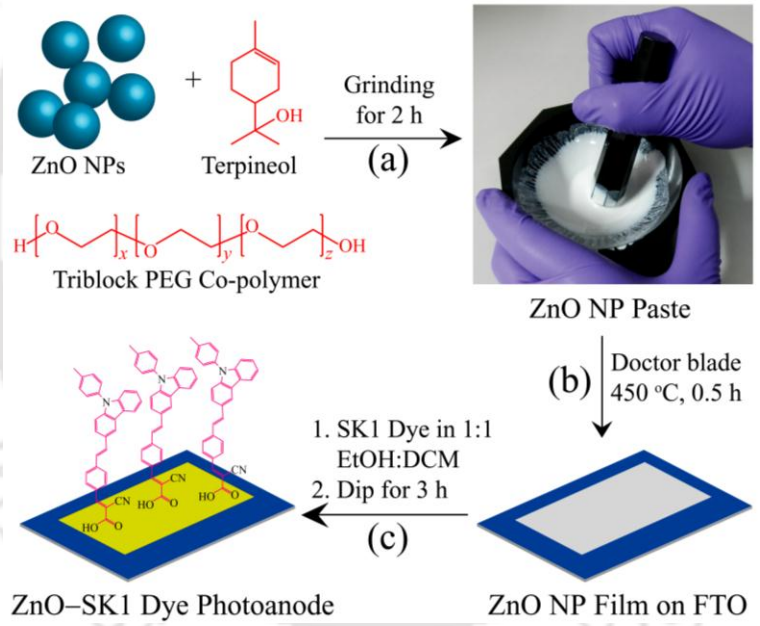

Scheme 5.3 General procedure for fabrication of ZnO nanoparticle based photoanode: (a) ZnO nanoparticle paste formation by grinding ZnO nanoparticles in terpineol and PEG-PPG-PEG triblock co-polymer for 2 h, (b) ZnO film deposition onto FTO substrate by doctor blade technique and calcination at 450 °C for 30 min, (c) dye sensitization by dipping the ZnO film into a 0.3 mM dye solution in ethanol/dichloromethane (1:1, v/v) for 8 h.

5.3. RESULTS AND DISCUSSIONS

5.3.1. Powder X-ray Diffraction Analysis

Phase purity of ZnO NWs and NPs were investigated by powder X-ray diffraction (XRD). From Figure **5.2a**, powder XRD pattern of vertically grown 1D ZnO NWs (red line) shows a strong appearance of (002) diffraction peak at a 2θ of 34.6°, confirming the characteristic 1D growth of ZnO NWs along the *c*-axis normal to the substrate.[32,33] The lattice planes (100), (002), (101),

(103), and (104) are indexed to the formation of the hexagonal phase of ZnO NWs with lattice constants of a = 0.3144 nm and c = 0.5108 nm (JCPDS Ref. No. 36-1451). To confirm the preferential 1D growth of ZnO NWs over ZnO seeded FTO substrates, its XRD pattern is compared with that of the bare ZnO NWs hydrothermally synthesized in the absence of ZnO seed layer (green line, Figure **5.2b**). The observed lattice planes (100), (002), (101), (102), (110), (103), (200), (112), and (201) for the bare ZnO NWs are also indexed to the formation of hexagonal wurtzite crystalline phase with lattice constants of a = 0.3247 nm and c = 0.5201 nm (JCPDS Ref. No. 05-0664). Notably, no characteristic high intensity diffraction peak ($2\theta \approx 34.6°$) originating from the (002) lattice plane of 1D ZnO NWs is observed in the powder XRD pattern for bare ZnO NWs. Alternately, Figure **5.2c** shows the lattice planes (100), (002), (101), (102), (110), (103), (200), (112), and (201) for ZnO NPs (blue line), which are indexed to the formation of hexagonal phase with lattice constants of a = 0.3249 nm and c = 0.5205 nm. The average crystallite sizes of 1D ZnO NWs and ZnO NPs, as estimated from Debye−Scherrer formula using eq. (1), are found to be ~48.9 nm and ~51.8 nm, respectively, by considering the maximum intensity planes, (002) for 1D ZnO NW and (101) for ZnO NPs.

$$D = (0.9 \times \lambda)/(\beta \times \cos\theta) \quad (1)$$

where λ, θ, and β are the X-ray wavelength (0.154 nm), Bragg diffraction angle, and full width at half-maximum (FWHM), respectively.

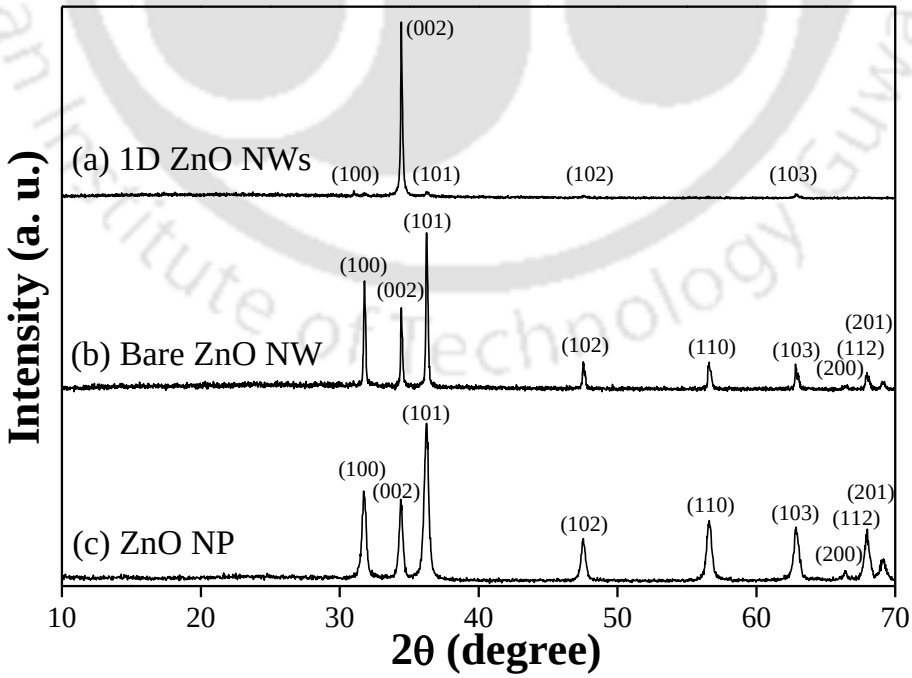

Figure 5.2 Powder X-ray diffraction (XRD) patterns for (a) templated growth of one-dimensional ZnO on ZnO seeded glass substrate, (b) hydrothermally grown bare ZnO nanowires, and (c) ZnO nanoparticles.

5.3.2. Normalized UV–Vis DRS Absorption Spectra

Figure **5.3a** illustrates the normalized UV–vis diffuse reflectance spectroscopy (DRS) absorption spectra of SK1 dye film on FTO (SK1), SK1-sensitized ZnO NP film on FTO (SK1–ZnO NP), and SK1-sensitized 1D ZnO NW film on FTO (SK1–1D ZnO NW) as a function of wavelength, against blank FTO substrate as a reference. The absorption spectrum of SK1 dye thin-film (black line) shows its maximum absorbance range of ~350–550 nm and a molar extinction coefficient of ~3.42 × 10^4 M^{-1} cm^{-1} at 400 nm. The absorption spectra of ZnO NPs (blue line) and 1D ZnO NWs (red line) show their typical UV absorption steeps at ~384 nm and ~378 nm, respectively.

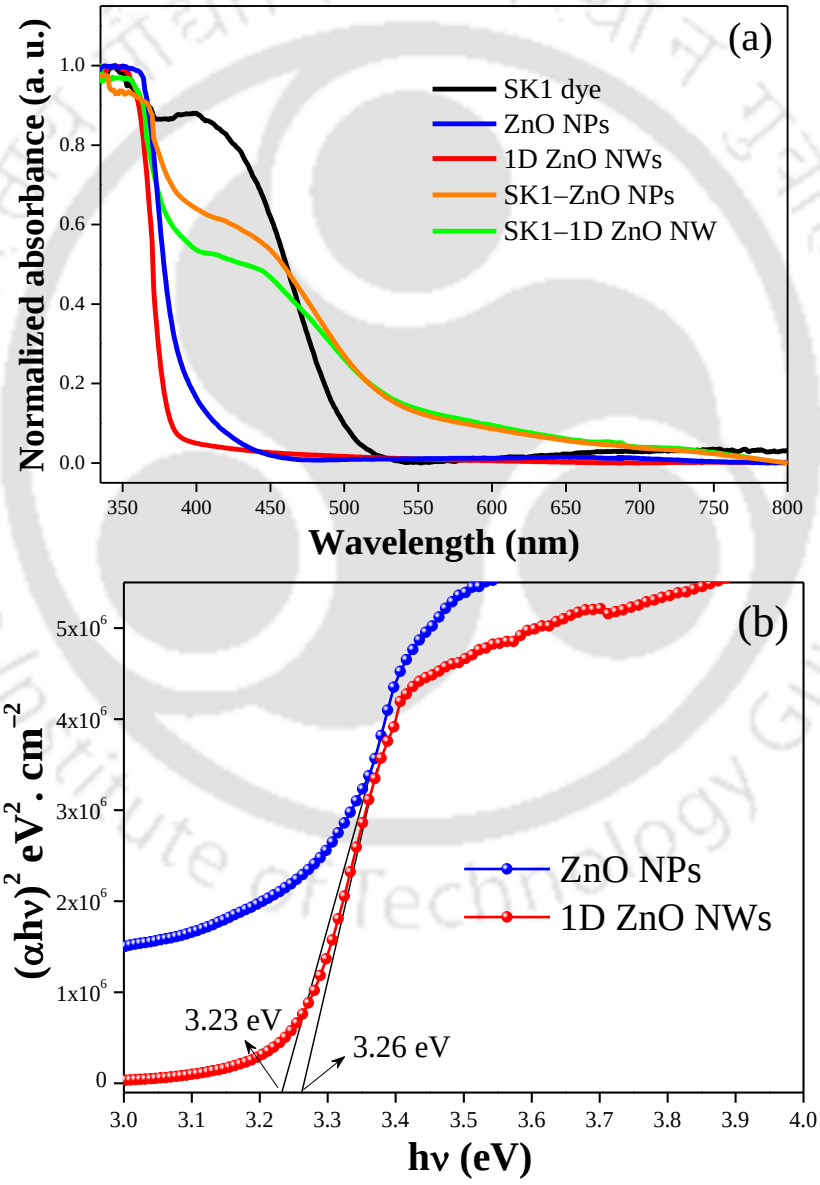

Figure 5.3 (a) Normalized UV–vis diffused reflectance spectra of SK1 dye, ZnO nanoparticle, 1D ZnO nanowire, SK1-sensitized ZnO NP, and SK1-sensitized 1D ZnO NW films on ZnO seed layered FTO substrates. (b) Tauc plots to estimate the band gap of ZnO nanoparticle and 1D ZnO nanowire films on FTO substrates.

Notably, there is a slight red shift that occurs in the absorption spectrum of ZnO NPs in contrast to 1D ZnO NWs, which is ascribed to the lower size dimension of ZnO NPs as compared to that of the NWs. The apparent red shift is further confirmed by a shift of ~0.03 eV in the optical band gap (E_g) of ZnO NPs (~3.23 eV) and 1D ZnO NWs (~3.26 eV), as estimated from the Tauc plot, where $(\alpha h\nu)^2$ is plotted against the photon energy (Figure **5.3b**). The optical band gaps are calculated using Tauc's relationship following equations (2) and (3)

$$(\alpha h\nu)^2 = C\,(h\nu - E_g) \quad (2)$$

$$\alpha = (A \times log\ e) / t \quad (3)$$

where α is the absorption coefficient of ZnO at a certain wavelength value, h is the Planck's constant, C is the proportionality constant, ν is the frequency of incident light, E_g is the band gap of ZnO, and t is the thickness (in cm) of ZnO film. It is also observed that the UV–vis spectra of SK1–ZnO NP (orange line) and SK1–1D ZnO NW (green line) show the absorption profiles for both ZnO and SK1 dye, confirming an enhanced molar absorptivity of ZnO upon dye anchoring.

5.3.3. Materials Morphology

Morphologies of 1D ZnO NWs, bare ZnO NWs, and ZnO NPs are investigated by field-emission scanning electron microscopy (FESEM), SEM, and transmission electron microscopy (TEM) analysis. Figure **5.4a** shows the top-view FESEM image of 1D ZnO NWs grown over ZnO seed layer, indicating a vertically aligned NW network. Cross-sectional FESEM image (Figure **5.4b**) 1D ZnO NW film estimates a thickness of ~5–7 μm, which is also confirmed using surface profilometer. To confirm the need of ZnO seed layer to achieve a vertically aligned growth of 1D ZnO NWs, SEM image of bare ZnO NWs (hydrothermally synthesized in absence of ZnO seed layer) is recorded (Figure **5.4c**), which confirms a random growth of ZnO NWs. The morphology of ZnO NWs grown over ZnO seed are further analysed by TEM (Figure **5.4d**), which indicates their 1D shape and an average diameter of ~45 nm. The inset to Figure **5.4d** shows the energy-dispersive X-ray spectroscopy (EDX) pattern confirming the presence of only Zn and O atoms. Figure **5.4e** shows a high-resolution TEM (HRTEM) image of 1D ZnO NWs depicting their well-defined lattice fringes with an interplanar d-spacing of 0.52 ± 0.006 nm along the [0002] direction of ZnO crystal growth, without having any crystal dislocations. The inset to Figure **5.4e** shows the inverse fast Fourier transform (IFFT) of the HRTEM image. This confirms an interplanar d-spacing of ~0.52 nm, which is clearly assignable to (002) lattice plane of wurtzite ZnO. On the other hand, the formation of spherical shaped ZnO NPs with an average diameter of ~50 nm is also confirmed from the representative TEM image, as shown in Figure **5.4f**.

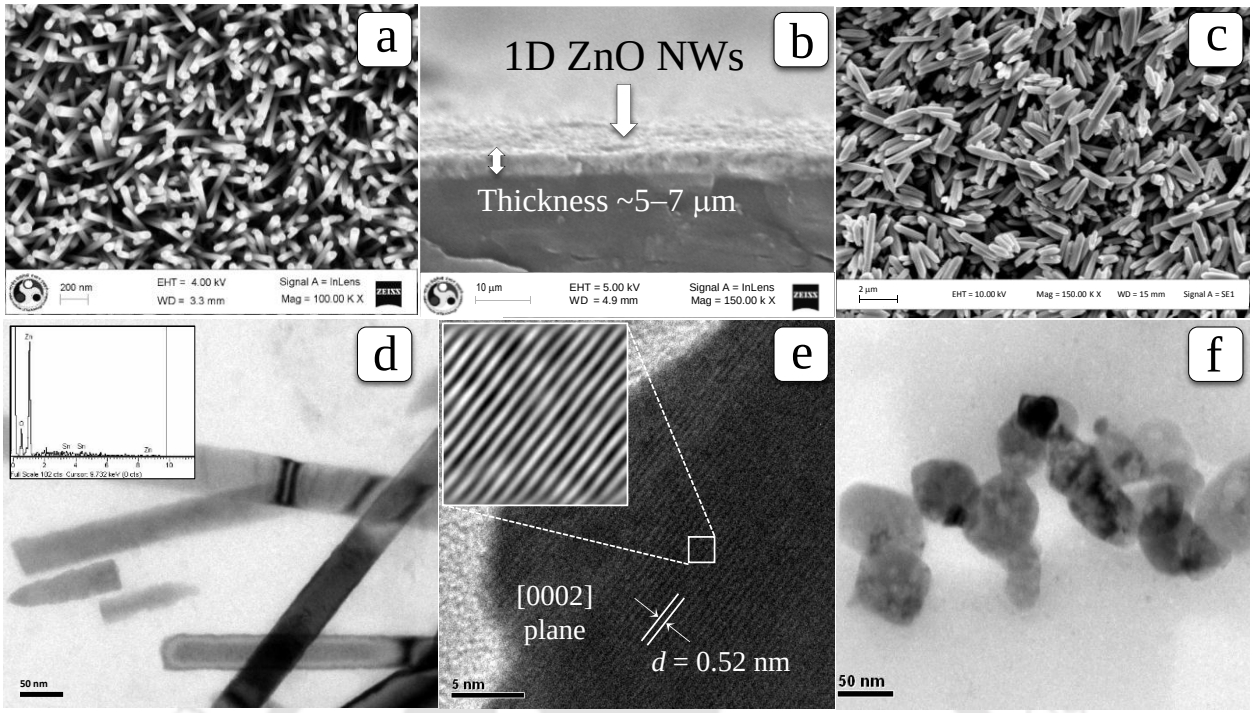

Figure 5.4 (a) Top-view and (b) cross-sectional field-emission scanning electron microscopy (FESEM) images of 1D ZnO nanowires (NWs) grown onto ZnO seed layered substrates. (c) SEM image of hydrothermally grown bare ZnO NWs. (d) Transmission electron microscopy (TEM) image of 1D ZnO NWs. *Inset*: Energy-dispersive X-ray spectroscopy (EDX) pattern of 1D ZnO NWs. (e) High-resolution TEM (HRTEM) image of 1D ZnO NWs. *Inset*: IFFT of the HRTEM image of 1D ZnO NWs. (f) TEM image of as-synthesized ZnO nanoparticles.

5.3.4. Density Functional Theory (DFT) Study of SK1 Dye

To gain an insight into the minimum energy geometric configuration and electronic density distribution of the frontier molecular orbitals of SK1 dye molecule, density functional theory (DFT) calculations are carried out using Accelrys Materials Studio 4.0. The theoretical picture of the frontier orbitals for SK1 dye was derived from the DFT approach. The molecular geometries of SK1 were optimized in DMol3 program package using generalized gradient approximation (GGA) with BLYP basis set. These simulations were carried out in a vacuum for the single molecule. Figure **5.5** depicts the optimized geometry of SK1 dye molecule along with its electron density map for the HOMO and LUMO levels. At the HOMO level, the electronic density of SK1 is homogeneously distributed over the carbazole unit (donor) and oligo-phenylenevinylene unit (π-linker), while at the LUMO level, an electronic excitation of SK1 occurs that results in an intramolecular charge transfer leading to an electron migration from the donor unit to the cyanoacrylic moiety (acceptor) through the π-linker group. It clearly indicates the excited-state electron injection of the dye molecule from its LUMO to the CB of ZnO *via* anchoring –COOH group attached to the cyanoacrylic acceptor.

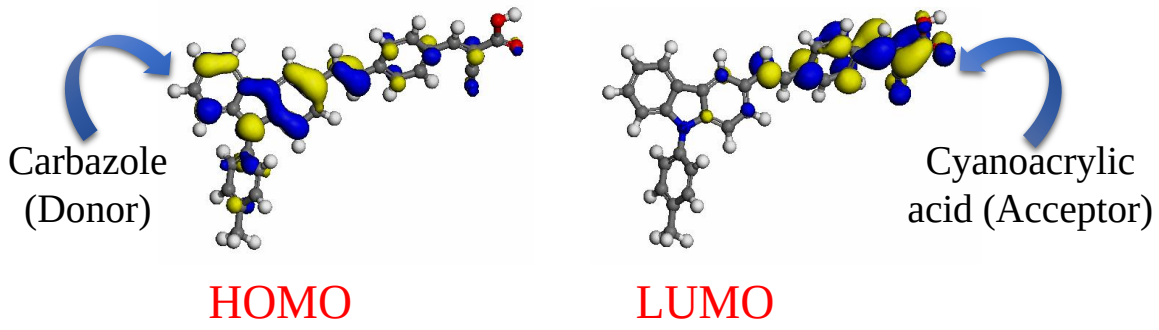

Figure 5.5 Frontier molecular orbitals of SK1 dye molecule as computed from the density functional theory at a B3LYP/6-31+G(d) level showing the electronic distributions of SK1 at the HOMO and LUMO levels.

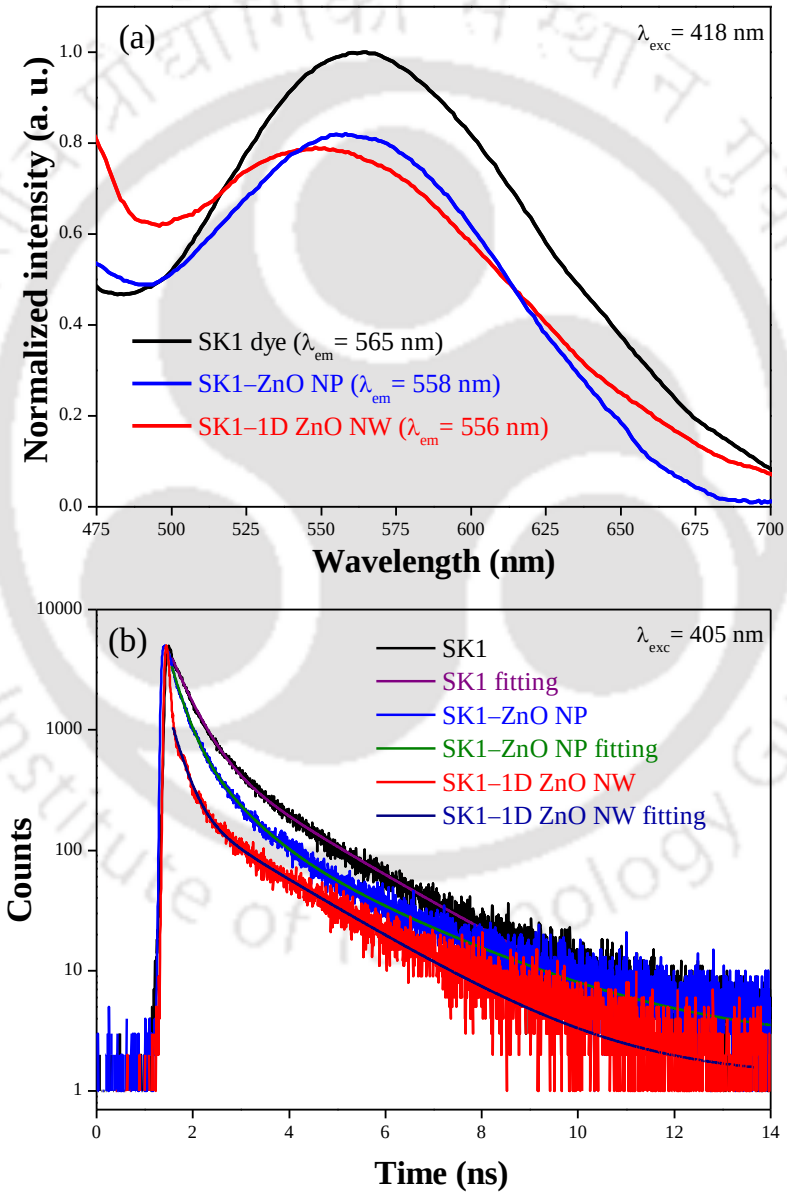

Figure 5.6 (a) Steady-state photoluminescence (PL) spectra at a 418 nm excitation and (b) time-resolved PL (TRPL) spectra at a 405 nm laser excitation with the respective TRPL fitting curves for the plain SK1 dye thin-film on FTO (SK1, black line), SK1-sensitized ZnO nanoparticle film on FTO (SK1–ZnO NP, blue line), and SK1-sensitized one-dimensional ZnO nanowire film grown on FTO (SK1–1D ZnO NW, red line).

5.3.5. Steady-State Photoluminescence (PL) and Time-Resolved PL Studies

To probe the electronic interactions between the dye and ZnO, steady-state photoluminescence (PL) spectra of SK1 dye (black line), SK1–ZnO NP (blue line), and SK1–1D ZnO NW (red line) are recorded at 418 nm excitation. Figure **5.6a** shows a significant quenching in the PL emission originating from the SK1 dye, when it is anchored onto the ZnO (NW and NP). It confirms the presence of excited-state electronic interactions between the SK1 dye and ZnO, indicating the deactivation of excited state *via* non-radiative processes involving the photoexcited charge transfer from the LUMO of SK1 to the CB of ZnO. Notably, relatively more quenching of the PL emission is observed in the case of 1D ZnO NWs in contrast to that of ZnO NPs, which is due to the intrinsically faster charge transport property of 1D ZnO NWs over the NPs.[34,35] In addition, a slight shift of ~7–9 nm in the PL emission maxima of SK1 after its adsorption onto the ZnO (NW and NP) ascribes the effective electronic interactions between the SK1 dye and ZnO.

To have an idea of the excited-state emission decay behavior of SK1 dye upon anchoring to ZnO, the time-resolved PL (TRPL) measurements are performed on plain SK1 (black line), SK1–ZnO NP (blue line), and SK1–1D ZnO NW (red line) films on FTO using a 405 nm diode laser excitation, as shown in Figure **5.6b**. The detailed spectroscopic and fitting parameters for the emission decays for SK1, SK1–ZnO NP, and SK1–1D ZnO NW are presented in Table **5.1**. To calculate the exciton lifetimes of the photoanodes, the TRPL curves were fitted with a bi-exponential function by following eq. (4) using FAST software (Edinburgh Instruments).

$$I(t) = \sum \alpha_i \exp\left(-\frac{t}{\tau_i}\right) \tag{4}$$

where α_i is the initial intensity of the decay component i having a lifetime of t. The average lifetimes τ_1 and τ_2 of SK1–ZnO NP and SK1–1D ZnO NW are calculated using eq. (5).

$$\langle\tau\rangle = \sum_i \alpha_i \tau_i^2 / \sum_i \alpha_i \tau_i \tag{5}$$

The kinetic curves depicted in Figure **5.6b** clearly indicate faster exciton lifetimes for SK1 dye in the presence of ZnO NWs and NPs. These lifetime values for the SK1 dye significantly decrease from ~0.41 ns (τ_1) and ~1.82 ns (τ_2) to ~0.26 ns (τ_1) and ~0.80 ns (τ_2) for the SK1–ZnO NP and to ~0.25 ns (τ_1) and ~0.72 ns (τ_2) for the SK1–1D ZnO NW, respectively. Notably, an average exciton lifetime ($\langle\tau\rangle$) of ~1.54 ns for the SK1 dye also decreases to ~0.68 ns (SK1–ZnO NP) and ~0.60 ns (SK1–1D ZnO NW). It is also noticed that the photoexcited charge injection from the SK1 to ZnO is slightly higher in the case of NWs in contrast to the NPs, which is due to a faster charge transportation through the 1D ZnO NWs.

Table 5.1. Fitting parameter (χ^2), initial intensity (α_1, α_2), excited-state lifetime (τ_1, τ_2), and average exciton lifetime ($\langle\tau\rangle$) for the SK1 thin-film spin-coated on FTO (SK1), SK1-sensitized ZnO nanoparticle film on FTO (SK1–ZnO NP), and SK1-sensitized one-dimensional ZnO nanowires grown on FTO (SK1–1D ZnO NW).

Sample	χ^2	α_1	α_2	τ_1 (ns)	τ_2 (ns)	$\langle\tau\rangle$ (ns)	k_{et} (s^{-1})
SK1	1.08	52.25	47.75	0.414	1.817	1.537	-
SK1–ZnO NP	1.06	36.93	39.47	0.266	0.803	0.675	8.29×10^8
SK1–1D ZnO NW	1.04	34.69	37.31	0.250	0.716	0.602	1.01×10^9

The aforementioned electronic interactions between ZnO and SK1 confirm the presence of photoexcited electron injection from the LUMO of SK1 to the CB of ZnO, which is facilitated by the higher vacant energy levels of ZnO.[36] By considering this electron transfer to be the only pathway for the deactivation of excited SK1, the transfer rate constants for electron injection (k_{ei}) from the SK1 dye to ZnO can be calculated from eq. (6), and are found to be ~8.29×10^8 s^{-1} for SK1–ZnO NP and ~1.01×10^9 s^{-1} for SK1–1D ZnO NW.

$$k_{ei} = \frac{1}{\tau_{SK1-ZnO}} - \frac{1}{\tau_{SK1}} \quad (6)$$

However, it should be noted that the PL decay curves also reflect the transportation inside ZnO, recombination rate at the ZnO–dye hetero interface, and the location of the Fermi level, eventually depending on the crystal defects present in ZnO. The electron relaxation time in the ZnO architectures can be correlated with the defect-mediated emission originating from ZnO.

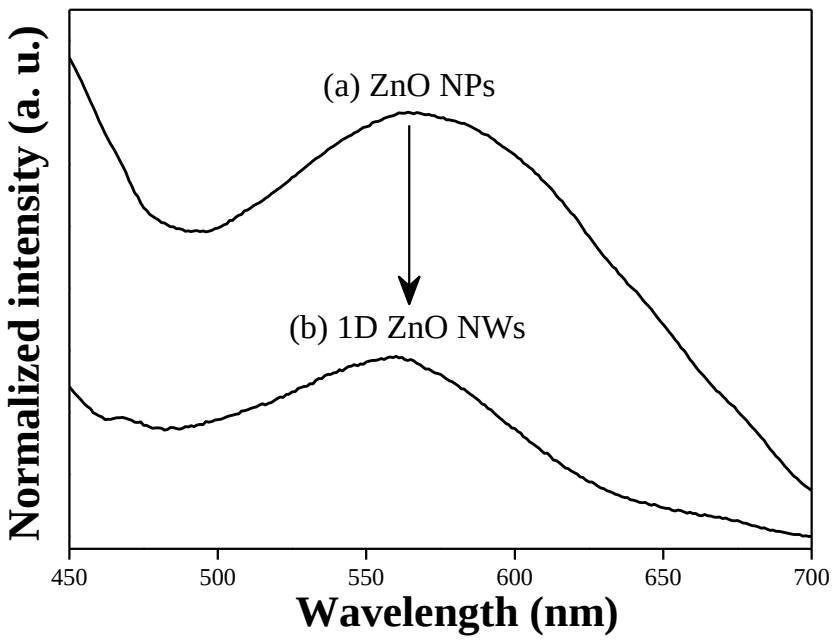

Figure 5.7 Steady-state photoluminescence (PL) spectra at a 410 nm excitation for the (a) one-dimensional ZnO nanowires grown on FTO and (b) ZnO nanoparticle film on FTO showing the defect emission peaks for ZnO.

In view of this, we have compared the steady-state PL spectra of 1D ZnO NW (grown) and ZnO NP (deposited) films on FTO substrates at 410 nm excitation, as shown in Figure **5.7**. The emission spectra for ZnO NWs and NPs exhibit defect-mediated emission peaks visibly in the wavelength range of ~450–580 nm, which are responsible for the transition from the CB of ZnO to the deep defect levels of ZnO created by oxygen vacancies.[22] The defect emission peak for 1D ZnO NWs is observed to be less prominent in contrast to that of the ZnO NPs, which is in good agreement with the single crystalline nature of 1D ZnO NWs as obtained from the powder XRD and TEM analysis (Figures **5.2a** and **5.4e**). The preferential unidirectional growth along the (002) direction offers less crystal defects in 1D ZnO NWs, favoring a longer excited-state relaxation time as compared to that of ZnO NPs.

5.3.6. Electrochemical Study of SK1 Dye

To estimate the HOMO of SK1 dye, cyclic voltammogram is recorded in anhydrous acetonitrile in presence of 0.1 M tetra-*n*-butylammonium hexafluorophosphate electrolyte (Figure **5.8**). An oxidation half-potential of +1.37 V (*vs.* NHE), observed for SK1, is equivalent to the HOMO at −5.62 eV, using eq. (7).[37] A more positive HOMO of SK1 in contrast to the redox potentials of I_3^-/I^- (−4.8 eV) and Co-bpy (−5.1 eV) electrolytes thus prompts an efficient dye regeneration.

$$E_{HOMO} = -(E_{onset,\,ox} - E_{1/2,\,ferrocene} + 4.8)\ eV \quad (7)$$

$$E_{LUMO} = E_g - E_{HOMO} \quad (8)$$

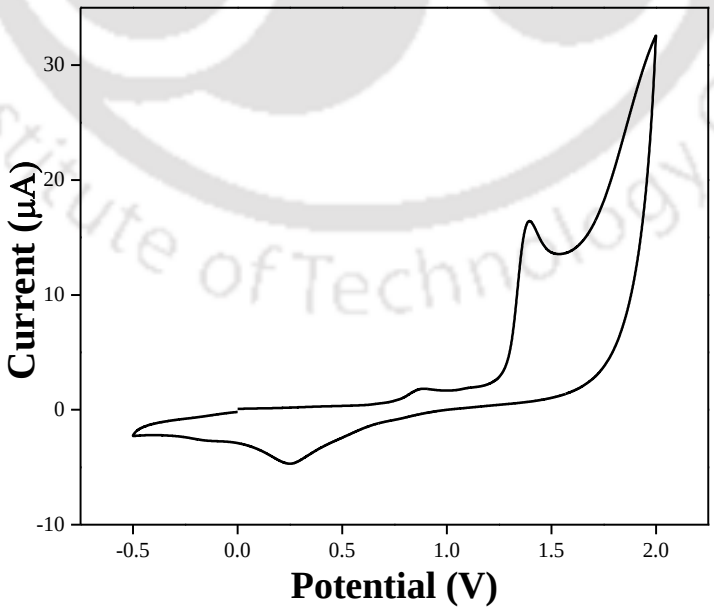

Figure 5.8 Cyclic voltammogram of SK1 dye recorded in anhydrous acetonitrile solvent at a scan rate of 50 $mV.s^{-1}$ using 0.1 M tetrabutylammonium hexafluorophosphate as the supporting electrolyte.

The LUMO of SK1 dye is estimated from the difference between its optical band gap (E_g) and the HOMO level, using eq. (8). An UV–vis absorption onset of SK1 probes its $E_g \approx 2.25$ eV (Figure **5.3**). Thus, the LUMO of SK1 is found to be at −3.37 eV, which is higher than the CB potential of ZnO (−4.3 eV). Such a favorable energy match between SK1 dye and ZnO makes an efficient photoexcited charge transfer possible from the LUMO of SK1 to the CB of ZnO.

5.3.7. Photovoltaic Performance

Photovoltaic performance of the fabricated DSCs are evaluated from their photocurrent–voltage (J–V) curves recorded at 100 mW.cm^2 under AM 1.5 G simulated solar spectrum (Figure **5.9a**). For the 1D ZnO NW-based DSCs (red line), a short-circuit current density (J_{sc}) ~12.0 mA/cm^2, an open-circuit voltage (V_{oc}) ~719 mV, and a fill factor (FF) ~64%, affording a PCE ~5.7% have been achieved by employing Co-bpy redox electrolyte. However, identical DSCs using I_3^-/I^- electrolyte (black line) resulted in a $J_{sc} \approx 12.2$ mA/cm^2, $V_{oc} \approx 629$ mV, and FF ≈ 61%, yielding a PCE ≈ 4.7%. Significantly, while changing the electrolyte from Co-bpy to I_3^-/I^-, the V_{oc} of the cells is found to increase by ~90 mV. Interestingly, ZnO NP based DSCs have also shown almost similar trends. ZnO NP-based DSCs resulted in $J_{sc} \approx 8.79$ mA/cm^2, $V_{oc} \approx 626$ mV, FF ≈ 63%, and PCE ≈ 3.6% for the Co-bpy electrolyte (green line), while the respective performance parameters using I_3^-/I^- electrolyte (blue line) are ≈ 9.1 mA/cm^2, ≈ 555 mV, ≈ 61%, and ≈ 3.2%. Thus, 1D ZnO NWs based DSCs have shown enhanced J_{sc} and V_{oc} values, in contrast to ZnO NP counterparts, which is ascribed to a faster electron transport through 1D NWs in contrast to NPs.

Photocurrent characteristics of the fabricated DSCs are evaluated from incident photon-to-current conversion efficiency (IPCE) values recorded against the wavelength (Figure **5.9b**). The representative IPCE curves of DSCs exhibit the highest values of ~60–62% (ZnO NWs) and ~47–48% (ZnO NPs) for both the electrolytes, with a broad plateau in the ~300–580 nm region ensuring a saturated light absorption of SK1 dye. This is also in good agreement with the UV–vis spectra of SK1 (Figure **5.3**). Moreover, the proximal band alignment between SK1 and ZnO makes it feasible to inject the photoinduced electrons from the LUMO of SK1 to the CB of ZnO (Figure **5.10**). Evidently, 1D NW-based DSCs have shown enhanced IPCE values in contrast to that of the NPs, which is due to a more efficient and faster charge transport property of 1D ZnO NWs (over ZnO NPs). Notably, for all the DSCs, slightly enhanced photocurrent response in the blue spectral region (~390–470 nm) is endowed in presence of Co-bpy electrolyte, in contrast to the I_3^-/I^- system. This is ascribed to a lower molar absorptivity of Co-bpy redox couple than that of the I_3^-/I^-. The photovoltaic performances of all the DSCs are summarized in Table **5.2**.

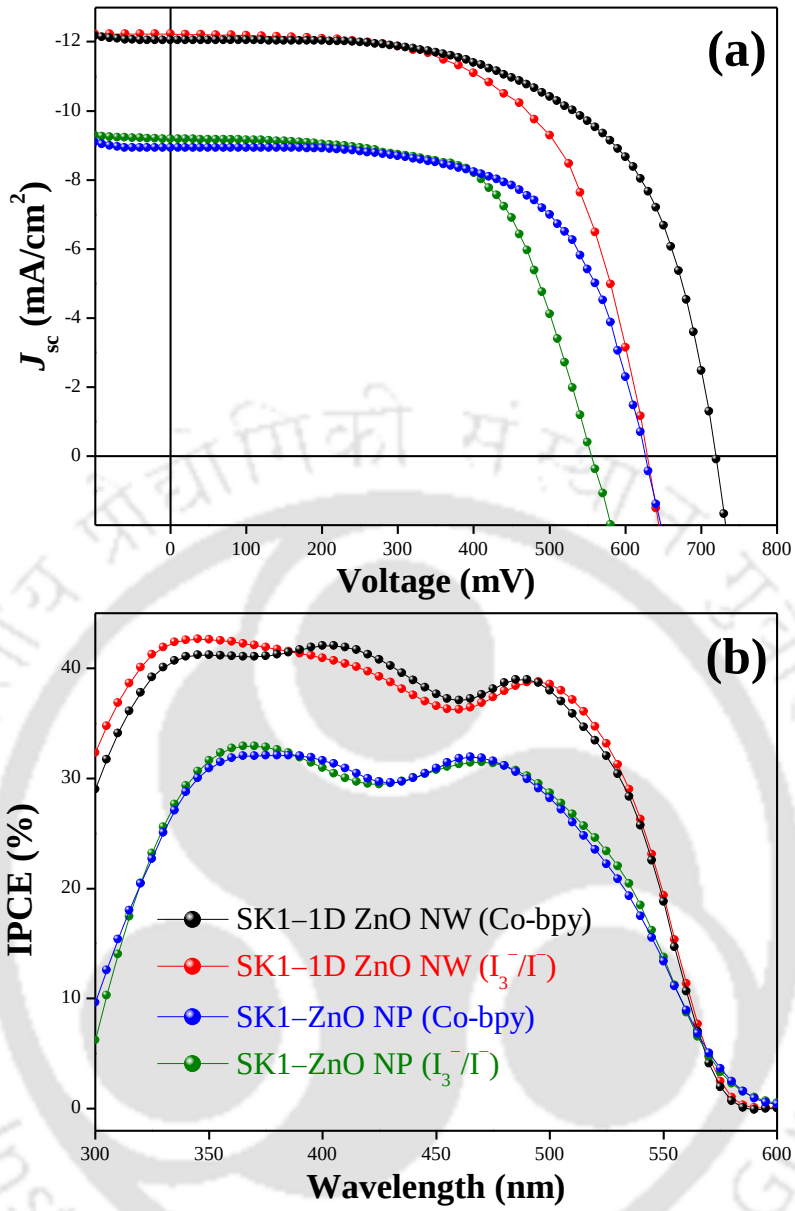

Figure 5.9 Comparison of the (a) short-circuit current density–voltage (J_{sc}–V) and (b) incident photon-to-current conversion efficiency (IPCE) plots for the fabricated dye-sensitized solar cells based on SK1–1D ZnO NW photoanodes employing I_3^-/I^- (black line) and Co-bpy (red line) and SK1–ZnO NP photoanodes employing I_3^-/I^- (blue line) and Co-bpy (green line) redox couples as the electrolytes.

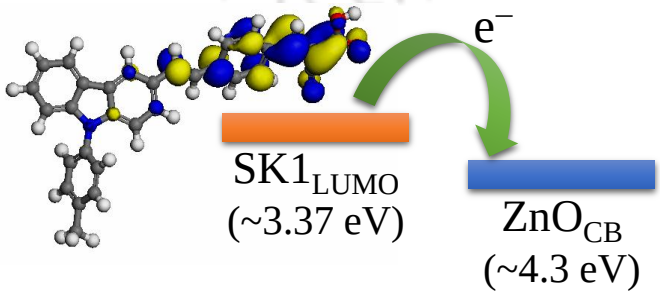

Figure 5.10 Schematic showing the pathway for the photoexcited charge transfer from the lowest-unoccupied molecular orbital (LUMO) of SK1 dye to the conduction band (CB) of ZnO.

Table 5.2 Short-circuit photocurrent density (J_{sc}), open-circuit voltage (V_{oc}), fill factor (*FF*), power conversion efficiency (η), maximum incident photon-to-current conversion efficiency ($IPCE_{max}$), and photoinduced electron lifetime (τ_{el}) for the fabricated dye-sensitized solar cells employing different photoanodes and redox electrolytes.[a]

Photoanode of the DSCs	Redox electrolyte	J_{sc} (mA/cm^2)	V_{oc} (mV)	*FF* (%)	η (%)	$IPCE_{max}$ (%)	τ_{el} (ms)
SK1–1D ZnO NW	Co-bpy	12.04 (11.99±0.3)	719 (701±26)	64.6 (63.8±1.7)	5.7 (5.1±0.9)	60	23.4
SK1–1D ZnO NW	I_3^-/I^-	12.22 (12.19±0.4)	629 (611±17)	61.2 (58.6±1.2)	4.7 (4.01±0.5)	62	22.3
SK1–ZnO NP	Co-bpy	8.93 (8.87±0.7)	626 (613±13)	63.7 (62.9±1.1)	3.6 (2.9±0.2)	47	15.4
SK1–ZnO NP	I_3^-/I^-	9.19 (9.11±0.5)	555 (524±36)	61.7 (60.9±0.9)	3.2 (3.4±0.4)	48	13.7

[a]Data reported are the results of the best performed devices out of 5 devices for each configuration. The average values and standard deviations for all the parameters evaluated for 5 device configurations are given in parentheses.

5.3.8. Chemisorption, BET Surface Area, and FTIR Analysis

An increment in the J_{sc} values from ~8.93–9.19 mA/cm^2 to ~12.04–12.22 mA/cm^2 for the DSCs has been observed (Table **5.2**) upon changing the morphology of the photoanodes from ZnO NPs to 1D ZnO NWs. To investigate the effect of ZnO architectures on the J_{sc} values, the amounts of SK1 dye chemisorbed onto the ZnO (NW *vs.* NP) surface are estimated using the dye-desorption experiments carried out in 0.1 mM NaOH solution in ethanol/water (1:1, v/v). The amounts of chemisorbed dyes onto the photoanodes are found to be ~1.93×10^{-7} mol.cm^{-2} for SK1–ZnO NP and ~1.37×10^{-7} mol.cm^{-2} for SK1–1D ZnO NW. The dye-desorption process shows slightly higher loading of SK1 dye in the case of ZnO NPs in contrast to 1D ZnO NWs, which is further ascribed to a relatively low BET surface area of 1D ZnO NW based photoanode (~19.3 m^2.g^{-1}) as compared to that for ZnO NP (~26.9 m^2.g^{-1}). Even if a higher BET surface area of ZnO NPs intercepts a better dye loading capability of the ZnO NP-based devices, a faster electron transport pathway provided by 1D ZnO NWs predominates the device performances. The chemisorption of SK1 dye onto ZnO surface are also confirmed by the FTIR spectra of plain SK1, SK1–ZnO NP, and SK1–1D ZnO NW against a blank FTO as the reference (Figure **5.11**). The SK1 dye shows the characteristic IR stretching bands at ~1787 cm^{-1} ($\nu_{C=O}$) and ~1597 cm^{-1} (ν_{C-O}) for the −COOH group, which are also observed for the SK1–1D ZnO NW (at ~1792 cm^{-1}, ~1599 cm^{-1}) and SK1–ZnO NP (at ~1794 cm^{-1}, ~1602 cm^{-1}). A slight shift in IR stretching frequencies for SK1 upon anchoring onto ZnO surface confirms the chemisorption of SK1 dye over ZnO.

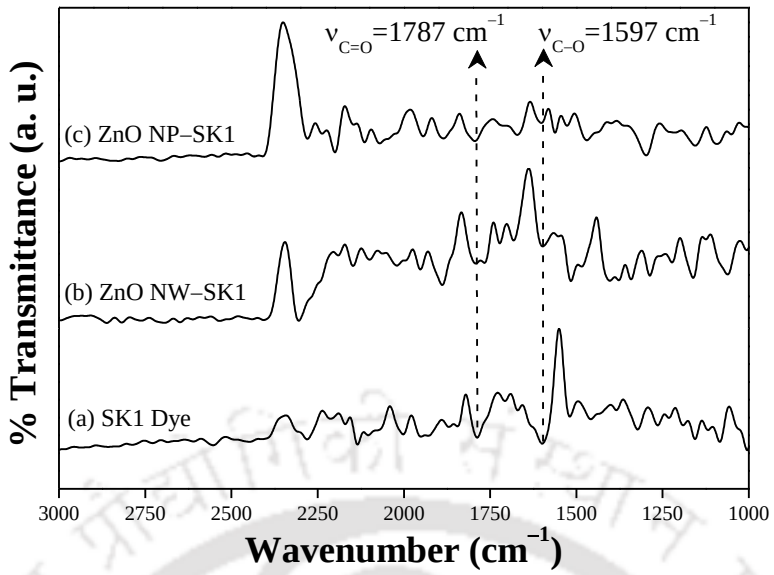

Figure 5.11 FTIR spectra of (a) SK1 dye, (b) SK1-sensitized one-dimensional ZnO nanowire (SK1–1D ZnO NW), and (c) SK1-sensitized ZnO nanoparticle (SK1–ZnO NP) films on FTO substrates.

5.3.9. Electrochemical Impedance Spectroscopy Analysis

To investigate the charge transfer and recombination processes occurring in the fabricated DSCs, electrochemical impedance spectroscopy (EIS) analysis of the cells are performed under the dark conditions at an applied bias equivalent to the V_{oc} and a frequency range of 10^{-1}–10^{5} Hz. As can be seen from Figure **5.12a**, Nyquist plots for both NW- and NP-based DSCs are composed of two semicircles. The right semicircle in the medium-frequency region appears due to the charge-transfer processes taking place at the ZnO/SK1 dye/electrolyte interface, and the left semicircle in the high-frequency region is ascribed to the redox reaction occurring at the Pt/electrolyte interface. Notably, 1D ZnO NW-based DSCs have shown a larger radius of the right semicircle in contrast to the ZnO NP-based DSCs. It indicates a prolonged electron lifetime or an enhanced charge recombination resistance in the case of NW-based DSCs; in other words, a longer distance is travelled by the photoexcited electrons in 1D ZnO NWs as compared to the ZnO NPs.

The analogous Bode plots (Figure **5.12b**) exhibit two distinct peaks at the mid- and high-frequency regions, indicating the presence of two diode interfaces for all the DSCs. Evidently the phase angle peak located at mid-frequency region shifts to a lower frequency value from ~10.33 Hz (Co-bpy) and ~11.61 Hz (I_3^-/I^-) for ZnO NPs to ~6.81 Hz (Co-bpy) and ~7.13 Hz (I_3^-/I^-) for ZnO NWs, respectively. Since the phase angle peak determines the electron diffusion time constant in the photoanodes, a prolonged photoinduced electron lifetime (τ_{el}) is observed for ZnO NW-based DSCs, in contrast to the NP counterparts. The value of τ_{el} can be derived from the relation, $\tau_{el} = (2\pi f_p)^{-1}$, where f_p is the maximum peak frequency in mid-frequency region.[38]

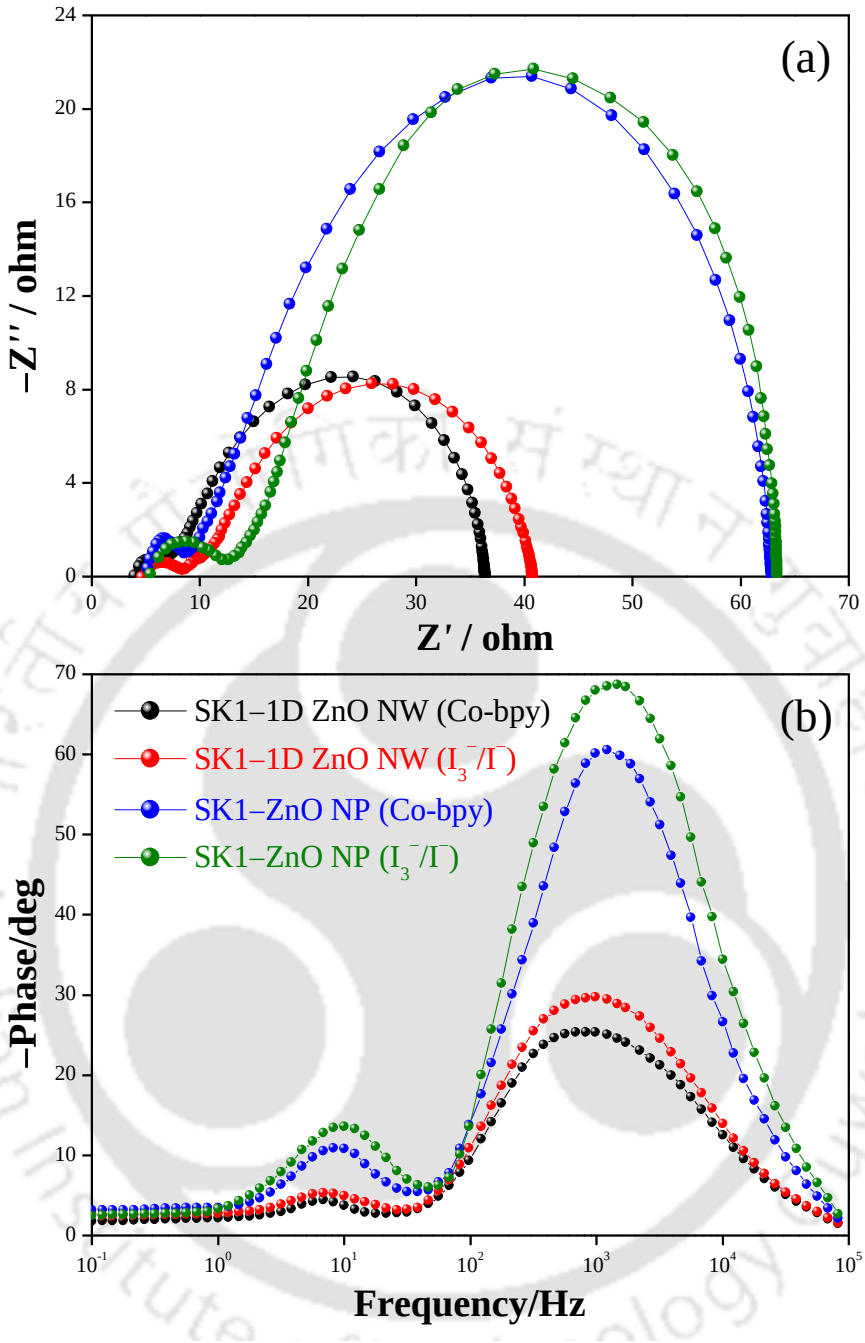

Figure 5.12 (a) Nyquist and (b) Bode phase plots for the fabricated devices composed of one-dimensional ZnO nanowire and ZnO nanoparticle based photoanodes employing Co-bpy and I_3^-/I^- redox couples as the electrolytes, under the dark conditions at open-circuit voltage and in a frequency range of 10^{-1}–10^5 Hz.

In essence, EIS analysis revealed a higher τ_{el} values of ~23.4 ms (Co-bpy) and ~22.3 ms (I_3^-/I^-) for the ZnO NW based DSCs as compared to ~15.4 ms (Co-bpy) and ~13.7 ms (I_3^-/I^-) for their ZnO NP counterparts (Table **5.2**). It also reduces the probability of electron–hole recombination in the DSCs composed of ZnO NWs. Thus, the prolonged τ_{el} values for ZnO NW based DSCs are also resembled to their higher V_{oc} values in contrast to that of the ZnO NP counterparts.

5.4. SUMMARY

- A metal-free, D–π–A-type carbazole derivative (SK1) has been synthesized and applied as a sensitizer for the hydrothermally grown 1D ZnO nanowire and ZnO nanoparticle based dye-sensitized solar cells.
- The persuasive role of ZnO nanowire based photoanodes, providing an efficient and fast charge transport through 1D pathway to enhance the device efficiency is established from the deprived performance of the devices with ZnO nanoparticle counterparts.
- Electronic interactions between SK1 and ZnO inducing the photoexcited charge transfer from the LUMO of SK1 to the conduction band of ZnO are evidenced by the quenching of photoluminescence and reduced exciton lifetime of SK1 upon anchoring onto ZnO.
- The electronic distributions of SK1 dye molecule are computed from DFT probing its D−π−A mediated intramolecular charge transfer from the carbazole (donor) to the cyanoacrylic (acceptor) moiety *via* an oligo-phenylenevinylene (π-linker) group.
- Electrochemical impedance spectroscopy revealed a prolonged electron lifetime in the 1D ZnO NW-based photoanodes as compared to the case of ZnO nanoparticles.

5.5. REFERENCES

1. Hagfeldt, A.; Boschloo, G.; Sun, L.; Kloo, L.; Pettersson, H. *Chem. Rev.* **2010**, *110*, 6595–6663.
2. Balasingam, S. K.; Kang, M. G.; Jun, Y. *Chem. Commun.* **2013**, *49*, 11457–11475.
3. Mishra, A.; Fischer, M. K. R.; Buerle, P. *Angew. Chem. Int. Ed.* **2009**, *48*, 2474–2499.
4. Yella, A.; Humphrey-Baker, R.; Curchod, B. F. E.; Ashari-Astani, N.; Teuscher, J.; Polander, L. E.; Mathew, S.; Moser, J. -E.; Tavernelli, I.; Rothlisberger, U.; Grätzel, M.; Nazeeruddin, M. K.; Frey, J. *Chem. Mater.* **2013**, *25*, 2733–2739.
5. Ito, S.; Miura, H.; Uchida, S.; Takata, M.; Sumioka, K.; Liska, P.; Comte, P.; Péchyb, P.; Grätzel, M. *Chem. Commun.* **2008**, 5194–5196.
6. Xianga, W.; Huangb, W.; Bachbcd, U.; Spiccia, L. *Chem. Commun.* **2013**, *49*, 8997–8999.
7. Guo, K.; Yan, K.; Lu, X.; Qiu, Y.; Liu, Z.; Sun, J.; Yan, F.; Guo, W.; Yang, S. *Org. Lett.* **2012**, *14*, 2214–2217.
8. Wang, Z.- S.; Cui, Y.; Dan-oh, Y.; Kasada, C.; Shinpo, A.; Hara, K. *J. Phys. Chem. C* **2008**, *112*, 17011–17017.
9. Li, S.-G.; Jiang, K.-J.; Huang, J.-H.; Yang, L.-M.; Song, Y.-L. *Chem. Commun.* **2014**, *50*, 4309–4311.
10. Hwang, S.; Lee, J. H.; Park, C.; Lee, H.; Kim, C.; Park, C.; Lee, M.-H.; Lee, W.; Park, J.; Kim, K.; Park, N.-G.; Kim, C. *Chem. Commun.* **2007**, 4887–4889.
11. Teng, C.; Yang, X.; Yuan, C.; Li, C.; Chen, R.; Tian, H.; Li, S.; Hagfeldt, A.; Sun, L. *Org. Lett.* **2009**, *11*, 5542–5545.
12. De Sousa, S.; Olivier, C.; Ducasse, L.; Le Bourdon, G.; Hirsch, L.; Toupance, T. *ChemSusChem* **2013**, *6*, 993–996.
13. Teng, C.; Yang, X.; Li, S.; Cheng, M.; Hagfeldt, A.; Wu, L.; Sun, L. *Chem.—Eur. J.* **2010**, *16*, 13127–13138.
14. Feldt, S. M.; Gibson, E. A.; Gabrielsson, E.; Sun, L.; Boschloo, G.; Hagfeldt, A. *J. Am. Chem. Soc.* **2010**, *132*, 16714–16724.
15. Bai, Y.; Zhang, J.; Zhou, D.; Wang, Y.; Zhang, M.; Wang, P. *J. Am. Chem. Soc.* **2011**, *133*, 11442–11445.
16. Tsao, H. N.; Yi, C.; Moehl, T.; Yum, J.-H.; Zakeeruddin, S. M.; Nazeeruddin, M. K.; Grätzel, M. *ChemSusChem* **2011**, *4*, 591–594.
17. Zhou, D.; Yu, Q.; Cai, N.; Bai, Y.; Wang, Y.; Wang. P. *Energy Environ. Sci.* **2011**, *4*, 2030–2034.
18. Kashif, M. K.; Nippe, M.; Duffy, N. W.; Forsyth, C. M.; Chang, C. J.; Long, J. R.; Spiccia, L.; Bach, U. *Angew. Chem. Int. Ed.* **2013**, *52*, 5527–5531.
19. Anta, J. A.; Guillén, E.; Tena-Zaera, R. *J. Phys. Chem. C* **2012**, *116*, 11413–11425.
20. Li, L.; Zhai, T.; Bando, Y.; Golberg, D. *Nano Energy* **2012**, *1*, 91–106.
21. Zhang, Q.; Cao, G. *Nano Today* **2011**, *6*, 91–109.

22. Chetia, T. R.; Barpuzary, D.; Qureshi, M. *Phys. Chem. Chem. Phys.* **2014**, *16*, 9625–9633.
23. Ren, S.; Zhao, N.; Crawford, S. C.; Tambe, M.; Bulović, V.; Gradečak, S. *Nano Lett.* **2010**, *11*, 408–413.
24. Ren, S.; Chang, L.-Y.; Lim, S.-K.; Zhao, J.; Smith, M.; Zhao, N.; Bulović, V.; Bawendi, M. G.; Gradečak, S. *Nano Lett.* **2011**, *11*, 3998–4002.
25. Sun, B.; Hao, Y.; Guo, F.; Cao, Y.; Zhang, Y.; Li, Y.; Xu, D. *J. Phys. Chem. C* **2012**, *116*, 1395−1400.
26. Liu, Y.; Jennings, J. R.; Huang, Y.; Wang, Q.; Zakeeruddin, S. M.; Grätzel, M. *J. Phys. Chem. C* **2011**, *115*, 18847−18855.
27. Park, H.; Chang, S.; Jean, J.; Cheng, J. J.; Araujo, P. T.; Wang, M.; Bawendi, M. G.; Dresselhaus, M. S.; Bulović, V.; Kong, J.; Gradečak, S. *Nano Lett.* **2013**, *13*, 233–239.
28. Liu, B.; Zeng, C. *J. Am. Chem. Soc.* **2003**, *125*, 4430−4431.
29. Barpuzary, D.; Khan, Z.; Vinothkumar, N.; De, M.; Qureshi, M. *J. Phys. Chem. C* **2012**, *116*, 150–156.
30. Chou, T. P.; Zhang, Q.; Cao, C. *J. Phys. Chem. C* **2007**, *111*, 18804–18811.
31. Fan, K.; Liu, M.; Peng, T.; Maa, L.; Dai, K. *Renewable Energy* **2010**, *35*, 555–561.
32. Vayssieres, L. *Adv. Mater.* **2003**, *15*, 464–466.
33. Chung, J.; Myoung, J.; Oh, J.; Lim, S. *J. Phys. Chem. C* **2010**, *114*, 21360–21365.
34. Zhan, X.; Wang, Q.; Wang, F.; Wang, Y.; Wang, Z.; Cao, J.; Safdar, M.; He, J. *ACS Appl. Mater. Interfaces* **2014**, *6*, 2878–2883.
35. Jeong, S.; Choe, M.; Kang, J.-W.; Kim, M. W.; Jung, W. G.; Leem, Y.-C.; Chun, J.; Kim, B.-J.; Park, S.-J. *ACS Appl. Mater. Interfaces* **2012**, *4*, 17–23.
36. Kongkanand, A.; Tvrdy, K.; Takechi, K.; Kuno, M.; Kamat, P. V. *J. Am. Chem. Soc.* **2008**, *130*, 4007–4015.
37. Popere, B. C.; Pelle, A. M. D.; Thayumanavan, S. *Macromolecules* **2011**, *44*, 4767−4776.
38. Peng, W.; Han, L.; Wang, Z. *Chem.—Eur. J.* **2014**, *20*, 8483–8487.

Chapter 6

MoS_2 Loaded Cu_2ZnSnS_4 as a Noble Metal Free Counter Electrode for $CuInS_2$–CdSe Quantum Dot Co-Sensitized Solar Cell

This chapter describes the utilization of MoS_2 loaded Cu_2ZnSnS_4 microspheres as an effective counter electrode for $CuInS_2$–CdSe quantum dot co-sensitized solar cells constructed with single crystalline ZnO nanowires. An ex-situ electrophoretic deposition of the quantum dot sensitizers onto ZnO nanowires has been established. The promising role of MoS_2 nanosheets acting as an electrical linker that interconnects the Cu_2ZnSnS_4 microspheres to improve charge transport and catalytic activity of the counter electrode are being demonstrated.

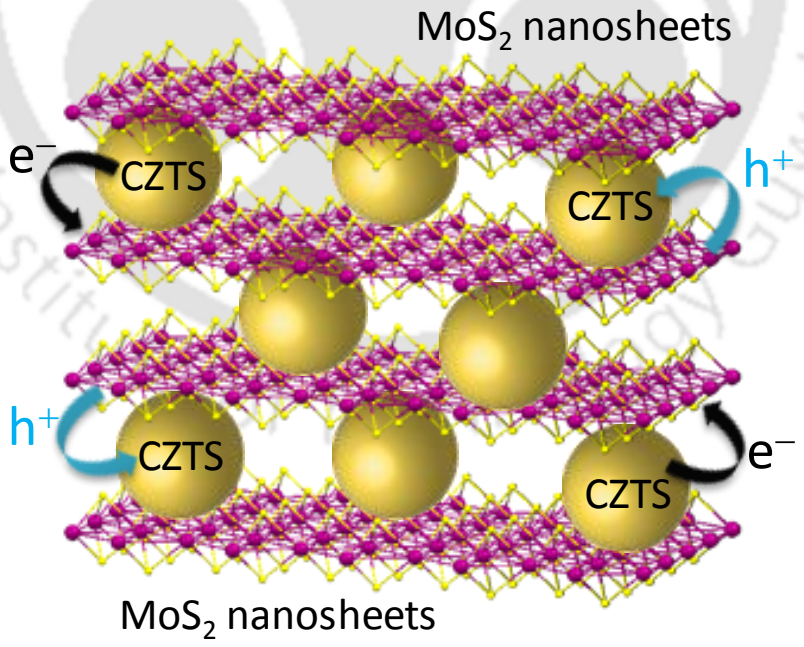

Journal of Materials Chemistry A D. Barpuzary *et al.* **2015**, 3, 14378–14388

6.1. INTRODUCTION

Quantum dot-sensitized solar cells (QDSCs) have attracted significant attention due to their involvement of quantum dots (QDs) ensuring fascinating advantages like size-controlled band gap tunability, enhanced light absorption, viable multiple exciton generation, feasibility to extract hot charge carriers, etc.[1–4] The basic design of a QDSC—a prototype of dye-sensitized solar cell (DSC)—contains a nanostructured semiconductor oxide material sensitized with QDs that generate electrons upon photon absorption and inject them into the semiconductor, a redox couple as the electrolyte, and a counter electrode (CE). In QDSCs, a number of QDs (CdS, CdSe, $CuInS_2$, $CuInSe_2$, Sb_2S_3, CdTe, PbS)[11–18] or combination of QDs[19,20] have been tested to adapt an efficient solar harvesting to afford several milestones in power conversion efficiency (PCE).[21–24] In addition to QDs, selection of a pertinent wide-band gap oxide material is equally credible to boost the efficiency of a solar cell. Since the discovery of DSCs,[25] mesoscopic TiO_2 films have been used as an excellent electron collector material. However, the enormously high surface area of TiO_2 matrices tends to clog the mesopores upon QD loading, which hinders the free-charge injection, carrier transport, diffusion of the electrolyte, and adequate loading of QDs into the interior of oxide films in QDSCs.[26] To avoid such glitches, one-dimensional (1D) morphology—nanorods, nanowires (NWs), nanotubes—based QD scaffolds were later on developed.[27] The use of such 1D structures is advantageous as they possess a single or quasi-single crystalline geometry, which facilitates a unidirectional pathway for facile charge transport, an increased electron diffusion length, and reduced grain-boundary scattering. In view of this, recent advancements of ZnO based architectures have paved a way to improve the charge transportation and QD loading in QDSCs, achieving high PCEs.[28,29] In essence, a superior electron mobility (ZnO ≈ 200–1000 $cm^2\ V\ s^{-1}$, TiO_2 ≈ 0.1–4 $cm^2\ V\ s^{-1}$), band offsets similar to that of TiO_2, higher crystallinity, fewer grain boundaries, and readily tunable morphologies with benchtop synthetic routes make ZnO a prime alternative to traditional TiO_2.[30] Earlier results from our group have also established the capitalization of stable morphologies of ZnO to exhibit faster charge transportability, smooth diffusion of electrolyte, and a retarded rate of charge recombination in solar cells.[31–34] Especially, epitaxially grown 1D ZnO NW based devices revealed an additional benefit of direct 1D electrical pathways promoting the transport and rapid collection of charge carriers injected from the sensitizers.

Another factor that influences the performance of a QDSC is loading of QDs onto mesoscopic oxide films. Targeting a few rudiments like high surface coverage and uniform

distribution of QDs, multiple *in situ* or *ex situ* strategies are often applied to deposit QDs onto oxide films with effective anchoring (Scheme **6.1**).[35–37] Despite they hold their own merits and demerits,[38] the selection of a specific technique or a combination of techniques to be used to load QDs depends on the physical nature, stability, and mode of anchoring of the QDs onto the oxide surface. Notably, electrophoretic deposition (EPD)—that drives ligand-capped and charged QDs (pre-synthesized) onto oxide based electrodes under an applied bias—technically sounds to be a promising ex situ approach.[39,40] This is credible to the typical advantages of EPD like a robust and uniformly distributed coverage of QDs in a short time span, effective anchoring of QDs onto oxide surface, rapid penetration of QDs up to the interior pores of oxide films, etc. Besides, EPD makes sequential loading of multiple QDs possible, allowing an efficient photon capturing tunability of the photoanodes to extend the spectral absorption window up to infrared regime.[24]

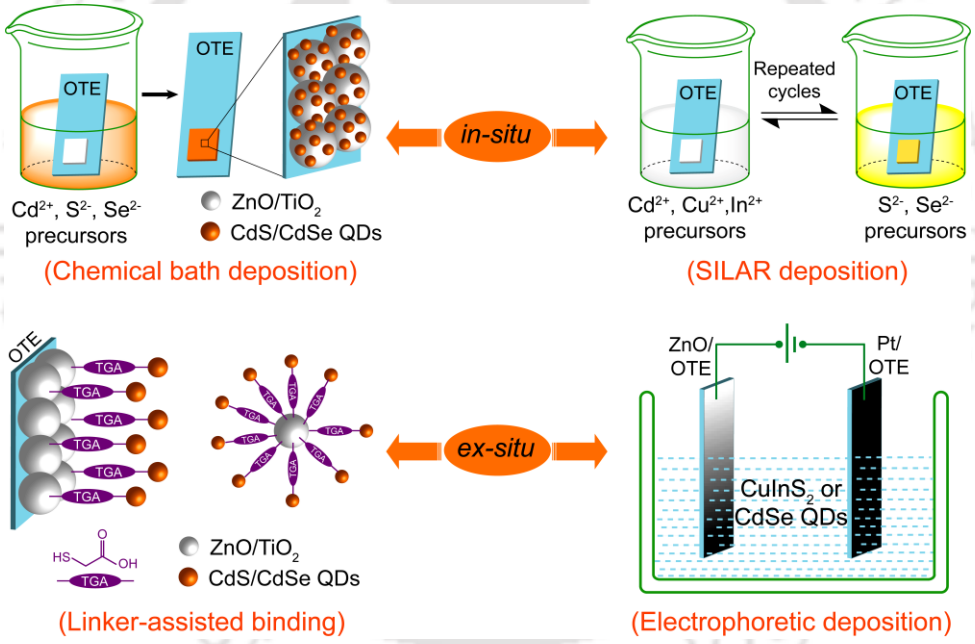

Scheme 6.1 Basic steps involved in commonly used *in-situ* and *ex-situ* methods for the deposition of quantum dots onto oxide materials. *In-situ* approach: Chemical Bath Deposition (CBD) and Successive Ionic-Layer Adsorption and Reaction (SILAR). *Ex-situ* approach: Linker-Assisted Binding and Electrophoretic Deposition (EPD).

On top of the oxide scaffolds and QD absorbers, the prime constituent of a QDSC is CE (mostly Pt). CEs account for the collection of electrons from the external circuit to electrolyte thereby triggering catalytic reduction of the redox couple. The electrolyte system is in turn responsible for the regeneration of oxidized photosensitizers. In general, iodide/triiodide (I_3^-/I^-), sulfide/polysulfide (S^{2-}/S_n^{2-}), and $Co^{2+/3+}$ complex based redox couple containing electrolytes are

used in solar cells depending on the aptness of their redox potentials with the valence band (VB) potential of sensitizer and work function of CE material. In view of this, taking into account an increasing demand, high-cost, high PCE, and industrialization of photovoltaic technology, the scientific quest to replace Pt with a low-cost CE material has explored a number of carbon materials, transition metal compounds (carbide, oxide, sulfide, nitride), conducting polymers or hybrids, and a class of inorganic chalcogenides due to their excellent properties such as electrical conductivity, chemical stability, and (electro)catalytic activity.[41] Even if the photovoltaic performance of most of these Pt-free CEs is explored in DSCs employing an I_3^-/I^- redox couple, an inevitable photodegradation of a majority of QD absorbers (if comes in direct contact with I_3^-/I^-) jeopardizes the stability and efficiency of QDSCs.[42] Consequently, an aqueous electrolyte, S^{2-}/S_n^{2-}, favoring an attenuated photocorrosion of QDs is often used in QDSCs.[43] However, using of Pt as a CE in the presence of S^{2-}/S_n^{2-} couple limits the efficiency of QDSCs due to the chemisorption of S-compounds onto Pt surface. Such a catalytic poisoning not only deteriorates the conductivity and electrocatalytic activity of Pt CE, but also increases the charge transfer resistance at the Pt/electrolyte interface.[44] To overcome such issues, recently CEs such as Cu_2ZnSnS_4 (CZTS) have been utilized wherein apart from resolving catalytic poisoning issues, the CE is more eco-friendly as well as economical due to the presence of earth-abundant elements; Cu, Sn, and Zn.[45–47] Even if the intrinsic peculiarities like a direct band gap (~1.5 eV) and a high absorption coefficient (>1 × 10^4 cm^{-1}) make CZTS an excellent absorber material, its excelling role as a CE is explored less for solar cells, especially in QDSCs.[48] It is worth noting that the modification/change in elemental composition of CZTS based CEs has been studied for solar cells achieving promising PCEs up to ~5.2–7.4%.[48–51] However, to the best of our knowledge, any co-catalyst loaded CZTS as a CE for solar cells has not been reported yet.

Based on the current understanding, herein we report for the first time, the utilization of a MoS_2 loaded CZTS based novel CE for an efficient QDSC containing ZnO NWs as a sensitizer scaffold, $CuInS_2$ and CdSe QDs photosensitizers, and a S^{2-}/S_n^{2-} redox couple as the electrolyte. Notably, CZTS–MoS_2 CE based QDSCs exhibit superior performances in contrast to bare CZTS counterparts. MoS_2 in its nanosheet form acts as an electrical linker that interconnects the CZTS microspheres favoring effective charge transport in the CE of the devices. We believe that the concept of MoS_2 loading onto CZTS might also allow us to get rid of the typical Mo back contact issues often encountered in CZTS based solar cells.[52,53] Our present work has established a maximum PCE of ~4.6% for QDSCs that can be ascribed to several factors: (1) involvement of

epitaxially grown ZnO NWs offering inherently faster transport and collection of charge carriers, (2) broad-visible range photon absorption achieved by a combination of $CuInS_2$ ($E_g \approx 1.5$ eV) and CdSe ($E_g \approx 1.7$ eV) QDs, (3) efficient QD loading attained by EPD route, and (4) effective electronic interactions between CZTS and MoS_2 achieved by a hydrothermal route. In addition, favorable band alignments among different components of the photoanode and CE (Scheme **6.2**) facilitate the charge transfer in the circuit in an efficient way.

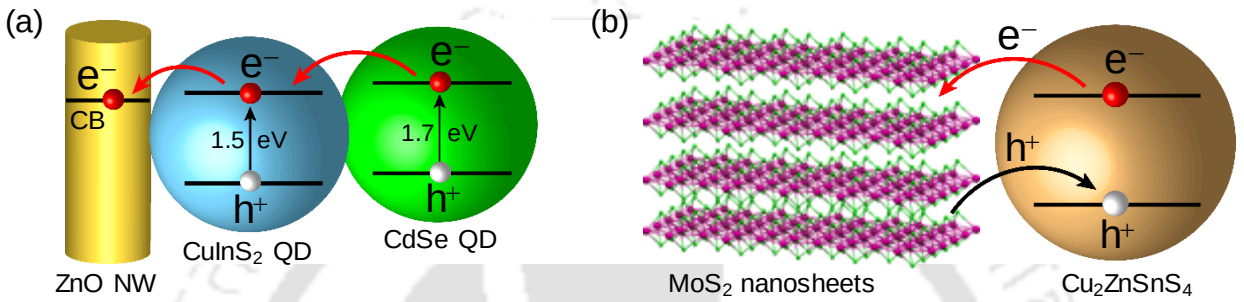

Scheme 6.2 Schematic showing the favorable band alignment mediated charge transfer processes occurring within various materials involved in the (a) photoanode: ZnO, $CuInS_2$, and CdSe (b) counter electrode: CZTS and MoS_2.

6.2. EXPERIMENTAL SECTION

6.2.1. Epitaxial Growth of One-dimensional ZnO Nanowires

Epitaxial growth of one-dimensional ZnO NWs onto ZnO seed layered FTO coated glass substrates were carried out using a simple hydrothermal route as discussed earlier in Chapter **4** Section **4.2.6**. Typically, ZnO seed layer was spin coated onto pre-cleaned FTO substrates and the hydrothermal growth of 1D ZnO NWs was completed at 90 °C within a period of 2 h using a 0.5 M $Zn(NO_3)_2.6H_2O$ and 0.5 M hexamine aqueous solution.[31,32,54]

6.2.2. Synthesis of $CuInS_2$ Quantum Dots

$CuInS_2$ QDs were synthesized following a reported protocol.[40,55] Typically, indium(III) chloride (0.226 g, 1 mmol) and copper(I) iodide (0.190 g, 1 mmol) were added to 1-dodecanethiol (5 mL) in a two-necked round bottom flask. An inert atmosphere was created by degassing under high-vacuum and then purged with Ar. Degasing and purging processes were repeated for twice. The reaction mixture was heated to 100 °C till a clear yellow coloration appeared and the temperature was then slowly raised to 180 °C. The reaction was monitored until the color of reaction mixture was changed from yellow to orange and finally to dark red, which is indicative of the nucleation and growth of $CuInS_2$ crystals. Any further crystal growth of $CuInS_2$ was arrested by instantly

reducing the temperature of the reaction to ~40–45 °C using a water bath. The reaction mixture was poured into chloroform and excess methanol was added to precipitate the QDs, which were collected by centrifugation (10,000 rpm). The washing with chloroform–methanol was repeated further for three times to eliminate the excess of 1-dodecanthiol. As-prepared $CuInS_2$ QDs were finally dispersed in chloroform and stored inside the glove box for further use.[26]

6.2.3. Synthesis of Cu_2ZnSnS_4 (CZTS) microspheres

A hydrothermal route was applied to synthesize the CZTS microspheres.[56] Typically, copper acetate monohydrate (0.472 g, 0.04 M), zinc nitrate hexahydrate (0.356 g, 0.02 M), and stannous chloride dihydrate (0.268 g, 0.02 M) were dissolved in a 15 mL ethylenediamine/water (1:9, v/v) mixture, where ethylenediamine performs the role of a chelating agent and a stabilizer. A 0.16 M thiourea aqueous solution (30 mL) was then added (drop wise) to the above solution. The system was degased under high-vacuum for 30 min to remove oxygen and then purged with Ar. The reaction mixture was further purged (bubbling) with Ar for 1 h to remove the dissolved oxygen. The reaction mixture was transferred into a Teflon vessel (100 mL capacity) and sealed inside a stainless steel autoclave, and heated at 180 ºC in an electronic oven for 24 h. In the hydrothermal process, CZTS is formed by the reduction of Cu^{2+} ions to Cu^{+} and oxidation of Sn^{2+} ions to Sn^{4+} *via* oxidation–reduction reactions due to the strong reducing nature of $SnCl_2$. The autoclave was cooled to room temperature and the solid was separated by centrifugation at 5000 rpm, washed three times with each of distilled water and ethanol. The powder form of CZTS was finally obtained by drying the sample overnight at 50 ºC in an electronic oven. Yield: 51 %.

6.2.4. Synthesis of MoS_2 Co-catalyst

Synthesis of MoS_2 co-catalyst was carried out using a reported hydrothermal route with slight modifications.[57] For the same, ammonium heptamolybdate (0.736 g, 0.63 mmol) and excess of thiourea (1.2 g, 15.7 mmol) were dissolved in distilled water (80 mL) in a Teflon vessel. Hexadecyl-trimethyl-ammonium bromide (CTAB; 0.096 g, 0.26 mmol) was then added as a surfactant to the above solution and stirred further for 30 min. The Teflon vessel was sealed inside a stainless steel autoclave and maintained at 200 ºC in an electronic oven for 24 h. The autoclave was cooled to room temperature. The black solid product obtained was separated by centrifugation (5000 rpm), followed by repeated washing with each of distilled water and ethanol for three times to remove the inorganic impurities. Finally, the sample was dried at 50 °C for 8 h in an electronic oven to obtain the MoS_2 co-catalyst in powder form. Yield: 62 %.

6.2.5. Loading of 1.0 wt % of MoS_2 to CZTS

The loading of 1.0 wt % of MoS_2 to CZTS was carried out hydrothermally by modifying the synthesis procedure for CZTS. For the typical synthesis, a precursor solution (80 mL) of CZTS was prepared in a Teflon vessel, degased and purged with Ar to remove the dissolved oxygen, and a calculated amount (with respect to CZTS yield) of presynthesized MoS_2 co-catalyst was added. The reaction mixture was sonicated for ~3 h under Ar atmosphere to get a homogeneous distribution of the CZTS precursor solution and MoS_2. The Teflon vessel was sealed inside a stainless steel autoclave, heated at 180 ºC in an electronic oven for 24 h, and cooled to room temperature. The black solid product was collected by centrifugation and repeatedly washed for three times with each of distilled water and ethanol. CZTS–MoS_2 was finally obtained in powder form by drying the sample overnight at 50 °C in an electronic oven. Yield: 58%.

6.2.6. Fabrication of ZnO–$CuInS_2$ Photoanode

The fabrication of ZnO–$CuInS_2$ photoanode was performed by an EPD method using a readily dispersed solution of $CuInS_2$ QDs in chloroform.[40] To deposit the QDs, a ZnO NW grown FTO substrate (ZnO/FTO) and a platinized FTO (Pt/FTO) were vertically fixed at a parallel distance of ~0.5 cm inside a glass cell as shown in Scheme **6.1**. To prepare Pt/FTO electrodes, a solution of hexachloroplatinic acid in *iso*-propanol was spin coated on cleaned, ozonized FTO substrates, followed by calcination at 450 °C for 15 min. The ZnO/FTO and Pt/FTO electrodes were then respectively connected to the positive and negative terminals of a Keithley 2400 SourceMeter. The glass cell was filled with a dispersed solution of $CuInS_2$ QDs in chloroform and a bias voltage of 150 $V.cm^{-1}$ was applied for a couple of min to deposit the QDs. The $CuInS_2$ deposited ZnO photoanodes (hereafter, ZnO–CIS) were taken out, rinsed with ethanol, dried by blowing argon and used for device fabrication. A schematic showing the deposition of $CuInS_2$ QDs onto 1D ZnO NWs (grown on FTO substrates) by an EPD method is illustrated in Scheme **6.3**.

6.2.7. Fabrication of ZnO–CdSe Photoanode

To fabricate CdSe QD deposited ZnO NW based photoanode (hereafter, ZnO–CdSe), CdSe QDs were deposited onto ZnO/FTO using a similar EPD setup as used to fabricate ZnO–CIS. In brief, a bias current of 0.60 $mA.cm^{-1}$ was applied between ZnO/FTO and Pt/FTO electrodes for 30 min using an aqueous solution of 0.02 M cadmium acetate, 0.04 M ethylenediaminetetraacetic acid disodium salt (EDTA), and 0.02 M sodium selenosulfate (Na_2SeSO_3).[24] Na_2SeSO_3 solution was prepared by refluxing Se (0.48 g, 6.0 mmol) and sodium sulfite (2.0 g, 15.8 mmol) in water (3 h).

6.2.8. Fabrication of ZnO–$CuInS_2$–CdSe Photoanode

$CuInS_2$–CdSe QD co-sensitized ZnO NW based photoanode (hereafter, ZnO–CIS–CdSe) was fabricated using a two-step EPD method. First, ZnO–CIS photoanode was fabricated by loading $CuInS_2$ QDs onto ZnO NWs under a bias voltage of ~150 $V.cm^{-1}$, as described in Section **6.2.6**. ZnO–CIS electrode was connected to the positive terminal of the power supply and CdSe QDs were then deposited under an bias current of 0.60 $mA.cm^{-2}$ against a Pt/FTO electrode connected to the negative terminal, as described in Section **6.2.7**.

6.2.9. Fabrication of CZTS and CZTS–MoS_2 Photocathode

To fabricate the CEs, CZTS–MoS_2 and CZTS powders were separately dispersed in ethanol under an ultrasonic bath (30 min). Meanwhile, FTO coated glass substrates were cleaned with soap solution, washed with plenty of distilled water, treated under an ultrasonic bath in acetone and *iso*-propanol (15 min for each), and subjected to ozone treatment for 15 min. The dispersed solutions of CZTS and CZTS–MoS_2 were then spin coated on FTO substrates at 500–1000 rpm. The FTO substrates were finally calcined at 300 °C for 10 min under a sulfur atmosphere.

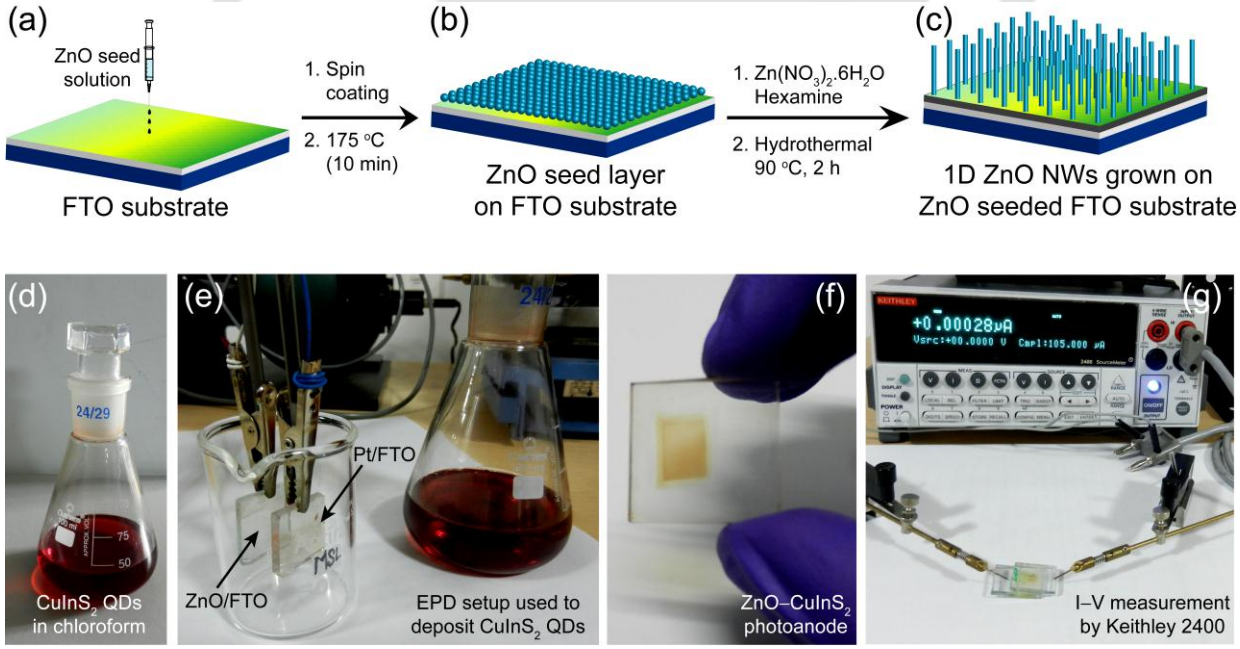

Scheme 6.3 General procedure used to fabricate a quantum dot sensitized solar cell involving ZnO nanowires and $CuInS_2$ quantum dots: (a) spin coating of ZnO seed solution on FTO coated glass substrate, followed by heating at ~175 °C for 10 min, (b) hydrothermal growth of ZnO nanowires over ZnO seed layered FTO substrate at 90 °C (2 h) using a 0.5 M zinc nitrate and 0.5 M hexamine aqueous solution, (d) $CuInS_2$ quantum dots dispersed in chloroform, (e) electrophoretic deposition (EPD) setup used to deposit $CuInS_2$ quantum dots onto ZnO nanowires by applying a bias voltage between ZnO/FTO (positive terminal) and Pt/FTO (negative terminal) electrodes, (f) $CuInS_2$ sensitized ZnO based photoanode, and (g) current–voltage measurement of the cell using a Keithley 2400 SourceMeter.

6.2.10. Device Fabrication and Characterization

The QDSCs were constructed by sandwiching the photoanodes and respective CEs using an easy-melt thermoplastic sealant (thickness ~50 µm). A drop of S^{2-}/S_n^{2-} electrolyte solution was injected to each of the cells through the pre-drilled holes on the CEs by vacuum capillary filling method. The cells were then sealed to avoid any electrolyte leakage. The S^{2-}/S_n^{2-} aqueous electrolyte solution was prepared by dissolving 1.0 M sulfur and 1.0 M sodium sulfite in water. No methanol was added to the electrolyte solution to avoid overestimation of actual PCE of the fabricated QDSCs. This often occurs due to the presence of a non-regenerative hole scavenging effect of methanol, if present in the electrolyte, producing higher photocurrents in the devices.

6.3. RESULTS AND DISCUSSIONS

6.3.1. Powder X-ray Diffraction Analysis

Phase purity of ZnO seed layer and NW films on FTO substrates and of metal chalcogenide QDs ($CuInS_2$ and CdSe) are confirmed from their respective powder XRD patterns. From Figure **6.1a**, a sharp (002) diffraction peak at $2\theta \approx 34.6°$ (excluding the diffraction peaks of FTO) is observed for ZnO seed layers spin coated on FTO substrate. This confirms a preferential *c*-axis texturing of seed layers of ZnO nanocrystals, which are obtained by thermal decomposition of zinc acetate salts.[58] Interestingly, the XRD pattern of as-grown ZnO NWs (Figure **6.1b**) over ZnO seed layer also exhibit a sharp (002) diffraction peak at $2\theta \approx 34.6°$, similar to that of ZnO seed layers.

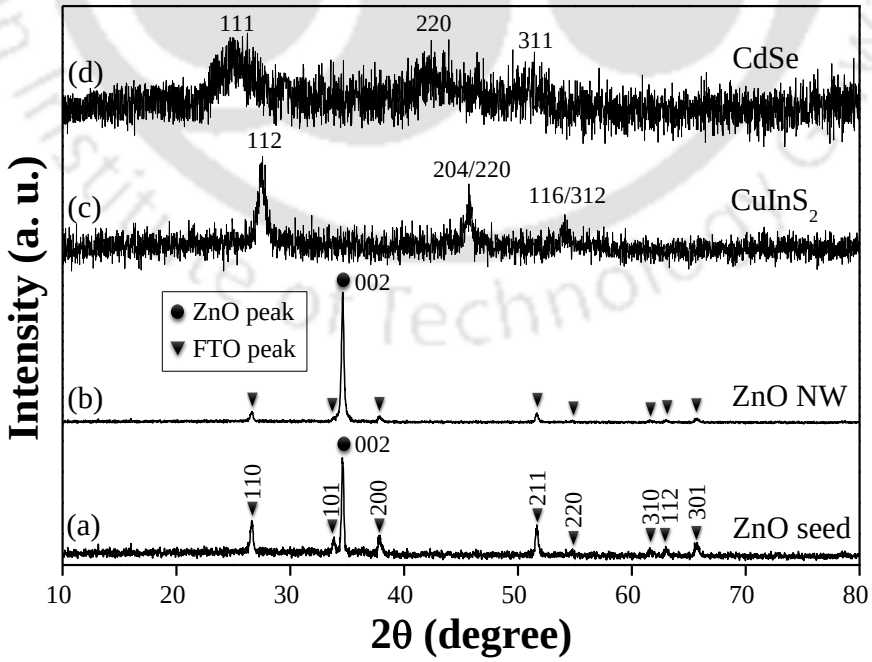

Figure 6.1 Powder X-ray diffraction (XRD) patterns of (a) ZnO seed layer on FTO substrate, (b) 1D ZnO nanowires epitaxially grown on ZnO seed layered FTO substrate, (c) $CuInS_2$ quantum dots, and (d) CdSe quantum dots.

The observed XRD patterns clearly indicate—(1) a similar type of crystal parameters for both ZnO seed layer and 1D NWs, and (2) an epitaxial growth of single crystalline ZnO NWs over a ZnO seeded platform in [0002] lattice orientation along the *c*-axis. The prevailing high-intensity (002) diffraction peaks for ZnO (seed layer and 1D NW) can be indexed to the formation of hexagonal wurtzite phase with a $P6_3mc$ space group symmetry (JCPDS Ref. No. #36-1451). In addition, the lattice constants calculated for both ZnO NWs (a = 0.3249 nm, c = 0.5208 nm) and ZnO seed layers (a = 0.3249 nm, c = 0.5208 nm) also exhibit exactly similar values.[58] Thus, it can be stated that pre-alignment of ZnO seed layer fully regulates the further crystal growth of 1D ZnO NWs. Epitaxial growth of ZnO NWs also intercepts their defect-free crystal growth in a preferential direction. As a result, hydrothermally grown ZnO NWs possess single crystallinity that further generates 1D pathways through their continuous crystal interiors and hence, exhibit faster charge transport properties. A weak defect emission peak at ~450–580 nm appears for 1D ZnO NWs upon photoexcitation (Figure **6.2**), which indicates the presence of weak transitions from the conduction band (CB) of ZnO to their deep defect levels created by oxygen vacancies.

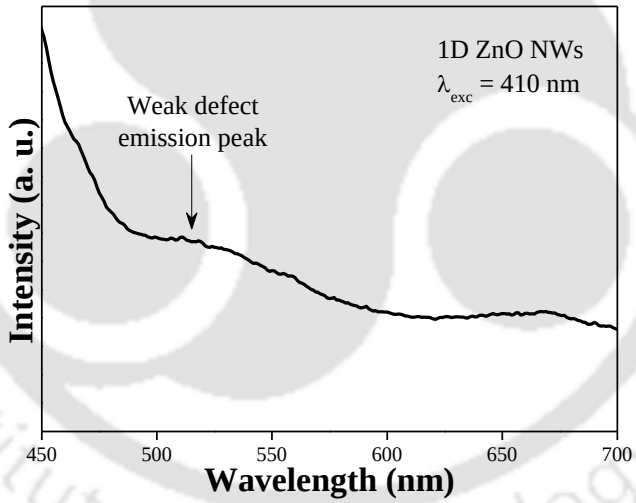

Figure 6.2 Steady state photoluminescence (PL) spectrum of hydrothermally grown 1D ZnO nanowires on FTO coated glass substrate showing the less prominent defect emission peak ~475–575 nm at a 410 nm excitation.

On the other hand, phase purity of nanocrystalline $CuInS_2$ and CdSe QDs are also confirmed by powder XRD. Figure **6.1c** shows the lattice planes (112), (204/220), and (116/312) for the as-synthesized $CuInS_2$ QDs, which are indexed to the formation of tetragonal phase (JCPDS Ref. No. #85-1575). Similarly, Figure **6.1d** shows the lattice planes (111), (220), and (311) for CdSe QDs, which are indexed to the formation of zinc blende phase of cubic crystal structured CdSe (JCPDS Ref. No. #19-0191). In addition, the appearance of broad diffraction peaks for $CuInS_2$ and CdSe QDs confirm their nano dimensions.

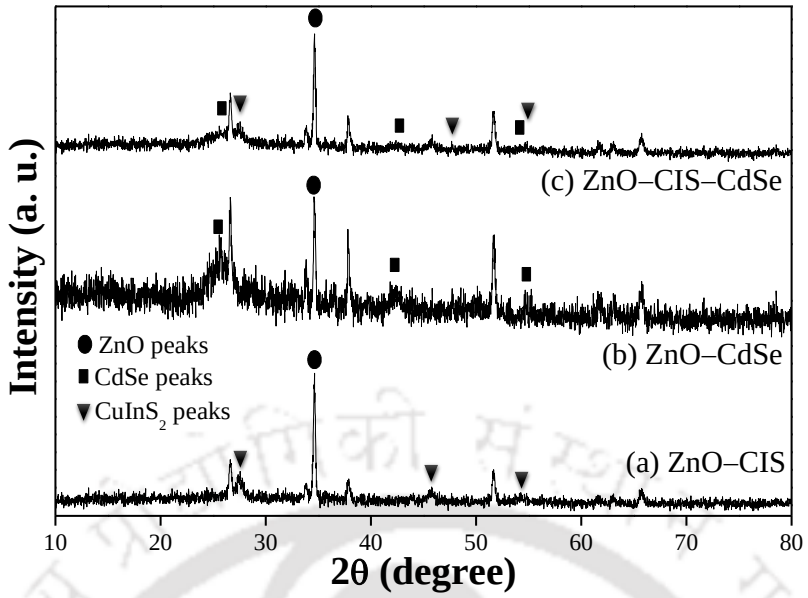

Figure 6.3 Powder X-ray diffraction (XRD) patterns of (a) ZnO–CIS, (b) ZnO–CdSe, and (c) ZnO–CIS–CdSe photoanodes showing the retention of individual peaks for ZnO (circles), $CuInS_2$ (triangles), and CdSe (squares).

Notably, well-resolved and broad diffraction peaks for $CuInS_2$ and CdSe QDs are apparent in the XRD patterns of all the photoanodes: ZnO–CIS, ZnO–CdSe, and ZnO–CIS–CdSe, as shown in Figure **6.3**. This indicates a successful loading of crystalline QDs onto ZnO using EPD route. Moreover, the strong appearance of characteristic (002) diffraction peaks in XRD patterns of all the photoanodes further indicates the retention of structure and single crystallinity of stable 1D ZnO NWs even after the deposition of QDs are performed under different bias conditions.

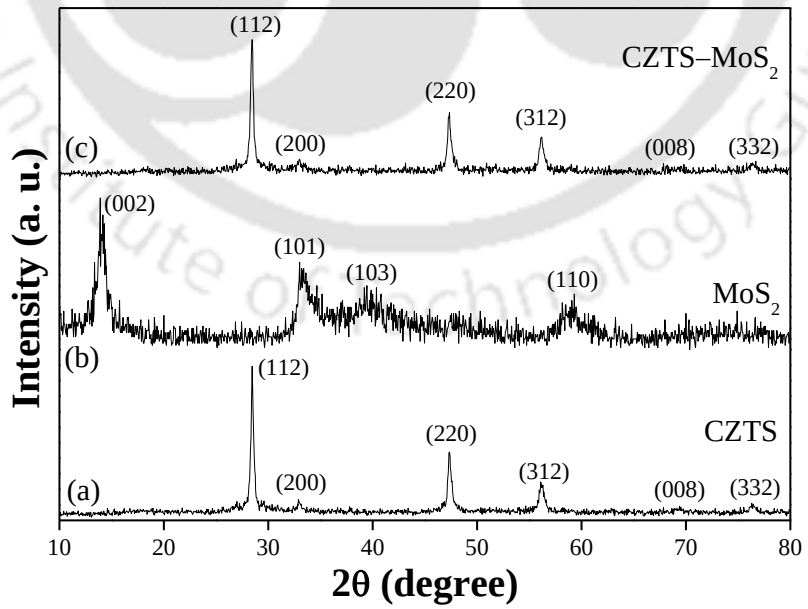

Figure 6.4 Powder X-ray diffraction (XRD) patterns of hydrothermally synthesized (a) Cu_2ZnSnS_4 microspheres (CZTS), (b) MoS_2 co-catalyst, and (c) 1.0 wt % of MoS_2 loaded Cu_2ZnSnS_4 microspheres (CZTS–MoS_2).

The crystallinity of CE materials are also confirmed using powder XRD. From Figure **6.4a**, the observed lattice planes (112), (200), (220), (312), (008), and (332) for CZTS microspheres can be indexed to the formation of tetragonal kesterite crystalline phase (JCPDS Ref. No. #26-0575). No diffraction peaks from any other crystalline forms (ZnS, Cu_2SnS_3) are detected. Similarly, from Figure **6.4b**, the observed broad diffraction peaks for (002), (100), (103), and (110) lattice planes of MoS_2 signifies its hexagonal phase and a nano dimension (JCPDS Ref. No. #75-1539). Thus, the XRD analysis clearly indicate that the synthesis of CZTS and MoS_2 can be carried out under the current hydrothermal conditions at a temperature of ~200 °C. However, it should be noted that the powder XRD pattern recorded for 1.0 wt % of MoS_2 co-catalyst loaded CZTS (CZTS–MoS_2, Figure **6.4c**) shows the diffraction peaks mainly for CZTS, while well-distinct diffraction peaks for MoS_2 remains silent. This could possibly be due to a low catalytic loading of MoS_2 to CZTS and a weaker crystalline nature of MoS_2 in contrast to the CZTS host. To investigate if there is any change in crystallite size of CZTS upon 1.0 wt % of MoS_2 loading, the average crystallite sizes of CZTS and CZTS–MoS_2 are estimated from the Debye–Scherrer formula, using eq. (1), by considering the maximum intensity (112) planes of CZTS[32]

$$D = \frac{0.9 \times \lambda}{\beta \times \cos\theta} \quad (1)$$

where λ, θ, and β are the X-ray wavelength (0.154 nm), Bragg diffraction angle, and full width at half-maximum (FWHM), respectively. Notably, the co-catalytic loading of 1.0 wt % of MoS_2 to CZTS does not exhibit any significant change in the crystallite size of CZTS (CZTS ≈ 22.9 nm, CZTS–MoS_2 ≈ 23.4 nm). This further indicates that the crystallinity of CZTS remain almost unaltered upon a 1.0 wt % of MoS_2 is co-catalytically loaded under current hydrothermal route. Alternately, the highest intensity (002) diffraction peak for MoS_2 at 2θ ≈ 14.48° corresponds to its average crystallite size of ~6.9 nm and an interlayer distance of ~0.66 nm.

6.3.2. Normalized UV–Vis DRS Absorption Spectra

The normalized UV–vis absorption spectra of 1D ZnO NWs, bare $CuInS_2$ QDs (in chloroform), bare CdSe QDs (obtained during the EPD), and the photoanodes (ZnO–CIS, ZnO–CdSe, and ZnO–CIS–CdSe) are illustrated in Figure **6.5**. The absorption spectrum of 1D ZnO NWs shows a typical absorption steep at ~384 nm, which indicates a wide-band gap of ZnO (Figure **6.5a**). Figure **6.5b** shows the characteristic broad absorption of bare $CuInS_2$ QDs in the visible range with an absorption onset at ~650 nm. In addition, $CuInS_2$ QDs also exhibit a less pronounced shoulder at ~520 nm reflecting a size quantized effect arising from the excitonic transitions,

whereas the non-appearance of sharp excitonic peaks can be ascribed to slight inhomogeneity in size and shape during the synthesis of the QDs.[40,59] Similarly, Figure **6.5c** shows a wide visible range light absorption (~400–700 nm) of bare CdSe QDs with an absorption onset at ~690 nm and excitonic peak at ~630 nm. Notably, the individual intrinsic absorption edges of $CuInS_2$ and CdSe QDs are also retained in the UV–vis spectra of all the photoanodes. This is indicative of a sufficient loading of QDs onto ZnO NWs by the EPD method (Figures **6.5d–f**). Interestingly, an enhanced molar absorptivity of ZnO–CIS–CdSe photoanode in contrast to that of ZnO–CIS and ZnO–CdSe reflects an efficient photon absorption achieved by the co-sensitization approach.

Optical properties of CZTS, CZTS–MoS_2, and MoS_2 are endorsed from their normalized UV-vis absorption spectra (Figure **6.6**). UV-vis spectra of CZTS (black line) and CZTS–MoS_2 (red line) exhibit their characteristic absorption features in a wide-visible range. Similarly, MoS_2 (green line) shows its typical broad absorption in the range of ~500 to 800 nm. The observed spectral features of MoS_2 nanosheets can be correlated with their excitonic peaks for the direct transitions and spin–orbit splitting at the VB. To be more precise, solid state absorption profile of MoS_2 exhibits three distinct peaks: (1) first excitonic peak at ~687 nm ascribed to a direct transition at the K point of the Brillouin zone, and (2) the second and third excitonic peaks at ~660 nm and ~590 nm (energy difference ~0.22 eV) arising due to the spin–orbit splitting of the top of VB at the K point for $K_4 \rightarrow K_5$ and $K_1 \rightarrow K_5$ transitions, respectively. Notably, in the solid state UV-vis study, we did not observe any sharp excitonic peak for MoS_2 corresponding to its direct transition originating from the deep VB to the CB. In contrast, the absorption spectrum of MoS_2 recorded in 1-methyl-2-pyrrolidone reveals the appearance of slight shoulders in the wavelength ranges ~350 to 500 nm (peak seen at 408 nm) and ~580 to 690 nm, indicating the presence of direct transitions in MoS_2.[60]

To further study the band energetics of CE materials, optical band gap energy (E_g) for the solid film samples are estimated from the Tauc's relation, using eq.s (2) and (3)[61]

$$(\alpha h\nu)^2 = C(h\nu - E_g) \quad (2)$$

$$\alpha = \frac{A \times \log e}{t} \quad (3)$$

where α is the absorption coefficient of CE material at a certain wavelength, h is the Planck's constant, C is a proportionality constant, ν is the frequency of incident light, and t is the thickness (in cm) of the film. The corresponding Tauc plots, where $(\alpha h\nu)^2$ is plotted as a function of photon energy (hν), estimate the E_g for CZTS (~1.66 eV, circles) and CZTS–MoS_2 (~1.62 eV, squares), as shown in Figure **6.7**.

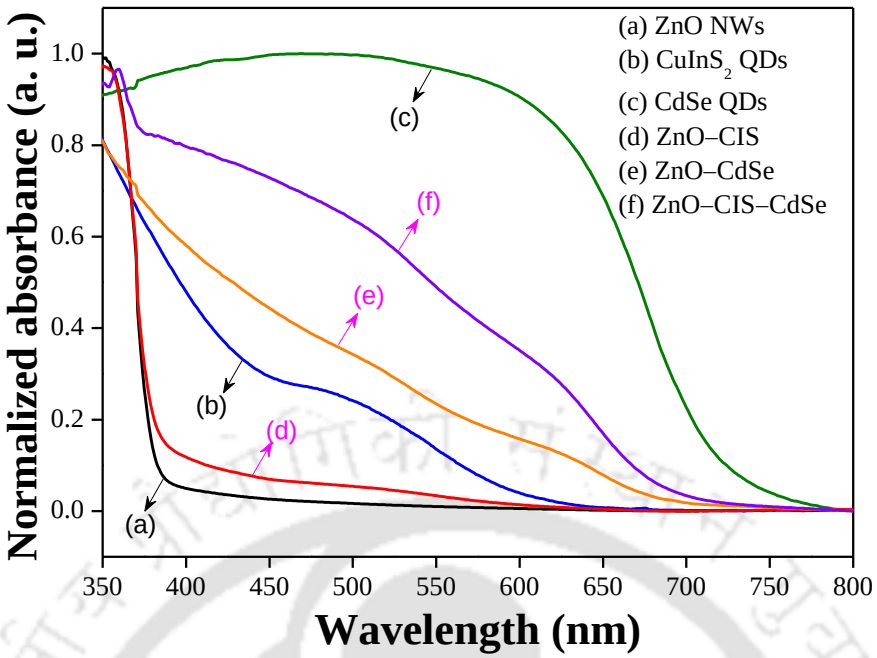

Figure 6.5 Normalized UV–vis absorption spectra of (a) 1D ZnO nanowires grown on FTO (black line), (b) $CuInS_2$ quantum dots (QDs) dispersed in chloroform (blue line), (c) CdSe QDs obtained during electrophoretic deposition (green line), (d) $CuInS_2$-sensitized ZnO NWs on FTO (ZnO–CIS, red line), (e) CdSe-sensitized ZnO NWs on FTO (ZnO–CdSe, orange line), and (f) $CuInS_2$/CdSe co-sensitized ZnO NWs on FTO (ZnO–CIS–CdSe, violet line).

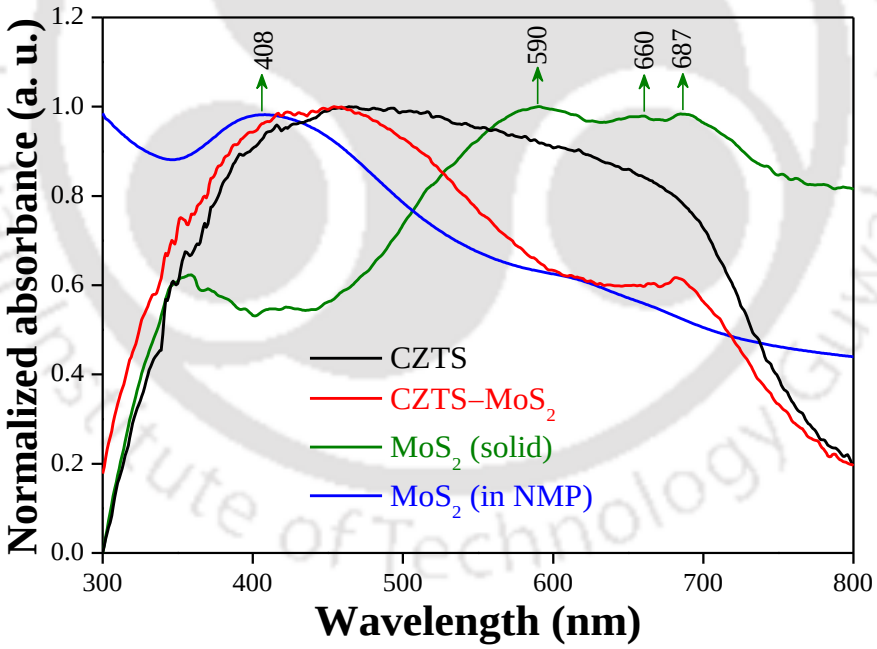

Figure 6.6 Normalized UV–vis diffused reflectance spectra of CZTS microspheres (black line), 1.0 wt % of MoS_2 loaded CZTS microspheres (red line), and MoS_2 in solid state (green line) and in 1-methyl-2-pyrrolidone (blue line).

Notably, a slight reduction (~0.04 eV) in E_g value is apparent for CZTS upon 1.0 wt % of MoS_2 loading, which is possibly be due to the presence of electronic interactions between CZTS and MoS_2 in CZTS–MoS_2. The Tauc plot also estimates an $E_g \approx 1.59$ eV for MoS_2 (triangles), which is indicative of a direct band gap of MoS_2 nanosheets owing to their monolayered distribution. It

is in good agreement to the fact that the optical property of MoS_2 can be readily tuned from an indirect to direct band gap by introducing quantum size effects *via* altering the morphology from the bulk to nano-dimensions.[62,63]

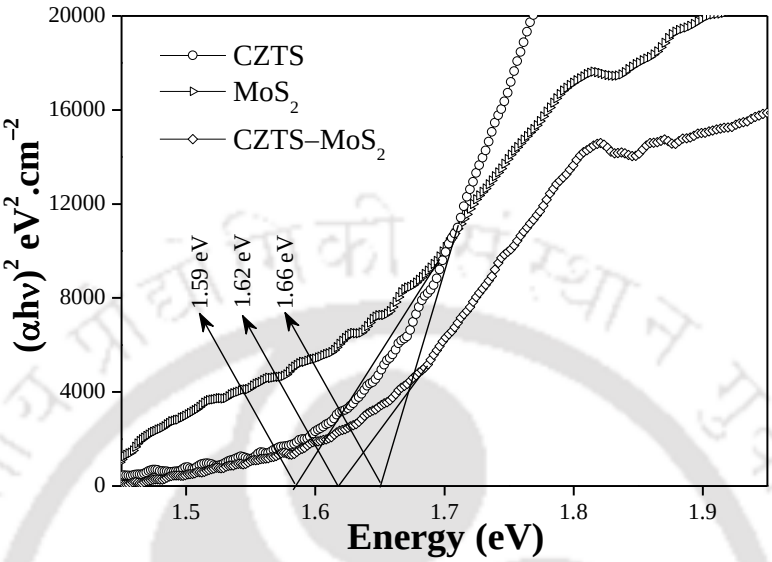

Figure 6.7 Tauc plots to estimate the band gaps of Cu_2ZnSnS_4 microspheres (CZTS; circles), MoS_2 co-catalyst (triangles), and 1.0 wt % of MoS_2 co-catalyst loaded Cu_2ZnSnS_4 microspheres (CZTS–MoS_2, squares).

6.3.3. Materials Morphology

The morphologies of 1D ZnO NWs, $CuInS_2$ QDs, CdSe QDs, CZTS microspheres, MoS_2 nanosheets, and CZTS–MoS_2 microspheres are investigated using various techniques such as, field-emission scanning electron microscopy (FESEM), energy-dispersive X-ray spectroscopy (EDS) mapping, transmission electron microscopy (TEM), and high-resolution TEM (HRTEM). Figure **6.8a** shows a representative FESEM image (top-view) of 1D ZnO NWs indicating their well-oriented vertical growth over ZnO seed layered FTO substrates. The as-grown ZnO NWs are also promising to improve the efficiency of QDSCs and DSCs due to their intrinsic properties such as, single crystalline nature, an optimum vertical length (~6–8 μm) favoring a faster charge transport, generation of 1D charge transfer pathways, and sufficient dye/QD loading ability.[31–34] Interestingly, in the present work, 1D ZnO NWs have shown an excellent stability against the external bias conditions applied to deposit the QDs. This is confirmed from the FESEM images of photoanodes (Figures **6.8b–d**), which clearly show the retention of 1D geometry of ZnO NWs even after the loading of QDs are performed under external bias of 150 mV cm^{-1} for $CuInS_2$ and 0.60 mA cm^{-1} for CdSe. However, in an EPD method, QD loading time should be optimized to ensure a sufficient adsorption of the QDs, and at the same time, to retain void-type structures in

photoanode for an easy diffusion of electrolyte. We have applied a time period of ~2–3 min to deposit $CuInS_2$ QDs, while 30 min was fixed for CdSe QDs.[40,24] To inspect the effects of higher QD loading time on morphology of photoanodes, we have deposited the QDs for prolonged time intervals and surface morphology of the photoanodes was performed using FESEM. Figure **6.9** reveals that such a persistent loading results in an agglomerated-type accumulation of QDs over ZnO NW films leading to a high surface coverage of QDs. This is not credible as it induces a few limitations such as, (1) blocking of mesopores/voids present in ZnO NW film, (2) a deteriorated loading of QDs into the inner pores of NW network, and (3) a retarded penetration/diffusion of redox electrolyte into the interior parts of mesoporous oxide films.

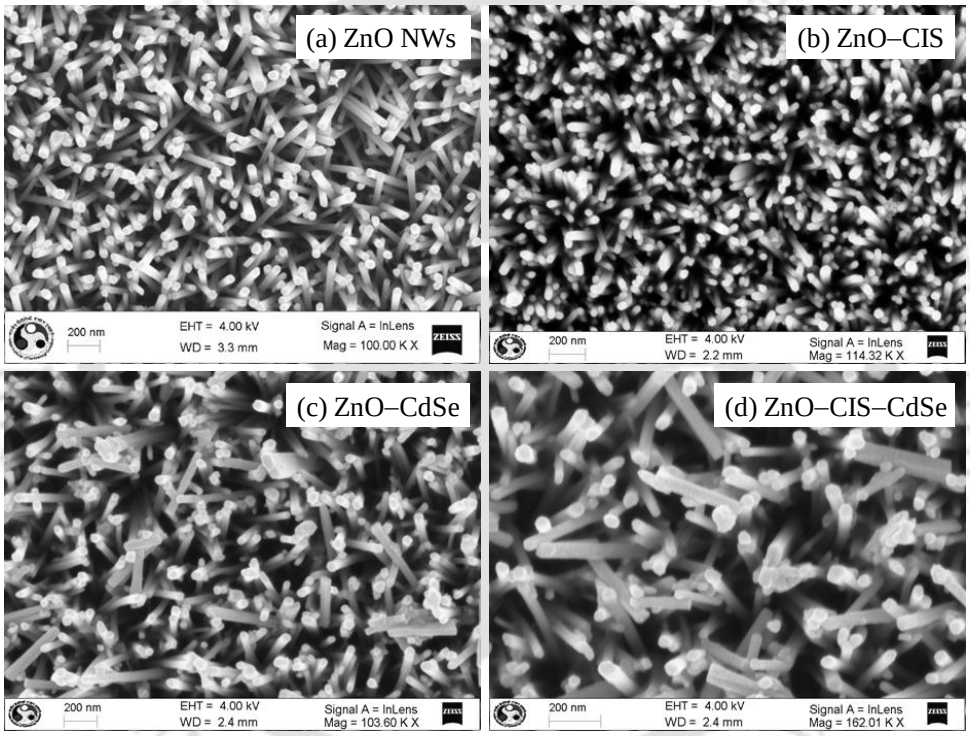

Figure 6.8 Field-emission scanning electron microscopy (FESEM) images of (a) 1D hydrothermally grown one-dimensional ZnO nanowires over ZnO seed layered FTO substrates (1D ZnO NWs) and the fabricated photoanodes (b) ZnO–CIS, (c) ZnO–CdSe, and (d) ZnO–CIS–CdSe.

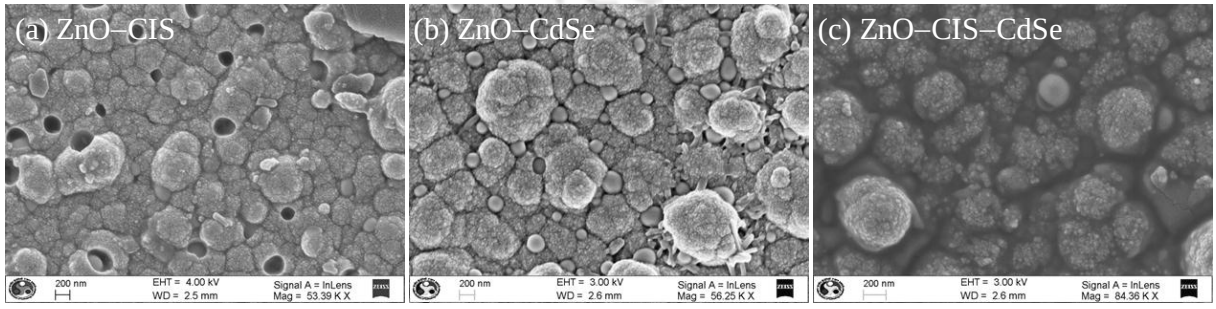

Figure 6.9 Field-emission scanning electron microscopy (FESEM) images of (a) ZnO–CIS, (b) ZnO–CdSe, and (c) ZnO–CIS–CdSe photoanodes fabricated at prolonged times periods for $CuInS_2$ and CdSe quantum dot deposition.

As can be seen from Figure **6.10**, both CZTS and CZTS–MoS_2 represent microspherical type of structures with estimated average diameters of ~200–250 nm. In addition, the mesoporous nature and void-type morphologies of CZTS and CZTS–MoS_2 microspheres are also apparent from Figure **6.10**. Such a morphology of CE materials not only provides sufficient active sites for the catalytic reduction of the electrolytes, but also facilitates the diffusion of electrolytes to the interiors of the CE films. Notably, the FESEM images of CZTS–MoS_2 composite reveal a relatively more agglomerated type features for the microspheres in contrast to those in the case of bare CZTS. This could be ascribed to an effective adhering of CZTS microspheres to MoS_2 nanosheets, readily achieved under the current hydrothermal synthetic conditions.

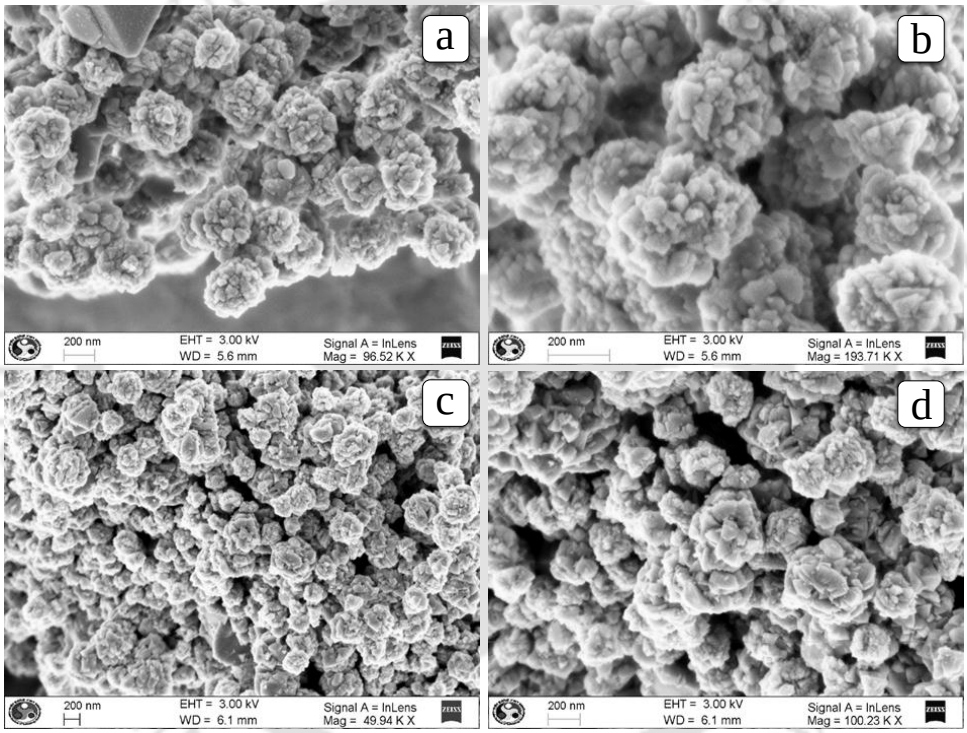

Figure 6.10 Field-emission scanning electron microscopy (FESEM) images of hydrothermally synthesized (a,b) Cu_2ZnSnS_4 (CZTS) microspheres and (c,d) 1.0 wt % of MoS_2 co-catalyst loaded Cu_2ZnSnS_4 (CZTS–MoS_2) microspheres at different magnifications.

To further elucidate the chemical composition of CE materials, EDS maps of bare CZTS and CZTS–MoS_2 composite were recorded. As can be seen, Figure **6.11a** shows the EDS map of CZTS microspheres indicating a homogeneous distribution of Cu, Zn, Sn, and S atoms in the sample. Similarly, Figure **6.11b** evidences an elemental distribution of Cu, Zn, Sn, S, and Mo atoms in CZTS–MoS_2 composite. *Please note*: EDS mapping was performed to overcome the experimentally observed elemental overlap issue between Mo and S atoms.

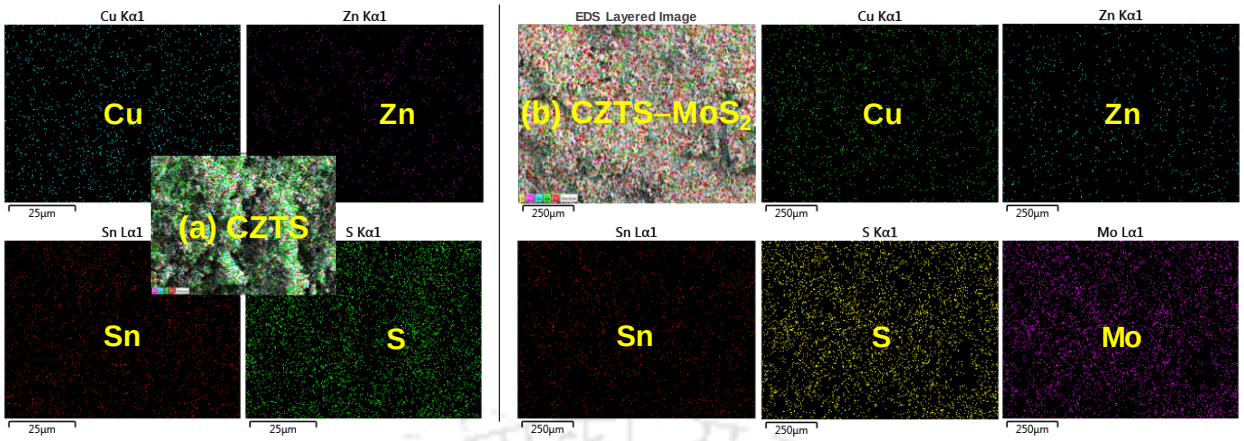

Figure 6.11 Energy-dispersive X-ray spectroscopy (EDS) maps of (a) Cu_2ZnSnS_4 microspheres (CZTS) and (b) 1.0 wt % of MoS_2 co-catalyst loaded Cu_2ZnSnS_4 microspheres (CZTS–MoS_2).

Morphology of various components used to fabricate the photoanodes and CEs are further studied by TEM analysis. A representative TEM image of bare 1D ZnO NWs is shown in Figure **6.12a**. The TEM image confirms a single crystalline nature and a 1D geometrical shape of ZnO NWs with an average diameter of ~40–50 nm. The crystalline nature of $CuInS_2$ QDs is evidenced from the well-defined lattice planes observed in the HRTEM image of $CuInS_2$ QDs (Figure **6.12b**). In addition, HRTEM image reveals a spherical shape of the $CuInS_2$ QDs with an average diameter of ~3–4 nm. The respective selected area electron diffraction (SAED) pattern of $CuInS_2$ QDs (Figure **6.12c**) are indexed to the (112), (220), and (312) lattice planes of $CuInS_2$. The inverse fast Fourier transform (IFFT) of the HRTEM image of $CuInS_2$ QDs further estimates an interplanar *d*-spacing of ~0.34 ± 0.006 nm (Figure **6.12d**). Similarly, the crystalline nature of CdSe QDs is confirmed by the well-distinct lattice patterns observed from their HRTEM image (Figure **6.12e**). HRTEM image also reveals a spherical shape, an average diameter of ~5–6 nm, and an interplanar *d*-spacing of ~0.35 nm of CdSe QDs. The SAED pattern (Figure **6.12f**) of CdSe QDs is indexed to their (111), (220), and (311) lattice planes, as also obtained from XRD.

To confirm the loading of $CuInS_2$ and CdSe QDs onto ZnO NWs by EPD method, TEM analysis of co-sensitized photoanode is performed. To prepare the sample, QD loaded ZnO NWs were scratched out from FTO substrates, sonicated in acetone (10 min), and dropped on Cu grid. A typical TEM image of a single ZnO NW loaded with $CuInS_2$ and CdSe QDs (Figure **6.12g**) estimates a thickness of ~15 nm for the QD layer deposited throughout the surface of ZnO NWs. The deposition of $CuInS_2$ and CdSe QDs is further confirmed by HRTEM image of QD loaded ZnO NW (Figure **6.12h**), which shows the well-distinct lattice fringes of both $CuInS_2$ and CdSe QDs. The IFFT of the HRTEM image (Figure **6.12i**) further estimates the interplanar *d*-spacing

of ~0.34 ± 0.005 nm for $CuInS_2$ QDs and ~0.35 ± 0.006 nm for CdSe QDs. The corresponding SAED pattern of QD loaded ZnO NW is depicted in the inset to Figure **6.12i**.

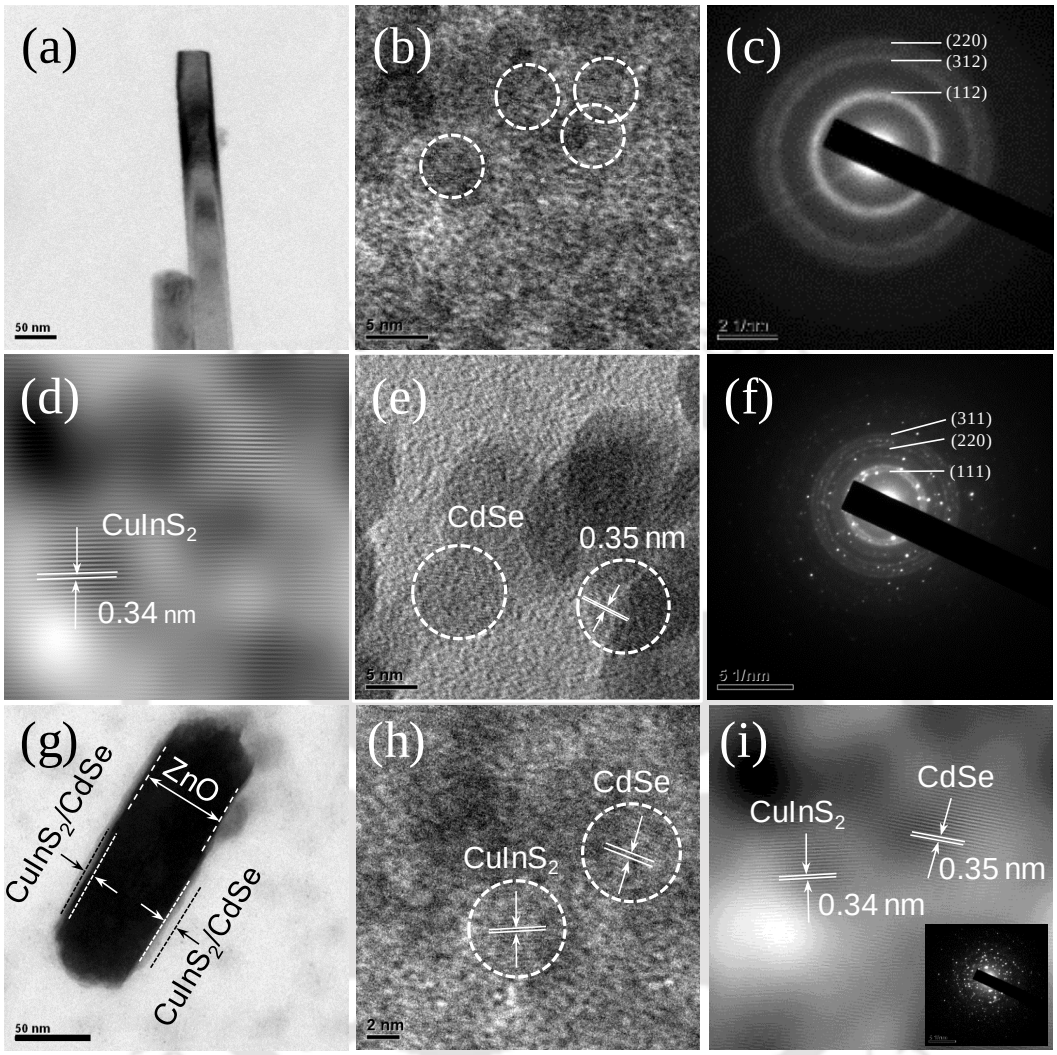

Figure 6.12 (a) Transmission electron microscopy (TEM) image of hydrothermally grown one-dimensional ZnO nanowires. (b) High-resolution TEM (HRTEM) image, (c) selected area energy diffraction (SAED) pattern, and (d) inverse fast Fourier transform (IFFT) of the HRTEM image of $CuInS_2$ quantum dots showing an interplanar *d*-spacing ~0.34 nm. (e) HRTEM image of CdSe quantum dots showing an interplanar *d*-spacing ~0.35 nm. (f) SAED pattern of CdSe quantum dots. (g) TEM image, (h) HRTEM image, and (i) IFFT of the HRTEM image of $CuInS_2$/CdSe co-sensitized one-dimensional ZnO nanowire showing well-defined lattice fringes of $CuInS_2$ and CdSe quantum dots. Inset to (i) shows the SAED pattern of $CuInS_2$/CdSe co-sensitized one-dimensional ZnO nanowires.

In addition to the photoanode materials, morphologies of the CE materials (CZTS, MoS_2, and CZTS–MoS_2) are also investigated using TEM analysis. Figure **6.13a** shows a representative TEM image of CZTS microspheres depicting an average diameter of ~200–250 nm. Similarly, the TEM image of MoS_2 nanosheets (Figure **6.13b**) shows a lateral size distribution in the range of ~3–10 nm for the smaller and larger fractions of MoS_2 nanoplatelets. For better understanding of the morphology, an illustrative HRTEM image of MoS_2 nanosheets is shown in Figure **6.13c**.

The single nanosheet of MoS_2 shows a thickness of ~8–10 nm with an estimated average length of ~40–50 nm. Further, the IFFT of the HRTEM image of MoS_2 (inset to Figure **6.13c**) estimates an interplanar *d*-spacing of ~0.66 ± 0.005 nm for the nanosheets. Figure **6.13d** shows the TEM image of 1.0 wt % of MoS_2 loaded CZTS microspheres, indicating the microspherical shape of CZTS–MoS_2 composite with an estimated diameter of ~200–250 nm. The HRTEM image of CZTS–MoS_2 (Figure **6.13e**) depicts the well-resolved lattice patterns of CZTS and MoS_2 entities. The corresponding SAED pattern of CZTS–MoS_2 is shown in the inset to Figure **6.13e**. The distinct lattice fringes of CZTS–MoS_2 are further resolved by the IFFT of its HRTEM image as shown in Figure **6.13f**. The IFFT image also estimates the interplanar *d*-spacings of CZTS and MoS_2, and are found to be ~0.31 ± 0.004 nm and ~0.66 ± 0.005 nm, respectively.

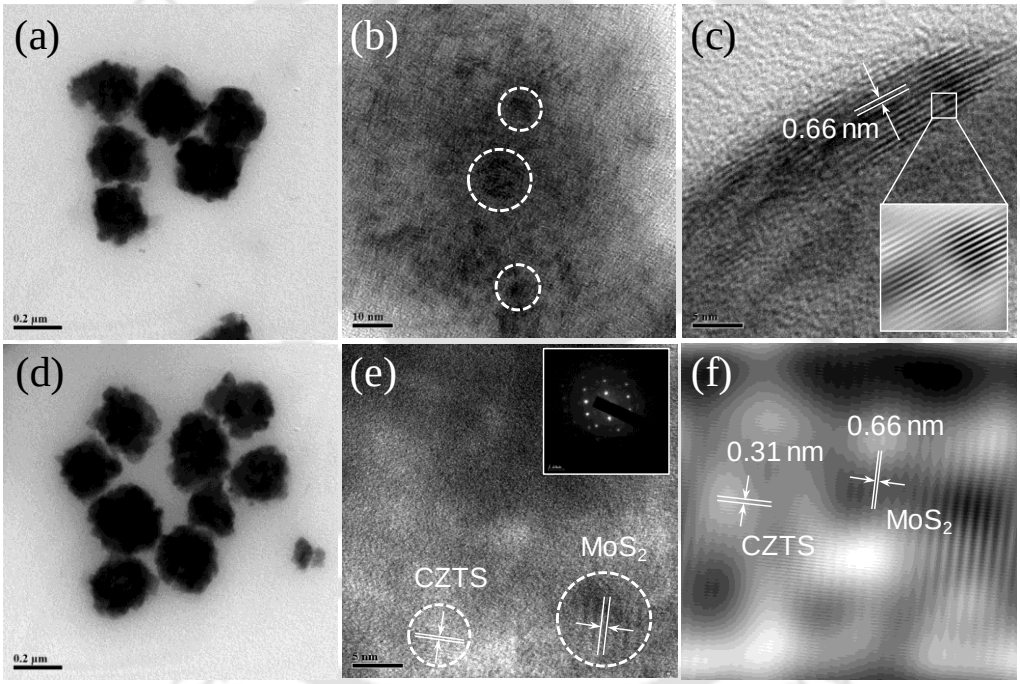

Figure **6.13** Transmission electron microscopy (TEM) images of (a) Cu_2ZnSnS_4 microspheres and (b) MoS_2 nanosheets. (c) HRTEM image of MoS_2 nanosheets. Inset to trace (c) shows the inverse fast Fourier transform of the HRTEM image of MoS_2 nanosheets. (d) TEM, (e) HRTEM, and (f) IFFT of the HRTEM image of 1.0 wt % of MoS_2 co-catalyst loaded Cu_2ZnSnS_4 microspheres showing the well-resolved lattice fringes of CZTS and MoS_2 components. Inset to trace (e) shows the SAED pattern of 1.0 wt % of MoS_2 loaded Cu_2ZnSnS_4 microspheres.

6.3.4. Steady-state Photoluminescence Study of Counter Electrodes

To gain an insight into electronic interactions between CZTS and MoS_2, steady-state PL spectra of bare CZTS (filled circle) and CZTS–MoS_2 (empty circle) are recorded at a 510 nm excitation. Figure **6.14** shows a quenching of PL emission originating from CZTS, when it is loaded with 1.0 wt % of MoS_2 co-catalyst. This confirms the presence of excited-state electronic interactions between CZTS and MoS_2 entities in their composite. It also leads to the deactivation of excited

state of CZTS *via* non-radiative processes, e.g., a favorable charge transfer from CZTS to MoS_2. Thus, it can be allegedly said that MoS_2 nanosheets can act as electrical bridge that interconnects the separated CZTS microspheres in the CE, thereby generating a faster charge transport network with a minimized electron–hole recombination in CZTS–MoS_2 composite.

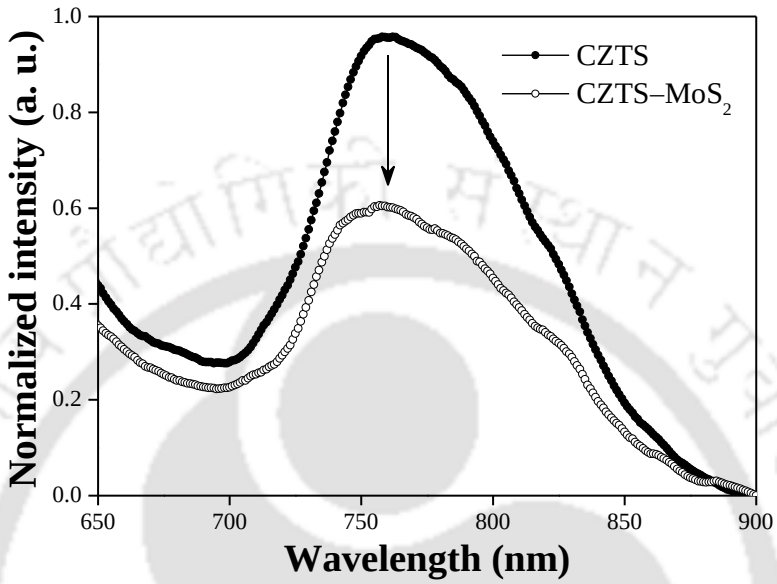

Figure 6.14 Steady-state photoluminescence (PL) spectra of CZTS (filled circle) and CZTS–MoS_2 (empty circle) solid films on FTO coated glass substrates at a 510 nm excitation.

To have a better understanding of charge transfer processes taking place within the CE materials, VB and CB edges of CZTS and MoS_2 are estimated from the corresponding absolute Mulliken electronegativity values.[64] Xu and Schoonen reported a simple method to estimate the absolute band positions of CB and VB for semiconductors using the absolute electronegativity (χ) values.[64] The top of VB (E_{VB}) at the semiconductor/electrolyte interface may be predicted from the χ value of semiconductor, using eq. (4). In general, χ of a multi-atomic compound (M_aX_b) may be defined as the geometric mean of χ values of constituent atoms.[65] The corresponding χ values for each atom can be derived from their ionization potential (IP) and electron affinity (EA) values, using eq. (5) and Mulliken electronegativity scale.[66]

$$E_{VB} = -\left\{(\chi_M^a \chi_X^b)^{\frac{1}{a+b}} - \frac{1}{2} \times E_g + 0.059(\mathrm{pH}_{zpc} - \mathrm{pH}) + E^e\right\} \quad (4)$$

$$\chi_M = \frac{1}{2} \times (IP_M + EA_M) \quad (5)$$

where χ_M and χ_X are absolute electronegativities of M and X atoms, respectively, E^e is energy of free electrons on the normal hydrogen scale (−4.5 eV), and E_g is band gap of the material.

Considering the point of zero charge, eq. (4) can be simplified to eq. (6). Therefore, E_{VB} and E_{CB} values can be calculated, using eq.s (6) and (7).

$$E_{VB} = \chi + \frac{1}{2} \times E_g - E^e \quad (6)$$

$$E_{CB} = E_{VB} - E_g \quad (7)$$

For MoS_2, IP and EA values for Mo atom are 7.10 eV and 0.746 eV, while the same for S atom are 10.36 eV and 2.08 eV, respectively.[67,68] From IP and EA values, absolute electronegativities of Mo and S are found to be 3.9 eV and 6.22 eV, respectively, using eq. (5). This further gives a χ value of 5.32 eV for MoS_2. Again, the Tauc plot estimates a band gap of ≈ 1.59 eV for MoS_2. The corresponding values of E_{VB} and E_{CB} of MoS_2 are calculated to be −5.9 eV and −4.3 eV, respectively, with respect to the vacuum level. Similarly, E_{VB} and E_{CB} for Cu_2ZnSnS_4 are found to be −5.1 eV and −3.4 eV, respectively. Such a favorable band proximity of MoS_2 and CZTS induces a facile charge transport from the CB of CZTS to that of MoS_2; on the contrary, a VB mediated hole migration from MoS_2 to CZTS is also prominent in CZTS–MoS_2 (Scheme **6.4**).

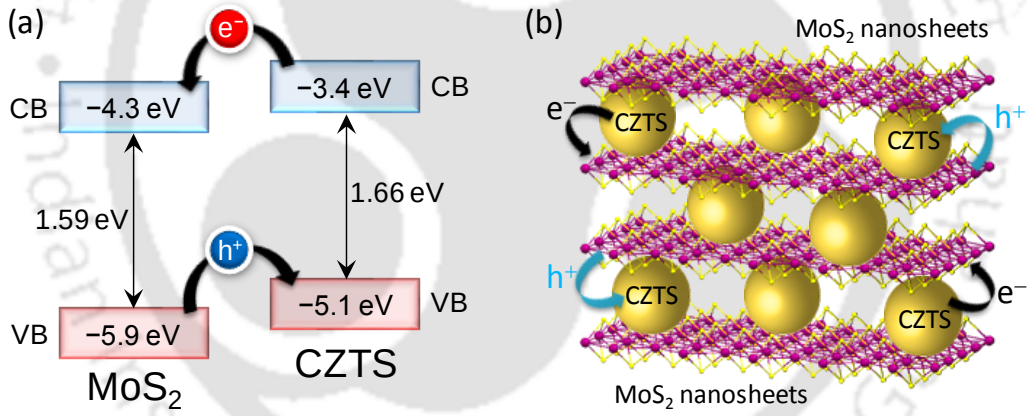

Scheme 6.4 (a) Estimated values for the top of the valence band (VB) and bottom of the conduction band (CB) for Cu_2ZnSnS_4 and MoS_2 and the favorable electron and hole charge transfer processes within the Cu_2ZnSnS_4–MoS_2 composite. *Please note*: The positions of VB and CB are calculated from the Mulliken electronegativity values of Cu_2ZnSnS_4 and MoS_2. (b) Schematic showing an interconnected charge transfer network of Cu_2ZnSnS_4 microspheres in the presence of MoS_2 nanosheets.

6.3.5. BET Surface Area and Pore Size Distribution Analysis

Nitrogen adsorption–desorption isotherm and corresponding Barrett–Joyner–Halenda pore size distribution plots for bare CZTS microspheres (filled circle) and 1.0 wt % of MoS_2 co-catalyst loaded CZTS (empty circle) are depicted in Figure **6.15**. As can be seen, both the plots exhibit type IV isotherms with H3 hysteresis loops, indicating a typical mesoporous nature of CZTS and CZTS–MoS_2. This is also favorable for an efficient catalytic performance of CEs. In addition, the

pore size distribution plots of CZTS and CZTS–MoS_2 (Inset to Figure **6.15**) show similar features of isotherms and identical pore diameters. This specifies that the surface morphology of CZTS microspheres remain unaltered even after the loading of 1.0 wt % of MoS_2 is performed under hydrothermal conditions. Notably, BET surface areas of CZTS and CZTS–MoS_2 are found to be ~18.5 m^2/g and ~20.0 m^2/g, respectively, which are adequate to produce sufficient number of active sites to accomplish an efficient reduction of redox electrolytes. Even if the co-catalytic loading of MoS_2 does not manifest a noticeable enrichment in the overall surface area, an interconnected mesoporous network of CZTS microspheres created by MoS_2 nanosheets allows a more facile collection and transfer of electrons and ions in contrast to the CZTS counterparts.

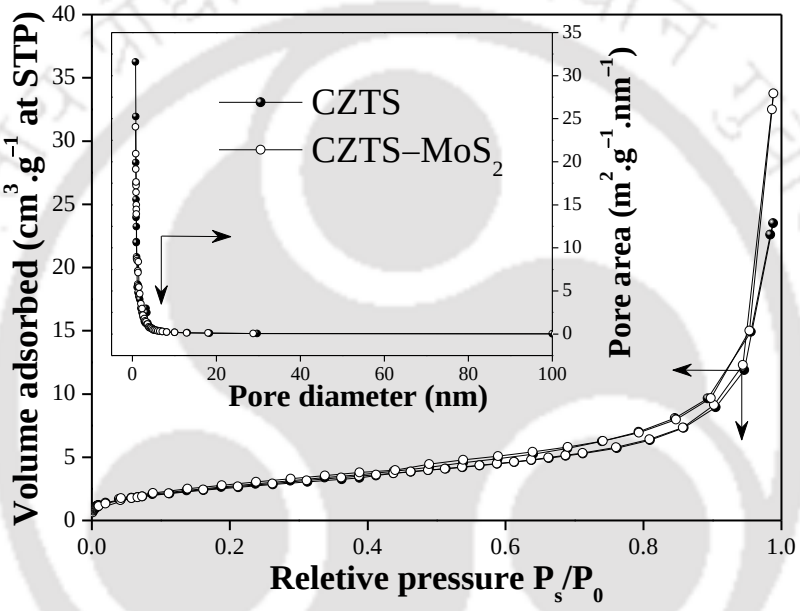

Figure 6.15 Nitrogen adsorption–desorption isotherms and Barrett–Joyner–Halenda pore size distribution plots for CZTS microspheres (filled circle) and 1.0 wt % of MoS_2 loaded CZTS microspheres (empty circle). Inset shows the corresponding pore area versus pore diameter plots for CZTS and 1.0 wt % of MoS_2 loaded CZTS.

6.3.6. Raman Spectroscopic Analysis

Figure **6.16** shows the Raman spectra of MoS_2 nanosheets, bare CZTS microspheres, and CZTS–MoS_2 composite under a 514.5 nm He–Ne laser excitation in a spectral range of 100–2000 cm^{-1}. Raman spectrum of MoS_2 nanosheets exhibit two prominent peaks at ~387 cm^{-1} and ~406 cm^{-1} (Figure **6.16a**), which are the typical E^1_{2g} (in-plane) and A_{1g} (out-of-plane) vibrational modes of MoS_2. The E^1_{2g} mode corresponds to an anti-phase oscillation of Mo and S atoms parallel to the surface plane, while A_{1g} mode represents the anti-phase oscillation of only S atoms (Mo atoms remain static) perpendicular to the surface plane. Figure **6.16a** also shows a difference of ~19 cm^{-1} between the E^1_{2g} (~387 cm^{-1}) and A_{1g} (~406 cm^{-1}) Raman bands, which is indicative of the monolayered arrangement of MoS_2 nanosheets. Similarly, from Figure **6.16b**, the strong

appearance of a single Raman peak at 331 cm^{-1} for CZTS microspheres confirms its formation of kesterite form without having any secondary phase (ZnS and Cu_2S). Interestingly, the Raman spectrum of 1.0 wt % of MoS_2 loaded CZTS microspheres also exhibit the corresponding Raman peaks for both of CZTS and MoS_2 entities, as shown in Figure **6.16c**. However, slight shifting of the intrinsic Raman peaks of CZTS and MoS_2 in the CSTS–MoS_2 composite ascribes the presence of intimate interactions between CZTS and MoS_2.

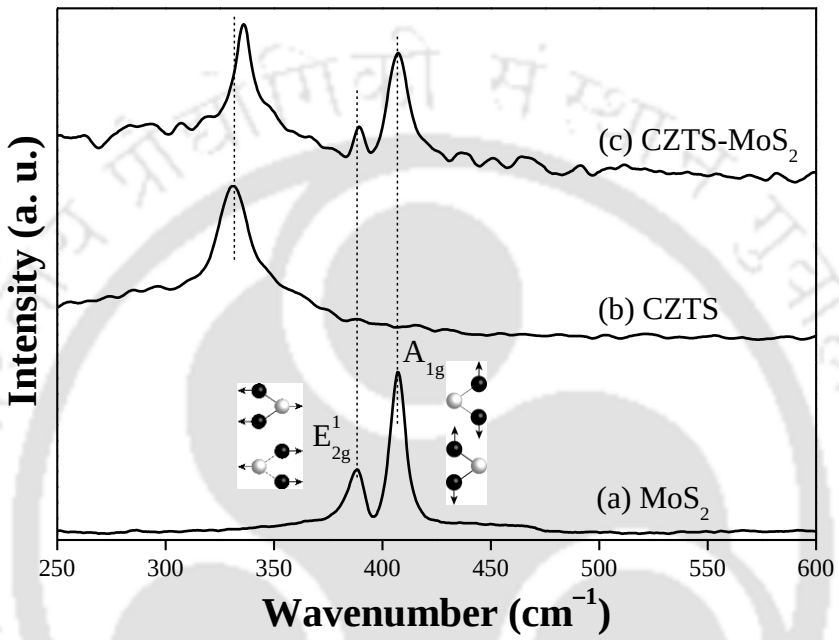

Figure 6.16 Raman spectra of (a) MoS_2 nanosheets, (b) Cu_2ZnSnS_4 microspheres, and (c) 1.0 wt % of MoS_2 loaded Cu_2ZnSnS_4 microspheres at a 514.5 nm He−Ne laser excitation. Inset to trace (a) shows the in-plane (E^1_{2g}) and out-of-plane (A_{1g}) vibrational modes for MoS_2 nanosheets (filled circle: S atom, empty circle: Mo atom).

6.3.7. Photovoltaic Performance

Photovoltaic performances of the QDSCs are evaluated against CZTS and CZTS–MoS_2 based CEs with a S^{2-}/S_n^{2-} redox couple as the electrolyte, under AM 1.5 G simulated solar spectrum at an intensity of 100 $mW.cm^{-2}$. The performance parameters such as, short-circuit current density (J_{sc}), open circuit voltage (V_{oc}), fill factor (FF), and PCE, for the cells are derived from current density–voltage (J_{sc}–V) plots (Figure **6.17a**) and summarized in Table **6.1**. In the case of CZTS CE, bare $CuInS_2$ QD sensitized devices resulted in a $J_{sc} \approx 4.72$ mA/cm^2, a $V_{oc} \approx 513$ mV, and a FF ≈ 35.9 % affording a PCE ≈ 0.87 %, whereas bare CdSe based QDSCs exhibited a $J_{sc} \approx 8.99$ mA/cm^2, a $V_{oc} \approx 606$ mV, and a FF ≈ 46.8 % yielding a PCE ≈ 2.55 %. Notably, $CuInS_2$/CdSe co-sensitized QDSCs exhibited a maximum PCE of ~4.17 % with a $J_{sc} \approx 12.78$ mA/cm^2, a $V_{oc} \approx$ 660 mV, and a FF ≈ 49.4 % against CZTS CE. Interestingly, upon changing the CE material from

bare CZTS to a 1.0 wt % of MoS_2 loaded CZTS, performance parameters of identical QDSCs are improved, as shown in Figure **6.17a**. As can be seen, $CuInS_2$/CdSe co-sensitized cell exhibited a maximum PCE of ~4.58 % with a $J_{sc} \approx 13.52$ mA/cm^2, a $V_{oc} \approx 669$ mV, and a FF ≈ 50.6 % against CZTS–MoS_2 CE, while $CuInS_2$ and CdSe sensitized devices resulted in following values: a $J_{sc} \approx 5.90$ mA/cm^2, a $V_{oc} \approx 531$ mV, and a FF ≈ 43.7 % yielding a PCE ≈ 1.36 % (for $CuInS_2$) and a $J_{sc} \approx 9.32$ mA/cm^2, a $V_{oc} \approx 614$ mV, and a FF ≈ 49.7 % yielding a PCE ≈ 2.84 % (for CdSe). The above results demonstrate that CZTS and CZTS–MoS_2 both act as effective CEs for QDSCs employing S^{2-}/S_n^{2-} as the redox electrolyte.

Excelling photovoltaic performances of CZTS–MoS_2 CE based QDSCs in contrast to the CZTS counterparts can be ascribed to a more facile charge transport achieved by CZTS microspheres upon MoS_2 loading. In essence, MoS_2 nanosheets functions as electrical bridges that interconnect CZTS microspheres, leading to a prominent charge transfer network in CEs. It is also observed that $CuInS_2$–CdSe co-sensitized QDSCs performed better as compared to the bare $CuInS_2$ and CdSe counterparts. This can be ascribed to an enhanced molar absorptivity of QDSCs employing co-sensitized photoanodes in contrast to $CuInS_2$ and CdSe counterparts. In addition, the overall high performance of all the fabricated QDSCs can be accredited to a number of factors such as, (1) an adequate loading of QDs onto the ZnO NWs by an EPD method, (2) a favorable band alignment among $CuInS_2$, CdSe, and ZnO offering an efficient photoinduced charge injection from the QDs to ZnO in the photoanodes, (3) facile charge migration and transport properties of ZnO NWs generated by the 1D pathways, (4) sufficient catalytic reduction of redox electrolyte due to the mesoporous nature of CE materials, and finally (5) an excellent charge transport property of bare as well as MoS_2 loaded CZTS microsphere based CEs.

Table 6.1 Short-circuit photocurrent density (J_{sc})^a, open-circuit voltage (V_{oc})^a, fill factor (FF), power conversion efficiency (PCE, η), maximum incident photon-to-current conversion efficiency ($IPCE_{max}$) and photoinduced electron lifetime (τ_{el}) values for the fabricated solar cells composed of one-dimensional ZnO nanowires, $CuInS_2$ and CdSe quantum dot photosensitizers, CZTS and CZTS–MoS_2 counter electrodes, and a S^{2-}/S_n^{2-} redox electrolyte.

QDSC photoanode	Counter electrode	J_{sc} (mA/cm^2)	V_{oc} (mV)	FF (%)	PCE (η, %)	$IPCE_{max}$ (%)
ZnO–CIS	CZTS	4.72 ± 0.26	513 ± 13	35.9	0.87	13
ZnO–CIS	CZTS–MoS_2	5.90 ± 0.19	531 ± 32	43.7	1.36	20
ZnO–CdSe	CZTS	8.99 ± 0.21	606 ± 57	46.8	2.55	50
ZnO–CdSe	CZTS–MoS_2	9.32 ± 0.09	614 ± 41	49.7	2.84	61
ZnO–CIS–CdSe	CZTS	12.78 ± 0.16	660 ± 14	49.4	4.17	66
ZnO–CIS–CdSe	CZTS–MoS_2	13.52 ± 0.18	669 ± 27	50.6	4.58	72

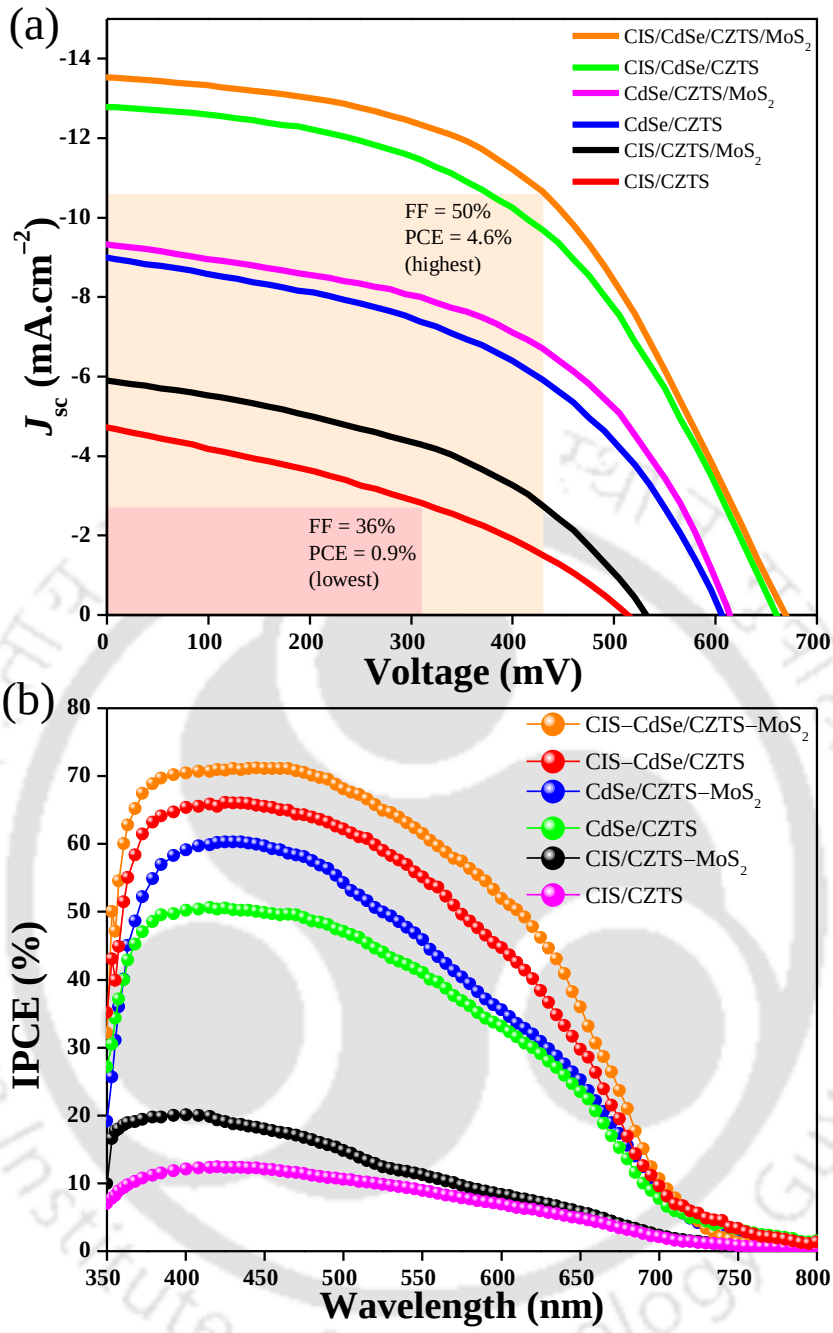

Figure 6.17 (a) Short-circuit current density–voltage (J_{sc}–V) plots for the fabricated QDSCs employing Cu_2ZnSnS_4 and 1.0 wt % of MoS_2 loaded Cu_2ZnSnS_4 microsphere based counter electrodes with sulfide/polysulfide (S^{2-}/S_n^{2-}) redox electrolyte under AM 1.5 G simulated solar illumination at an intensity of 100 $mW.cm^{-2}$. (b) Incident photon-to-current conversion efficiency (IPCE) plots for the fabricated QDSCs.

To have a better understanding of the photocurrent behavior of fabricated QDSCs, their IPCE values are recorded against a wavelength range of 360–800 nm, as depicted in Figure **6.17b**. It is clearly observed that all the QDSCs exhibits an efficient photosensitization in the visible range, which is directly correlated to the visible-light absorptivity of QD sensitizers ($CuInS_2$ and CdSe) loaded onto the respective photoanodes. As can be seen, $CuInS_2$ based

QDSCs exhibited lower IPCE values with a maximum of ~13 % (against CZTS CE) and ~20 % (against CZTS–MoS_2 CE), while the identical devices with CdSe counterparts achieved $IPCE_{max}$ of ~50 % and ~61 %, respectively. Fascinatingly, $CuInS_2$/CdSe co-sensitized QDSCs afforded the $IPCE_{max}$ of ~66 % and ~72 % against CZTS and CZTS–MoS_2 CEs, respectively. In general, IPCE values of the QDSCs can be ascribed to the efficiencies of (1) photon harvesting by the QD sensitizers, (2) photoinduced electron injection from the QDs to ZnO and collection at the FTO electrode, and (3) faster charge transport in the CE favoring the regeneration of redox electrolyte. It is therefore expected to obtain maximum IPCE values at the wavelength range where the photon absorption by the QD sensitizers is maximum. The UV–vis spectra (Figure **6.5**) of the photoanodes reveals an enhancement in light absorption in an order: ZnO–CIS < ZnO–CdSe < ZnO–CIS–CdSe. A similar pattern is also observed for the IPCE values of the fabricated QDSCs, which indicates that the highest photocurrent is readily generated by the QDSCs composed of $CuInS_2$–CdSe co-sensitized photoanodes. This is in good agreement with the corresponding J_{sc} values obtained from the J_{sc}–V curves of the devices (Figure **6.17a**). Moreover, a suitable band alignment among CdSe, $CuInS_2$, and ZnO plays a significant role to improve the photogenerated charge injection from the QDs to ZnO, leading to an efficient charge transport by ZnO NWs and their collection at the FTO electrode. Additionally, an electrically interconnected network of CZTS microspheres, generated by a co-catalytic loading of MoS_2, induces a facile charge transport in CZTS–MoS_2 CE in contrast to the CZTS counterparts. As a result, CZTS–MoS_2 CE based QDSCs exhibited superior IPCE values in contrast to the devices based on CZTS CEs. The $IPCE_{max}$ values of all the QDSCs are summarized in Table **6.1**.

6.3.8. Electrochemical Impedance Spectroscopy Analysis

To investigate the effects of MoS_2 loading on electron transport and recombination properties of the fabricated QDSCs, EIS measurements are carried out for the best-performed devices under the dark conditions at an external bias equivalent to V_{oc} at a frequency range of 10^{-1}–10^5 Hz. EIS analysis of the QDSCs mainly accounts for the charge transfer and recombination processes taking place at the CE/electrolyte interface in the high-frequency region (10^3–10^5 Hz) and ZnO/QD/electrolyte interface in the mid-frequency region (10^{-1}–10^3 Hz), and the diffusion of electrolyte in the low-frequency region (10^{-1}–10^{-2} Hz). From Figure **6.18a** it is observed that the Nyquist plots for $CuInS_2$/CdSe co-sensitized cells depict two semicircles for each of the devices. The first semicircle in the mid-frequency region accounts for the charge transfer processes taking place at the ZnO/QD/electrolyte interface, while a second semicircle in the high-frequency region

ascribes the redox reactions taking place at the CE/electrolyte interface. The co-catalytic loading of MoS_2 to CZTS lowers the internal charge recombination between the CE and the redox electrolyte, thereby enhances the J_{sc} values. Ideally, the J_{sc} values of solar cells depend on their series resistance (R_s). Interestingly, a lower value of series resistance (R_s) is observed for the QDSC fabricated with CZTS–MoS_2 CE in contrast to the CZTS counterpart. In general, R_s for a typical QDSC can be derived from the Nyquist plot, using eq. (8)[31]

$$R_S = R_{TCO} + R_{ct} + R_d \tag{8}$$

where R_{TCO} is the electron transport resistance at the FTO electrode, proportional to the sheet resistance of FTO and contact resistance at the FTO/ZnO interface, R_{ct} is the electron transfer resistance at the electrolyte/CE/FTO interface that directly depends on the carrier transport resistance at the CE surface, and R_d is the Nernst diffusion impedance within the electrolyte.

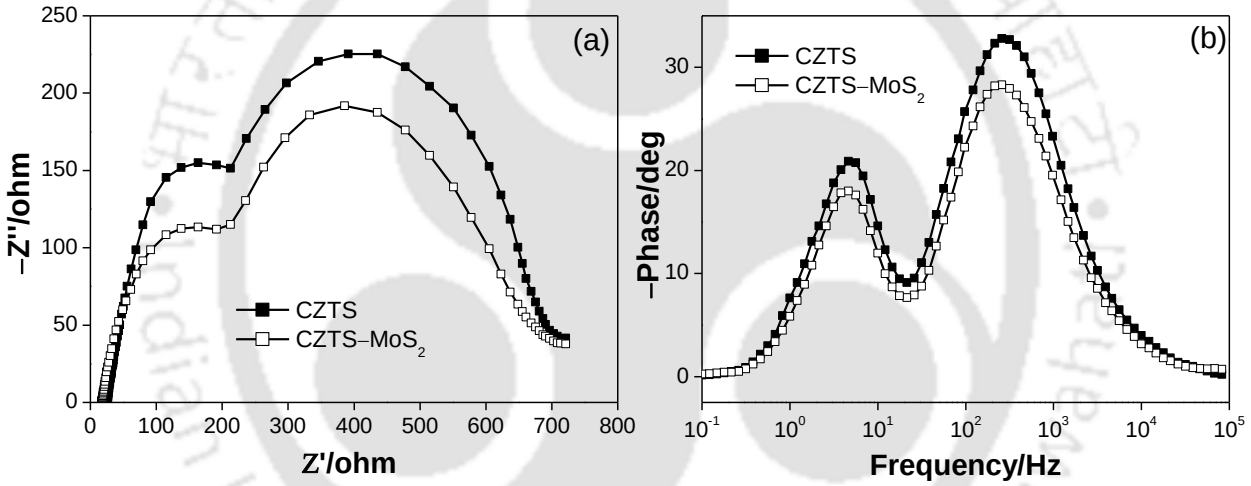

Figure 6.18 (a) Nyquist and (b) Bode phase plots for the $CuInS_2$/CdSe quantum-dot co-sensitized solar cells against Cu_2ZnSnS_4 (CZTS) and 1.0 wt % of MoS_2 loaded Cu_2ZnSnS_4 (CZTS–MoS_2) microsphere based counter electrodes with S^{2-}/S_n^{2-} as a electrolyte under the dark conditions at open-circuit voltage in a frequency range of 10^{-1}–10^5 Hz.

In the present work, CZTS–MoS_2 exhibits a more facile charge transport in CEs in contrast to the bare CZTS due to the formation of an electrically interconnected network of CZTS microspheres upon MoS_2 loading. This further retards R_{ct} value at the electrolyte/CE/FTO interface and hence a lowering of R_s is evidenced from the Nyquist plot upon MoS_2 loading. However, the values of R_h and R_d do not change much because of the involvement of identical anode and electrolyte in both the cells. It is also noticed that the V_{oc} of QDSCs are marginally improved by changing the CEs from CZTS to CZTS–MoS_2, which could be attributed to the lowering of interfacial charge recombination in the devices upon the addition of MoS_2 in the CEs.

Figure **6.18b** shows the corresponding Bode plots for $CuInS_2$/CdSe co-sensitized QDSCs with different CEs. It is observed that Bode plots for both the QDSCs represent two distinct peaks corresponding to two diode interfaces of the devices. The peak observed at the mid-frequency region accounts for the electron diffusion time constant in photoanode, which can further give the lifetime of photoinduced electron (τ_{el}) at the photoanodes, using eq. (9)

$$\tau_{el} = \left(2\pi f_p\right)^{-1} \tag{9}$$

where f_p is the maximum peak frequency in the mid-frequency region. The characteristic peak frequencies of CZTS and CZTS–MoS_2 based co-sensitized QDSCs are found to be located at ~4.91 Hz and ~4.59 Hz, respectively. The corresponding τ_{el} values for the fabricated QDSCs are found to be ~32.4 ms (for CZTS) and ~34.6 ms (for CZTS–MoS_2).

6.4. SUMMARY

- Fabrication of an efficient QDSC involving a noble metal free counter electrode utilizing MoS_2 loaded CZTS–MoS_2 is demonstrated.
- Epitaxially grown 1D ZnO NWs have revealed an excellent stability against the external bias conditions applied for the electrodeposition of QDs.
- A $CuInS_2$–CdSe co-sensitization approach provided an efficient photon harvesting ability of the QDSCs in contrast to the bare $CuInS_2$ or CdSe counterparts, which is also reflected in an improved PCE of co-sensitized QDSCs
- MoS_2 in its nanosheets form performs the role of an electrical bridge that interconnects the CZTS microspheres, leading to a prominent charge transfer network in the CE owing to a favorable band alignment between CZTS and MoS_2 entities in their composite.
- Electrochemical impedance spectroscopy revealed a lower series resistance of the QDSCs composed of CZTS–MoS_2 based CE in contrast to the bare CZTS counterpart.

4.5. REFERENCES

1. Kamat, P. V. *J. Phys. Chem. Lett.* **2013**, *4*, 908–918.
2. Kamat, P. V. *Acc. Chem. Res.* **2012**, *45*, 1906–1915.
3. Tisdale, W. A.; Williams, K. J.; Timp, B. A.; Norris, D. J.; Aydil, E. S.; Zhu, X. Y. *Science* **2010**, *328*, 1543−1547.
4. Kamat, P. V. *J. Phys. Chem. C* **2008**, *112*, 18737–18753.
5. Li, L.; Yang, X.; Gao, J.; Tian, H.; Zhao, J.; Hagfeldt, A.; Sun, L. *J. Am. Chem. Soc.* **2011**, *133*, 8458–8460.
6. Wang, H.; Bai, Y. S.; Zhang, H.; Zhang, Z. H.; Li, J. H.; Guo, L. *J. Phys. Chem. C* **2010**, *114*, 16451–16455.
7. Robel, I.; Subramanian, V.; Kuno, M.; Kamat, P. V. Quantum Dot Solar Cells. *J. Am. Chem. Soc.* **2006**, *128*, 2385–2393.
8. Lee, H. J.; Yum, J.-H.; Leventis, H. C.; Zakeeruddin, S. M.; Haque, S. A.; Chen, P.; Seok, S. I.; Grätzel, M.; Nazeeruddin, M. K. *J. Phys. Chem. C* **2008**, *112*, 11600–11608.
9. Chang, J.-Y. Chang, S. C.; Tzing, S.-H.; Li, C.-H. *ACS Appl. Mater. Interfaces* **2014**, *6*, 22272–22281.
10. Chang, C.-C.; Chen, J.-K.; Chen, C.-P.; Yang, C.-H.; Chang, J.-Y. *ACS Appl. Mater. Interfaces* **2013**, *5*, 11296–11306.
11. Li, W.; Pan, Z.; Zhong, X. *J. Mater. Chem. A* **2015**, *3*, 1649–1655.
12. Panthani, M. G.; Stolle, C. J.; Reid, D. K.; Rhee, D. J.; Harvey, T. B.; Akhavan, V. A.; Yu, Y.; Korgel, B. A. *J. Phys. Chem. Lett.* **2013**, *4*, 2030–2034.
13. Boix, P. P.; Larramona, G.; Jacob, A.; Delatouche, B.; Mora-Seró, I.; Bisquert, J. *J. Phys. Chem. C* **2012**, *116*, 1579–1587.
14. Im, S. H.; Lim, C.-S.; Chang, J. A.; Lee, Y. H.; Maiti, N.; Kim, H.-J.; Nazeeruddin, M. K.; Grätzel, M.; Seok, S. I. *Nano Lett.* **2011**, *11*, 4789–4793.
15. Bang, J. H.; Kamat, P. V. *ACS Nano* **2009**, *3*, 1467–1476.
16. Yu, X.-Y.; Lei, B.-X.; Kuang, D.-B.; Sua, C.-Y. *Chem. Sci.* **2011**, *2*, 1396–1400.
17. Jumabekov, A. N.; Deschler, F.; Böhm, D.; Peter, L. M.; Feldmann, J.; Bein, T. *J. Phys. Chem. C* **2014**, *118*, 5142–5149.
18. Tao, L.; Xiong, Y.; Liu, H.; Shen, W. *Nanoscale* **2014**, *6*, 931–938.
19. Li, T.-L.; Lee, Y.-L.; Teng, H. *Energy Environ. Sci.* **2012**, *5*, 5315–5324.
20. Chang, J. Y.; Lin, J. M.; Su, L. F.; Chang, C. F. *ACS Appl. Mater. Interfaces* **2013**, *5*, 8740–8752.
21. Santra, P. K.; Kamat, P. V. *J. Am. Chem. Soc.* **2012**, *134*, 2508–2511.
22. Tian, J.; Lv, L.; Wang, X.; Fei, C.; Liu, X.; Zhao, Z.; Wang, Y.; Cao, G. *J. Phys. Chem. C* **2014**, *118*, 16611−16617.
23. Zhang, Q.; Guo, X.; Huang, X.; Huang, S.; Li, D.; Luo, Y.; Shen, Q.; Toyoda, T.; Meng, Q. *Phys. Chem. Chem. Phys.* **2011**, *13*, 4659–4667.
24. Yu, X.-Y.; Liao, J.-Y.; Qiu, K.-Q.; Kuang, D.-B.; Su, C.-Y. *ACS Nano* **2011**, *5*, 9494–9500.
25. O'Regan B.; Grätzel, M. *Nature* **1991**, *353*, 737–740.
26. Seol, M.; Ramasamy, E.; Lee, J.; Yong, K. *J. Phys. Chem. C* **2011**, *115*, 22018–22024.
27. Tian, J.; Uchaker, E.; Zhang, Q.; Cao, G. *ACS Appl. Mater. Interfaces* **2014**, *6*, 4466−4472.
28. Yu, M.; Long, Y.-Z.; Sun, B.; Fan, Z. *Nanoscale*, **2012**, ***4***, 2783–2796.

29. Fan, J. D.; Hao, Y.; Cabot, A.; Johansson, E. M. J.; Boschloo, G.; Hagfeldt, A. *ACS Appl. Mater. Interfaces* **2013**, *5*, 1902−1906.
30. Gonzalez-Valls, I.; Lira-Cantu, M. *Energy Environ. Sci.* **2009**, *2*, 19–34.
31. Barpuzary, D.; Banik, A.; Panda, A. N.; Qureshi, M. *J. Phys. Chem. C* **2015**, *119*, 3892–3902.
32. Barpuzary, D.; Patra, A. S.; Vaghasiya, J. V.; Solanki, B. G.; Soni, S. S.; Qureshi, M. *ACS Appl. Mater. Interfaces* **2014**, *6*, 12629–12639.
33. Chetia, T. R.; Barpuzary, D.; Qureshi, M. *Phys. Chem. Chem. Phys.* **2014**, *16*, 9625–9633.
34. Barpuzary, D.; Qureshi, M. *ACS Appl. Mater. Interfaces*, **2013**, *5*, 11673–11682.
35. Choi, Y.; Seol, M.; Kim, W.; Yong, K. *J. Phys. Chem. C* **2014**, *118*, 5664−5670.
36. Becker, M. A.; Radich, J. G.; Bunker, B. A.; Kamat, P. V. *J. Phys. Chem. Lett*. **2014**, *5*, 1575−1582.
37. Santra, P. K.; Kamat, P. V. *J. Am. Chem. Soc.* **2013**, *135*, 877–885.
38. Liu, I-P.; Chang, C.-W.; Teng, H.; Lee, Y.-L. *ACS Appl. Mater. Interfaces* **2014**, *6*, 19378–19384.
39. Salant, A.; Shalom, M.; Hod, I.; Faust, A.; Zaban, A.; Banin, U. *ACS Nano* **2010**, 4, 5962–5968.
40. Santra, P. K.; Nair, P. V.; Thomas, K. G.; Kamat, P. V. *J. Phys. Chem. Lett.* **2013**, *4*, 722–729.
41. Yun, S.; Hagfeldt, A.; Ma, T. *Adv. Mater.* **2014**, *26*, 6210–6237.
42. Shalom, M.; Dor, S.; Rühle, S.; Grinis, L. *J. Phys. Chem. C* **2009**, *113*, 3895–3898.
43. Jovanovski, V.; Gonzalez-Pedro, V.; Gimenez, S.; Azaceta, E.; Cabanero, G.; Grande, H.; Tena-Zaera, R.; Mora-Sero, I.; Bisquert, J. *J. Am. Chem. Soc.* **2011**, *133*, 20156–20159.
44. Savariraj, A. D.; Viswanathan, K. K.; Prabakar, K. *ACS Appl. Mater. Interfaces* **2014**, *6*, 19702−19709.
45. Xin, X. K.; He, M.; Han, W.; Jung, J. H.; Lin, Z. Q. *Angew. Chem., Int. Ed.* **2011**, *50*, 11739−11742.
46. Dai, P. C.; Zhang, G.; Chen, Y. C.; Jiang, H. C.; Feng, Z. Y.; Lin, Z. J.; Zhan, J. H. *Chem. Commun.* **2012**, *48*, 3006–3008.
47. Xu, J.; Yang, X.; Yang, Q.-D.; Wong, T.-L..; Lee, C.-S. *J. Phys. Chem. C* **2012**, *116*, 19718–19723.
48. Cao, Y.; Xiao, Y.; Jung, J.-Y.; Um, H.-D.; Jee, S.-W.; Choi, H. M.; Bang, J. H.; Lee, J.-H. *ACS Appl. Mater. Interfaces* **2013**, *5*, 479−484.
49. Chen, H.; Kou, D.; Chang, Z.; Zhou, W.; Zhou, Z.; Wu, S. *ACS Appl. Mater. Interfaces* **2014**, *6*, 20664–20669.
50. Yuan, S. J.; Zhou, Z. J.; Hou, Z. L.; Zhou, W. H.; Yao, R. Y.; Zhao, Y.; Wu, S. X. *Chem.—Eur. J.* **2013**, *19*, 10107–10110.
51. Fairbrother, A.; García-Hemme, E.; Izquierdo-Roca, V.; Fontané, X.; Pulgarín-Agudelo, F. A.; Vigil-Galán, O.; Peérez-Rodríguez, A.; Saucedo, E. *J. Am. Chem. Soc.* **2012**, *134*, 8018–8021.
52. Scragg, J. J.; Kubart, T.; Watjen, J. T.; Ericson, T.; Linnarsson, M. K.; Bjorkman, C. P. *Chem. Mater.* **2013**, *25*, 3162–3171.
53. Scragg, J. J.; Waĺtjen, J. T.; Edoff, M.; Ericson, T.; Kubart, T.; Platzer-Bjoĺrkman, C. *J. Am. Chem. Soc.* **2012**, *134*, 19330–19333.

54. Park, H.; Chang, S.; Jean, J.; Cheng, J. J.; Araujo, P. T.; Wang, M.; Bawendi, M. G.; Dresselhaus, M. S.; Bulović, V.; Kong, J.; Gradečak, S. *Nano Lett.* **2013**, *13*, 233–239.
55. Li, L. A.; Pandey, A.; Werder, D. J.; Khanal, B. P.; Pietryga, J. M.; Klimov, V. I. *J. Am. Chem. Soc.* **2011**, *133*, 1176–1179.
56. Liu, W. C.; Guo, B. L.; Wu, X. S.; Zhang, F. M.; Mak, C. L.; Wong, K. H. *J. Mater. Chem. A*, **2013**, *1*, 3182–3186.
57. Wang, W.; Zhang, K.; Qiao, Z.; Li, L.; Liu, P.; Yang, Y. *Ind. Eng. Chem. Res.* **2014**, *53*, 10301–10309.
58. Greene, L. E.; Law, M.; Tan, D. H.; Montano, M.; Goldberger, J.; Somorjai, G.; Yang, P. *Nano Lett.* **2005**, *5*, 1231–1236.
59. Kolny-Olesiak, J.; Weller, H. *ACS Appl. Mater. Interfaces* **2013**, *5*, 12221−12237.
60. Gopalakrishnan, D.; Damien, D.; Shaijumon, M. M. *ACS Nano* **2014**, *8*, 5297–5303.
61. Barpuzary, D.; Khan, Z.; Vinothkumar, N.; De, M.; Qureshi, M. *J. Phys. Chem. C* **2012**, *116*, 150–156.
62. Muscuso, L.; Cravanzola, S.; Cesano, F.; Scarano, D.; Zecchina, D. *J. Phys. Chem. C* **2015**, *119*, 3791–3801.
63. Wilcoxon, J. P.; Samara, G. A. *Phys. Rev. B* **1995**, *51*, 7299–7303.
64. Xu, Y.; Schoonen, A. A. *Am. Mineral.* **2000**, *85*, 543–556.
65. Netherco, Ah. *Phys. Rev. Lett.* **1974**, *33*, 1088–1091.
66. Mulliken, R. S. *J. Chem. Phys.* **1934**, *2*, 782–793.
67. Moore, C. E. *Nat. Stand. Ref. Data Ser.* (Nat. Bur. Stand., U.S. 1970) **1970**, NSRDS-NBS 34.
68. Hotop, H.; Lineberger, W. C. *J. Phys. Chem. Ref. Data* **1985**, *14*, 731–750.

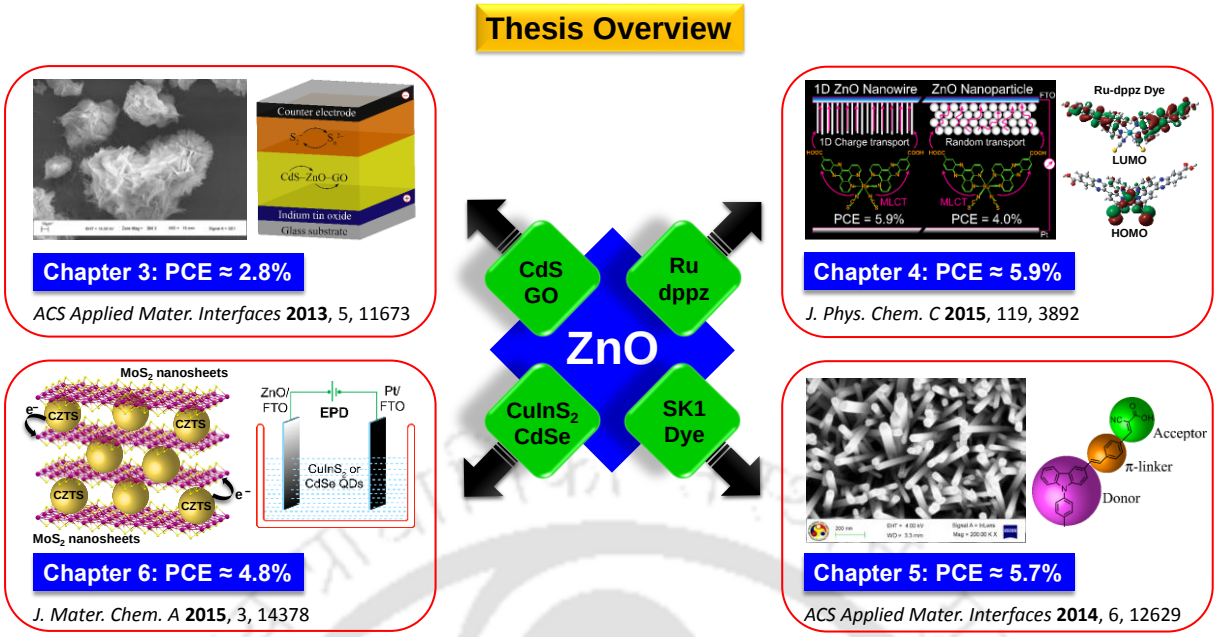

Power Conversion Efficiency (PCE) Comparison Table

Table 1. Comparison of the photovoltaic performance of ZnO based dye-sensitized solar cells by our approaches to the available literature reports as described in Chapter 1.

ZnO structures	Sensitizer	J_{sc} (mA.cm^{-2})	V_{oc} (V)	FF (%)	η (%)	Ref.
Hierarchical aggregates	N719	19.8	0.64	59	7.5	86
ZnO NWs/TiO_2 shell	N719	15.5	0.77	-	7.0	93
Commercial nanopowders	N719	18.1	0.62	58	6.6	94
ZnO tetrapod/SnO_2/ZnO core–shell NPs	N719	16.3	0.65	59	6.3	95
ZnO aggregates/TiO_2 shell	N3	15.8	0.70	56	6.3	96
Hierarchical aggregates	N3	21.0	0.66	44	6.1	97
Nanosheet	D149	18.0	0.53	63	6.1	98
One dimensional NWs	**Ru-dppz**	**11.2**	**0.80**	**63**	**5.9**	**Chap. 4**
One dimensional NWs	**SK1**	**12.0**	**0.71**	**64**	**5.7**	**Chap. 5**
Oriented porous film	D149	12.2	0.69	65	5.6	99
NPs + scattering hollow cavities	N719	15.7	0.56	62	5.5	100
NPs	D102	17.4	0.63	48	5.4	101
Hierarchical aggregates	N3	18.7	0.65	45	5.4	102
Hierarchical aggregates	D205	12.2	0.65	67	5.3	103
ZnO/Nb_2O_5 shell	N719	12.4	0.71	59	5.2	104
Tetrapod-like ZnO nanopowders	D149	12.4	0.60	65	4.9	105
Nanosheets/NWs	N719	10.9	0.68	65	4.8	106

Self-assembled nanostructures	N719	10.7	0.71	62	4.7	107
NWs/NPs	N3	15.2	0.61	46	4.2	108
Hierarchical NWs/nanoporous layer	D149	12.3	0.57	58	4.1	109
Mesoporous film	N719	11.8	0.65	52	4.0	110
NPs	**Ru-dppz**	**8.9**	**0.70**	**66**	**4.0**	**Chap. 4**
NPs	**SK1**	**8.9**	**0.62**	**63**	**3.6**	**Chap. 5**
Hierarchical NWs	N719	8.8	0.68	53	2.6	111
NWs	D102	14.1	0.55	34	2.6	112
Nanorods	Z907	6.4	0.72	49	2.3	113
NWs	N719	9.3	0.67	34	2.1	114

Table 2. Comparison of the photovoltaic performance of ZnO based semiconductor-sensitized solar cells by our approaches to the available literature reports as described in Chapter 1.

ZnO structures	**Sensitizer**	**J_{sc} (mA.cm^{-2})**	**V_{oc} (V)**	**FF (%)**	**η (%)**	**Ref.**
ZnO tetrapods	ZnSe/CdSe/ZnSe	17.3	0.76	47	6.2	87
Branched nanorods and nanotetrapod	CdS/CdSe	16.5	0.70	45	5.2	125
NP film/microsphere	CdS/CdSe	17.1	0.56	53	5.0	126
NW array	$Zn_xCd_{1-x}Se$	18.0	0.65	40	4.7	127
NPs passivated with TiO_2	CdS/CdSe	15.4	0.62	49	4.6	128
One dimensional NWs	**$CuInS_2$/CdSe**	**13.5**	**0.67**	**50**	**4.5**	**Chap. 6**
NW array	ZnSe/CdSe	11.9	0.83	45	4.5	129
NPs	CdS/CdSe	10.4	0.68	62	4.4	130
Nano-tetrapods	CdS/CdSe	13.8	0.72	42	4.2	131
NW array	CdS/CdSe	17.3	0.62	38	4.1	132
NW array	ZnSe/CdSe	11.4	0.81	43	4.0	133
NW array	CdS/CdSe	12.6	0.68	42	3.6	134
ZnO nanorods passivated with TiO_2	CdS/CdSe	9.9	0.61	52	3.1	135
Branched n-Si NW/ZnO nanorods	CdS/CdSe	11.0	0.71	38	3.0	136
NP based nanourchins	**CdS/GO**	**7.3**	**0.70**	**54**	**2.8**	**Chap. 3**
Nanosheets	CdS/CdSe	19.3	0.49	28	2.6	138
NPs/nanorods	CdS/CdSe	7.8	0.55	57	2.4	139
NWs/mesoporous hollow spheres	CdS/CdSe	9.0	0.51	51	2.3	140
NWs	CdS/CdSe	8.3	0.55	51	2.3	141

Book Chapter

1. **D. Barpuzary**, M. Qureshi; *Graphene Filled Polymers in Photovoltaic* in "Graphene-Based Polymer Nanocomposites in Electronics." Eds.: K. K. Sadasivuni, D. Ponnamma, etc., **Springer Series on Polymer and Composite Materials**; Springer International Publishing: Switzerland, 157–191 (**2015**) ISBN 978-3-319-13875-6

Journal Articles

1. **D. Barpuzary**, A. Banik, G. Gogoi, M. Qureshi; *Noble metal-free counter electrode utilizing Cu_2ZnSnS_4 loaded with MoS_2 for efficient solar cells based on ZnO nanowires co-sensitized with $CuInS_2$–CdSe quantum dots*.
J. Mater. Chem. A 3, 14378–14388, (**2015**) DOI: 10.1039/C5TA03396A

2. **D. Barpuzary**, A. Banik, A. N. Panda, M. Qureshi; *Mimicking the heteroleptic dyes for an efficient one-dimensional ZnO based dye-sensitized solar cell using the homoleptic ruthenium(II) dipyridophenazine complex as a photosensitizer*.
J. Phys. Chem. C 119, 3892–3902, (**2015**) DOI: 10.1021/JP510422D

3. **D. Barpuzary**, A. S. Patra, J. V. Vaghasiya, B. G. Solanki, S. S. Soni, M. Qureshi; *Highly efficient one-dimensional ZnO nanowire-based dye-sensitized solar cell using a metal-free, D–π–A-type, carbazole derivative with more than 5% power conversion*.
ACS Applied Mater. Interfaces 6, 12629–12639 (**2014**) DOI: 10.1021/AM5026193

4. T. R. Chetia, **D. Barpuzary**, M. Qureshi; *Enhanced photovoltaic performance utilizing effective charge transfers and light scattering effects by the combination of mesoporous, hollow 3D-ZnO along with 1D-ZnO in CdS quantum dot sensitized solar cells*.
Phys. Chem. Chem. Phys. 16, 9625–9633 (**2014**) DOI: 10.1039/C3CP55276D

5. A. S. Patra, N. Vinothkumar, **D. Barpuzary**, M. De, M. Qureshi; *Strontium doped lanthanum manganites for efficient and robust photocatalytic water oxidation coupled with graphene oxide*.
Mater. Lett. 131, 125–127 (**2014**) DOI:10.1016/J.MATLET.2014.05.176

6. **D. Barpuzary**, M. Qureshi; *Enhanced photovoltaic performance of semiconductor-sensitized ZnO–CdS coupled with graphene oxide as a novel photoactive material*.
ACS Applied Mater. Interfaces 5, 11673–11682 (**2013**) DOI: 10.1021/AM403268W

7. **D. Barpuzary**, Z. Khan, N. Vinothkumar, M. De, M. Qureshi; *Hierarchically grown urchinlike CdS@ZnO and CdS@Al_2O_3 heteroarrays for efficient visible-light-driven photocatalytic hydrogen generation*.
J. Phys. Chem. C 116, 150–156 (**2012**) DOI: 10.1021/JP207452C

8. Z. Khan, T. R. Chetia, A. K. Vardhaman, **D. Barpuzary**, C. V. Satri, M. Qureshi; *Visible light assisted photocatalytic hydrogen generation and organic dye degradation by CdS–metal oxide hybrids in presence of graphene oxide*.
RSC Adv. 2, 12122–12128 (**2012**) DOI: 10.1039/C2RA21596A

9. Z. Khan, **D. Barpuzary**, O. Baswant, S. Sutradhar, M. Qureshi; *Directed growth of 1D cadmium sulfide by chemically anchored Al_2O_3 and ZnO nanoparticles*.
Mater. Lett. 65, 1168–1171 (**2011**) DOI:10.1016/J.MATLET.2011.01.029

Oral Presentations

1. **D. Barpuzary**; *Role of epitaxially grown ZnO nanowires in efficient dye-sensitized solar cells based on Ru-dppz and metal-free carbazole dyes*. **Chem Convene** at the Department of Chemistry, Indian Institute of Technology Guwahati, Guwahati, Assam, India (**2015**)

2 **D. Barpuzary**; *Solar-to-power conversion employing metal oxide/chalcogenide based hybrid nanomaterials for photocatalytic hydrogen production and photovoltaic device applications*. **Indo–Sweden Workshop** at Center for Nanotechnology, Indian Institute of Technology Guwahati, Guwahati, Assam, India (**2014**)

Presentations in Conferences

1. *Enhanced photovoltaic performance of semiconductor sensitized ZnO–CdS coupled with graphene oxide as a novel photoactive material*. **International Conference on Nano Science and Technology** (**ICONSAT**) at Punjab University, Chandigarh, India (**2014**)

2 **International Conference on Nano Science and Nanotechnology** (**ICANN**) at Center for Nanotechnology, Indian Institute of Technology Guwahati, Guwahati, Assam, India (**2014**)

3. *Design and development of photovoltaic cells based on metal oxide–metal chalcogenide–graphene oxide composites*. **Frontiers in Chemical Sciences** (**FICS**) at the Department of Chemistry, Indian Institute of Technology Guwahati, Guwahati, Assam, India (**2012**)

4. *Metal oxide–metal chalcogenide–graphene oxide composites: Design and development of photovoltaic cells*. **ICMS-Cambridge University Winter School on Frontiers in Materials Science** at Jawaharlal Nehru Centre for Advanced Scientific Research, Bangaluru, India (**2011**)